UNIVERSITÀ DEGLI STUDI DI PADOVA

Department of Physics and Astronomy

master's degree in astronomy

Master's Degree Thesis

Analysis and characterization of fresh craters on Mars

Supervisor:
Prof. Monica Lazzarin
Co-supervisor:
Dr. Gabriele Cremonese
Co-supervisor:
Dr. Alice Lucchetti

Candidate:
Stefano Cammisa
Matr.:1181551

Academic Year 2018-2019

Abstract

Impact craters are present all throughout our Solar System and are often old, large and clearly visible structures on most planetary bodies. Especially on Mars, thanks to high resolution imaging it was possible to discover small craters formed in the last years and not modified by any process, known as fresh craters. We study the characteristics of this population and search for correlations with various parameters of the Martian surface. Considering a database of 279 fresh craters, we measure the diameter of each crater and the extension of the ejecta material. We look for possible relationships between these parameters and characteristics of the Martian surface such as dust cover index, thermal inertia and the age of the terrain. We found that most of the known craters have been identified in areas with a low dust cover index, indicating a dust-rich terrain. Most of the craters in our sample are small, being less than 10 m in diameter, with just very few cases of craters larger than 30 m. The area of the ejecta around the impact has a distribution that peaks around 10^4 m^2. We did not find any correlation between the crater diameter, the area of the ejecta and the dust cover index and thermal inertia, while the mean diameter of the craters seems to decrease for younger terrains. In addition, we calculated the average azimuth of the direction of the rays of not symmetrical ejecta but no correlations with the other parameters have been found. These results can be enlarged widening the database of fresh craters thanks to high resolution images that will be acquired by ongoing and future missions around Mars. We conclude that more studies, with a larger sample and new imaging instruments, are necessary.

Contents

Introduction

Impact cratering is a common process on different planetary bodies surfaces. The formation of an impact crater is a fast process that involves high-velocity collisions between solid bodies. The impact cratering mechanism usually involves an impactor hitting the surface of the planet forming a bowl-shaped depression. The rate of impact cratering in the Solar System reached its maximum during the Late Heavy Bombardment between 4.1 and 3.8 Gya. Nowadays, the cratering rate is way lower but impacts still happen throughout the Solar System. There are different impact craters morphologies depending on the impactor, its velocity and the target properties involved in the impact. In this work we study a specific category of impact craters, the so-called fresh craters located on the surface of Mars. Fresh craters have been formed in the last few decades and have not been strongly altered by geological processes.
The analysis of fresh craters is a quite recent subject because their discoveries needed very high resolution images covering the surface of the planet. In this work, we analyzed the distribution of fresh craters located on the surface of Mars deriving their global characteristics in order to enlarge the knowledge about the planet surface. Specifically, we analyze fresh craters properties in terms of crater diameter, ejecta area and orientation in order to find any correlation with the geological terrain in which the craters formed. This study can give us a new insight on the geology of the subsurface of Mars, which is otherwise difficult to access, and the process of formation of the craters and their ejecta.
In the first chapter, we give an overview of the main characteristics of Mars, such as geological features, chronology, topography and internal structure. In the second chapter we explain the impact cratering formation process and the main properties of fresh craters, the objective of our study. In the third chapter, we report the dataset used for the analysis, while in the fourth chapter we present the obtained results discussing our findings. Finally, we highlight the future works and perspective derived from this work.

Chapter 1

Mars

1.1 Main characteristics

Mars is the fourth planet from the Sun in our Solar System, orbiting the star at an average distance of 1.524 AU (2.279×10^9 km) and completing one revolution in 686.97 Earth days (1.88 years). Even though Mars is just slightly more than half the size of the Earth in radius and about $\frac{1}{10}$ of our planet in terms of mass, it shares many similarities with Earth and is the most similar planet to our own. A day on Mars is just 37 minutes longer than one on Earth, and its axial tilt is $\sim 25°11'$, compared to the $\sim 23°26'$ of our planet (Table 1).
Due to this axial tilt, seasons exist on Mars and temperatures can vary widely, ranging from a minimum of 130 K (−143°C) at the poles during winter to a maximum of 308 K (35°C) in the summer at the equator. The two polar ice caps consist mostly of water ice, which lies below a layer of frozen carbon dioxide (dry ice). Seasonal changes affect the ice caps, with the dry ice layer becoming thicker during winter and sublimating when the temperature rises.
A huge difference between Mars and the Earth is the atmosphere. The atmosphere of Mars is thin and rarefied compared to Earth's, with an atmospheric pressure of just 0.006 times of that of our planet. Carbon dioxide accounts for about 94.9% of the atmosphere of Mars (compared to 0.04% on the Earth), with 2.8% of nitrogen (N_2), 2.1% of argon and traces of oxygen, carbon monoxide and other gases (Franz et al. 2017).
Unlike the Earth, Mars does not have a strong global magnetic field but shows small signs of local activity. Observations revealed that parts of the planet's crust appear to have been magnetized in the past. Plate tectonic activity also was probably present in early Mars before the magnetic field faded due to the planetary dynamo ceasing to function about 4 billion years

	Earth	Mars	Ratio (Mars/Earth)
Mass	5.972×10^{24} kg	6.417×10^{23} kg	0.107
Mean radius	6371.0 km	3389.5 km	0.532
Mean density	5.514 g/cm^3	3.933 g/cm^3	0.713
Surface gravity	9.807 m/s^2	3.721 m/s^2	0.379
Escape velocity	11.19 km/s	5.03 km/s	0.450
Semimajor axis	1.496×10^9 km (1.000 AU)	2.279×10^9 km (1.524 AU)	1.524
Eccentricity	0.0167	0.0935	5.599
Inclination to the ecliptic	0.00°	1.85°	-
Orbital period	365.26 d (1.00 yr)	686.97 d (1.88 yr)	1.88
Rotation period	23.9345 h (0.9973 d)	24.6229 h (1.0259 d)	1.029
Axial tilt	23.44° (23°26′)	25.19° (25°11′)	1.075
Min. surface temperature	184 K (−89°C)	130 K (−143°C)	
Mean surface temperature	288 K (15°C)	210 K (−63°C)	
Max. surface temperature	330 K (57°C)	308 K (35°C)	
Atmosphere	N_2 (78%), O_2 (21%)	CO_2 (95%)	
Surface pressure	101.325 kPa (1.000 atm)	0.636 kPa (0.006 atm)	0.006
Satellites	1	2	2

Table 1: Fact sheet of Earth and Mars.

ago (Gya). The solar wind hitting the planet then stripped Mars of the remaining magnetic field. Without the protection of the magnetic field, the atmosphere of Mars was also hit by solar storms and most of it was lost. Now, the solar wind interacts directly with the Martian ionosphere, causing more atmospheric loss and aurora events (Jakosky et al. 2015, Schneider et al. 2015).
In addition, Mars has two small and irregularly shaped moons, Phobos and Deimos, which may be captured asteroids.

1.2 Internal structure and topography

Like Earth, Mars has an internal structure differentiated into a core, a mantle and the crust. Due to the lack of a strong planet-wide magnetic field, the core is believed to be solid and viscous and is composed mainly of iron and nickel. An inactive silicate mantle surrounds the core. The crust is largely basaltic and varies in thickness from a few kilometers to over 100 km and is generally thicker in the southern hemisphere (Neumann et al. 2004). Large quantities of frozen water are thought to be present just beneath the surface, forming a permafrost that stretches for almost all the higher latitude regions in both hemispheres (Kostama et al. 2006). Currently, there is no

liquid water on the surface of Mars and the atmospheric pressure is too low to sustain it, but numerous geologic features suggest that it may have existed in the past forming rivers, channels, deltas and possibly a large ocean in the northern half of the planet (Dohm et al. 2009).
Indeed, there is a striking dichotomy in the Martian topography, with the northern hemisphere being lower and flatter than the southern highlands. The southern hemisphere appears highly cratered, representing the older surfaces on Mars, while the sparsely cratered northern lowlands are thought to be younger. The reason for such a difference is attributed to a huge impact with a body of the size of Pluto in the early history of Mars (Andrews-Hanna et al. 2008).
There are many prominent features in the Martian geography, as the equatorial volcanic plateau, called Tharsis, that dominates the western hemisphere of Mars. This region hosts some of the largest volcanoes in the Solar System, like the three shield volcanoes Ascraeus Mons, Pavonis Mons and Arsia Mons. Just west of the Tharsis region, Olympus Mons rises 22 km over the surrounding plains, making it the largest volcano of any planet in the Solar System. On the eastern side of the Tharis region, the Valles Marineris canyon system runs for about 4,000 km.
Large impact craters include the Hellas region in the south and the Utopia Planitia within the northern plains of the Borealis Basin. The Hellas impact basin has the lowest altitude on Mars, with an height difference of 9,000 m between the rim and the basin floor and a depth of over 7,000 m below the reference zero point. The Utopia region is also recognized as a large impact basin (McGill 1989) just north-west of another large volcano called Elysium Mons, which is flanked by two smaller volcanoes (Figure 1).

1.3 The Martian surface

The Martian surface is covered in fine regolith and littered with rocks and boulders of any dimension. The regolith is mainly made up of silicates and contains elements such as magnesium, potassium, sodium and chlorine (McSween et al. 2009). The relatively high concentration of perchlorates in the soil makes it toxic for humans (Davila et al. 2013). The Martian soil has a characteristic red colour because of the high presence of iron oxide. Because of this reddish appearance, Mars is also known as the "Red Planet". Dust storms are common on Mars and can occasionally evolve into global events that cover the entire planet. Since Mars is very dry, the dust lifted from the surface can remain in the atmosphere far longer than on Earth, and dust storms can last for months. Dust devils also happen on the Martian

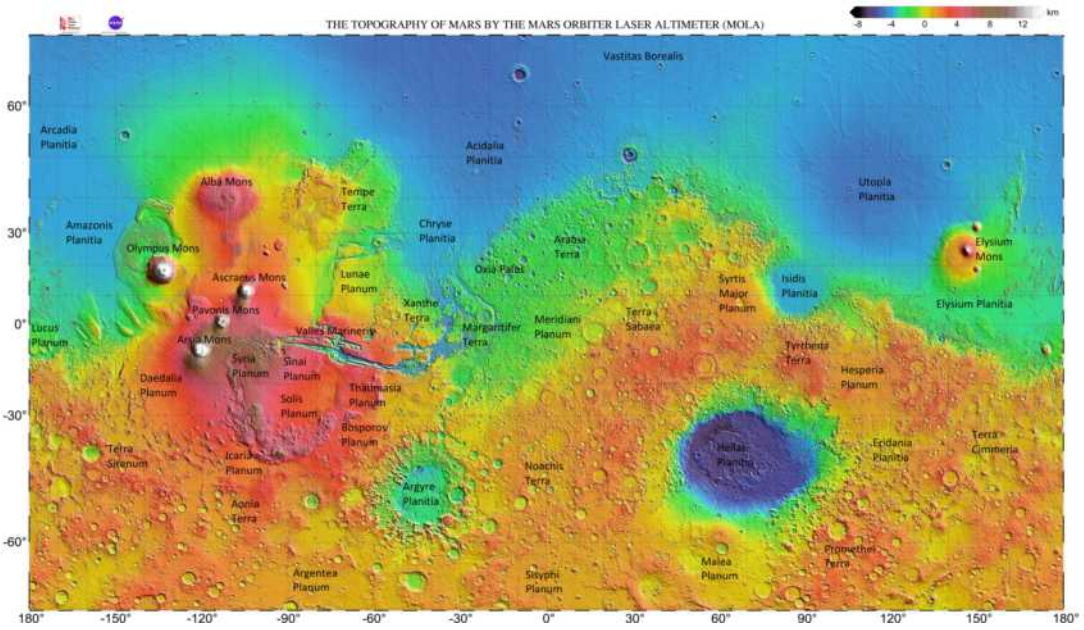

Figure 1: Topography map of Mars by the Mars Orbiter Laser Altimeter (MOLA). Blues and purples show the lowest elevations while the highest one are in brown and white. The dichotomy between the northern and southern hemisphere is evident, while the large region on the west is the so-called Tharsis.

surface and are wider and taller than the terrestrial ones (Balme & Greeley 2006).

1.4 Geologic history

The geologic history of Mars is divided into the three following periods: Noachian, Hesperian and Amazonian (Figure 2). A pre-Noachian period, stretching from the formation of the planet until about 4.1 Gya, can be recognized but, almost certainly, all features dating back to this period have been erased. The north-south hemisphere dichotomy is thought to date back to this early period (Carr & Head 2010).

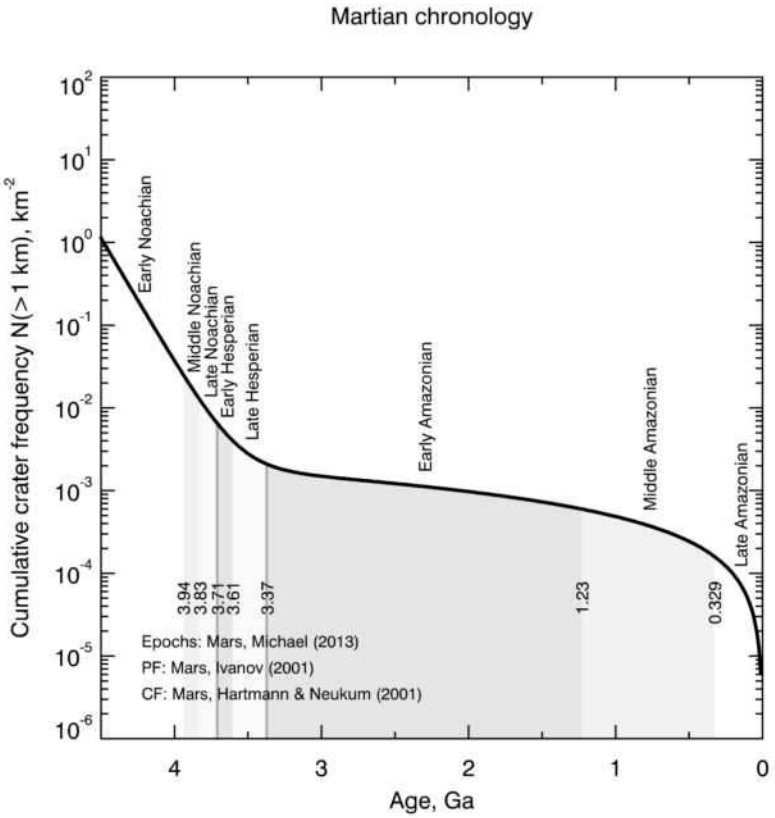

Figure 2: Chronology of Mars epochs.

1.4.1 Noachian period

The Noachian period is the shortest one and experienced the formation of the earliest terrains on Mars between 4.1 and 3.7 Gya. This period roughly corresponds to the age of the Late Heavy Bombardment and, hence, it is characterized by high rates of impact cratering. The Noachian period is named after Noachis Terra, which is a region that dates back to this period. During the Noachian, extensive volcanism occurred in the Tharsis region. Outgassing from this volcanic activity and the generation of heat from numerous large impacts may have contributed to the formation of an atmosphere denser than it is today and a warmer and wetter climate. This condition allowed liquid water to exist and subsequent precipitations may have helped the formation of lakes and rivers in the southern hemisphere, in addition to a large ocean in the north (Malin & Edgett 2003). Noachian terrains appear more eroded than later terrains and this behavior suggests that erosion rates dropped significantly at the end of this period. Many valley networks and deltas can be found in Noachian-aged terrains. Although their origin is still debated, this kind of structures are rare in younger regions, suggesting that the Noachian experienced some peculiar weather conditions compared to later epochs (Carr & Head 2010).
The Hellas impact basin is also thought to have been formed during this period because of the Late Heavy Bombardment. It is thought that a sea or large ice-covered lakes filled the interior of this region during the Noachian period (Moore & Wilhelms 2001).

1.4.2 Hesperian period

The Hesperian period, named after the large lava plain in the southern highlands called Hesperia Planum, lasted from around 3.7 to 3.0 Gya. The period begins at the end of the Late Heavy Bombardment and, with the decrease of the number of large impacts, widespread volcanism became the dominant geologic process all over the planet.
The climate of Mars during the Hesperian started transitioning from warmer to colder and from wetter to dryer, becoming closer to what we see today. As a result of this cooling process, water began to freeze and a thick cryosphere above a layer of liquid water formed in the upper crust (Clifford 1993). The cryosphere sometimes cracked because of volcanic or tectonic activity rapidly releasing large quantities of liquid water from the subsurface. This resulted in catastrophic flooding, leading to the formation of ephemeral bodies of water residing in topographic lows and to the excavation of outflow channels like those around Chryse Planitia. This process may have deposited sedi-

ments that formed the Vastitas Borealis plains of the northern hemisphere (Kresvlasky & Head 2002, Carr & Head 2010).
During the Hesperian, all the large shield volcanoes of Mars had began to form. In the Tharsis region, the immense weight of the volcanic bulge produced many fractures (fossae) and ridges, in addition to the large canyon system of the Valles Marineris (Werner 2009).

1.4.3 Amazonian period

The Amazonian period covers most of the history of Mars, starting 3.0 Gya and continuing to the present day. It is named after Amazonis Planitia, a northern plain characterized, like most younger terrains, by low cratering rates. In this period, the climate became cold and very arid. The geologic activity dropped significantly after the end of the Hesperian and the Martian surface during this period has been mainly characterized by the presence of ice, especially at high latitudes. Many Amazonian features formed because of the presence, accumulation or movement of ice. Much of the ice present today at the poles is thought to have been accumulated during the Late Amazonian. Occasional melting of the ice formed many gullies that can be seen today in many mid and high latitude regions. Volcanism became sparse and probably occurred episodically only in the most active regions like Tharsis and Elysium (Carr & Head 2010).
Low impact rates, low volcanism and the decline of erosion and weathering rates brought a low level of geomorphological changes compared to earlier periods. Geologic activity has been sporadically occurring in relatively recent times, like the formation of the Athabasca Valles outflow channels in Elysium Planitia, which were created in the last 200 million years (Berman & Hartmann 2002).

Chapter 2

Impact craters

Impact craters can be found on all the solid bodies of the Solar System. The terrestrial planets, satellites and asteroids show signs of impacts, with some bodies being heavily cratered like Mercury and the Moon. In other cases, as Earth and Venus, various processes like erosion and tectonic activity can erase the impact craters. On the Jovian satellite Io the volcanic activity is so intense that craters are rapidly covered or destroyed and no impact craters are clearly recognizable (Smith et al. 1979).
The amount of craters in a certain area can be used to date the terrain. Indeed, the heavily cratered regions correspond to older surfaces that have been exposed to impacts for a longer period of time, while the younger terrains experienced fewer impacts. The cratering rate varies widely across the Solar System from the young terrains of Io to some 4 Gy old surfaces on the Moon (Rossi & van Gasselt 2018).
On Mars (Figure 3), the current cratering rate is much lower than it was in the early history of the planet (Daubar et al. 2013). There was a spike in the number of impacts with the Late Heavy Bombardment, but the impact rate has been roughly constant during the last 3.6 Gy (Rossi & van Gasselt 2018). The analysis of the Martian cratering rate throughout the planet made it possible to estimate the age of different regions and define the three geologic periods explained in the previous chapter. As previously reported, the southern hemisphere of Mars shows older surfaces, while the northern plains are sparsely cratered and younger.
The formation of new craters on the Martian surface is a process that is still ongoing to this day. This category of craters, often very small, is of great importance to study the properties of the terrain and the subsurface of Mars. The population of recent impact sites that formed in the last few decades and have not been altered by various processes is called fresh craters and it will be the target of this thesis.

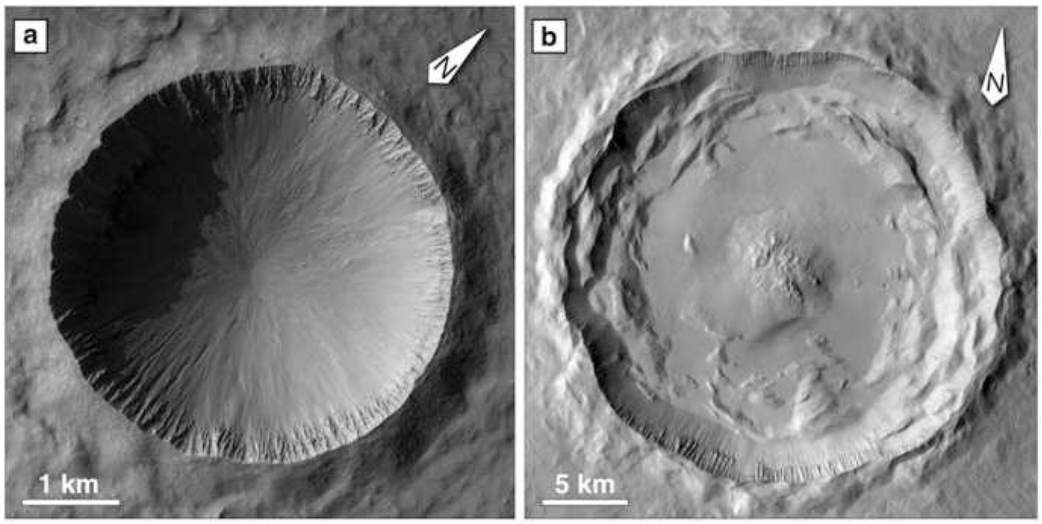

Figure 3: Two examples of impact craters on Mars, a simple crater on the left and a larger complex crater with a central peak on the right (Rossi & van Gasselt 2018).

2.1 The cratering process

The formation of an impact crater is a fast process that involves high-velocity collisions between solid bodies. The initial velocity of the impactor depends on its orbital velocity and the gravitational attraction with the target. If the main body has an atmosphere, the impacting body can be decelerated and even destroyed before hitting the ground. If the impactor reaches the ground, the cratering process begins and it can be distinguished in three different stages (Figure 4).

2.1.1 Contact and compression

The first stage begins with the contact of the impactor with the ground of the main object. The impacting body is immediately compressed and deformed. The shock waves originating from the point of impact cause a huge difference in pressure, density and temperature. They propagate over the impactor and the ground and attenuate with distance as they travel through the surface of the target. Heating and compression caused by the shock waves deforms irreversibly the impacted region and the reached temperature is in most cases enough to melt or vaporize almost completely the impactor. This first stage lasts just some tenths of a second even for large impacts (Rossi & van Gasselt 2018).

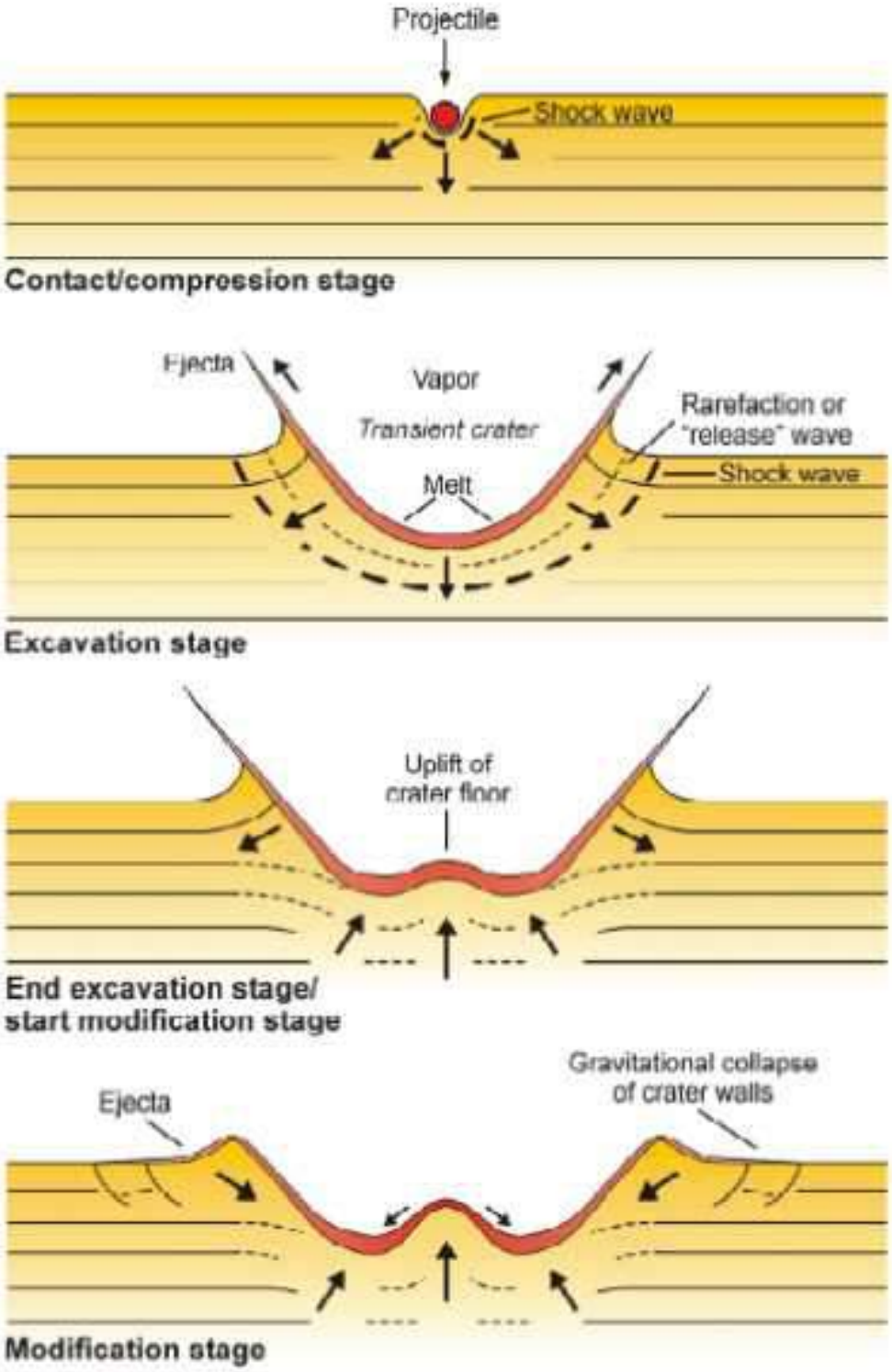

Figure 4: The phases of the impact cratering process (Osinski 2004).

2.1.2 Excavation

In the excavation stage the crater is formed and grows as the target material accelerated by the impact moves away from the contact point. On the ground, shock waves propagate hemispherically from the initial contact area and excavation happens downwards and outwards from the point of impact. A significant quantity of material, coming from the upper one third to half of the cavity, is ejected from the crater area and will later deposit around the region. Target material from the deeper parts of the cavity is displaced only downwards. The crater stops growing when the remaining kinetic energy is not enough to displace the material further, the result is what is called transient cavity. At this point the crater has usually a depth-to-diameter ratio of about $\frac{1}{3}$ (Rossi & van Gasselt 2018).

2.1.3 Modification

When the excavation phase is over, the transient cavity has reached its maximum size but it is not in a stable configuration yet and it starts collapsing under gravity. Depending on the cavity size, the collapse may result in a bowl-shaped simple crater for the cavities smaller than a few kilometers, while larger ones become complex craters with terraced rims and an uplift of the central region. For very large craters the complexity increases, the central peak may collapse under its own weight and form internal rings in what is classified as a peak-ring crater. The largest craters, with a diameter of hundreds or thousands of kilometers, develop a structure with multiple concentric rings (Rossi & van Gasselt 2018).

2.1.4 Ejecta

The material ejected from the cavity is deposited within a few crater radii and forms the so called ejecta. The velocity of this material depends on its initial position, as it will be faster if ejected from around the center of the crater and slower if ejected from the outer regions near the rim. In large impacts, the material can acquire a velocity higher than the escape velocity and leave the impacted object entirely. The distribution of the ejected material around the crater depends on multiple factors other than the impactor velocity and nature, such as the angle of the impact and the composition of the atmosphere and the ground. When the debris of ejected material hit the ground they can form smaller secondary craters (Rossi & van Gasselt 2018). The ejecta morphology can be very different depending on the characteristics of the terrain in the region where the crater is formed, hence, studying

the ejecta can provide an insight on the composition of the surface and the subsurface. In some cases on Mars, ejecta characterization can reveal the distribution of underground ice, with high-latitude impacts exposing more ice than equatorial ones (Dundas et al. 2014).
Due to its atmosphere and the presence of a volatile-rich ground, Mars has some unique ejecta morphologies with layered deposits of material. The ejecta can be formed by a single layer (Single Layered Ejecta, SLE), a double layer (Double Layered Ejecta, DLE) or multiple layers (Multiple Layered Ejecta, MLE). Most of the craters on Mars are SLE, with DLE and MLE being less common, but other rarer morphologies can be found.
Pancake (Pn) craters, for example, are characterized by a single very thick layer and are considered to be old DLE craters where the outer thinner layer has eroded. Another unusual morphology is the Low Aspect Ratio Layered Ejecta (LARLE) that shows a large thin layer of ejecta and can be linked with the presence of ice as they can be found mostly in high-latitude regions, although there are some equatorial examples of LARLE. Eroded versions of LARLE morphologies are the Pedestal (Pd) craters characterized by an ejecta layer atop an elevated plateau (Barlow & Boyce 2016) (Figure 5).

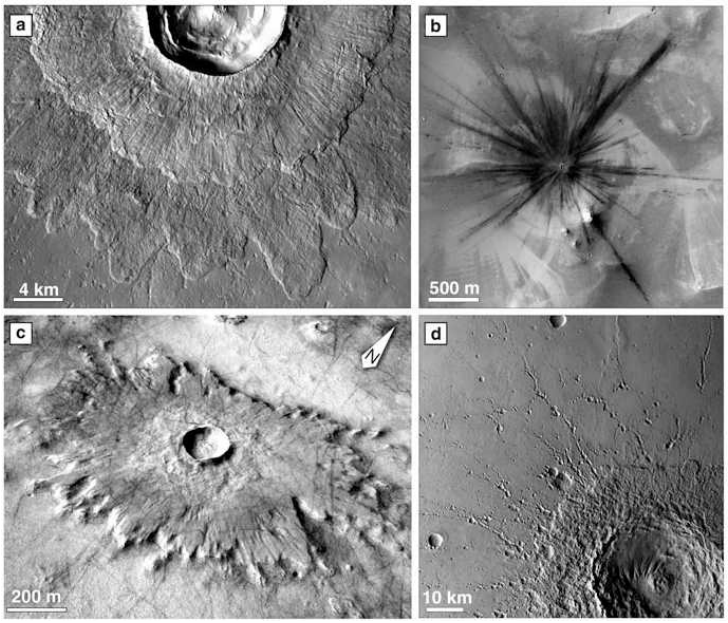

Figure 5: Examples of ejecta morphologies on Mars: (a) detail of a Double-Layered-Ejecta (DLE) crater; (b) radial ejecta rays departing from a small crater; (c) a pedestal crater; (d) detail of secondary craters around a large impact basin (Rossi & van Gasselt 2018).

2.2 Fresh craters

The formation of impact craters is a process that continues to happen today throughout the Solar System even though the impact rate is, as noted above, way lower than what it was in the early phases of the history of our planetary system. New craters that formed in the last few decades, years or even months, are known as fresh craters. They can be identified by the absence of associated impact-related dark surface markings in previous images of the same site.
Large impacts are rare and most of the new craters observed today are very small, just a few meters in diameter. That is why just recently it has been possible to study this population of fresh craters on Mars, thanks to the development of new high-resolution cameras on board the spacecrafts orbiting the planet multiple times. This allows the study of the evolution of fresh craters and their ejecta in unprecedented detail. In addition, the use of multiple cameras with different resolutions and filters allows to investigate the composition of the ejecta and the characteristics of the region where the crater has formed. The study of fresh craters and their ejecta thus gives us a new way to study the Martian terrain and subsurface.
In the last decades a few hundreds fresh craters have been identified, mostly thanks to orbiting spacecrafts like the Mars Global Surveyor (MGS) and especially the Mars Reconnaissance Orbiter (MRO), which has provided a continuous monitoring of the Martian surface since its orbital injection in 2006. The actual number of impacts may be even higher than the number of fresh craters detected due to new impacts fading and not being discovered before they disappear.
Often fresh craters are part of a cluster of two or more individual craters. This happens when the impactor is fragmented after entering the Martian atmosphere, sometimes dividing in tens or hundreds of small pieces each impacting the surface and forming a different crater. Clusters of fresh craters can be distinguished from secondary craters mostly because of their distribution, which is not in rays radially extending from a central impact as it is the case of secondary craters. In addition, many different types of ejecta morphologies can be found around fresh craters, depending on how the impact happened and the characteristics of the terrain in which the crater has formed (Figure 6). This allows us to get a better understanding on how the various morphologies of ejecta are formed extending the results on fresh craters to older impact sites.
The discovery and analysis of fresh craters is of great importance for numerous reasons. For example, it allowed to refine the current Martian cratering rate comparing it to the model predictions, even if only the smallest craters

can be expected to have formed in statistically significant numbers (Daubar et al. 2013). The formation of fresh craters allows to have an unique opportunity to understand the subsurface of Mars, that would be otherwise inaccessible. It has been thus possible to observe the presence of underground ice, especially in the high-latitude regions, and get a deeper understanding of the Martian geologic history and chronology (Dundas et al. 2014).
Thanks to multiple imaging over time, it has been possible to study the evolution of halos and ejecta features around the craters over a period of various years. We can thus obtain numerous informations about the composition of the ejecta and the subsurface. (Daubar et al. 2016). In addition, the mean depth to diameter (d/D) ratio of the known fresh craters, which is related to the target material properties and the characteristics of the impact, has been calculated. The result is that this ratio on Mars is just slightly higher than expected for an impact on a rocky surface (Daubar et al. 2014).

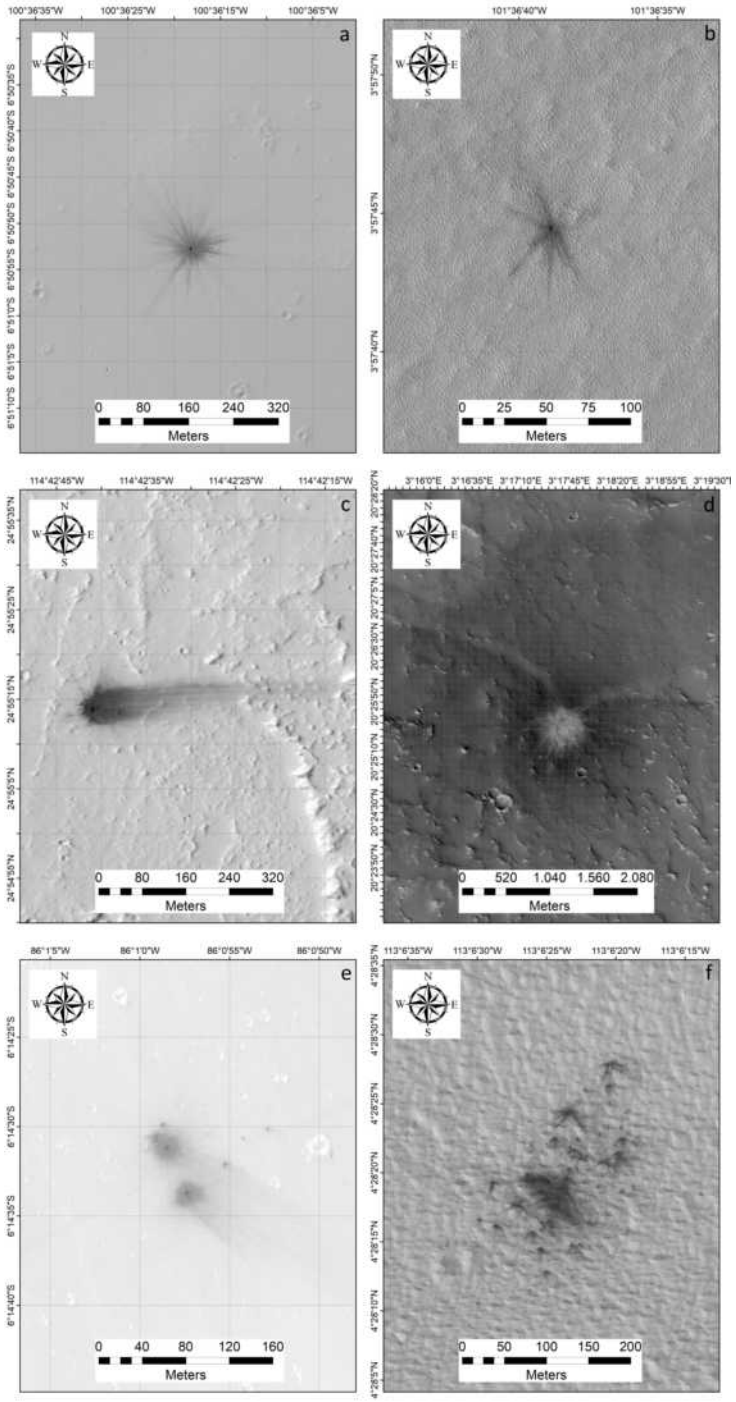

Figure 6: Examples of different morphologies among fresh craters on Mars: (a) HiRISE image ESP_016331_1730 (b) HiRISE image PSP_010740_1840 (c) HiRISE image ESP_018784_2050 (d) HiRISE image PSP_004038_2005 (e) HiRISE image PSP_007496_1735 (f) HiRISE image ESP_022964_1845.

Chapter 3

Dataset and methods

In this chapter, we present the images used to analyze the fresh craters located on the surface of Mars. In particular, the images acquired by two different cameras onboard Mars missions have been considered for the analysis, Context Camera (CTX) and High Resolution Imaging Science Experiment (HIRISE). We consider the database of fresh craters previously published (Daubar et al. 2013, Daubar et al. 2014, Daubar et al. 2016, Bart et al. 2019) analyzing their distribution, in terms of diameter, area and ejecta extension. In addition, we correlate the location of fresh craters with different surface parameters and characteristic, such as elevation, age, dust cover index and thermal inertia, to understand if there is a common trend between the fresh impact craters analyzed. The data used and the methodology applied for the analysis are explained in greater detail in the following subsections.

3.1 Fresh craters database

New impacts on the Martian surface are now recognized and identified thanks to two instruments on the Mars Reconnaissance Orbiter (MRO) (Figure 7), the Context Camera (CTX) and the High Resolution Imaging Science Experiment (HiRISE). While orbiting Mars, MRO flies over the same region numerous times, allowing to take multiple images of the same area. The comparison between CTX images taken at different times enables the identification of changes in the terrain. Dark spots present in newer images but not in older ones can suggest the formation of a new crater. The candidate impact site is then imaged with the high-resolution camera HiRISE that allows a closer look at the region to confirm that a recent impact has occurred (Daubar et al. 2013).

Figure 7: The Mars Reconnaissance Orbiter spacecraft (nasa.gov).

3.1.1 Context Camera (CTX)

The Context Camera (CTX) on MRO produces images with a 6 m/pixel resolution of a broad area spanning a few tens of kilometers across. The images taken with this camera provide context maps for the more focused and targeted observations made by other instruments such as HiRISE. In addition, two stereo CTX images of the same region taken at different angles can be used to acquire a 3D coverage of the area and create a digital terrain model (DTM) (Bell III et al. 2013).

3.1.2 High Resolution Imaging Science Experiment (HiRISE)

The High Resolution Imaging Science Experiment (HiRISE) on MRO provides high-resolution 0.25 m/pixel images, allowing to resolve small objects with unprecedented detail. The imaged area is smaller than the CTX area. HiRISE uses three different color bands: blue-green (400-600 nm), red (550-850 nm) and near infrared (800-1000 nm). In this work we used the images acquired in the red band. In addition, HiRISE can produce high-accuracy stereo pairs to create high-resolution DTMs. This DTMs are useful in order

to obtain the topography of the structures and, hence, to calculate the depth of the crater. (Delamere et al. 2003).

3.1.3 Data selection

An initial list of 260 recent impact sites scattered all over the Martian surface was derived from the previous literature on fresh craters (Daubar et al. 2013, Daubar et al. 2014, Daubar et al. 2016, Bart et al. 2019). The study of this sample allows us to make a statistical analysis of various characteristics of the ejecta (such as the shape, the extent, the age of the terrain) of the fresh craters under study. For each site both an HiRISE and a CTX image were acquired using the online tools Planetary Image Locator Tool (PILOT) of the USGS Astrogeology Science Center and the Murray Laboratory for Planetary Visualization of the California Institute of Technology. For every impact site, we used the earliest HiRISE and CTX images of the region where the crater is clearly visible.

3.2 Dataset

To analyze the HiRISE and CTX images we used the geographic information system ArcGIS, developed by Esri. We used ArcGIS to identify the position of all the impact sites, the extent of their ejecta and various information about the characteristics of the terrain where the crater formed. In some cases, we were able to obtain the orientation and length of the ejecta rays. In addition, we consider different physical parameters of the Mars surface characterizing the location of the fresh impact craters in order to provide a global statistical characterization of the craters under study. In the following we report the methodology developed for the analysis.

3.2.1 MOLA and THEMIS maps

First of all, we uploaded on ArcGIS the global maps of the Martian surface. We used the global map generated by the Mars Orbiter Laser Altimeter (MOLA) instrument on the Mars Global Surveyor (MGS) spacecraft. This instrument measured the topography, surface roughness and near-infrared reflectivity of the Martian surface. The horizontal grid size of the MOLA map ranges from $\sim$463 m/pixel at lower latitudes to $\sim$115 m/pixel in the polar region, while the elevation uncertainty is of the order of $\sim$1 m with respect to the center of mass of the planet (Smith et al. 2001). We used the MOLA map to have a reconstruction of the topography and the elevation of

all the surface of the planet. In this way, we are able to estimate the elevation of the fresh impact craters locations.
In addition, we used the 100 m/pixel resolution global mosaic generated by the infrared camera Thermal Emission Imaging System (THEMIS) on the 2001 Mars Odyssey spacecraft. This instrument investigated the Martian surface using nine different infrared filters centered from 6.8 to 14.9 μm. The analysis made by THEMIS allowed to determine various mineralogical properties of the terrain and to recognize dust-covered regions from the dust-free ones (Christensen et al. 2004).
A detailed understanding of the distribution of dust can be achieved using two different parameters: the dust cover index (DCI) and thermal inertia.

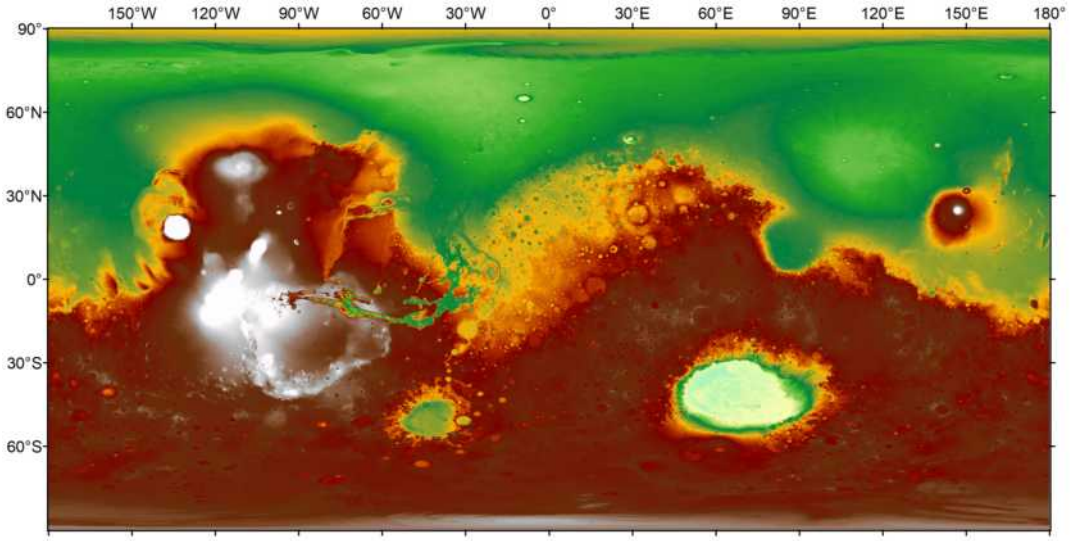

Figure 8: The map generated by the Mars Orbiter Laser Altimeter (MOLA) (Smith et al. 2001).

3.2.2 Dust cover index

The dust cover index (DCI) is a measure of the surface dust present on Mars that is independent of thermal inertia and albedo. The terrain with the lowest quantities of dust have a DCI approaching 0.99, while lower values suggest a higher presence of surface dust, with a DCI close to 0.89. Terrains with DCI$\geq$0.97 are considered to be dust-free (Pajola et al. 2019). In this work we use the 3.5 km resolution map of DCI made by Ruff & Christensen (2002) that has been obtained from the data acquired by the Thermal Emission Spectrometer (TES) on board the Mars Global Surveyor (MGS) mission (Figure 9).

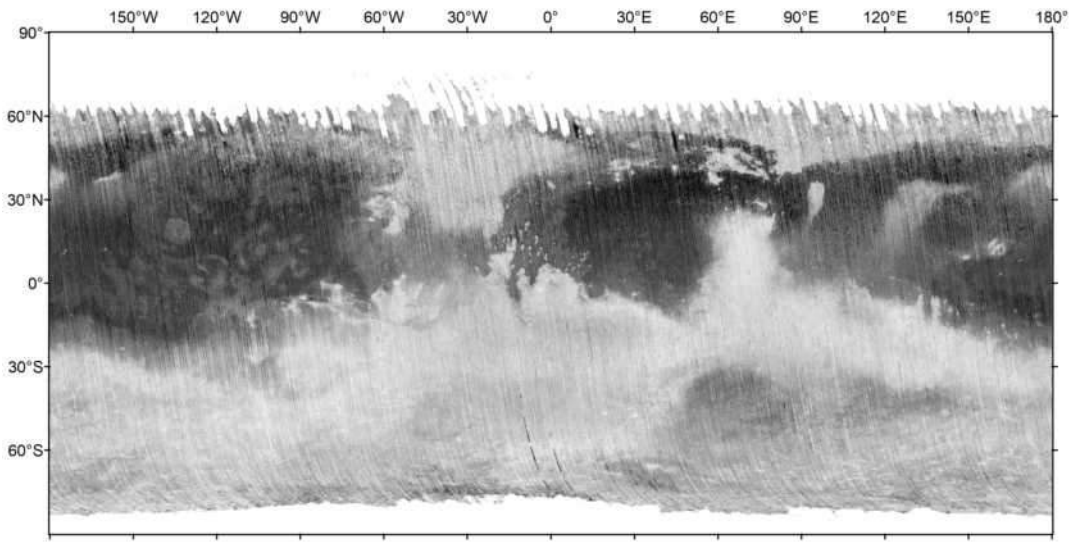

Figure 9: The 3.5 km resolution map of dust cover index made by Ruff & Christensen (2002). A darker shade indicates lower DCI (dustier terrain), while lighter areas are partially or completely dust-free. There is no data coverage at high-latitude regions.

3.2.3 Thermal inertia

Another parameter linked with the presence of dust is the thermal inertia. It is measured in Thermal Inertia Units (TIU) i.e. $\frac{J}{m^2 s^{\frac{1}{2}} K}$. A dust-rich terrain has a thermal inertia $<$150 TIU, while a rocky region has a thermal inertia $>$1250 TIU. Terrains with a moderate inertia component fall on intermediate values of thermal inertia (Pajola et al. 2019). In this work, we used the 3 km resolution MGS-TES global day-side and night-side thermal inertia maps reported by Putzig et al. (2005) and Putzig & Mellon (2007) (Figure 10 and Figure 11).

3.2.4 Surface exposure ages

We used the global geologic map of Mars compiled by Tanaka et al. (2014) to characterize the age of the terrain around the crater. The authors divided the entire planet into numerous geologic regions each identified with the epoch in which it formed (Figure 12). For the purpose of this map the three geologic periods of the history of Mars have been each subdivided in smaller epochs. The Noachian and Amazonian periods have been divided into a Early, Middle and Late phase, while the Hesperian period is divided only in an Early and a Late phase. In some cases this subdivision is not easy and

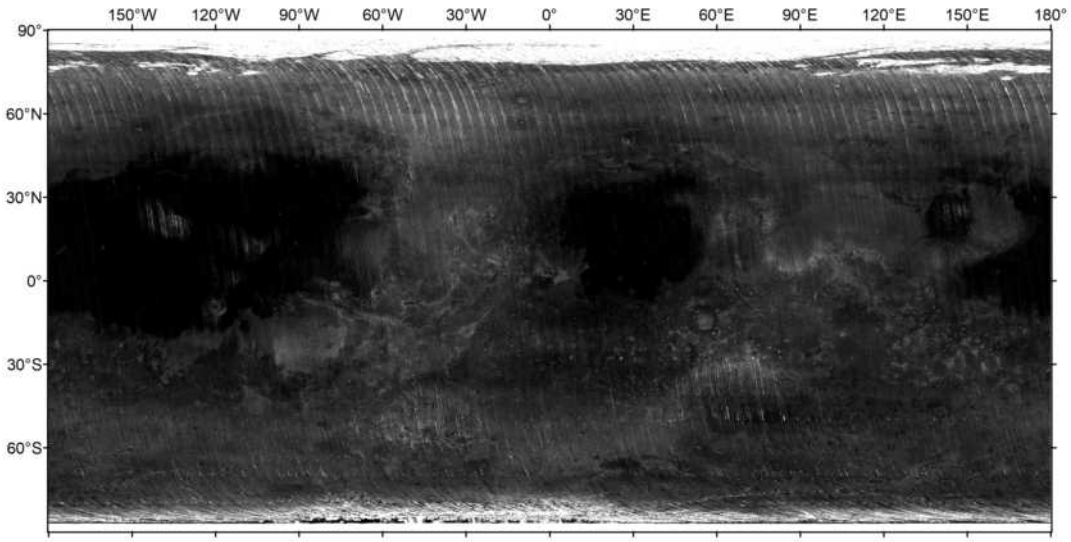

Figure 10: The 3 km resolution map of global day-side thermal inertia made by Putzig et al. (2005) and Putzig & Mellon (2007). A darker shade is associated with a lower thermal inertia and a dust-rich terrain, while lighter areas are more rocky. There is no data coverage at high-latitude regions.

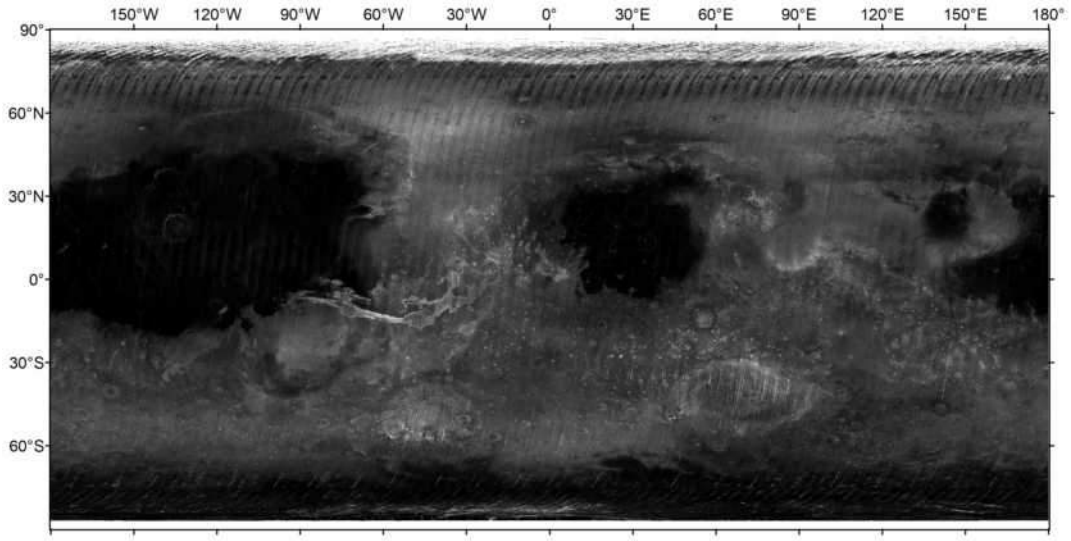

Figure 11: The 3 km resolution map of global night-side thermal inertia made by Putzig et al. (2005) and Putzig & Mellon (2007). A darker shade is associated with a lower thermal inertia and a dust-rich terrain, while lighter areas are more rocky. There is no data coverage at high-latitude regions.

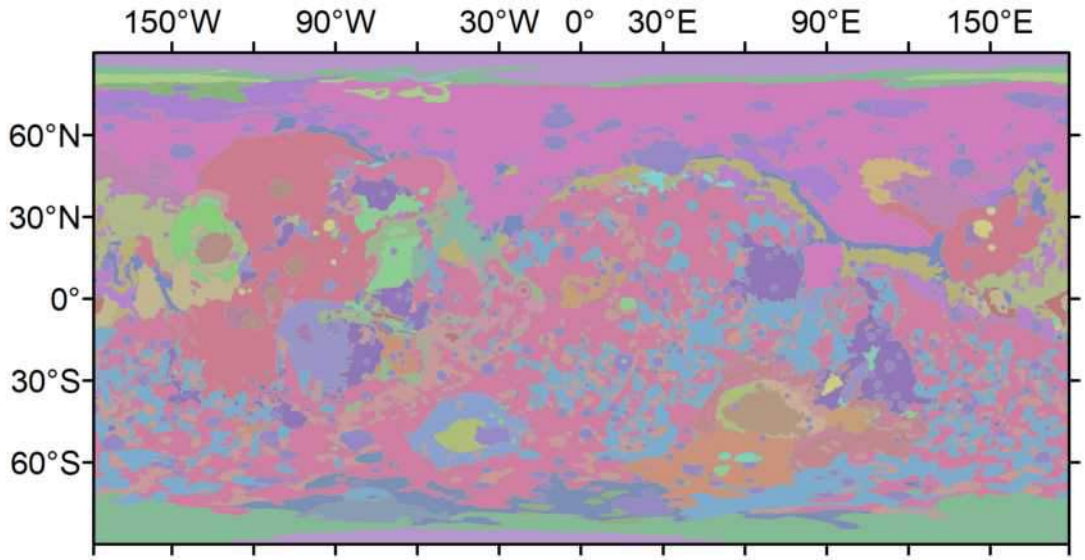

Figure 12: The global geologic map of Mars compiled by Tanaka et al. (2014) divides the entire planet into numerous geologic regions each identified with the epoch in which it formed.

some regions are only classified as Noachian, Hesperian or Amazonian. In addition, some regions appear to have characteristics belonging to different or transitional periods and have been thus classified as Hesperian/Noachian and Amazonian/Hesperian.

3.3 Methods: mapping of craters and their ejecta

After the global maps, we uploaded on ArcGIS all the HiRISE and CTX images of the 260 impact sites derived from the literature. We converted the coordinates of the HiRISE images into the Simple Cylindrical system used by the MOLA map. This prevents the images from appearing in the wrong position. We checked that every HiRISE image corresponded to the correct CTX image and, using the impact sites coordinates from the literature, we verified that all the images were in the right position on the MOLA map.
We analyzed the images to find the fresh craters. Most of the images contain just one impact site, some have two or more. In the case of multiple craters we selected only the most prominent ones, resulting in some images having two, three or four impact sites in the final sample. Where there was a cluster of fresh craters we sometimes selected one crater that seemed to be the principal impact site, even if it is often difficult to identify the location of

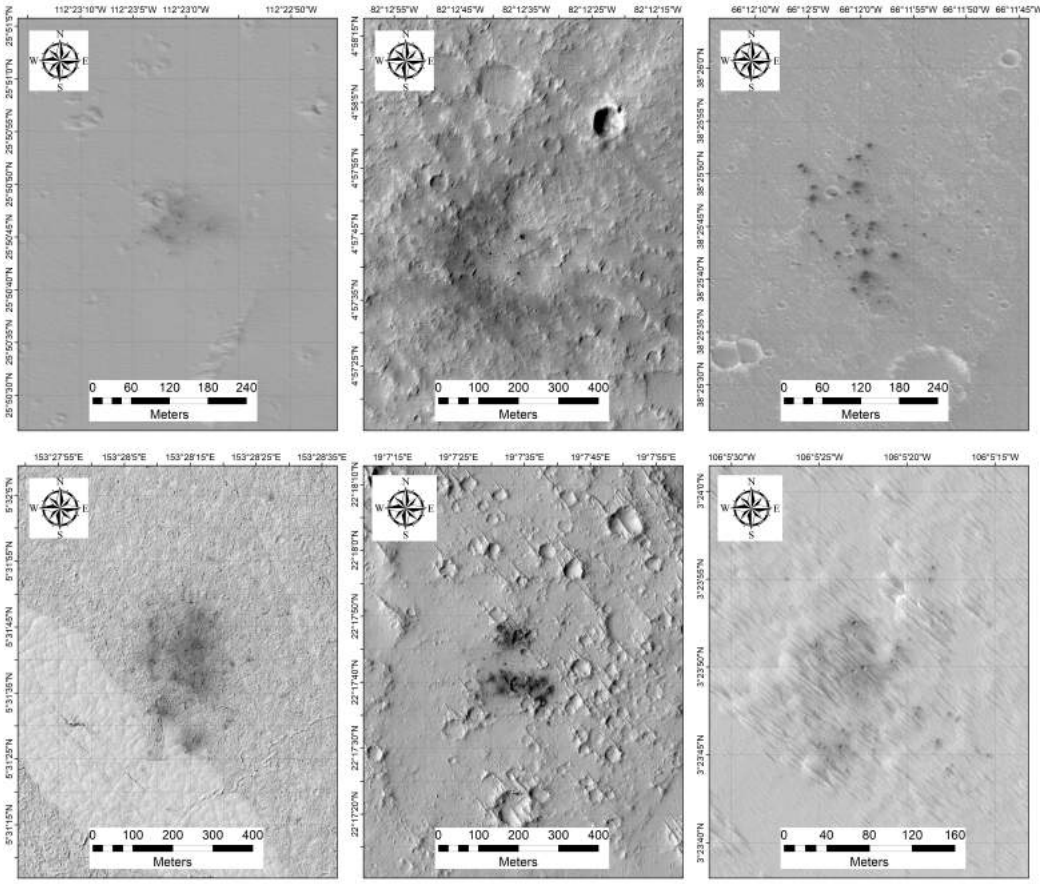

Figure 13: The six excluded sites with a cluster of fresh craters (ESP_013694_2060, ESP_016238_1850, ESP_016501_2185, ESP_016559_1855, ESP_017566_2025, ESP_026445_1835).

the main impact as craters in clusters tend to be approximately all of similar size.

From the initial sample we excluded eleven impact sites, six of them were clusters (ESP_013694_2060, ESP_016238_1850, ESP_016501_2185, ESP_016559_1855, ESP_017566_2025, ESP_026445_1835) (Figure 13), while in five cases there was no visible ejecta around the crater (PSP_002249_1805, PSP_003674_1855, ESP_015908_2310, ESP_020592_1785, ESP_020803_2010) (Figure 14). The final sample consisted of 279 fresh craters in 249 images.

Using ArcGIS, we analyzed the HiRISE images to identify the ejecta around every fresh crater, marking each one with a red area. The ejecta usually appears as a dark halo on the surface that gradually fades the farther it gets

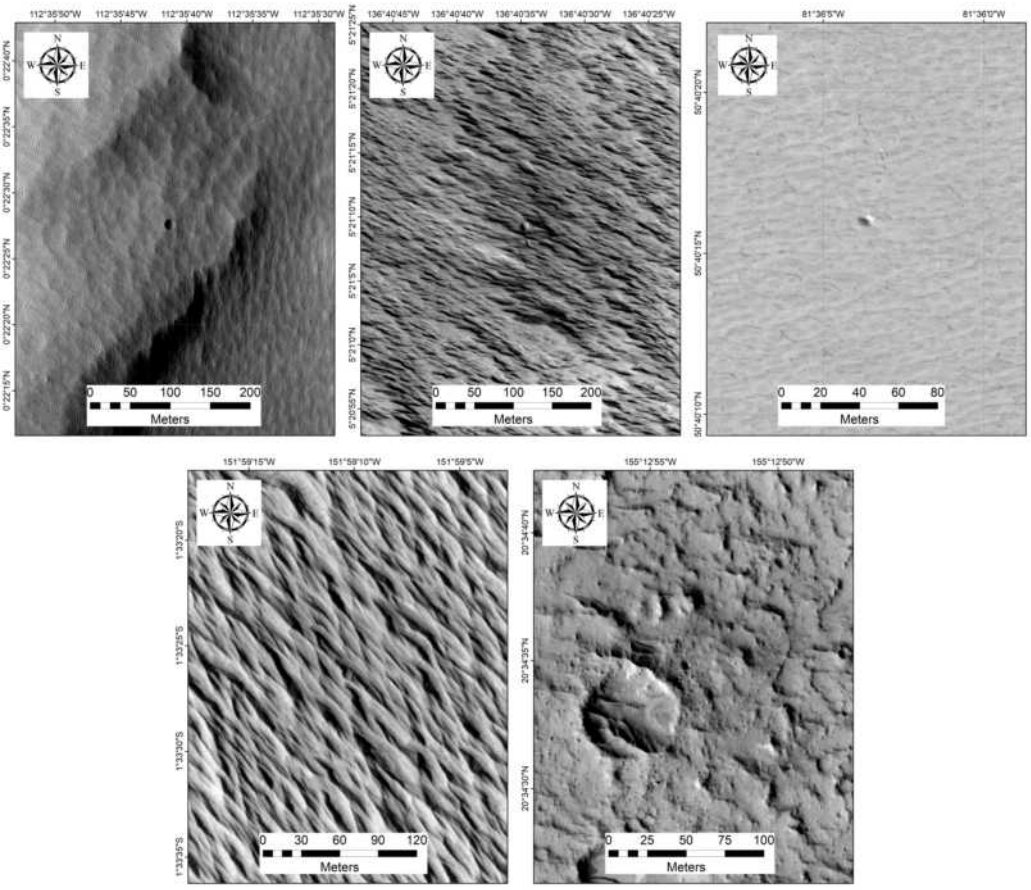

Figure 14: The five excluded sites where no ejecta was visible around the crater (PSP_002249_1805, PSP_003674_1855, ESP_015908_2310, ESP_020592_1785, ESP_020803_2010).

from the impact site. The halo that forms the ejecta can surround entirely the crater and have an almost circular shape or it can present multiple rays that depart from the center. The orientation of the rays of asymmetrical ejecta has been subjected to further research later in this work.
In addition, we marked the area of every crater with a circle and calculated the corresponding diameter. We then computed the area of every ejecta subtracting the area of its crater. This was done to have a precise estimate of just the area of the ejecta, independently from the size of the crater.
For every fresh crater in our sample we took the values of dust cover index, thermal inertia day and thermal inertia night of the site using data from the maps described above. Two high-latitude impact sites (ESP_017868_2440, ESP_018125_2445) lie at $\sim 64°$, in the polar region where there is no data

coverage for the dust cover index. However, for these two craters we still have the thermal inertia values.
In addition, we used the global geologic map of the Martian surface to identify the age of the terrain in which the impact happened. For every crater we took from the geologic map the epoch of the corresponding region.
Lastly, among our sample of 279 fresh craters, we identified 85 cases of not symmetric ejecta in which the rays departing from the crater were clearly visible. We marked every ray with a yellow line on ArcGIS and computed the length and the azimuth (the clockwise angle from the north direction) of each line. For every crater we calculated the weighted mean of the azimuth, with the weights being the length of the ejecta ray (Figure 15).
The entire fresh crater catalogue is reported in the appendix, where we report the original image, the image with the ejecta marked with a red area and, when possible, the image with the ejecta rays marked with yellow lines.
In the following table, we report the data obtained for every crater. The columns reported the *HiRISE ID*, which is the name of the image in the HiRISE database, *Area*, which stands for the area of the ejecta, while *Diam.* is the diameter of the crater. Moreover, it is also reported the *DCI* that is the dust cover index while *TI* stands for thermal inertia, reported in Thermal Inertia Units (TIU). When it was possible to measure the orientation of the ejecta, it reported the *Azimuth*, which is the mean azimuth of the ejecta rays weighted with the length of the rays.

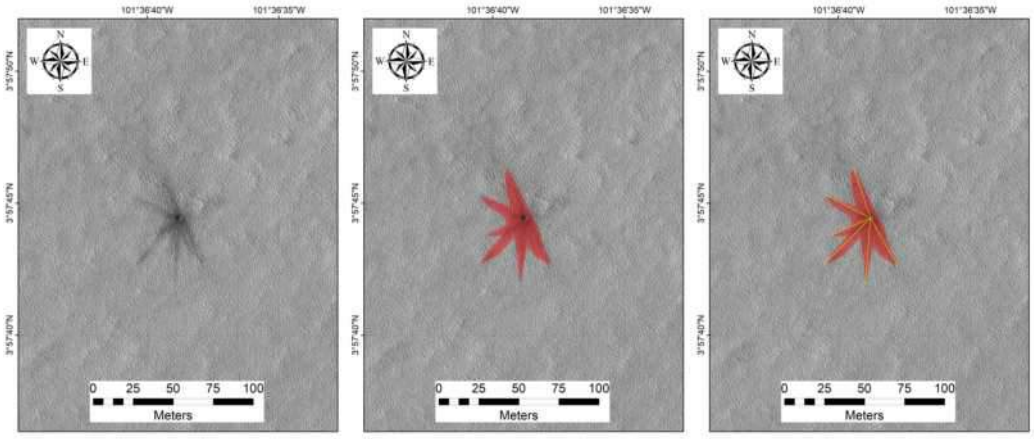

Figure 15: Example of an impact site from our sample (PSP_010740_1840), on the right the initial image, in the center the ejecta has been marked with a red area, on the left six yellow lines mark the ejecta rays.

Latitude	Longitude	HiRISE ID	Area (m^2)	Diam.(m)	DCI	TI day	TI night	Epoch	Azimuth
27.055°	268.332°	PSP_002736_2075	398962.9	15.5	0.930	42	96	Hesperian	129.7
−0.033°	226.907°	PSP_002764_1800	2185001.3	22.3	0.936	26	52	Amaz./Hesp.	
21.958°	14.604°	PSP_003075_2020	572684.0	23.9	0.926	73	62	Middle Noach.	
26.158°	23.627°	PSP_003101_2065	1064841.1	14.5	0.926	50	46	Middle Noach.	
6.989°	247.914°	PSP_003172_1870	1898009.4	12.8	0.933	41	154	Amaz./Hesp.	313.2
13.709°	275.674°	PSP_003527_1940	420945.1	9.1	0.939	91	49	Amaz./Hesp.	
28.455°	25.196°	PSP_003602_2085	792096.2	17.1	0.930	15	40	Middle Noach.	
1.686°	199.382°	PSP_003754_1815	948988.2	12.0	0.930	34	41	Amaz./Hesp.	
19.774°	207.425°	PSP_003780_2000	40971.9	10.2	0.941	36	94	Late Amaz.	
23.087°	52.879°	PSP_003812_2035	228119.2	14.6	0.935	117	168	Middle Noach.	299.3
13.851°	208.582°	PSP_003925_1940	4789586.2	9.4	0.933	81	54	Late Amaz.	
28.990°	26.926°	PSP_003958_2095	102039.0	9.3	0.912	18	33	Middle Noach.	
5.469°	224.353°	PSP_004030_1855	3223808.9	24.5	0.930	18	41	Amaz./Hesp.	
20.427°	3.295°	PSP_004038_2005	1457683.6	20.9	0.938	81	119	Middle Noach.	183.0
11.365°	203.505°	PSP_004123_1915	38314.7	8.8	0.929	55	43	Late Hesp.	
25.501°	221.757°	PSP_004175_2060	16377.9	6.7	0.931	66	41	Late Amaz.	
23.976°	189.297°	PSP_004374_2040	13334.4	3.8	0.933	30	41	Hesp./Noach.	88.0
4.771°	180.145°	PSP_004414_1850	286154.6	4.4	0.931	39	45	Late Amaz.	
−3.616°	234.243°	PSP_004689_1765	52031.8	11.0	0.935	35	57	Amaz./Hesp.	
0.374°	247.405°	PSP_004728_1805	560.5	3.5	0.941	77	79	Amazonian	
−8.786°	182.673°	PSP_004770_1710	559750.4	8.4	0.934	34	51	Amaz./Hesp.	
25.601°	52.147°	PSP_005579_2060	90744.8	11.4	0.938	182	178	Middle Noach.	177.2
−0.755°	200.066°	PSP_005666_1790	480033.0	10.0	0.944	43	79	Amaz./Hesp.	
2.479°	224.105°	PSP_005942_1825	523905.1	19.1	0.930	30	25	Amaz./Hesp.	
15.230°	184.317°	PSP_006629_1955	38891.3	7.2	0.928	70	54	Late Amaz.	
24.676°	261.522°	PSP_006758_2050	46476.9	6.7	0.944	28	82	Amaz./Hesp.	
25.604°	188.579°	PSP_006998_2060	56113.8	2.7	0.935	34	46	Late Amaz.	
10.375°	250.216°	PSP_007009_1905	75683.1	10.0	0.939	95	62	Amaz./Hesp.	
9.049°	259.507°	PSP_007246_1890	57659.2	5.1	0.939	27	44	Amaz./Hesp.	53.2
14.524°	268.850°	PSP_007272_1945	696840.6	13.7	0.927	74	81	Amaz./Hesp.	304.5
6.118°	254.341°	PSP_007378_1860	26638.0	5.6	0.932	40	127	Amaz./Hesp.	
−6.242°	273.984°	PSP_007496_1735	1445.6	1.5	0.933	161	113	Early Hesp.	115.7
−6.242°	273.984°	PSP_007496_1735	1103.2	1.4	0.933	161	113	Early Hesp.	126.0
0.933°	191.746°	PSP_007499_1810	1517842.9	13.5	0.944	39	54	Hesp./Noach.	
−50.599°	305.983°	PSP_007561_1290	76276.3	9.7	0.973	402	387	Hesp./Noach.	
−50.170°	70.101°	PSP_007596_1295	15932.2	5.6	0.961	108	189	Late Hesp.	
12.979°	267.931°	PSP_007773_1930	1980.3	4.7	0.945	26	32	Amaz./Hesp.	268.4
12.979°	267.931°	PSP_007773_1930	2645.1	3.7	0.945	26	32	Amaz./Hesp.	225.9
12.979°	267.931°	PSP_007773_1930	1743.1	3.4	0.945	26	32	Amaz./Hesp.	262.6
12.979°	267.931°	PSP_007773_1930	1011.2	3.1	0.945	26	32	Amaz./Hesp.	271.4
−7.383°	256.028°	PSP_007879_1725	6097.9	7.0	0.944	74	54	Late Hesp.	120.6
40.374°	136.576°	PSP_008015_2205	34822.4	8.5	0.943	168	168	Middle Amaz.	299.7
22.017°	40.245°	PSP_008045_2020	1497.7	4.0	0.931	21	50	Middle Noach.	
37.481°	222.260°	PSP_008236_2180	2342.7	3.5	0.946	52	82	Early Hesp.	92.0
10.420°	278.408°	PSP_008300_1905	13634.3	5.5	0.932	58	42	Amaz./Hesp.	269.3
−3.107°	233.105°	PSP_009185_1770	2568.7	5.1	0.931	35	13	Late Amaz.	
−15.934°	217.398°	PSP_009212_1640	510.3	2.7	0.939	40	67	Middle Noach.	277.4
−7.052°	210.263°	PSP_009265_1730	287860.9	29.1	0.937	62	37	Middle Noach.	
3.000°	195.645°	PSP_009305_1830	13518.2	4.3	0.937	31	43	Hesp./Noach.	226.5
46.351°	176.891°	PSP_009978_2265	8218.8	4.7	0.932	235	244	Late Hesp.	288.9
43.297°	164.210°	PSP_010084_2235	12404.1	6.4	0.945	112	177	Early Hesp.	
3.155°	249.178°	PSP_010147_1830	55969.5	4.9	0.955	30	87	Amaz./Hesp.	121.0
5.009°	149.849°	PSP_010177_1850	11010.0	2.2	0.943	88	137	Late Amaz.	
0.499°	242.327°	PSP_010200_1805	1119.7	4.6	0.947	46	22	Amaz./Hesp.	
0.499°	242.327°	PSP_010200_1805	2312.7	3.7	0.947	46	22	Amaz./Hesp.	
−9.720°	181.380°	PSP_010255_1700	33005.0	3.1	0.925	57	20	Amaz./Hesp.	
−1.280°	250.120°	PSP_010292_1785	35895.6	6.2	0.929	62	84	Amaz./Hesp.	
−1.928°	233.131°	PSP_010319_1780	295.9	3.5	0.932	52	20	Amaz./Hesp.	
−1.928°	233.131°	PSP_010319_1780	350.7	3.1	0.932	52	20	Amaz./Hesp.	
−4.505°	265.906°	PSP_010331_1755	2222.0	3.3	0.921	127	92	Noachian	126.8
−2.955°	287.823°	PSP_010528_1770	1951.0	2.7	0.950	127	72	Early Hesp.	
38.938°	123.713°	PSP_010547_2195	14952.5	6.9	0.944	182	172	Amazonian	288.9
45.067°	164.702°	PSP_010585_2255	30871.5	4.5	0.940	159	158	Early Hesp.	
15.650°	266.216°	PSP_010621_1960	5814.2	3.7	0.934	26	60	Amaz./Hesp.	
55.583°	150.603°	PSP_010625_2360	730.7	4.2	0.964	265	254	Late Hesp.	
33.172°	268.110°	PSP_010634_2135	8344.9	5.3	0.937	20	35	Late Hesp.	

Latitude	Longitude	HiRISE ID	Area (m^2)	Diam.(m)	DCI	TI day	TI night	Epoch	Azimuth
−2.021°	246.574°	PSP_010635_1780	4727.6	6.5	0.939	79	25	Late Amaz.	
3.962°	258.389°	PSP_010740_1840	1010.7	3.3	0.941	25	57	Amaz./Hesp.	237.4
46.179°	188.495°	PSP_010861_2265	391601.1	12.1	0.923	197	116	Amazonian	
8.093°	167.008°	PSP_010862_1880	11815.5	4.9	0.925	82	62	Late Amaz.	
40.322°	221.222°	ESP_011295_2205	17441.2	8.6	0.935	79	42	Amaz./Hesp.	
40.322°	221.222°	ESP_011295_2205	7210.5	6.8	0.935	79	42	Amaz./Hesp.	
40.322°	221.222°	ESP_011295_2205	4983.8	5.4	0.935	79	42	Amaz./Hesp.	267.7
−14.399°	253.854°	ESP_011360_1655	894.0	2.1	0.946	153	196	Late Hesp.	292.7
6.113°	32.289°	ESP_011368_1860	3738.7	3.1	0.934	36	24	Middle Noach.	170.6
6.113°	32.289°	ESP_011368_1860	233.6	1.8	0.934	36	24	Middle Noach.	161.0
−2.355°	278.259°	ESP_011425_1775	2670781.2	50.1	0.951	79	89	Early Hesp.	106.2
39.565°	190.046°	ESP_011428_2200	738.9	3.1	0.935	65	123	Hesp./Noach.	
39.565°	190.046°	ESP_011428_2200	348.8	2.2	0.935	65	123	Hesp./Noach.	
28.587°	271.504°	ESP_011491_2090	5358.0	2.5	0.926	32	44	Amaz./Hesp.	
−1.568°	256.136°	ESP_011584_1785	282024.1	6.2	0.935	54	21	Amaz./Hesp.	81.6
2.386°	266.725°	ESP_011610_1825	11668.2	7.2	0.937	54	28	Late Hesp.	
8.625°	46.830°	ESP_011618_1885	10909.5	3.2	0.937	50	51	Middle Noach.	
8.625°	46.830°	ESP_011618_1885	5456.5	2.6	0.937	50	51	Middle Noach.	
29.513°	267.400°	ESP_011623_2100	6928.2	6.7	0.938	38	55	Amaz./Hesp.	
1.074°	24.437°	ESP_011698_1810	9640.6	6.2	0.937	125	164	Middle Noach.	
1.074°	24.437°	ESP_011698_1810	1779.4	3.3	0.937	125	164	Middle Noach.	
29.660°	249.383°	ESP_011716_2100	2089.7	4.7	0.932	44	57	Early Hesp.	
29.926°	274.403°	ESP_011781_2100	13996.6	3.2	0.919	40	30	Amaz./Hesp.	
−4.375°	217.119°	ESP_012047_1755	16265.2	8.4	0.933	23	65	Middle Noach.	
2.910°	250.769°	ESP_012349_1830	2836.0	2.7	0.935	39	35	Amaz./Hesp.	161.1
23.291°	257.960°	ESP_012375_2035	3563.8	7.0	0.937	43	70	Late Hesp.	
23.291°	257.960°	ESP_012375_2035	7974.2	5.5	0.937	43	70	Late Hesp.	
−2.668°	260.527°	ESP_012441_1775	2018.6	5.9	0.943	62	115	Late Hesp.	
5.303°	205.782°	ESP_012588_1855	228285.1	9.5	0.934	48	68	Late Hesp.	331.4
−8.615°	43.477°	ESP_013161_1715	114433.0	5.2	0.950	109	164	Early Noach.	
4.431°	201.397°	ESP_013287_1845	7178.8	4.0	0.934	28	45	Amaz./Hesp.	
−17.348°	211.929°	ESP_013590_1625	3147.5	5.0	0.936	263	69	Early Noach.	115.9
−5.734°	226.414°	ESP_013629_1740	66160.2	9.6	0.937	80	44	Amaz./Hesp.	
25.429°	282.590°	ESP_013640_2055	8567.6	5.6	0.937	65	76	Early Hesp.	
−5.249°	258.669°	ESP_013641_1745	4887.2	3.5	0.931	28	51	Late Hesp.	154.5
−9.013°	236.369°	ESP_013655_1710	3193.1	8.3	0.943	57	51	Amazonian	
11.476°	255.011°	ESP_013707_1915	12493.0	3.0	0.945	227	78	Amazonian	
10.681°	203.020°	ESP_013788_1910	2244.7	1.6	0.932	41	50	Late Hesp.	265.4
−4.370°	264.598°	ESP_013799_1755	133765.4	9.9	0.939	30	32	Late Hesp.	
2.221°	236.494°	ESP_013800_1820	3860.1	6.3	0.932	94	69	Hesperian	
2.221°	236.494°	ESP_013800_1820	2286.7	5.7	0.932	94	69	Hesperian	
−4.305°	218.330°	ESP_013893_1755	161714.7	8.0	0.937	59	47	Amaz./Hesp.	
0.160°	263.752°	ESP_014010_1800	268760.1	5.2	0.936	28	11	Amaz./Hesp.	52.6
14.760°	230.115°	ESP_014143_1950	20122.8	5.5	0.928	15	38	Late Amaz.	
32.747°	37.632°	ESP_014150_2130	346881.3	13.1	0.923	48	61	Middle Noach.	
12.101°	268.838°	ESP_014168_1920	7037.3	4.7	0.935	34	70	Amaz./Hesp.	
−0.630°	248.913°	ESP_015949_1795	32561.8	38.0	0.939	131	13	Amazonian	
3.417°	235.231°	ESP_015989_1835	14650.2	5.9	0.936	88	82	Hesperian	
20.806°	33.641°	ESP_016115_2010	5996.8	3.2	0.933	17	84	Early Noach.	298.5
2.539°	264.110°	ESP_016133_1825	1159.1	3.8	0.938	50	62	Amaz./Hesp.	255.0
10.599°	186.484°	ESP_016149_1905	603.8	2.7	0.934	77	50	Amaz./Hesp.	
10.599°	186.484°	ESP_016149_1905	587.7	2.0	0.934	77	50	Amaz./Hesp.	
10.599°	186.484°	ESP_016149_1905	189.4	1.9	0.934	77	50	Amaz./Hesp.	
10.599°	186.484°	ESP_016149_1905	230.2	1.4	0.934	77	50	Amaz./Hesp.	
−4.219°	220.551°	ESP_016161_1755	15102.5	10.6	0.941	23	73	Amaz./Hesp.	
−7.302°	258.141°	ESP_016186_1725	3461.4	19.9	0.950	70	47	Late Hesp.	
−6.019°	236.034°	ESP_016200_1740	6470.6	4.9	0.931	57	52	Late Amaz.	296.3
39.373°	149.375°	ESP_016203_2195	552116.1	20.1	0.929	77	92	Late Hesp.	
25.886°	247.886°	ESP_016239_2060	3663.5	3.2	0.934	47	60	Late Amaz.	
29.437°	49.148°	ESP_016299_2095	1571096.5	25.7	0.941	166	167	Amaz./Hesp.	
−6.848°	259.395°	ESP_016331_1730	17391.3	6.0	0.942	56	81	Late Hesp.	
2.598°	264.196°	ESP_016344_1825	5676.7	6.0	0.932	24	20	Amaz./Hesp.	
−6.420°	202.396°	ESP_016465_1735	2839.0	5.6	0.937	97	41	Amaz./Hesp.	
43.778°	203.307°	ESP_016557_2240	9838.0	5.9	0.944	212	202	Amaz./Hesp.	
43.778°	203.307°	ESP_016557_2240	4547.4	5.1	0.944	212	202	Amaz./Hesp.	
43.778°	203.307°	ESP_016557_2240	2517.2	4.3	0.944	212	202	Amaz./Hesp.	

Latitude	Longitude	HiRISE ID	Area (m^2)	Diam.(m)	DCI	TI day	TI night	Epoch	Azimuth
−4.168°	246.709°	ESP_016582_1760	1356.9	4.3	0.937	51	29	Late Amaz.	
−7.343°	202.860°	ESP_016610_1725	1000.0	3.7	0.945	33	57	Middle Noach.	
−13.223°	246.319°	ESP_016648_1665	4398.9	8.2	0.951	45	66	Amaz./Hesp.	
6.126°	276.706°	ESP_016660_1860	5448.4	3.0	0.934	95	51	Amaz./Hesp.	283.1
−1.496°	200.624°	ESP_016676_1785	54458.5	9.8	0.943	19	77	Amaz./Hesp.	
5.419°	245.466°	ESP_016793_1855	1508.5	4.3	0.934	51	59	Late Amaz.	
32.294°	28.959°	ESP_016814_2125	13338.4	8.7	0.924	52	71	Middle Noach.	
32.934°	42.656°	ESP_016919_2130	407.0	2.2	0.917	72	55	Middle Noach.	
44.222°	164.201°	ESP_016954_2245	362943.1	26.8	0.945	131	145	Early Hesp.	
44.350°	152.925°	ESP_016994_2245	38366.9	6.5	0.924	157	189	Late Hesp.	11.5
2.397°	272.255°	ESP_017003_1825	10945.4	4.3	0.939	101	79	Amaz./Hesp.	43.2
−28.017°	36.011°	ESP_017025_1515	6726.1	7.4	0.976	125	213	Middle Noach.	
−4.545°	256.913°	ESP_017030_1755	17336.9	6.4	0.941	88	162	Late Hesp.	92.4
−0.965°	37.833°	ESP_017038_1790	74883.0	4.7	0.937	53	62	Middle Noach.	
−1.791°	227.471°	ESP_017097_1780	36424.9	8.1	0.930	31	26	Amaz./Hesp.	
36.915°	148.297°	ESP_017192_2170	55382.9	8.4	0.929	94	101	Late Hesp.	
30.791°	219.235°	ESP_017229_2110	139508.9	4.8	0.930	48	34	Amazonian	145.3
7.827°	166.881°	ESP_017231_1880	14051.9	4.8	0.929	115	91	Late Amaz.	
35.517°	36.348°	ESP_017262_2160	21276.5	6.5	0.918	62	78	Middle Noach.	345.7
35.517°	36.348°	ESP_017262_2160	9677.5	3.8	0.918	62	78	Middle Noach.	350.4
25.311°	36.795°	ESP_017328_2055	3212.5	4.6	0.925	30	32	Middle Noach.	
4.742°	12.439°	ESP_017329_1850	8316.0	5.3	0.949	242	151	Hesp./Noach.	
13.243°	260.953°	ESP_017333_1935	220567.8	7.4	0.935	57	73	Amaz./Hesp.	174.8
−10.839°	176.007°	ESP_017389_1690	2294.0	2.6	0.928	96	42	Hesperian	
24.073°	268.927°	ESP_017425_2045	17390.1	6.1	0.933	27	84	Early Hesp.	
−1.326°	30.799°	ESP_017447_1785	195860.9	16.5	0.951	27	55	Middle Noach.	
−3.938°	264.973°	ESP_017478_1760	2752.2	4.7	0.939	100	18	Late Hesp.	
30.494°	178.249°	ESP_017481_2110	100804.9	9.4	0.949	47	22	Early Hesp.	229.6
9.019°	241.368°	ESP_017492_1890	34504.8	4.1	0.941	20	89	Early Hesp.	11.7
7.295°	241.965°	ESP_017637_1875	543.5	3.2	0.941	35	79	Amaz./Hesp.	139.9
2.742°	29.533°	ESP_017658_1830	53537.9	5.0	0.939	51	88	Amaz./Hesp.	314.4
18.667°	209.148°	ESP_017770_1990	20887.7	3.0	0.908	50	82	Late Amaz.	6.5
18.667°	209.148°	ESP_017770_1990	16092.8	2.5	0.908	50	82	Late Amaz.	7.5
18.667°	209.148°	ESP_017770_1990	10339.5	2.5	0.908	50	82	Late Amaz.	6.8
53.274°	46.258°	ESP_017789_2335	66262.5	3.3	0.948	205	191	Middle Amaz.	
27.505°	26.964°	ESP_017803_2080	68232.0	3.8	0.935	72	64	Middle Noach.	283.5
−4.556°	254.957°	ESP_017808_1755	3481.6	7.1	0.945	95	132	Late Hesp.	
2.127°	259.687°	ESP_017821_1820	4856.9	3.4	0.946	32	153	Amaz./Hesp.	
63.919°	44.878°	ESP_017868_2440	54093.5	5.3		364	246	Late Hesp.	
50.51°	265.196°	ESP_017926_2310	14141.4	9.8	0.949	139	135	Amaz./Hesp.	
7.493°	245.188°	ESP_017927_1875	66845.5	8.9	0.929	64	19	Amaz./Hesp.	
5.543°	177.891°	ESP_017969_1855	138051.3	7.9	0.927	92	54	Late Amaz.	
39.302°	293.787°	ESP_017991_2195	2281.7	3.0	0.940	141	177	Amaz./Hesp.	
−6.644°	254.705°	ESP_018019_1735	11201.5	7.1	0.969	22	20	Late Hesp.	159.7
−2.953°	259.188°	ESP_018032_1770	4851.9	4.3	0.933	31	53	Late Hesp.	
−3.792°	264.801°	ESP_018045_1760	352881.5	16.1	0.933	39	64	Late Hesp.	
38.648°	280.244°	ESP_018097_2190	6631.9	6.7	0.934	32	55	Early Hesp.	295.8
64.288°	231.501°	ESP_018125_2445	50713.5	4.4		321	167	Late Hesp.	110.8
18.474°	209.201°	ESP_018192_1985	11615.2	6.6	0.917	51	43	Late Amaz.	99.6
−15.346°	250.627°	ESP_018217_1645	694.2	5.1	0.960	84	120	Late Noachian	
−15.346°	250.627°	ESP_018217_1645	628.7	4.2	0.960	84	120	Late Noachian	
−2.566°	183.966°	ESP_018404_1775	7264.5	4.9	0.932	27	26	Hesperian	
12.331°	271.464°	ESP_018493_1925	5641.2	3.6	0.919	43	70	Amaz./Hesp.	
−8.878°	217.642°	ESP_018561_1710	309.2	3.0	0.930	34	86	Amaz./Hesp.	
−8.878°	217.642°	ESP_018561_1710	297.4	2.7	0.930	34	86	Amaz./Hesp.	
60.987°	238.723°	ESP_018573_2415	47504.2	7.3	0.967	237	184	Late Hesp.	
−6.325°	254.717°	ESP_018586_1735	18126.5	9.9	0.944	91	41	Late Hesp.	
40.341°	185.501°	ESP_018707_2205	3647.5	3.2	0.956	249	188	Late Amaz.	
−3.017°	256.204°	ESP_018731_1770	29744.1	11.4	0.944	21	59	Late Hesp.	
54.767°	196.848°	ESP_018746_2350	7151.8	3.3	0.949	223	207	Late Hesp.	
24.921°	245.289°	ESP_018784_2050	21491.0	5.2	0.935	20	48	Amaz./Hesp.	86.8
23.604°	169.066°	ESP_018800_2040	595.8	2.1	0.931	118	164	Late Amaz.	
46.611°	133.706°	ESP_018854_2270	18265.0	3.1	0.941	274	240	Late Hesp.	
36.014°	282.014°	ESP_019165_2165	2209.3	5.2	0.921	47	41	Early Hesp.	
36.014°	282.014°	ESP_019165_2165	1830.2	5.1	0.921	47	41	Early Hesp.	
37.341°	182.194°	ESP_019195_2175	65927.7	8.2	0.966	155	211	Late Amaz.	

Latitude	Longitude	HiRISE ID	Area (m^2)	Diam.(m)	DCI	TI day	TI night	Epoch	Azimuth
49.353°	189.666°	ESP_019287_2295	1246.9	1.8	0.948	209	254	Amazonian	
27.054°	245.366°	ESP_019707_2075	3030.4	4.9	0.922	24	66	Amaz./Hesp.	
40.424°	77.603°	ESP_019779_2205	470.2	2.0	0.928	316	253	Late Hesp.	
41.017°	126.301°	ESP_019830_2215	623726.8	14.5	0.935	249	227	Amazonian	
26.936°	27.301°	ESP_019926_2070	690229.9	4.8	0.927	37	40	Middle Noach.	
−0.066°	274.104°	ESP_019983_1800	105420.7	4.9	0.943	80	95	Amaz./Hesp.	11.3
32.249°	112.389°	ESP_020714_2125	35597.7	4.5	0.958	383	326	Amaz./Hesp.	351.2
0.372°	284.325°	ESP_020787_1805	4622.0	4.0	0.940	67	44	Early Hesp.	
30.310°	245.200°	ESP_020841_2105	3006.1	4.2	0.938	18	61	Amaz./Hesp.	126.6
22.814°	219.910°	ESP_020842_2030	387.9	4.4	0.933	141	60	Late Amaz.	
1.506°	281.637°	ESP_020853_1815	9545.1	3.4	0.935	73	72	Noachian	0.5
16.322°	252.323°	ESP_020854_1965	393.7	6.2	0.936	33	85	Amaz./Hesp.	
23.335°	225.246°	ESP_020855_2035	37889.1	7.5	0.939	30	155	Amazonian	
7.060°	172.361°	ESP_020857_1870	6772.2	5.9	0.922	28	44	Late Amaz.	
18.935°	202.796°	ESP_020869_1990	2384.6	2.9	0.933	78	49	Amaz./Hesp.	202.5
5.324°	252.312°	ESP_020920_1855	1066.3	4.5	0.932	36	53	Amaz./Hesp.	105.7
3.763°	235.960°	ESP_020947_1840	10622.2	6.1	0.934	57	29	Amaz./Hesp.	102.9
9.470°	239.516°	ESP_020960_1895	4997.6	5.5	0.940	43	101	Early Hesp.	
−1.344°	141.567°	ESP_021768_1785	9460.8	2.9	0.933	167	122	Early Hesp.	
9.034°	239.950°	ESP_021883_1890	51738.6	7.6	0.938	67	148	Early Hesp.	
12.270°	196.484°	ESP_022056_1925	5089.9	3.4	0.932	77	55	Late Hesp.	
−10.660°	231.077°	ESP_022279_1690	15456.8	4.0	0.932	56	58	Amaz./Hesp.	
23.919°	41.471°	ESP_022299_2040	13265.1	2.2	0.934	33	53	Middle Noach.	110.5
3.117°	53.383°	ESP_022536_1830	1864.0	2.6	0.954	131	134	Amaz./Hesp.	
−7.729°	229.362°	ESP_022912_1720	3713.4	4.7	0.937	10	8	Amaz./Hesp.	
4.472°	246.893°	ESP_022964_1845	3014.4	3.0	0.935	24	68	Late Amaz.	
6.774°	275.679°	ESP_023108_1870	17648.1	5.7	0.937	64	48	Amaz./Hesp.	221.3
1.829°	46.910°	ESP_023156_1820	213718.2	9.6	0.934	68	43	Middle Noach.	
−6.630°	156.445°	ESP_023363_1735	17368.1	5.4	0.931	80	145	Hesperian	
7.062°	251.771°	ESP_023399_1870	11791.0	9.2	0.934	34	70	Amaz./Hesp.	212.3
3.241°	235.100°	ESP_023426_1835	9795.7	4.7	0.935	150	138	Hesperian	122.2
3.241°	235.100°	ESP_023426_1835	2937.5	4.5	0.935	150	138	Hesperian	131.5
3.614°	235.908°	ESP_023571_1835	5576.5	4.5	0.935	28	40	Amaz./Hesp.	109.7
−0.268°	262.285°	ESP_024203_1795	76529.8	9.7	0.937	8	47	Amaz./Hesp.	280.5
25.663°	41.615°	ESP_024211_2060	1157.1	2.0	0.917	22	56	Middle Noach.	
25.663°	41.615°	ESP_024211_2060	1689.3	1.6	0.917	22	56	Middle Noach.	
25.663°	41.615°	ESP_024211_2060	1335.7	1.6	0.917	22	56	Middle Noach.	
21.585°	234.771°	ESP_024349_2020	3011.8	3.8	0.936	44	45	Late Amaz.	316.8
−0.441°	225.189°	ESP_024389_1795	4052.1	4.6	0.937	40	20	Amaz./Hesp.	
8.871°	47.660°	ESP_024646_1890	41594.8	6.1	0.932	38	107	Middle Noach.	
17.484°	259.150°	ESP_024836_1975	295176.7	9.4	0.935	275	58	Amaz./Hesp.	116.1
7.457°	279.168°	ESP_025732_1875	2083.6	2.8	0.939	209	41	Amaz./Hesp.	
43.901°	204.347°	ESP_025840_2240	730339.8	7.2	0.933	181	201	Late Hesp.	
3.702°	275.991°	ESP_025864_1835	68286.7	7.0	0.950	65	25	Amaz./Hesp.	
4.865°	279.362°	ESP_025943_1850	669.4	3.0	0.938	67	110	Amaz./Hesp.	
11.840°	275.694°	ESP_026009_1920	84900.6	4.3	0.938	46	54	Amaz./Hesp.	77.1
35.318°	201.373°	ESP_026038_2155	1280.6	3.8	0.951	46	78	Amazonian	
13.261°	15.788°	ESP_026124_1935	83610.5	6.3	0.933	36	44	Middle Noach.	5.6
2.579°	248.522°	ESP_026221_1825	36609.3	11.6	0.939	86	89	Amazonian	
47.717°	225.134°	ESP_026248_2280	28670.2	8.1	0.933	111	96	Amaz./Hesp.	
20.543°	268.569°	ESP_026418_2010	3714.1	3.4	0.937	39	61	Amaz./Hesp.	40.9
24.106°	279.799°	ESP_026589_2045	1675.2	3.1	0.940	97	75	Early Hesp.	
5.131°	290.591°	ESP_026892_1850	1986326.2	35.5	0.953	202	126	Early Hesp.	12.7
19.096°	260.735°	ESP_026893_1995	1898.4	2.4	0.935	40	63	Amaz./Hesp.	125.9
19.096°	260.735°	ESP_026893_1995	373.9	2.0	0.935	40	63	Amaz./Hesp.	130.0
−8.650°	225.048°	ESP_026934_1715	160140.7	15.8	0.943	42	101	Amaz./Hesp.	
−8.880°	235.772°	ESP_026960_1710	5504.6	5.7	0.937	69	26	Amaz./Hesp.	
18.189°	247.669°	ESP_026999_1985	11224.5	9.1	0.940	16	58	Amaz./Hesp.	
−1.342°	279.731°	ESP_027077_1785	161092.4	10.4	0.957	160	105	Early Hesp.	174.6
−8.415°	199.220°	ESP_027080_1715	5045.1	4.6	0.946	58	50	Middle Noach.	
1.011°	235.798°	ESP_027316_1810	2864.7	6.3	0.933	34	65	Amaz./Hesp.	
−5.812°	190.371°	ESP_027410_1740	378973.6	13.8	0.942	75	23	Early Hesp.	
3.290°	246.827°	ESP_027975_1835	7212.6	9.6	0.933	50	121	Amazonian	
26.902°	281.149°	ESP_028000_2070	62925.1	9.6	0.938	15	79	Early Hesp.	
26.902°	281.149°	ESP_028000_2070	46571.6	7.9	0.938	15	79	Early Hesp.	
26.738°	281.209°	ESP_028633_2070	1718.9	5.1	0.939	67	59	Early Hesp.	

Latitude	Longitude	HiRISE ID	Area (m^2)	Diam.(m)	DCI	TI day	TI night	Epoch	Azimuth
24.582°	291.109°	ESP_028659_2050	370142.8	10.7	0.944	40	71	Early Hesp.	
−2.799°	280.052°	ESP_028976_1770	21250.8	4.2	0.949	180	62	Early Hesp.	
−6.935°	198.549°	ESP_028979_1730	164.6	3.5	0.941	64	46	Middle Noach.	
−9.239°	295.830°	ESP_029015_1705	5244.8	9.7	0.952	212	173	Early Hesp.	
39.092°	190.276°	ESP_029256_2195	1370958.9	12.5	0.941	124	141	Amazonian	
13.336°	283.772°	ESP_029701_1935	582627.5	15.6	0.937	99	89	Amaz./Hesp.	
18.676°	219.911°	ESP_030178_1990	99825.5	8.9	0.929	116	65	Amazonian	
18.222°	244.905°	ESP_030243_1985	604.4	3.5	0.932	70	80	Late Hesp.	65.4
0.783°	234.845°	ESP_030705_1810	29223.5	9.7	0.939	57	20	Amaz./Hesp.	
−2.165°	158.562°	ESP_032211_1780	254051.3	7.9	0.936	104	105	Early Hesp.	
−17.268°	225.230°	ESP_033870_1625	7406.3	5.6	0.937	15	31	Amaz./Hesp.	
5.368°	26.007°	ESP_035354_1855	4340.5	2.9	0.943	19	42	Middle Noach.	
−13.418°	225.897°	ESP_036916_1665	655657.4	15.3	0.936	22	21	Amaz./Hesp.	
29.203°	22.179°	ESP_036976_2095	348456.2	13.6	0.921	56	37	Middle Noach.	
23.858°	265.925°	ESP_037033_2040	1751859.2	4.7	0.936	19	45	Amaz./Hesp.	

Chapter 4

Data analysis and discussion

In this chapter, we present the analysis of the data we acquired on the Martian fresh craters and we discuss the results obtained in this work. In the following, we examine the distribution of the impact sites on the surface and the size of the craters and their ejecta. We correlate these parameters with the characteristics of the surface around the impact size, using the values of dust cover index, thermal inertia and the age of the terrain previously reported. Lastly, we study the orientation of the rays of not symmetric ejecta.

4.1 Fresh crater distribution

We highlighted the position of the fresh craters considered in this work on the MOLA map of the Martian surface (Figure 16). Most of the craters are located around the equator and in low-to-mid latitude regions mostly towards the northern hemisphere, with just three cases of craters above 60° N. In the southern hemisphere, the crater distribution extends only to $\sim$ 17° S, with just one crater around 28° S and two located at $\sim$ 50° S, one in Argyre Planitia and one in the Hellas Basin.
Regarding the longitude distribution, the sample can be divided into two sections. The greater portion of fresh craters is located in the area between $\sim$ 110° E and $\sim$ 60° W, that comprises the area around Elysium Mons, Amazonis Planitia and all the Tharsis region. The smaller portion is located almost entirely between 0° and 60° E, around Arabia Terra and Terra Sabaea. This regions coincide with the areas that display an higher presence of dust, as confirmed by the dust cover index map, that shows a darker shade in these areas (Figure 17). The detection of fresh craters is thus biased towards dusty locations because in these regions it is easier to detect the dark blast zone

formed by the impact (Dundas et al. 2014).

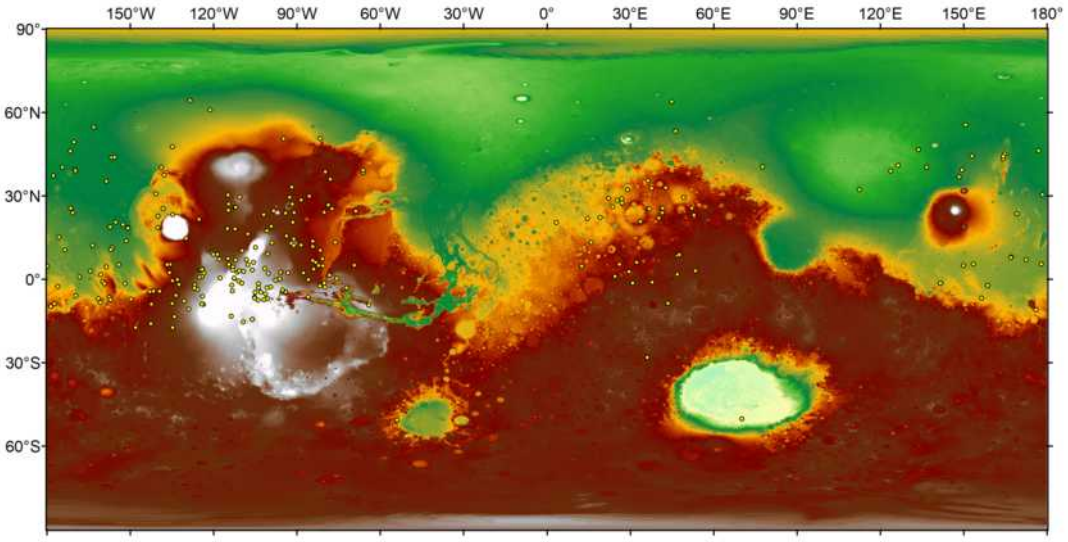

Figure 16: Distribution of our fresh craters sample on the surface of Mars.

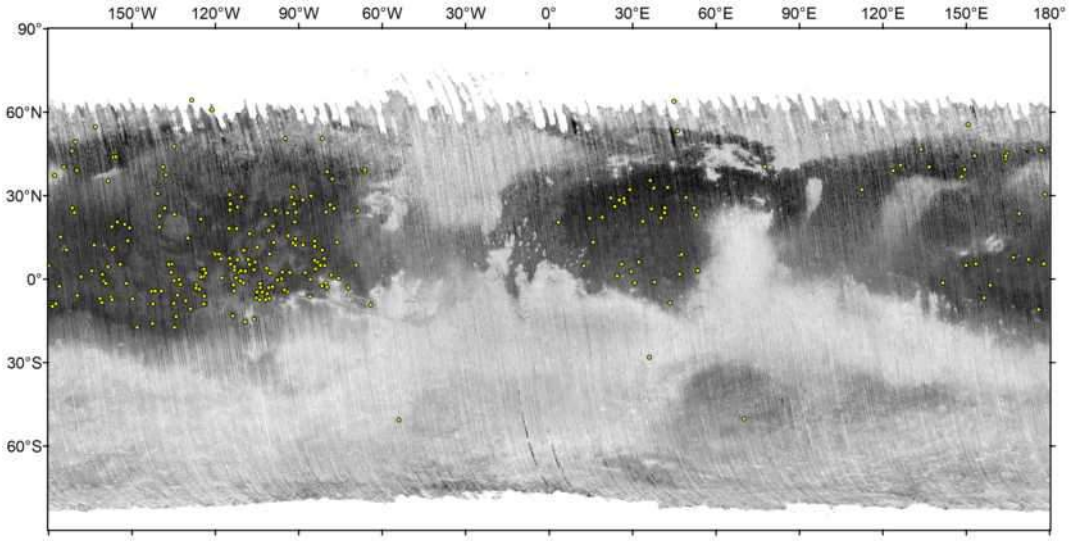

Figure 17: The detection of fresh craters is biased towards the dustier regions, denoted by a darker shade in the dust cover index map.

4.2 Crater diameter and area of the ejecta

As noted in the previous chapters, large impacts are rare and most new impacts form a small crater. This is confirmed by our sample as most craters have a diameter smaller than 10 meters, with a majority of craters with diameters between 2 and 6 meters, while the smallest ones are just 1.4 meters across. Only two craters have a diameter between 30 and 40 meters (ESP_026892_1850, ESP_015949_1795), while the bigger one (ESP_011425_1775) has a diameter around 50 meters (Figure 18).
Similarly, the area of the ejecta tends to be small for most craters, with a peak between 10^3 and 10^4 m^2, but there are some larger ones with an extension exceeding 10^6 m^2 (Figure 19).
Plotting the diameter of the crater against the area of its ejecta, we derive that larger craters have usually a more extensive ejecta (Figure 20). However, there are exceptions to this common trend. Indeed, there are a few large craters having an ejecta smaller than expected, but also modest craters with a vast ejecta. This happens because there are multiple factors influencing the formation of the ejecta, such as the composition and velocity of the impactor. In addition, the fresh craters could have been discovered too late after its formation and the ejecta may have already partially faded away.

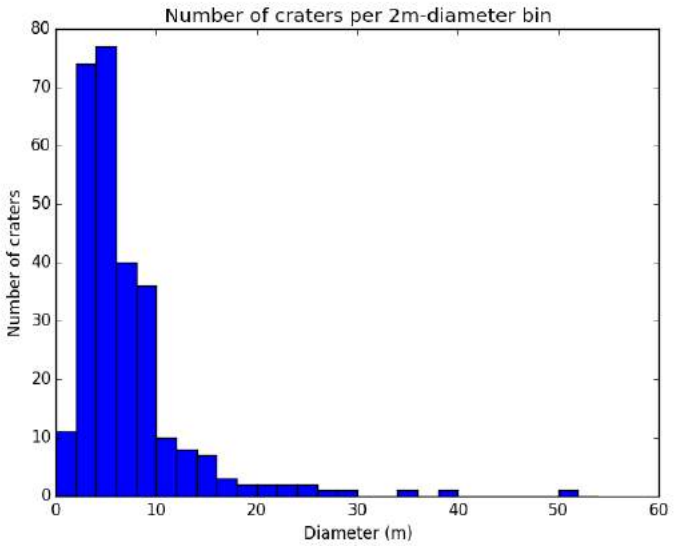

Figure 18: In this plot it is reported the number of craters versus the diameter in meters. Assuming a bin of 2 meters for the diameter, we highlight that most of the craters display a diameter smaller than 10 m.

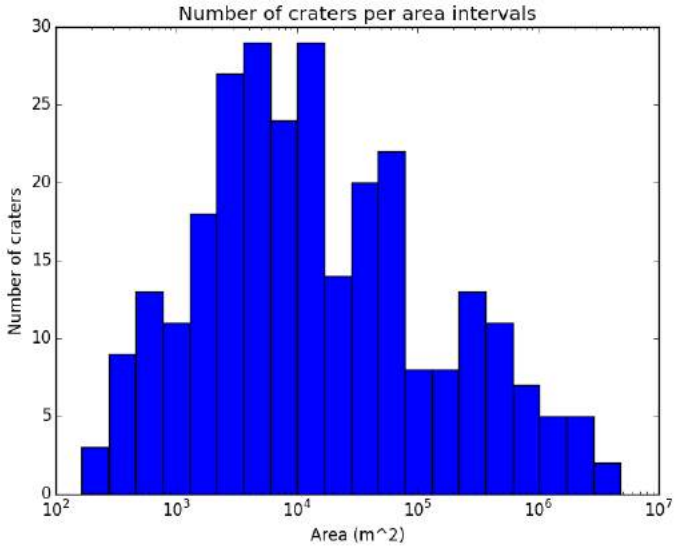

Figure 19: In this plot it is reported the number of craters versus the area of the ejecta in square meters. A peak around an area of 10^4 m^2 is well shown.

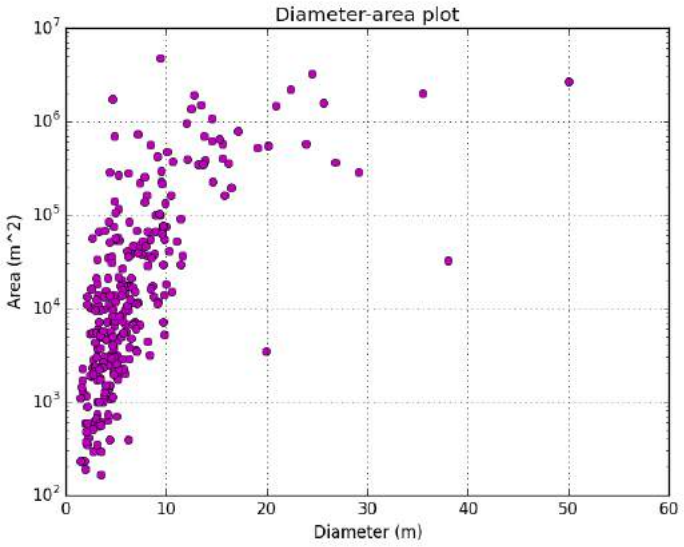

Figure 20: In this plot it is reported the diameter of the craters (in meters) versus the area of the ejecta (in square meters). The ejecta tends to be greater for larger craters.

4.3 Dust cover index and thermal inertia

As noted previously, the detection of the fresh craters is biased towards dustier regions since in this areas it is easier to see the impact blast zone. According to Ruff & Christensten (2002), who compiled the dust cover index map used in this work, there is a bimodal distribution of this index, with a peak around 0.935 for dusty terrains and a taller peak at 0.97 for dust-free regions. In our sample, most sites have a dust cover index between 0.93 and 0.95, with a peak around 0.935, indicating the prevalence of dusty terrains. Instead, just very few craters have a dust cover index above 0.96.
We plotted both the crater diameter and the area of the ejecta against the dust cover index, but the distribution does not seem to suggest any correlation. The plot suggests that the craters with large diameter tend to form in areas with average values of dust cover index. It is possible that this distribution is just due to the greater abundance of impact sites in regions with dust cover index in that interval, giving an higher probability to find larger craters (Figure 21 and Figure 22).

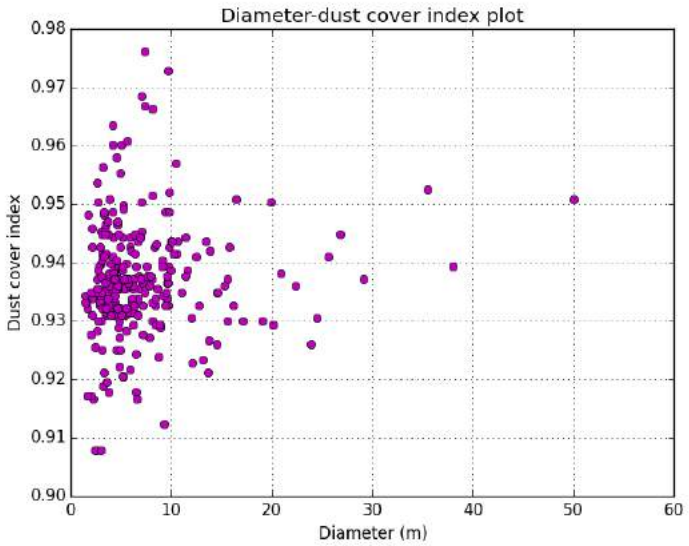

Figure 21: In this plot it is reported the diameter of the craters in meters versus the dust cover index.

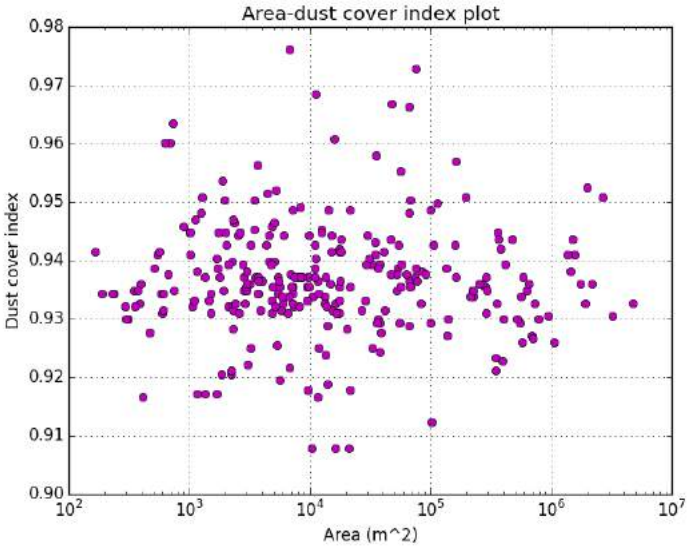

Figure 22: In this plot it is reported the area of the ejecta in square meters versus the dust cover index.

The same situation can be seen for the values of thermal inertia, for both the day and night case. The majority of craters have values of thermal inertia $<$100 TIU, indicating a dust-rich terrain. As the case of dust cover index, we plotted the correlation of thermal inertia day and night against the diameter of the crater (Figure 23 and Figure 24) and the area of the ejecta (Figure 25 and Figure 26), without any indication of clear correlations between these values.
We carried out another analysis regarding the dust cover index and its influence on the formation of the craters. We selected four craters with DCI$>$0.95 (ESP_017025_1515, PSP_007561_1290, ESP_018019_1735, ESP_016648_1665), four with 0.93$<$DCI$<$0.95 (ESP_018586_1735, ESP_026999_1985, ESP_013799_1755, ESP_021883_1890) and four with DCI$<$0.93 (ESP_017097_1780, ESP_017927_1875, PSP_006629_1955, PSP_003958_2095), each with a diameter between 7 and 10 meters.
We compared the characteristics of the selected fresh craters that have a similar diameter (Figure 27). There is not any clear difference between the impact sites considered but the craters formed in terrains with higher dust cover index (less dust), appear to be more defined with more elevated ridges.

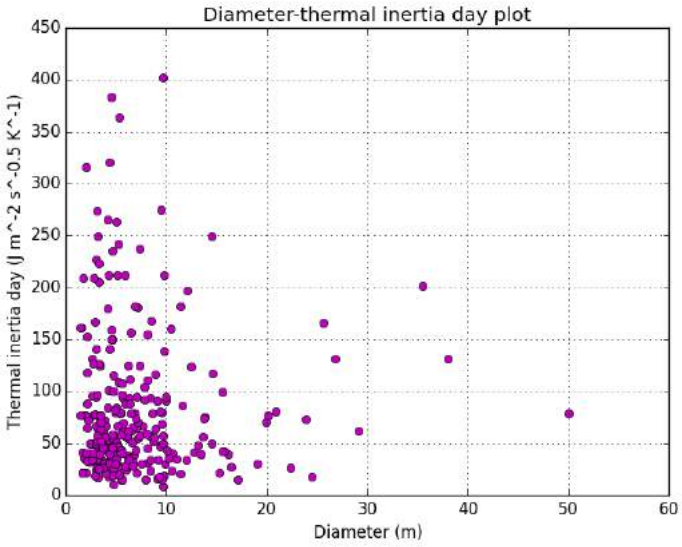

Figure 23: In this plot it is reported the diameter of the craters in meters versus the thermal inertia day in TIU.

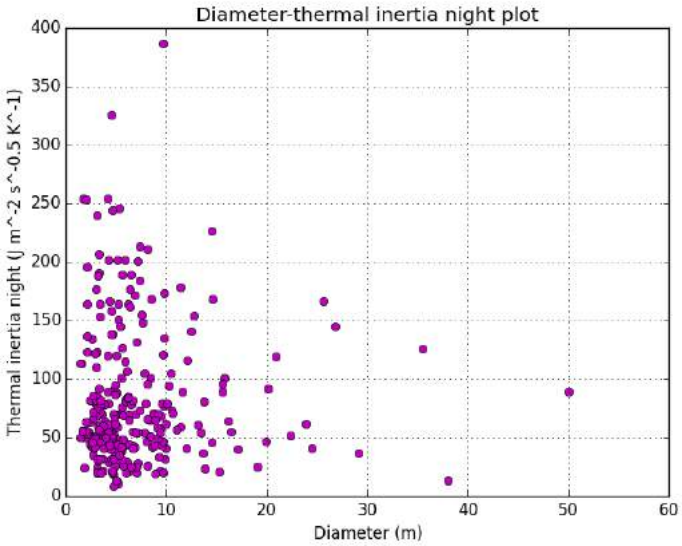

Figure 24: In this plot it is reported the diameter of the craters in meters versus the thermal inertia night in TIU.

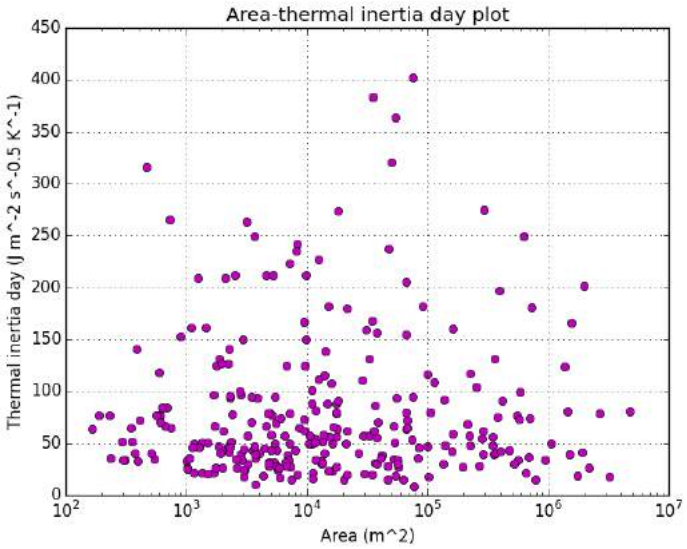

Figure 25: In this plot it is reported the area of the ejecta in square meters versus the thermal inertia day in TIU.

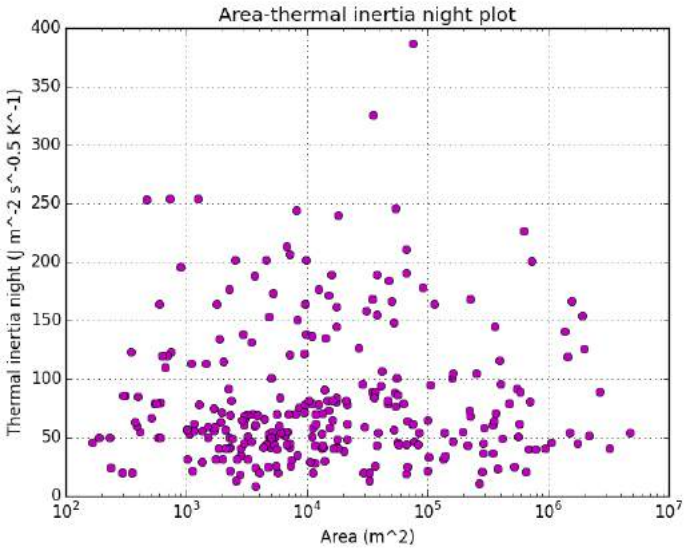

Figure 26: In this plot it is reported the area of the ejecta in square meters versus the thermal inertia night in TIU.

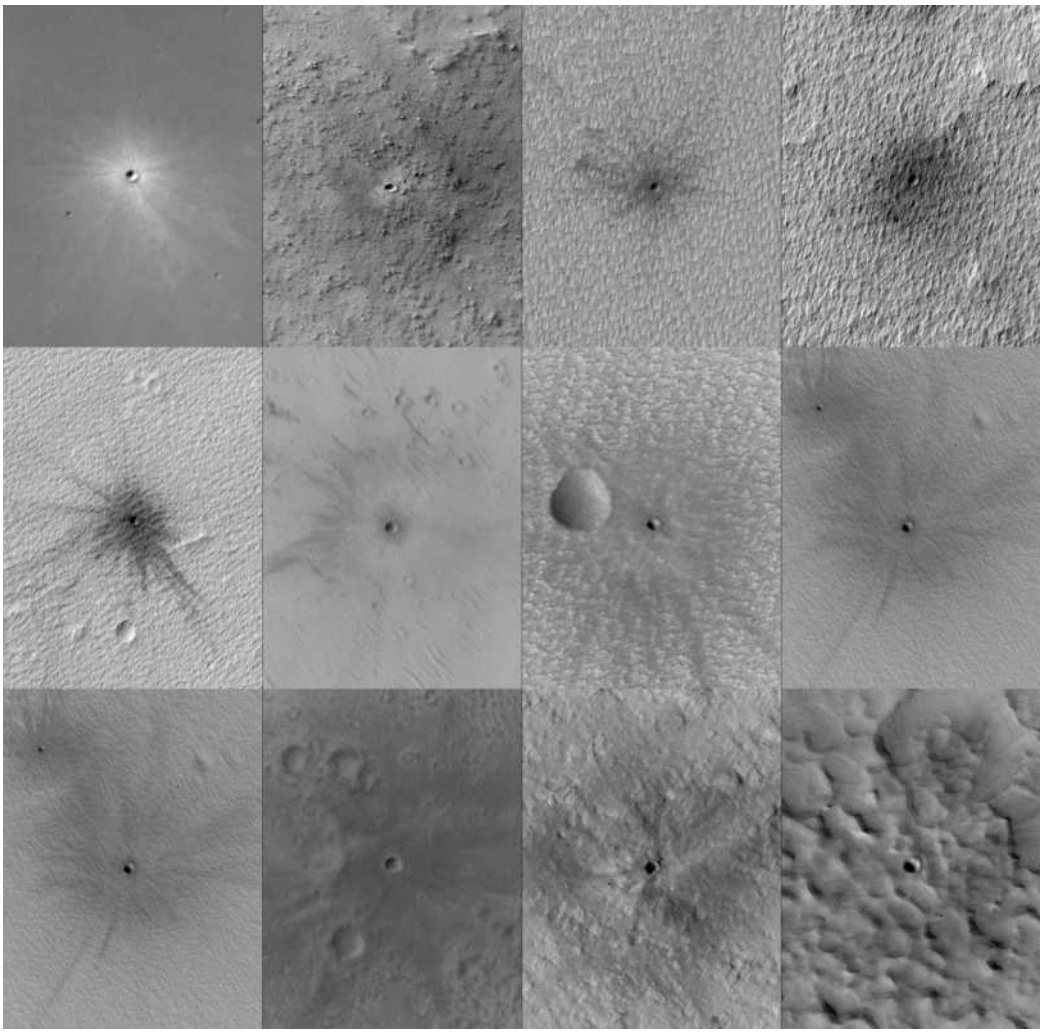

Figure 27: Comparison between craters of similar size but located in terrains with different values of dust cover index. In the first row the craters with DCI>0.95, in the second one the craters with 0.93<DCI<0.95, and in the last one the craters with DCI<0.93.

4.4 Craters surface age

We analyzed the age of the terrain in which the fresh craters formed using the global geologic map of Mars compiled by Tanaka et al. (2014). Terrains that formed in different ages also have different compositions, this can influence the formation of the craters and the ejecta.
For this analysis, we excluded some uncertain cases where the epoch given by the geologic map was just Noachian (2 craters), Hesperian (9 craters) or Amazonian (15 craters), without further specification. Almost half of the craters can be found in terrains marked as Amazonian/Hesperian, signaling a region with mixed characteristics or dating back to the transitional period between the two geologic epochs. This type of relatively recent terrain can indeed be found in most of the regions where our fresh crater sample is located. Instead, only about 50 craters formed in terrains dating back to the Noachian period, as most of the regions with this terrain are found in the southern hemisphere, where our sample is limited (Figure 28).
We then studied possible correlations between the diameter of the crater and the epoch of the terrain. We excluded from the sample not just the uncertain cases explained previously, but also the epochs with less than 20 craters (Early Noachian: 3 craters, Late Noachian: 2 craters, Hesperian/Noachian: 7 craters, Middle Amazonian: 2 craters). We can see that the mean diameter seems to be decreasing in more recent terrains after a maximum in the Early Hesperian epoch, but our sample is too limited to infer that there is an actual relation between the size of the crater and the age of the terrain (Figure 29).
We carried out the same analysis with the same sample correlating the area of the ejecta with the epoch of the region. In this case there is not any correlation between these parameters (Figure 30).

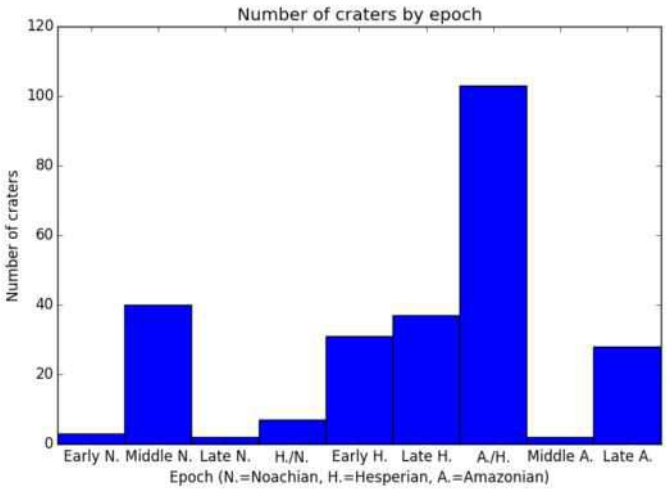

Figure 28: In this plot it is reported the number of craters versus the epoch of the terrain.

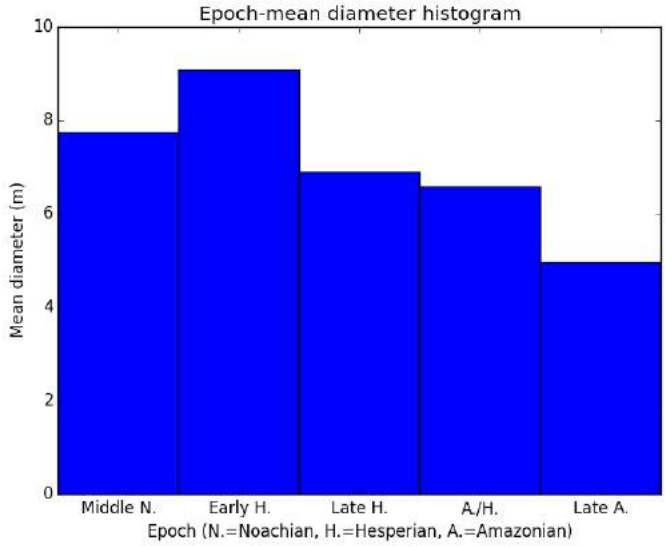

Figure 29: In this plot it is reported the mean diameter of the craters (in meters) versus the epoch of the terrain.

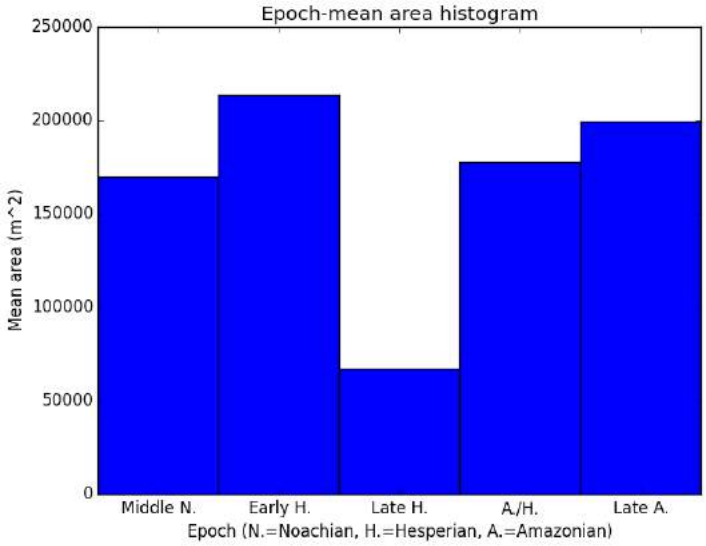

Figure 30: In this plot it is reported the mean area of the ejecta (in square meters) versus the epoch of the terrain.

4.5 Orientation of ejecta rays

Our last analysis regarded a limited portion of our sample. We selected 85 cases of not symmetric ejecta with visible rays departing from the central impact site. We calculated the mean azimuth of the rays, weighted with their lengths. We analyzed the distribution of the direction of the rays on the surface. Considering our bias in the location of the fresh craters, the distribution seems to be quite homogeneous in both latitude and longitude (Figure 31 and Figure 32). In addition, we divided the sample in bins of 30° each, but also in this case there does not seem to be a bias towards certain intervals of azimuth (Figure 33).

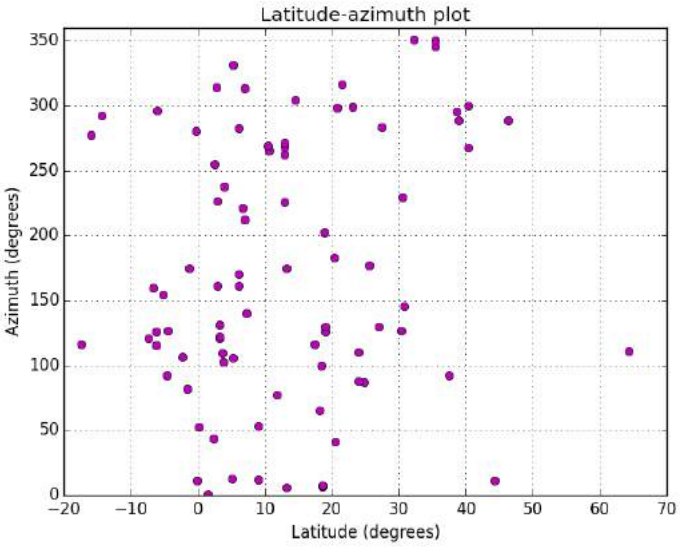

Figure 31: In this plot it is reported the mean azimuth of the ejecta rays (in degrees) versus the latitude of the crater (in degrees).

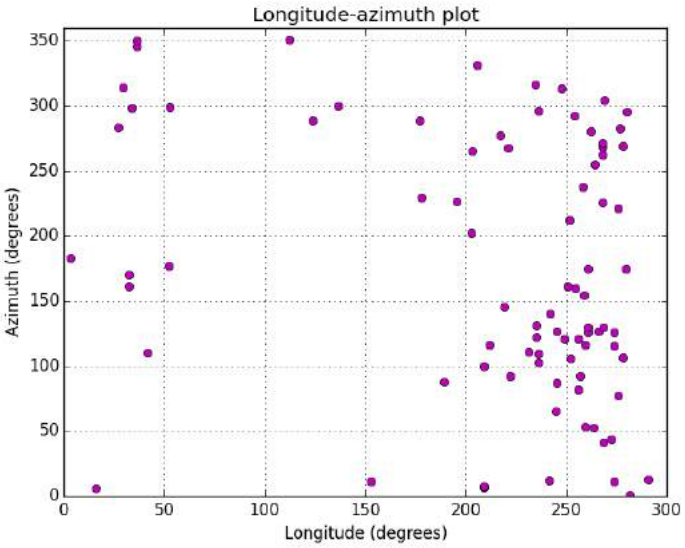

Figure 32: In this plot it is reported the mean azimuth of the ejecta rays (in degrees) versus the longitude of the crater (in degrees).

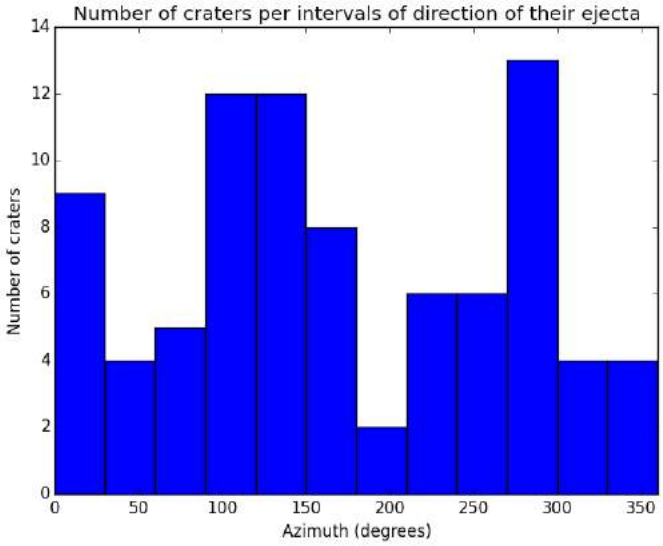

Figure 33: In this plot it is reported the number of craters against the azimuth of ejecta rays divided in bins of 30°.

4.6 Results

We found that the distribution of the fresh craters identified on the Martian surface is biased towards dusty terrains, because dust makes it easier to detect the dark blast zone generated by the impacts. Most of the craters are very small, with a diameter usually smaller than 10 meters, while the areas of the ejecta are typically around 10^4 m^2. We also noted that larger ejecta tend to correspond to wider craters, but there are some exceptions owing to different terrains and impactors. We did not find any correlation between the diameter of the craters and various parameters of the terrain such as dust cover index and thermal inertia. We also did not find correlations between the area of the ejecta and the same parameters. The mean diameter of the craters seems to be decreasing for impact sites in more recent terrains, but with our limited sample it is difficult to assume that there is a real correlation between these parameters. Instead, there is no correlation between the area of the ejecta and the age of the terrain. In addition, our study reported that the orientation of ejecta rays in the case of not symmetric ejecta does not show any bias towards certain intervals of orientation in azimuth, or towards their latitude or longitude.

Conclusion and future works

In this work, we globally characterize the fresh craters located on the surface of Mars thanks to the high resolution images acquired by the CTX and HiRISE instruments onboard the MRO space mission. We correlate the diameter and area of the crater ejecta with different parameters, such as topography, dust cover index and surface exposure age in order to find any correlation between the craters and the terrain in which they formed. Hence, this work enlarges the knowledge of the fresh craters located on the surface of the planet. Indeed, we found that ejecta usually increase with the crater diameter, while we did not derive any correlation between the crater ejecta and both the amount of dust and the age of the terrain in which they formed. No relationships have been found also for the orientation of ejecta and their location. Anyway, the limited size of our sample makes it difficult to state the presence of correlations between the studied parameters and, thus, future studies are necessary.
For future analysis, we need a larger database because the current one consists of about only 300 fresh craters. This can be achieved with a continuous monitoring of the Martian surface by the spacecrafts that are currently orbiting the planet, together with future missions observations. Larger samples will allow us to better define the existence of any correlation between the physical characteristics of the fresh craters and the ones of the terrain in which they formed. In addition, a continuous imaging of already discovered impact sites can provide us new insight about the history of the evolution of the crater and its ejecta and the composition of the terrain along with the weathering processes affecting the surface. We need also to decrease the observational bias towards dusty terrains in the detection of fresh craters, hence, an extensive imaging campaign of terrains with less or no dust is needed.
This can be done thanks to images acquired by the Colour and Stereo Surface Imaging System (CaSSIS) on the Mars Trace Gas Orbiter (TGO) currently orbiting the planet. The CaSSIS images with a resolution of 4.5 m can enlarge the coverage of the planet at high resolution and, hence, allow the

discovery of new possible impact sites. In addition, CaSSIS can provide 3D reconstruction of the surface through the Digital Terrain Model (DTM). In this way, we will be able to obtain also the elevation of the crater area deriving its depth and ejecta thickness. Furthermore, since CaSSIS operates using four filters in the visible range, it is possible to obtain information about the composition of the terrain and the ejecta. This can help to better catalogue the different ejecta behaviour. New CaSSIS images can also be obtained on sites already observed by CTX in order to study any possible changes in the appearance of the ejecta that can be useful to analyze the evolution of the fresh craters.

Appendix

In this appendix we report all our sample of 279 craters in 249 sites. For each site the original HiRISE image is reported on the right and the image with the ejecta marked by a red area is reported on the left. In the cases in which it was possible to study the orientation of the ejecta rays, the image with the red area is in the center while on the left there is the image with the ejecta rays marked with yellow lines. The sites are reported in chronological order of acquisition of the image by HiRISE, from the oldest to the most recent ones.
In addition, for each crater there is a table under the image with all the data we used and found in this work. In the table, *HiRISE ID* is the name of the image in the HiRISE database, *Area* stands for the area of the ejecta, while *Diam.* is the diameter of the crater. *DCI* is the dust cover index while *TI* stands for thermal inertia, reported in Thermal Inertia Units (TIU). In the cases where is reported, *Azimuth* is the mean azimuth of the ejecta rays weighted with the length of the rays.

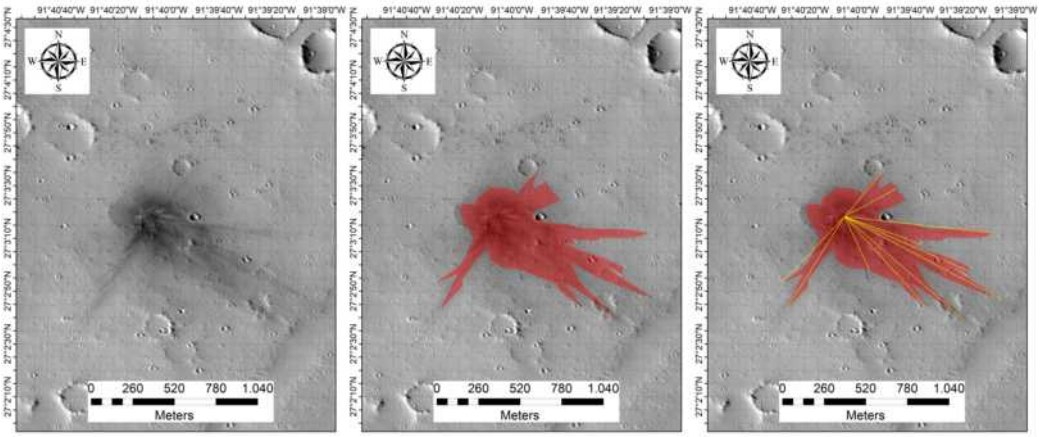

Latitude	Longitude	HiRISE ID	Area (m^2)	Diam.(m)	DCI	TI day	TI night	Epoch	Azimuth
27.055°	268.332°	PSP_002736_2075	398962.9	15.5	0.930	42	96	Hesperian	129.7

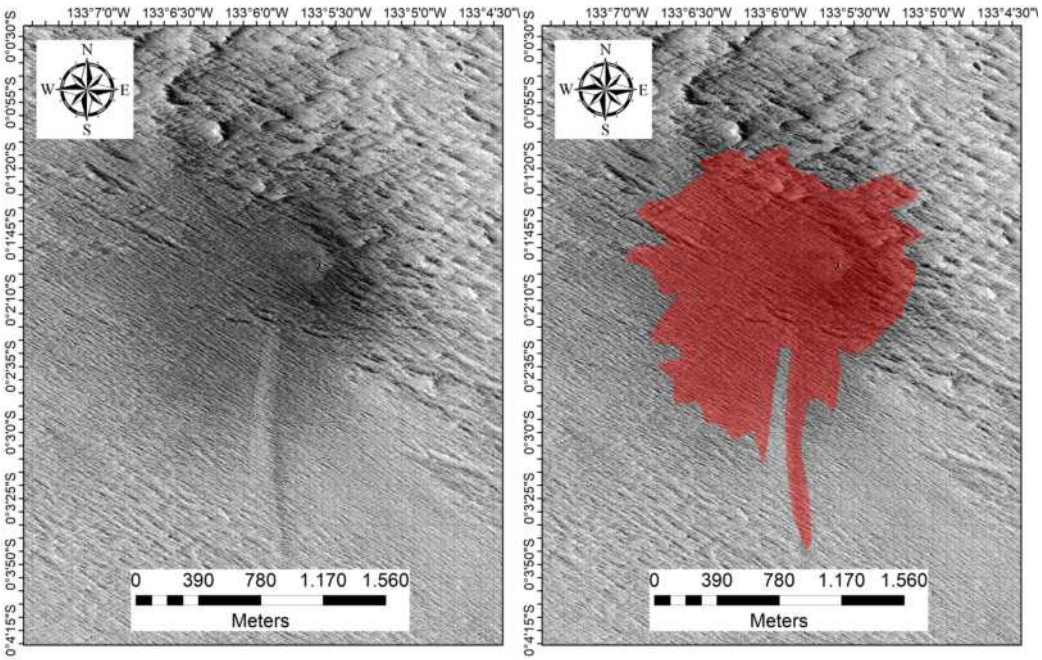

Latitude	Longitude	HiRISE ID	Area (m^2)	Diam.(m)	DCI	TI day	TI night	Epoch
−0.033°	226.907°	PSP_002764_1800	2185001.3	22.3	0.936	26	52	Amaz./Hesp.

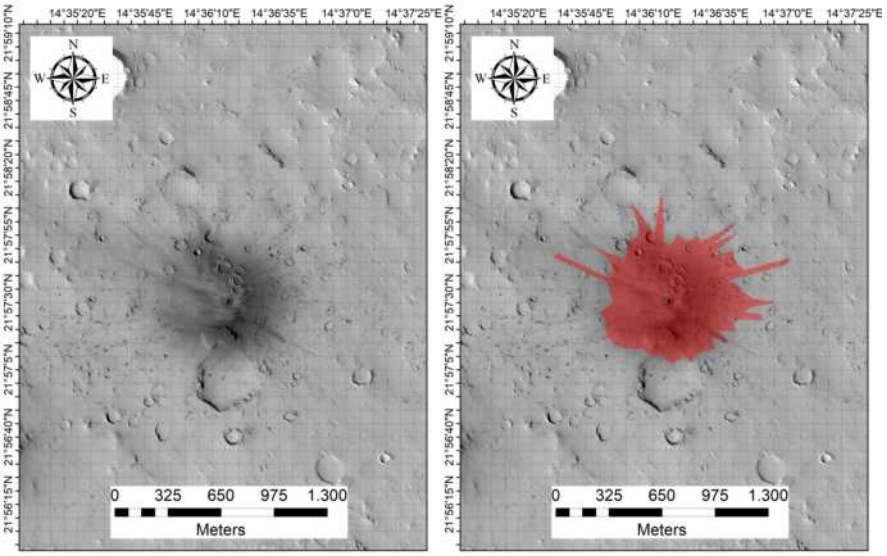

Latitude	Longitude	HiRISE ID	Area (m^2)	Diam.(m)	DCI	TI day	TI night	Epoch
21.958°	14.604°	PSP_003075_2020	572684.0	23.9	0.926	73	62	Middle Noach.

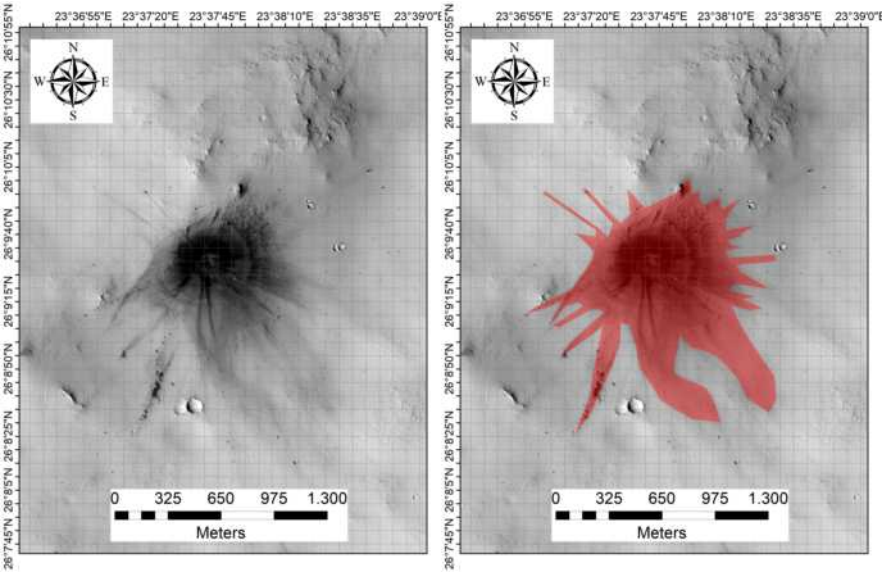

Latitude	Longitude	HiRISE ID	Area (m^2)	Diam.(m)	DCI	TI day	TI night	Epoch
26.158°	23.627°	PSP_003101_2065	1064841.1	14.5	0.926	50	46	Middle Noach.

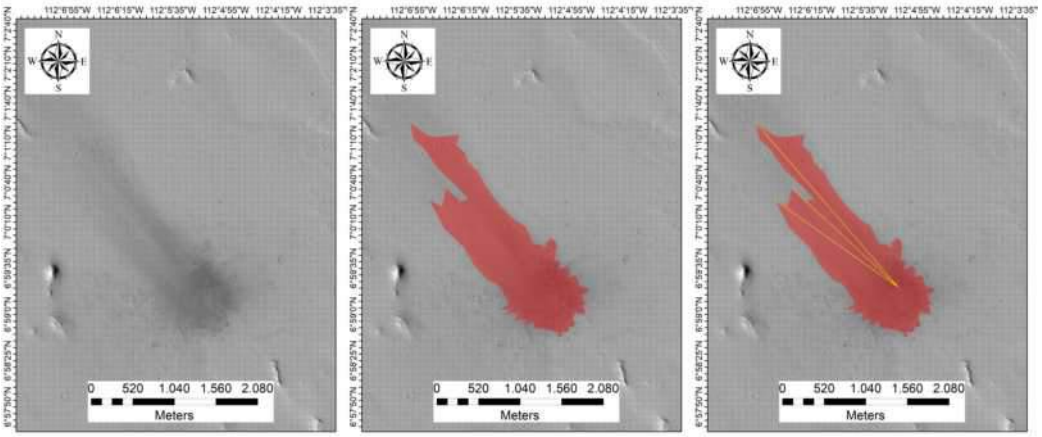

Latitude	Longitude	HiRISE ID	Area (m^2)	Diam.(m)	DCI	TI day	TI night	Epoch	Azimuth
6.989°	247.914°	PSP_003172_1870	1898009.4	12.8	0.933	41	154	Amaz./Hesp.	313.2

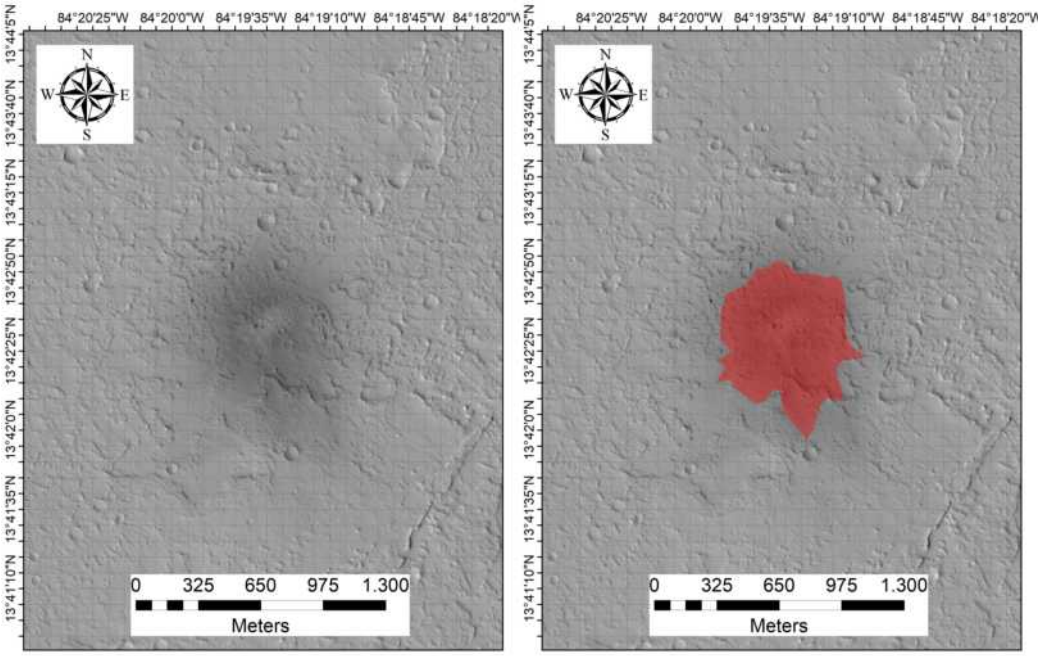

Latitude	Longitude	HiRISE ID	Area (m^2)	Diam.(m)	DCI	TI day	TI night	Epoch
13.709°	275.674°	PSP_003527_1940	420945.1	9.1	0.939	91	49	Amaz./Hesp.

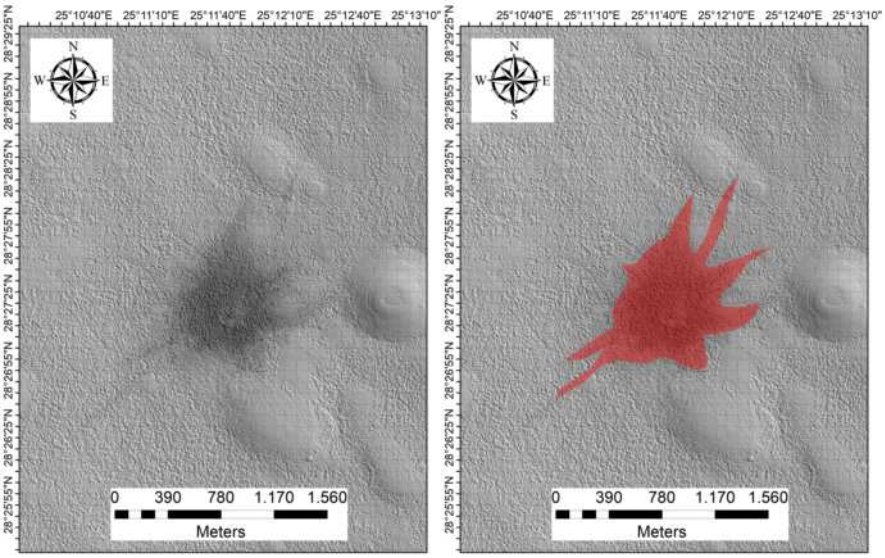

Latitude	Longitude	HiRISE ID	Area (m^2)	Diam.(m)	DCI	TI day	TI night	Epoch
28.455°	25.196°	PSP_003602_2085	792096.2	17.1	0.930	15	40	Middle Noach.

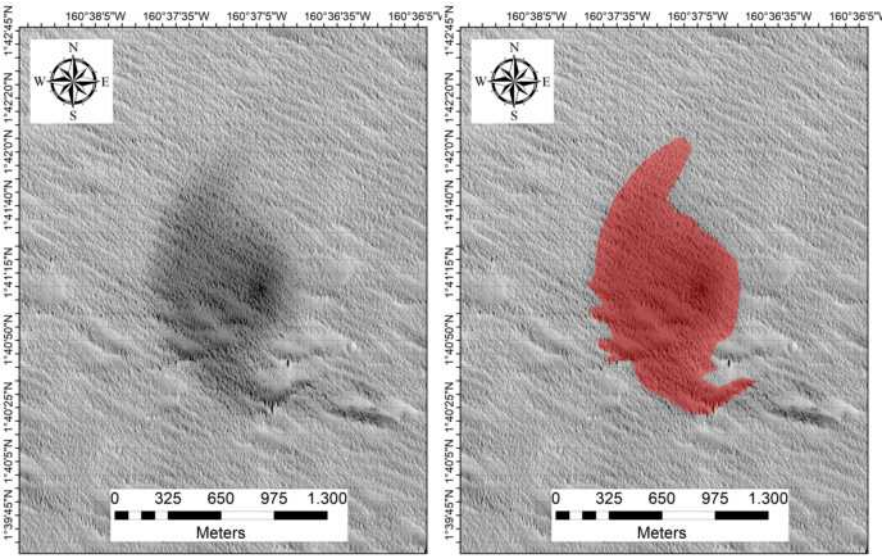

Latitude	Longitude	HiRISE ID	Area (m^2)	Diam.(m)	DCI	TI day	TI night	Epoch
1.686°	199.382°	PSP_003754_1815	948988.2	12.0	0.930	34	41	Amaz./Hesp.

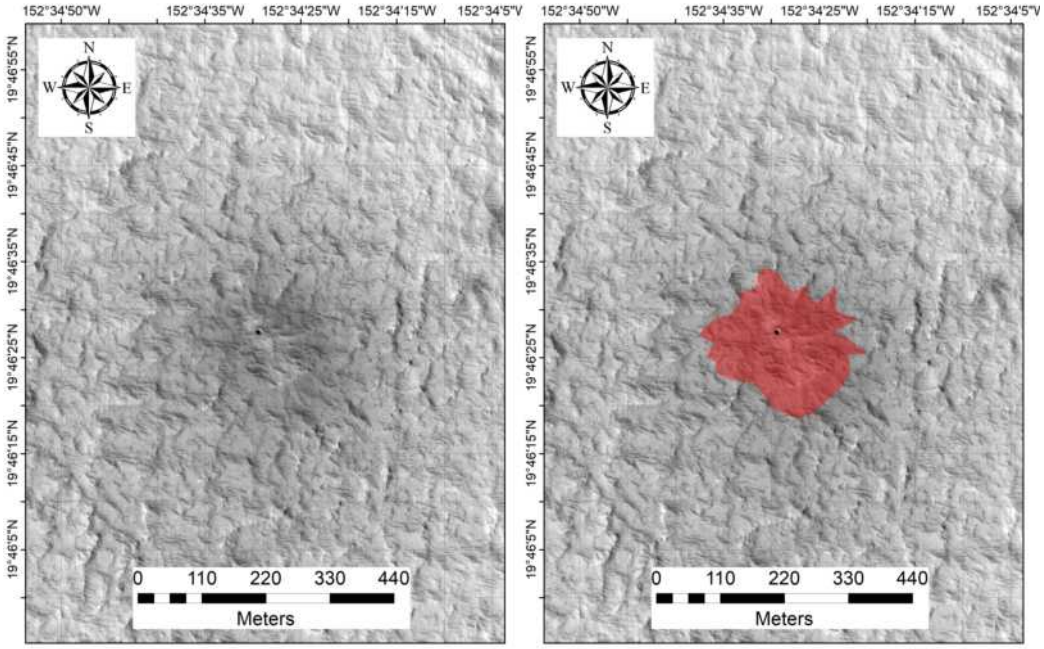

Latitude	Longitude	HiRISE ID	Area (m^2)	Diam.(m)	DCI	TI day	TI night	Epoch
19.774°	207.425°	PSP_003780_2000	40971.9	10.2	0.941	36	94	Late Amaz.

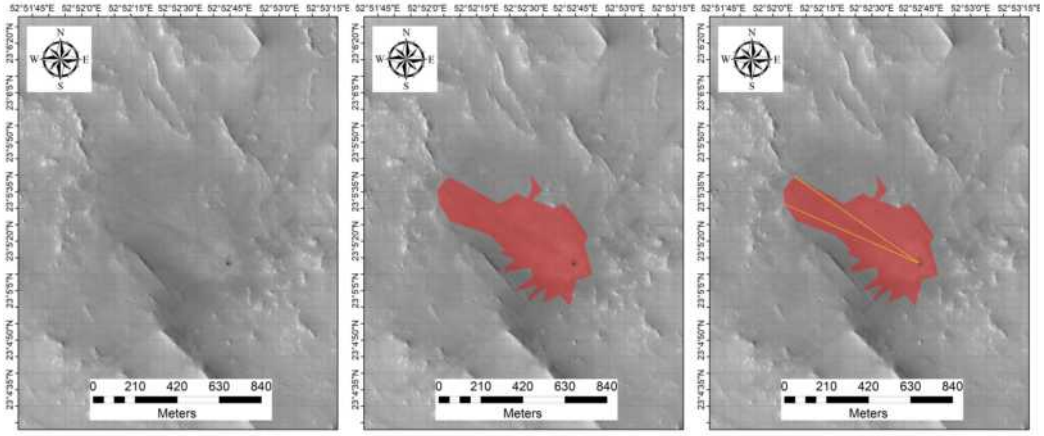

Latitude	Longitude	HiRISE ID	Area (m^2)	Diam.(m)	DCI	TI day	TI night	Epoch	Azimuth
23.087°	52.879°	PSP_003812_2035	228119.2	14.6	0.935	117	168	Middle Noach.	299.3

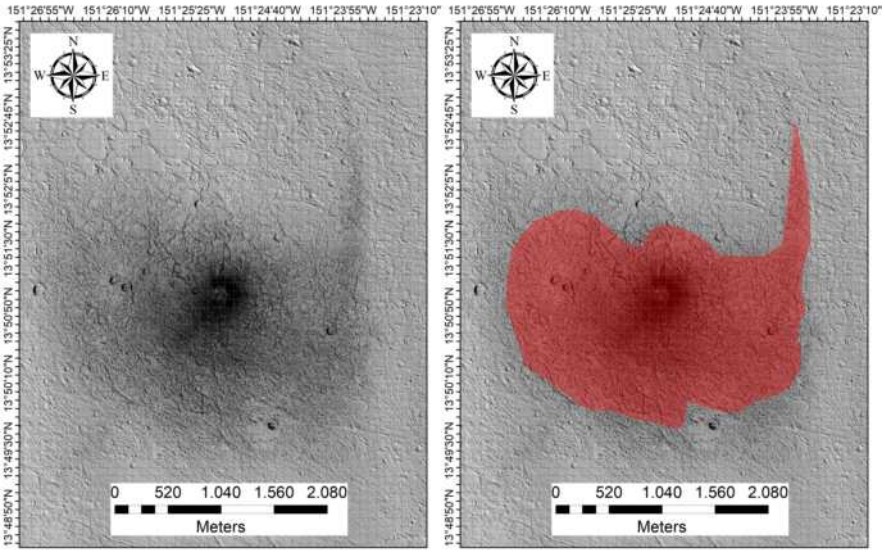

Latitude	Longitude	HiRISE ID	Area (m^2)	Diam.(m)	DCI	TI day	TI night	Epoch
13.851°	208.582°	PSP_003925_1940	4789586.2	9.4	0.933	81	54	Late Amaz.

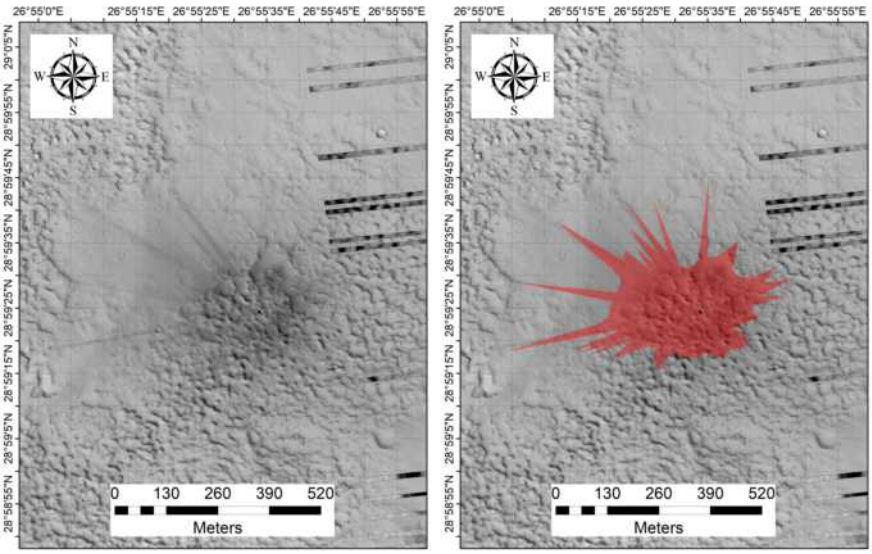

Latitude	Longitude	HiRISE ID	Area (m^2)	Diam.(m)	DCI	TI day	TI night	Epoch
28.99°	26.926°	PSP_003958_2095	102039.0	9.3	0.912	18	33	Middle Noach.

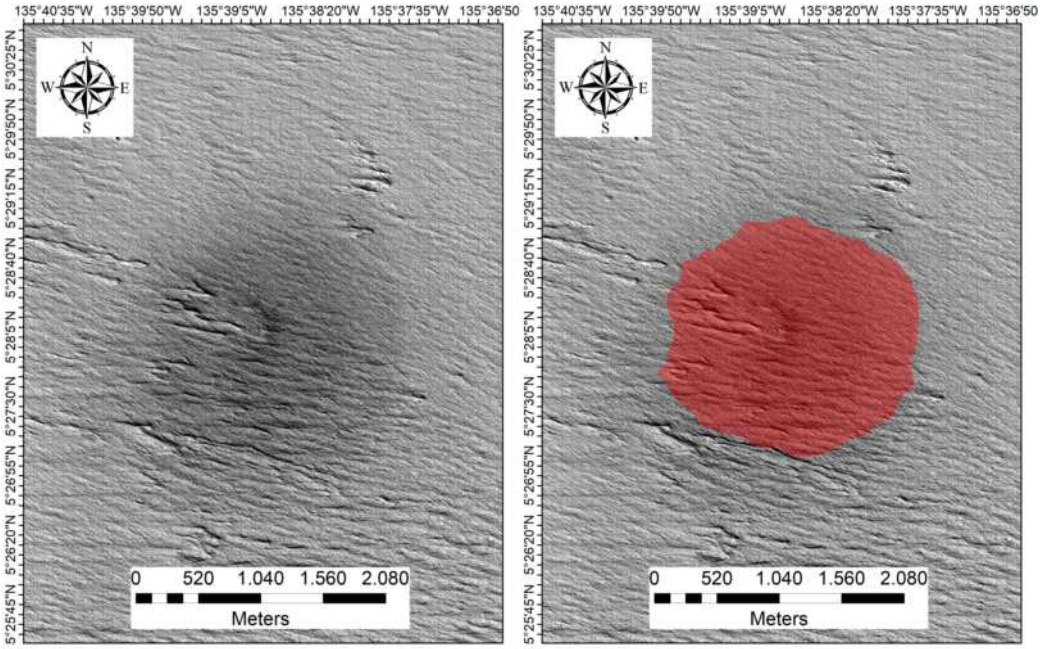

Latitude	Longitude	HiRISE ID	Area (m^2)	Diam.(m)	DCI	TI day	TI night	Epoch
5.469°	224.353°	PSP_004030_1855	3223808.9	24.5	0.930	18	41	Amaz./Hesp.

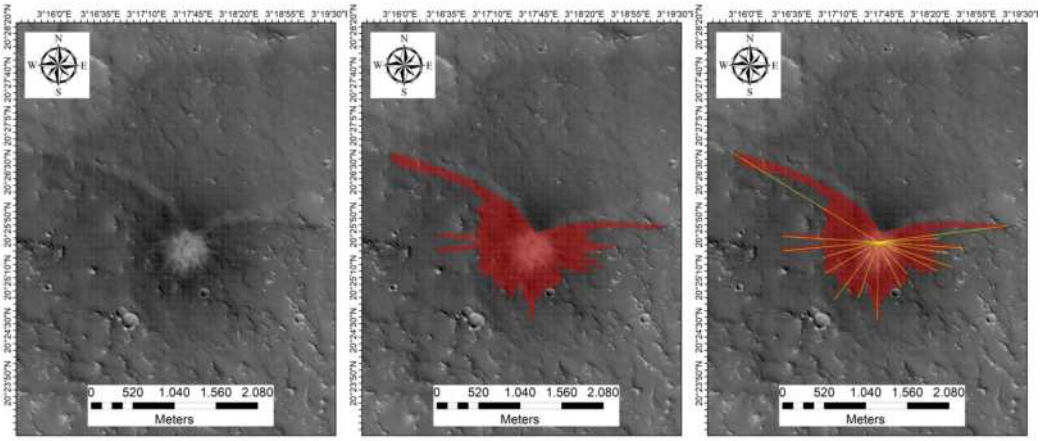

Latitude	Longitude	HiRISE ID	Area (m^2)	Diam.(m)	DCI	TI day	TI night	Epoch	Azimuth
20.427°	3.295°	PSP_004038_2005	1457683.6	20.9	0.938	81	119	Middle Noach.	183.0

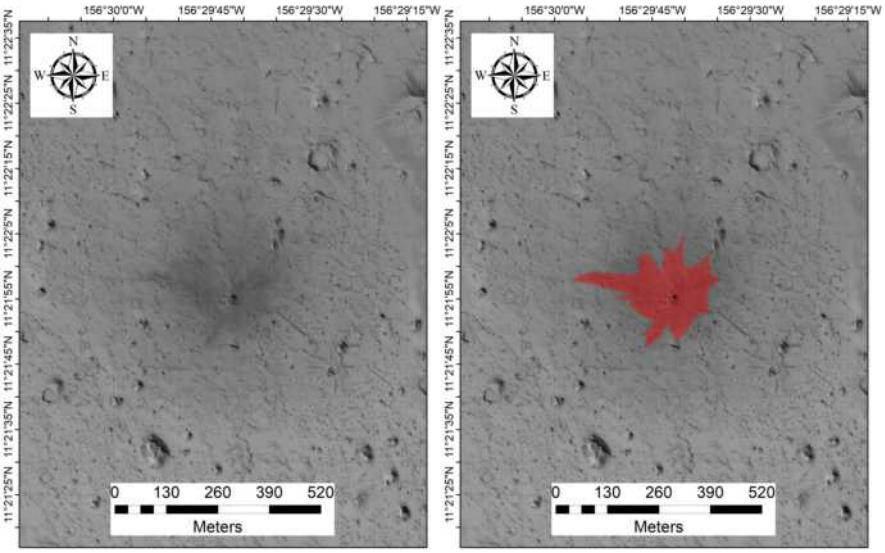

Latitude	Longitude	HiRISE ID	Area (m^2)	Diam.(m)	DCI	TI day	TI night	Epoch
11.365°	203.505°	PSP_004123_1915	38314.7	8.8	0.929	55	43	Late Hesp.

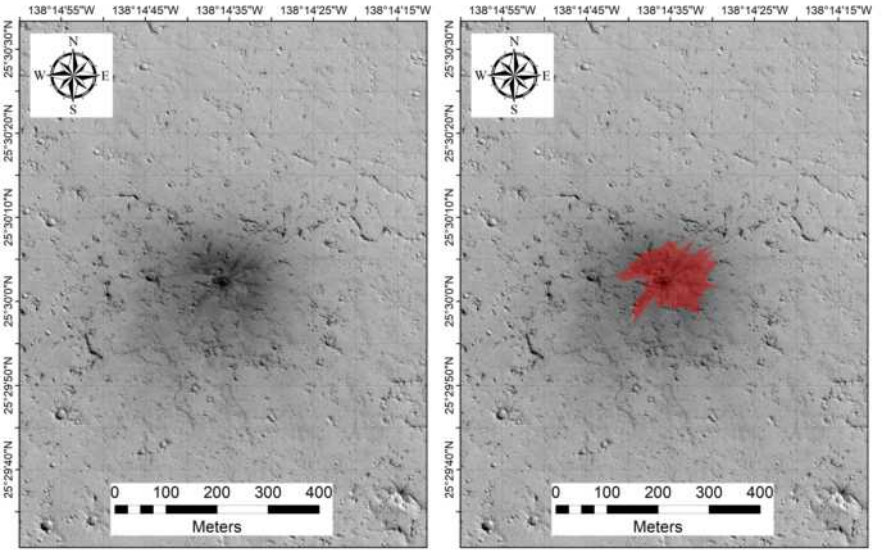

Latitude	Longitude	HiRISE ID	Area (m^2)	Diam.(m)	DCI	TI day	TI night	Epoch
25.501°	221.757°	PSP_004175_2060	16377.9	6.7	0.931	66	41	Late Amaz.

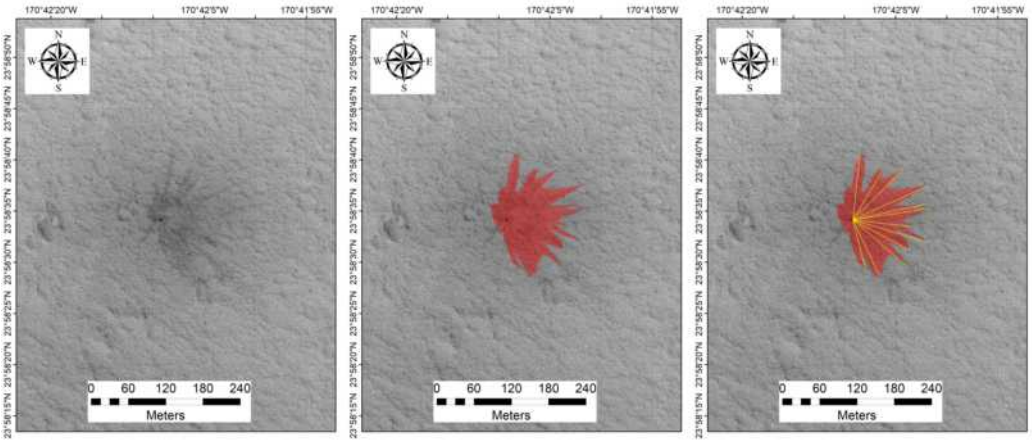

Latitude	Longitude	HiRISE ID	Area (m^2)	Diam.(m)	DCI	TI day	TI night	Epoch	Azimuth
23.976°	189.297°	PSP_004374_2040	13334.4	3.8	0.933	30	41	Hesp./Noach.	88.0

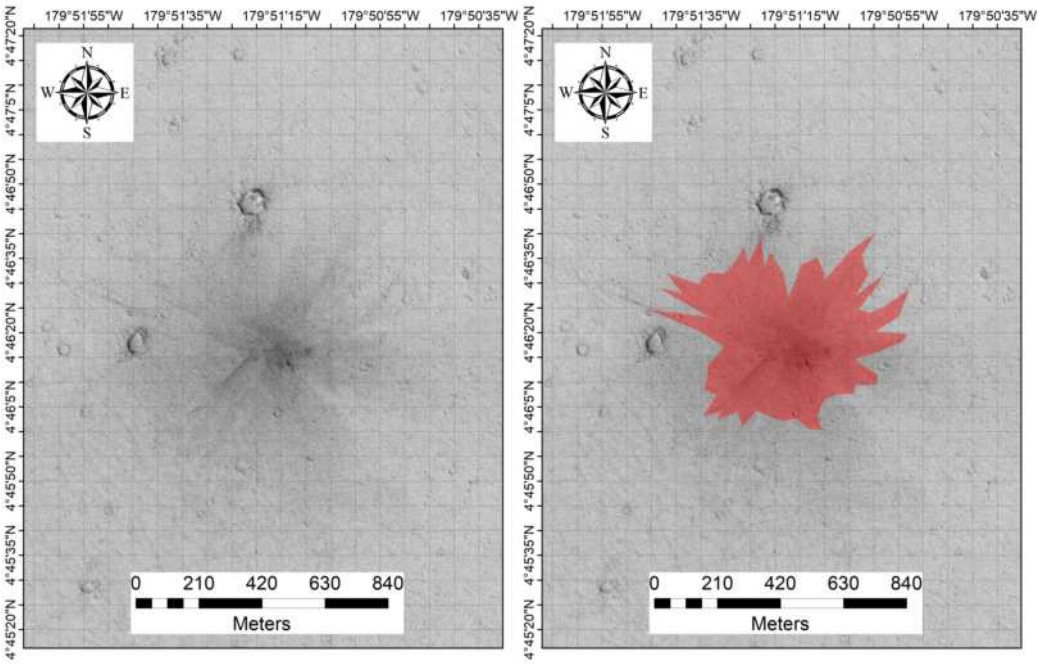

Latitude	Longitude	HiRISE ID	Area (m^2)	Diam.(m)	DCI	TI day	TI night	Epoch
4.771°	180.145°	PSP_004414_1850	286154.6	4.4	0.931	39	45	Late Amaz.

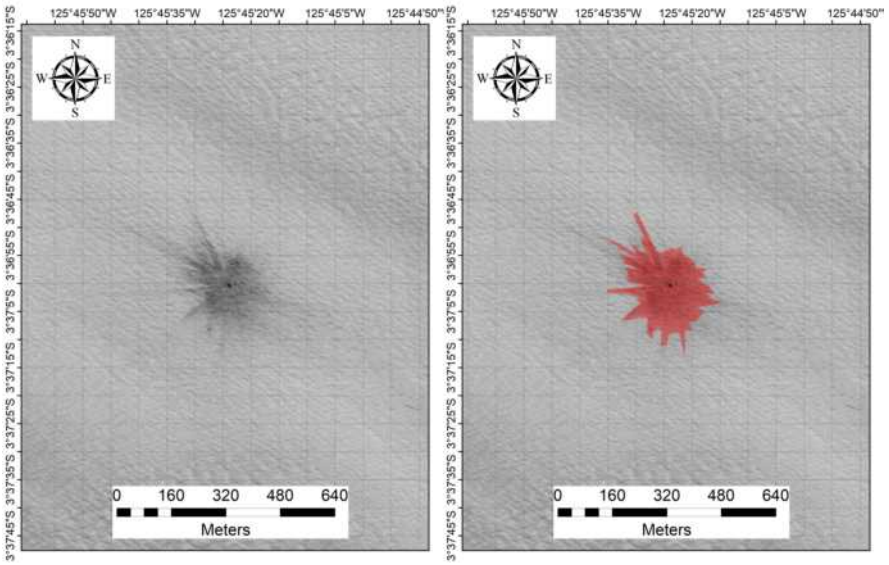

Latitude	Longitude	HiRISE ID	Area (m^2)	Diam.(m)	DCI	TI day	TI night	Epoch
−3.616°	234.243°	PSP_004689_1765	52031.8	11.0	0.935	35	57	Amaz./Hesp.

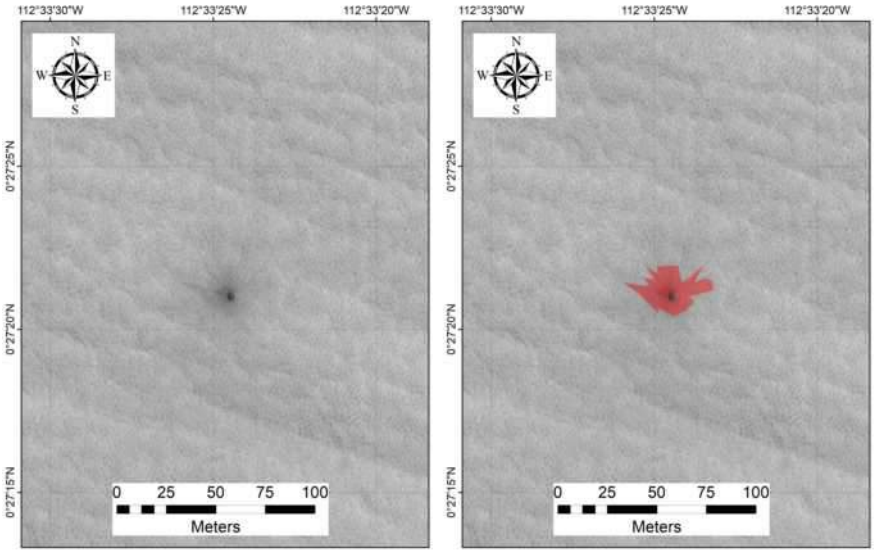

Latitude	Longitude	HiRISE ID	Area (m^2)	Diam.(m)	DCI	TI day	TI night	Epoch
0.374°	247.405°	PSP_004728_1805	560.5	3.5	0.941	77	79	Amazonian

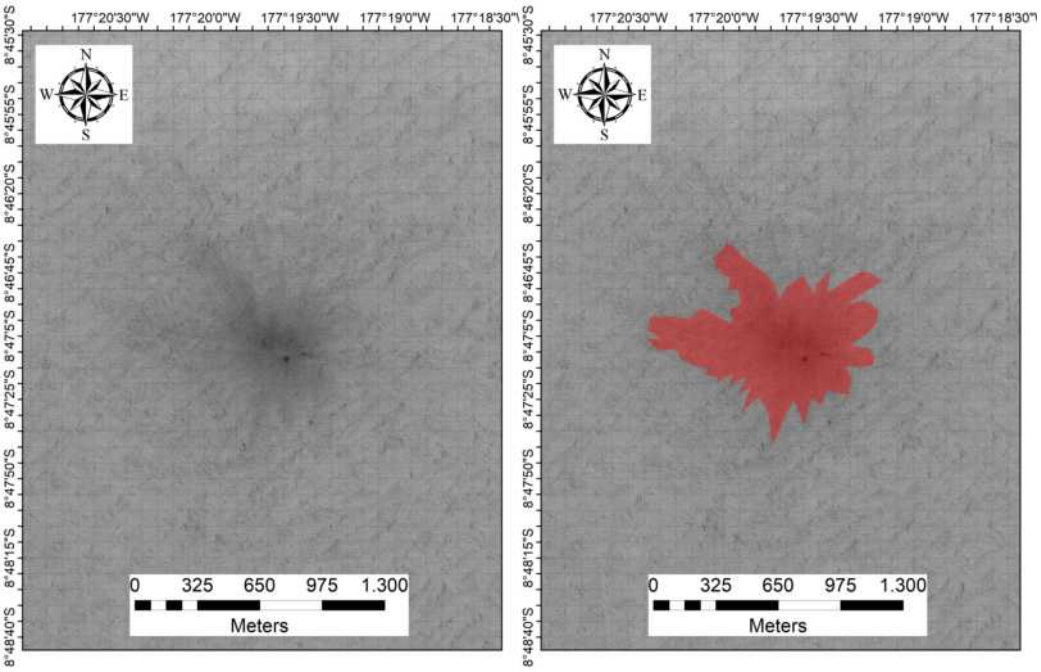

Latitude	Longitude	HiRISE ID	Area (m^2)	Diam.(m)	DCI	TI day	TI night	Epoch
−8.786°	182.673°	PSP_004770_1710	559750.4	8.4	0.934	34	51	Amaz./Hesp.

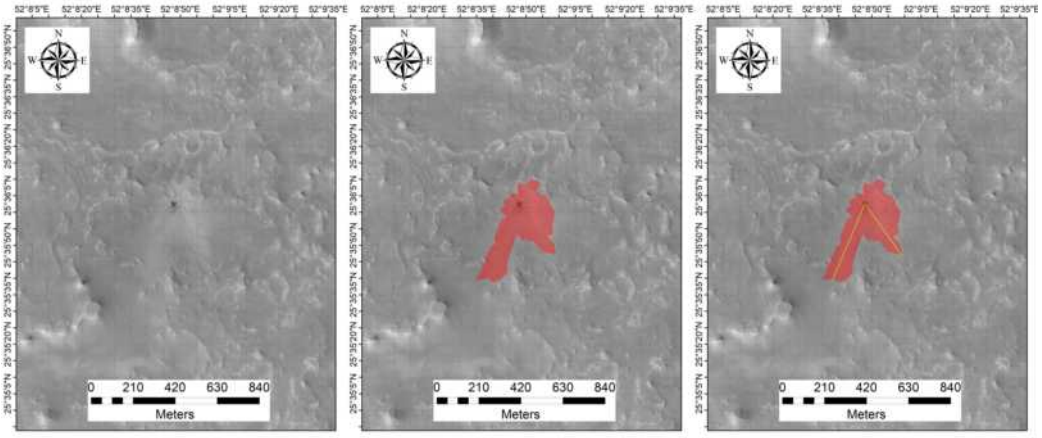

Latitude	Longitude	HiRISE ID	Area (m^2)	Diam.(m)	DCI	TI day	TI night	Epoch	Azimuth
25.601°	52.147°	PSP_005579_2060	90744.8	11.4	0.938	182	178	Middle Noach.	177.2

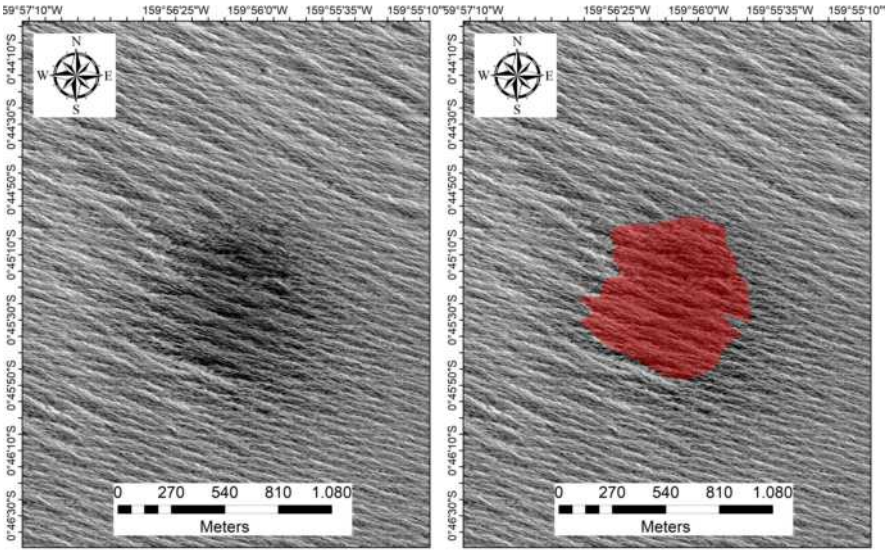

Latitude	Longitude	HiRISE ID	Area (m^2)	Diam.(m)	DCI	TI day	TI night	Epoch
$-0.755°$	200.066°	PSP_005666_1790	480033.0	10.0	0.944	43	79	Amaz./Hesp.

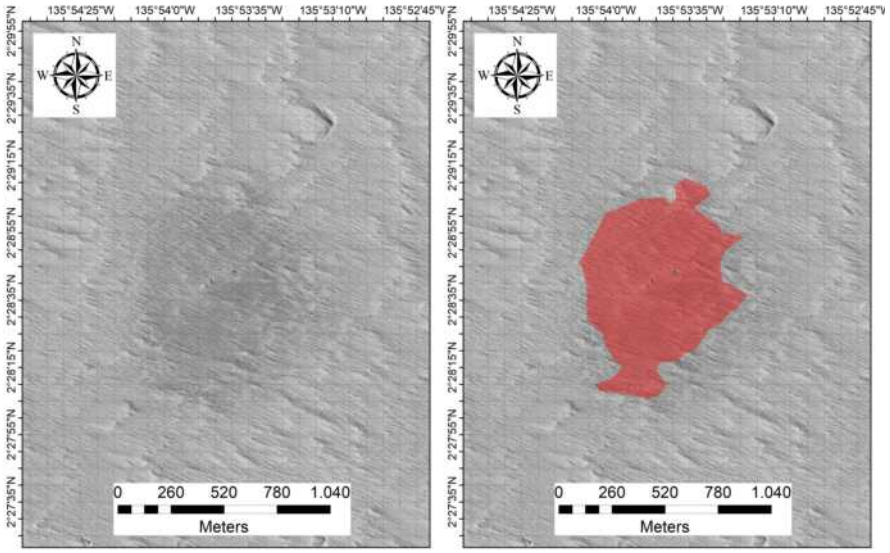

Latitude	Longitude	HiRISE ID	Area (m^2)	Diam.(m)	DCI	TI day	TI night	Epoch
2.479°	224.105°	PSP_005942_1825	523905.1	19.1	0.930	30	25	Amaz./Hesp.

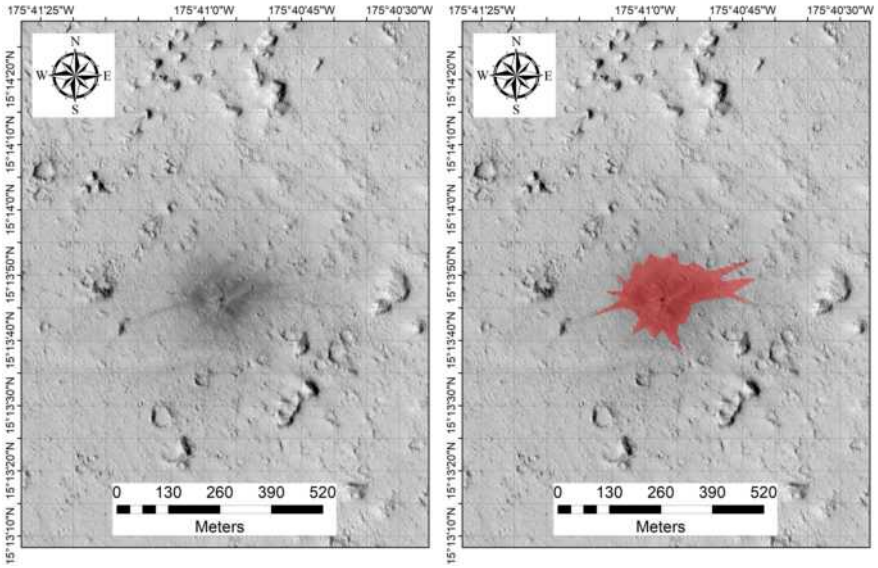

Latitude	Longitude	HiRISE ID	Area (m^2)	Diam.(m)	DCI	TI day	TI night	Epoch
15.230°	184.317°	PSP_006629_1955	38891.3	7.2	0.928	70	54	Late Amaz.

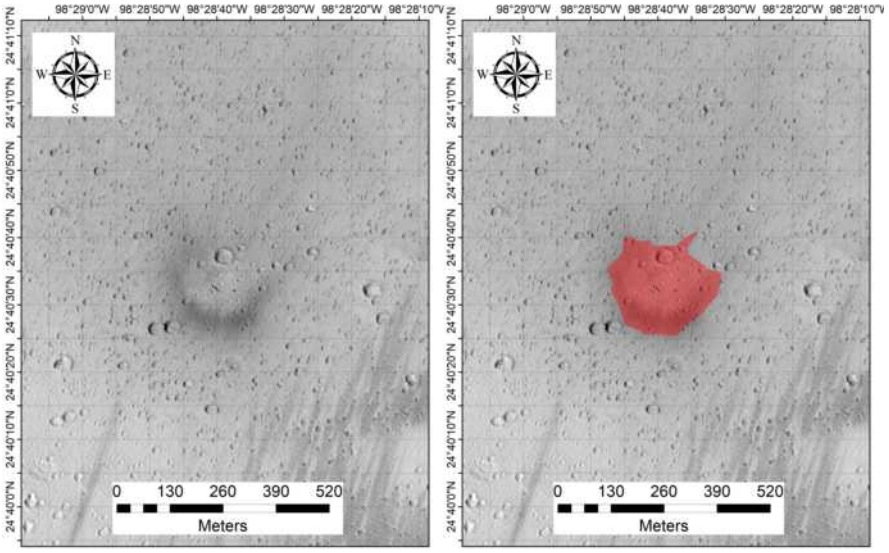

Latitude	Longitude	HiRISE ID	Area (m^2)	Diam.(m)	DCI	TI day	TI night	Epoch
24.676°	261.522°	PSP_006758_2050	46476.9	6.7	0.944	28	82	Amaz./Hesp.

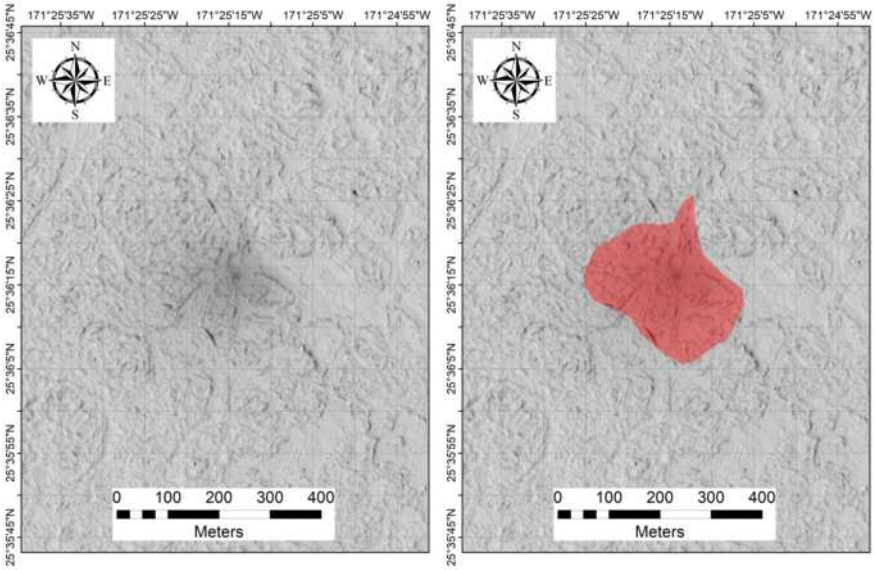

Latitude	Longitude	HiRISE ID	Area (m^2)	Diam.(m)	DCI	TI day	TI night	Epoch
25.604°	188.579°	PSP_006998_2060	56113.8	2.7	0.935	34	46	Late Amaz.

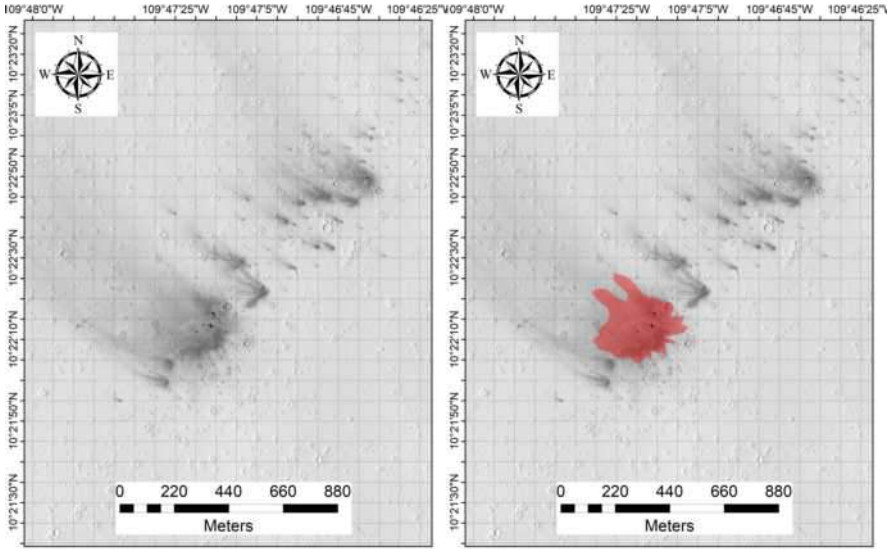

Latitude	Longitude	HiRISE ID	Area (m^2)	Diam.(m)	DCI	TI day	TI night	Epoch
10.375°	250.216°	PSP_007009_1905	75683.1	10.0	0.939	95	62	Amaz./Hesp.

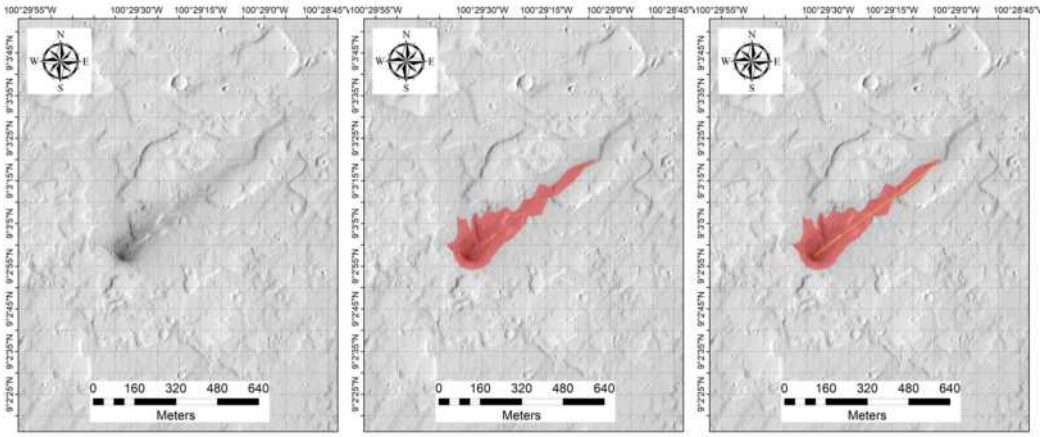

Latitude	Longitude	HiRISE ID	Area (m^2)	Diam.(m)	DCI	TI day	TI night	Epoch	Azimuth
9.049°	259.507°	PSP_007246_1890	57659.2	5.1	0.939	27	44	Amaz./Hesp.	53.2

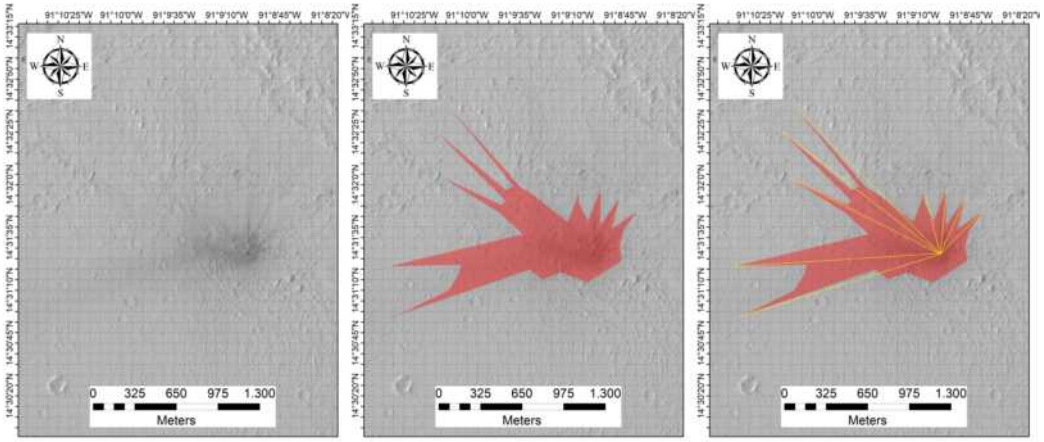

Latitude	Longitude	HiRISE ID	Area (m^2)	Diam.(m)	DCI	TI day	TI night	Epoch	Azimuth
14.524°	268.850°	PSP_007272_1945	696840.6	13.7	0.927	74	81	Amaz./Hesp.	304.5

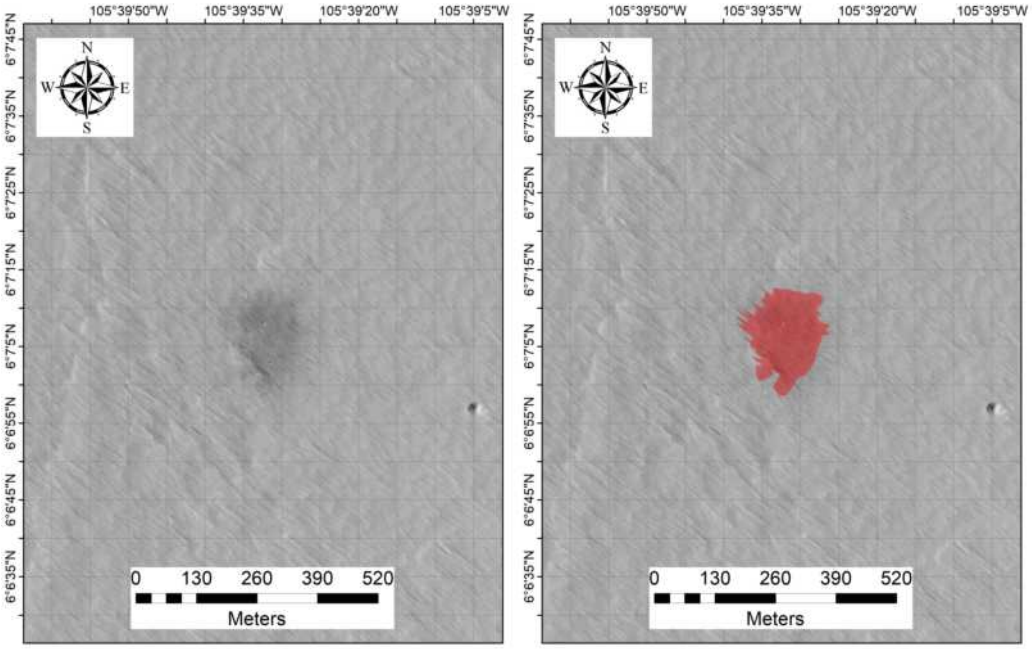

Latitude	Longitude	HiRISE ID	Area (m^2)	Diam.(m)	DCI	TI day	TI night	Epoch
6.118°	254.341°	PSP_007378_1860	26638.0	5.6	0.932	40	127	Amaz./Hesp.

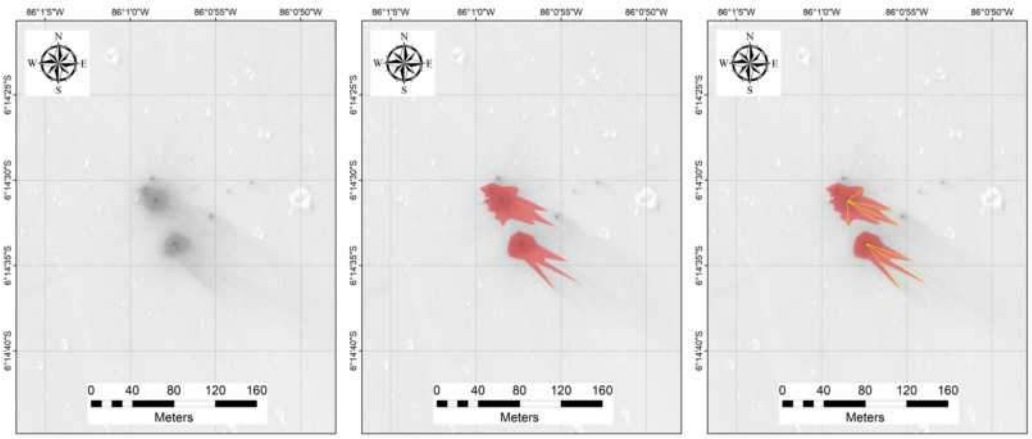

Latitude	Longitude	HiRISE ID	Area (m^2)	Diam.(m)	DCI	TI day	TI night	Epoch	Azimuth
−6.242°	273.984°	PSP_007496_1735	1445.6	1.5	0.933	161	113	Early Hesp.	115.7
−6.242°	273.984°	PSP_007496_1735	1103.2	1.4	0.933	161	113	Early Hesp.	126.0

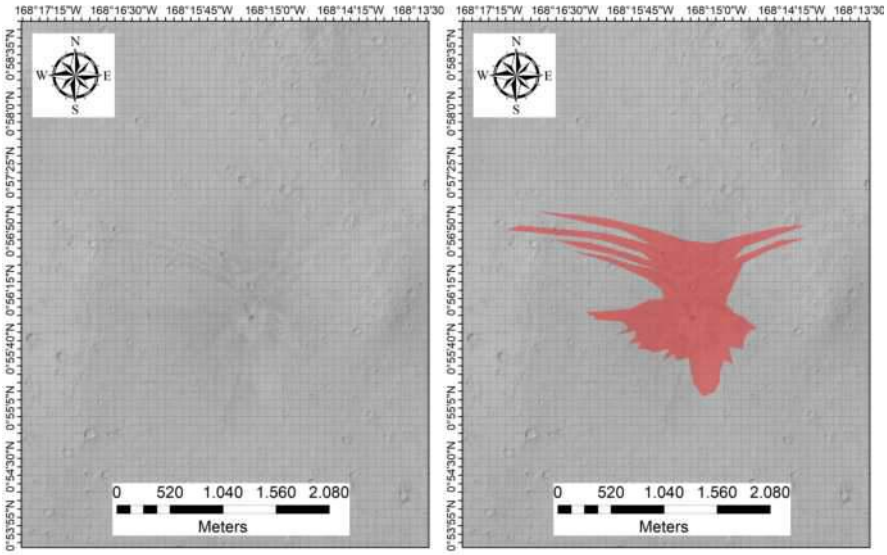

Latitude	Longitude	HiRISE ID	Area (m^2)	Diam.(m)	DCI	TI day	TI night	Epoch
0.933°	191.746°	PSP_007499_1810	1517842.9	13.5	0.944	39	54	Hesp./Noach.

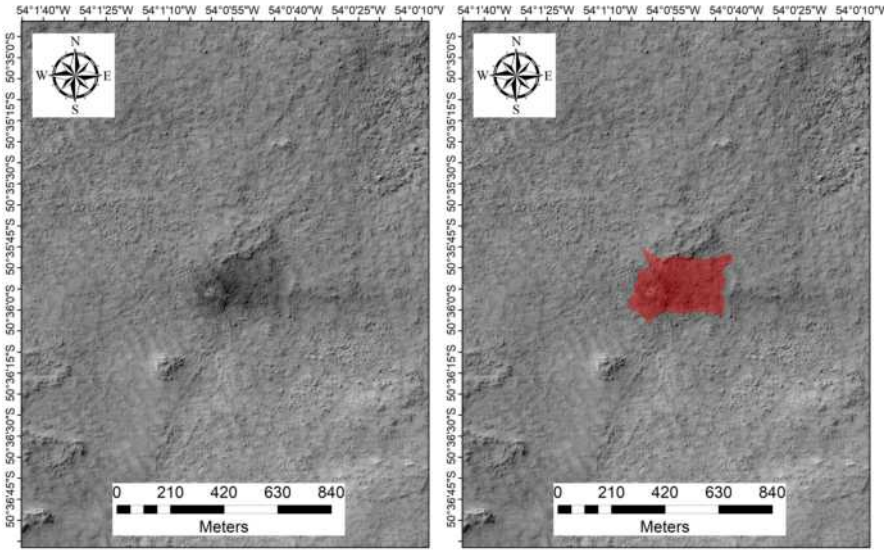

Latitude	Longitude	HiRISE ID	Area (m^2)	Diam.(m)	DCI	TI day	TI night	Epoch
−50.599°	305.983°	PSP_007561_1290	76276.3	9.7	0.973	402	387	Hesp./Noach.

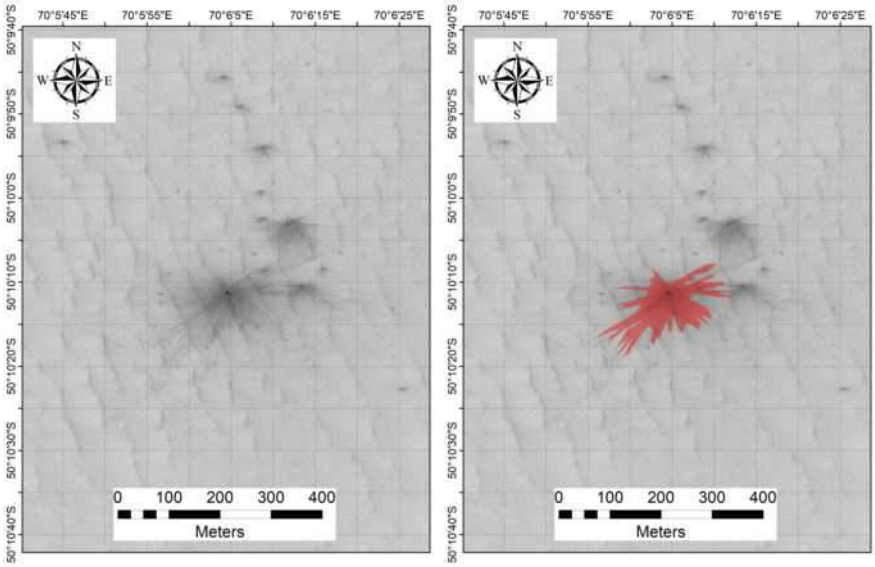

Latitude	Longitude	HiRISE ID	Area (m^2)	Diam.(m)	DCI	TI day	TI night	Epoch
−50.170°	70.101°	PSP_007596_1295	15932.2	5.6	0.961	108	189	Late Hesp.

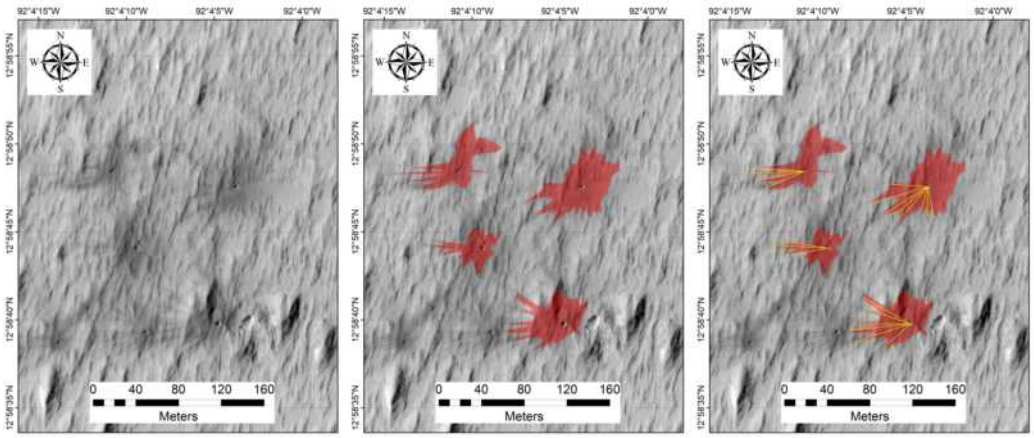

Latitude	Longitude	HiRISE ID	Area (m^2)	Diam.(m)	DCI	TI day	TI night	Epoch	Azimuth
12.979°	267.931°	PSP_007773_1930	1980.3	4.7	0.945	26	32	Amaz./Hesp.	268.4
12.979°	267.931°	PSP_007773_1930	2645.1	3.7	0.945	26	32	Amaz./Hesp.	225.9
12.979°	267.931°	PSP_007773_1930	1743.1	3.4	0.945	26	32	Amaz./Hesp.	262.6
12.979°	267.931°	PSP_007773_1930	1011.2	3.1	0.945	26	32	Amaz./Hesp.	271.4

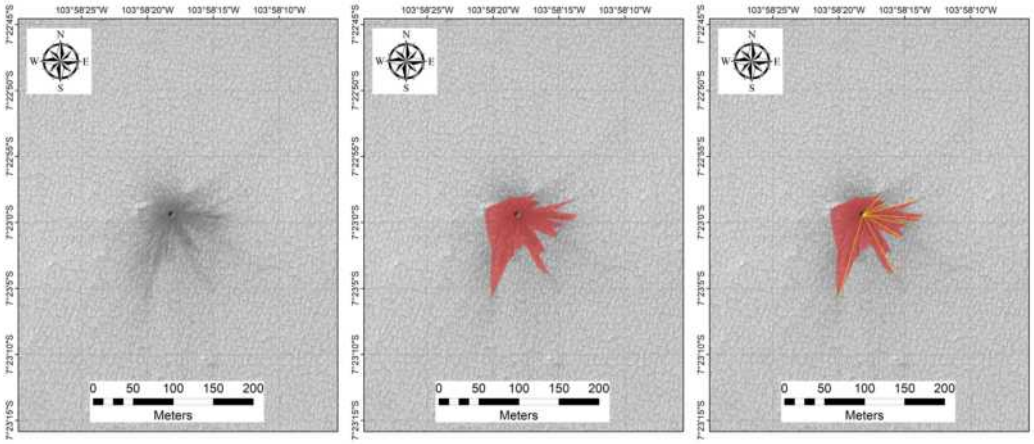

Latitude	Longitude	HiRISE ID	Area (m^2)	Diam.(m)	DCI	TI day	TI night	Epoch	Azimuth
−7.383°	256.028°	PSP_007879_1725	6097.9	7.0	0.944	74	54	Late Hesp.	120.6

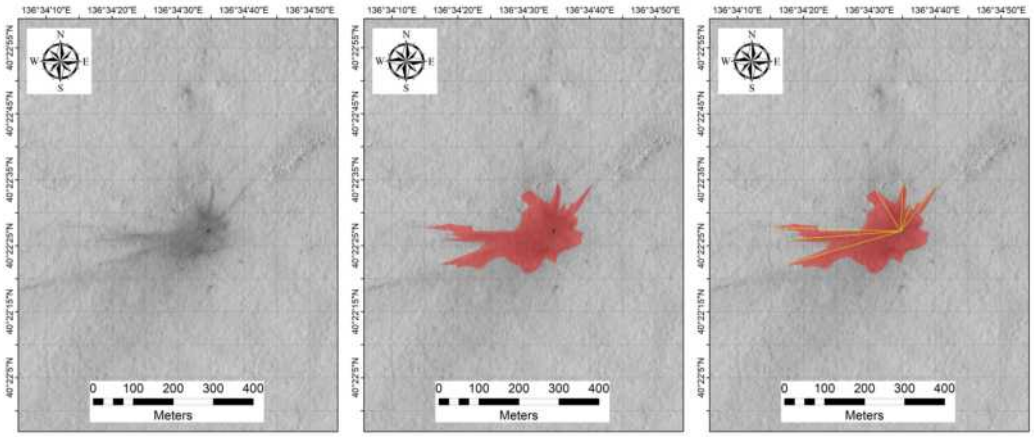

Latitude	Longitude	HiRISE ID	Area (m^2)	Diam.(m)	DCI	TI day	TI night	Epoch	Azimuth
40.374°	136.576°	PSP_008015_2205	34822.4	8.5	0.943	168	168	Middle Amaz.	299.7

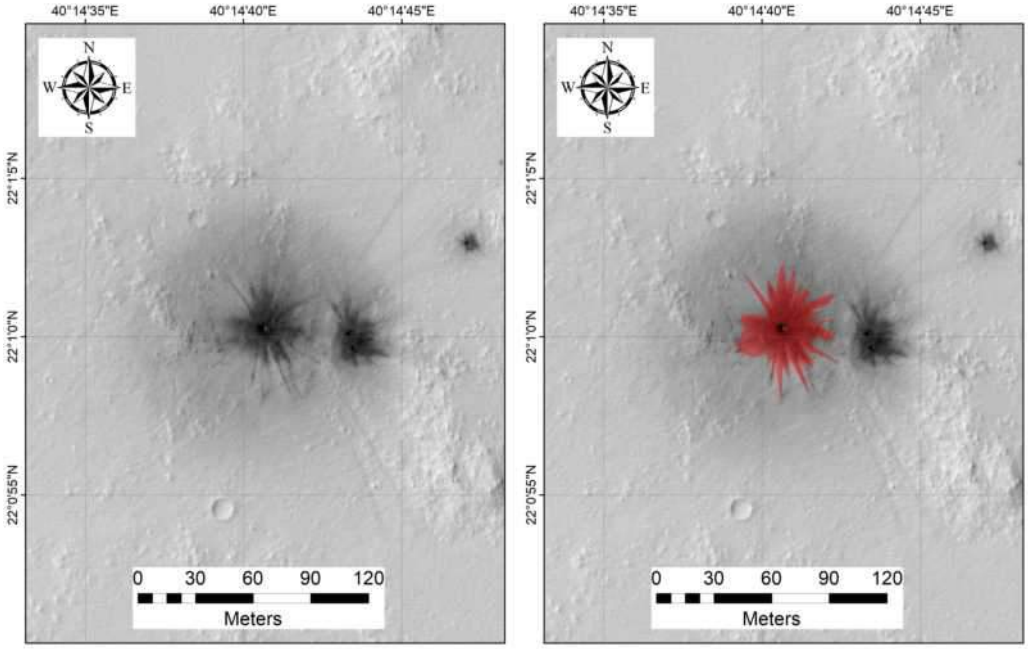

Latitude	Longitude	HiRISE ID	Area (m^2)	Diam.(m)	DCI	TI day	TI night	Epoch
22.017°	40.245°	PSP_008045_2020	1497.7	4.0	0.931	21	50	Middle Noach.

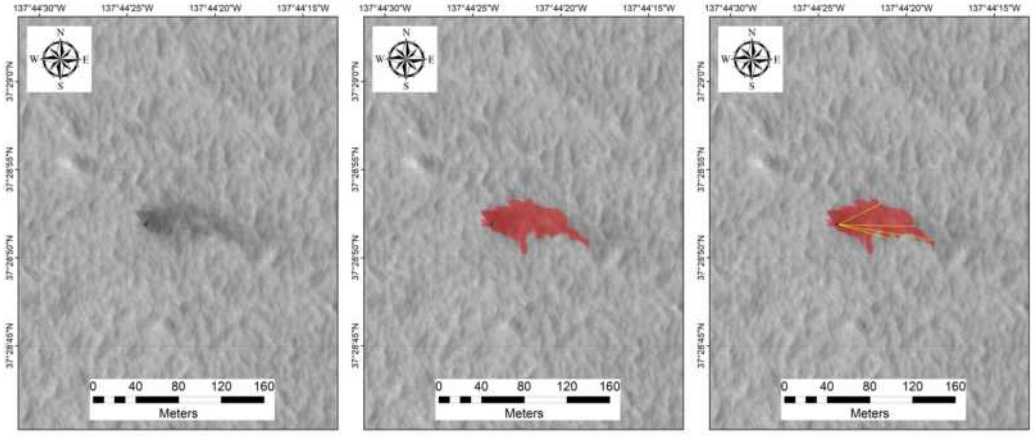

Latitude	Longitude	HiRISE ID	Area (m^2)	Diam.(m)	DCI	TI day	TI night	Epoch	Azimuth
37.481°	222.260°	PSP_008236_2180	2342.7	3.5	0.946	52	82	Early Hesp.	92.0

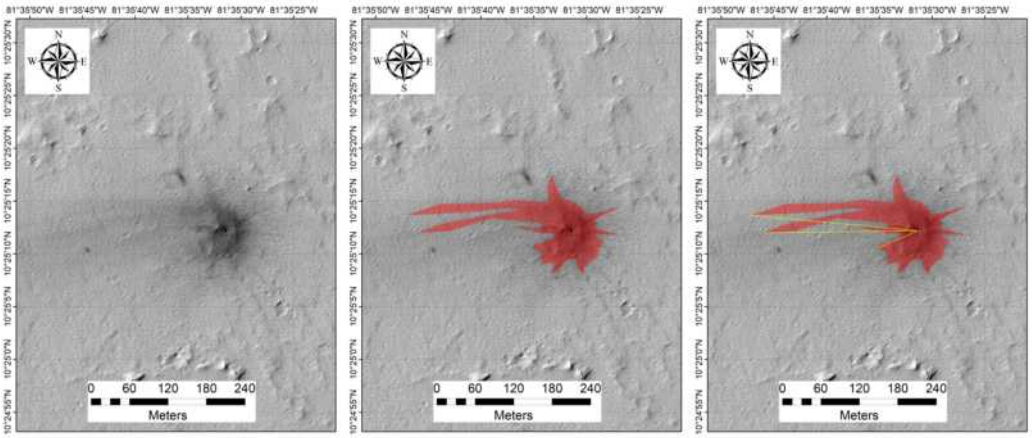

Latitude	Longitude	HiRISE ID	Area (m^2)	Diam.(m)	DCI	TI day	TI night	Epoch	Azimuth
10.420°	278.408°	PSP_008300_1905	13634.3	5.5	0.932	58	42	Amaz./Hesp.	269.3

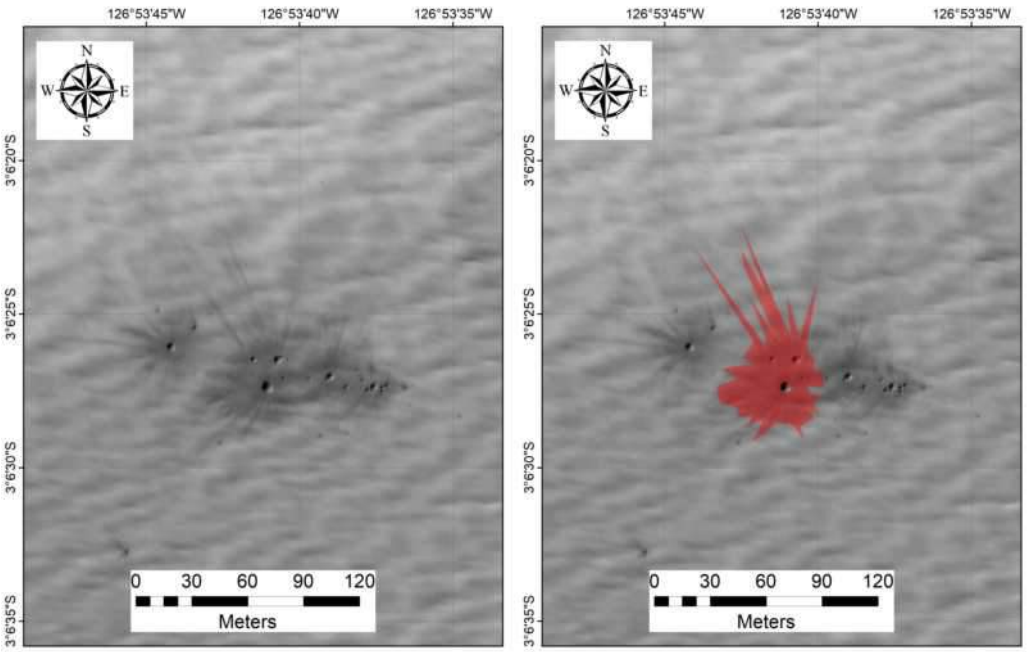

Latitude	Longitude	HiRISE ID	Area (m^2)	Diam.(m)	DCI	TI day	TI night	Epoch
−3.107°	233.105°	PSP_009185_1770	2568.7	5.1	0.931	35	13	Late Amaz.

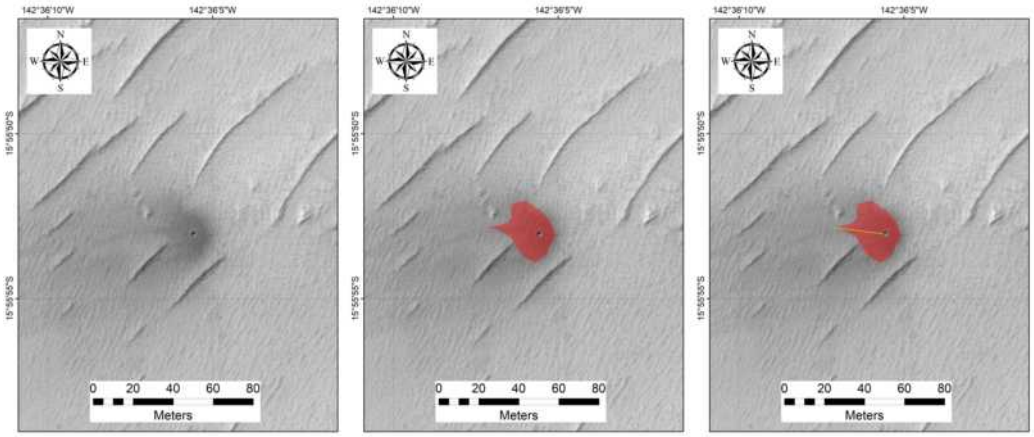

Latitude	Longitude	HiRISE ID	Area (m^2)	Diam.(m)	DCI	TI day	TI night	Epoch	Azimuth
−15.934°	217.398°	PSP_009212_1640	510.3	2.7	0.939	40	67	Middle Noach.	277.4

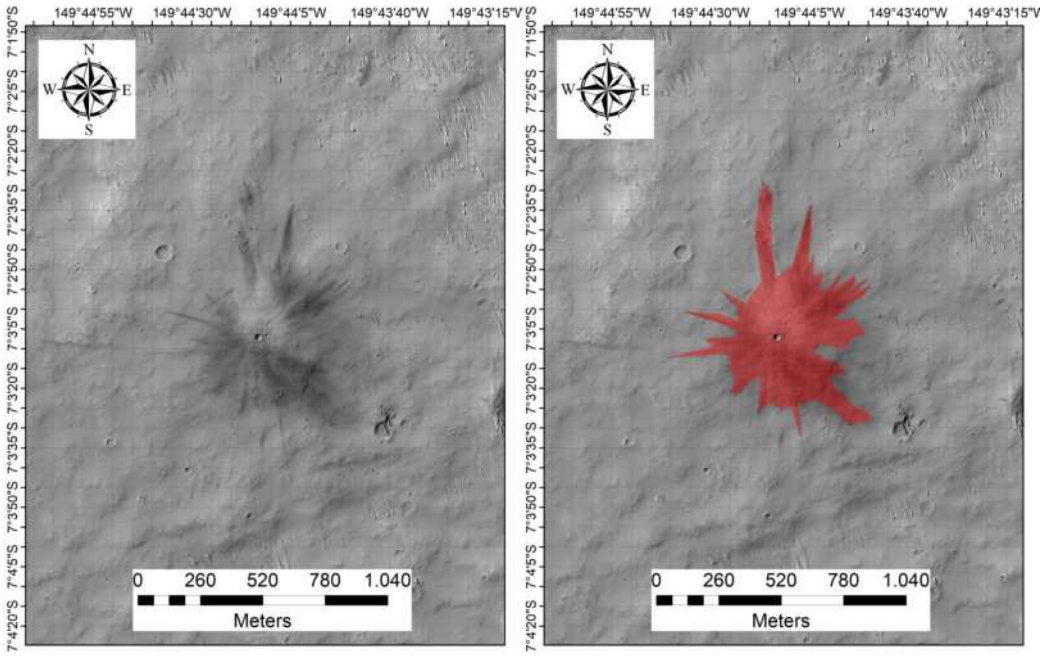

Latitude	Longitude	HiRISE ID	Area (m^2)	Diam.(m)	DCI	TI day	TI night	Epoch
−7.052°	210.263°	PSP_009265_1730	287860.9	29.1	0.937	62	37	Middle Noach.

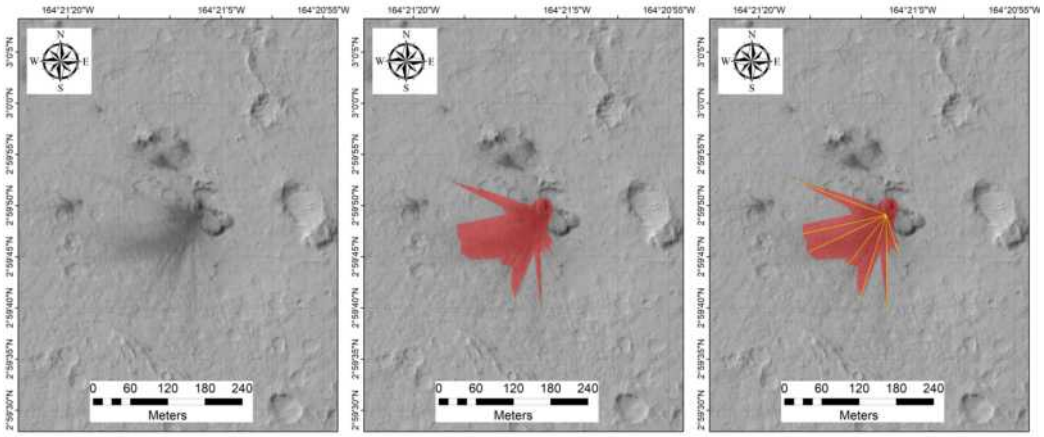

Latitude	Longitude	HiRISE ID	Area (m^2)	Diam.(m)	DCI	TI day	TI night	Epoch	Azimuth
3.000°	195.645°	PSP_009305_1830	13518.2	4.3	0.937	31	43	Hesp./Noach.	226.5

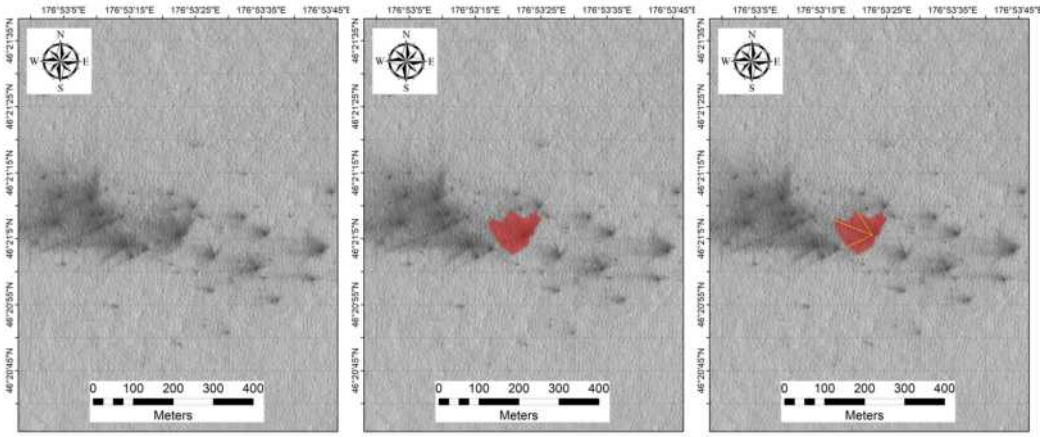

Latitude	Longitude	HiRISE ID	Area (m^2)	Diam.(m)	DCI	TI day	TI night	Epoch	Azimuth
46.351°	176.891°	PSP_009978_2265	8218.8	4.7	0.932	235	244	Late Hesp.	288.9

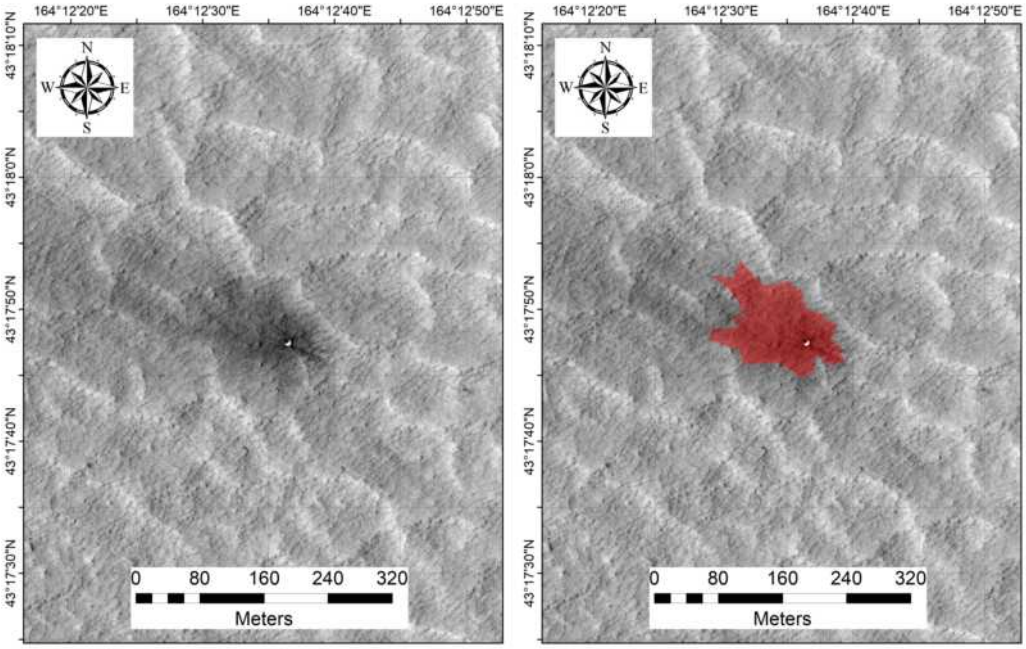

Latitude	Longitude	HiRISE ID	Area (m^2)	Diam.(m)	DCI	TI day	TI night	Epoch
43.297°	164.210°	PSP_010084_2235	12404.1	6.4	0.945	112	177	Early Hesp.

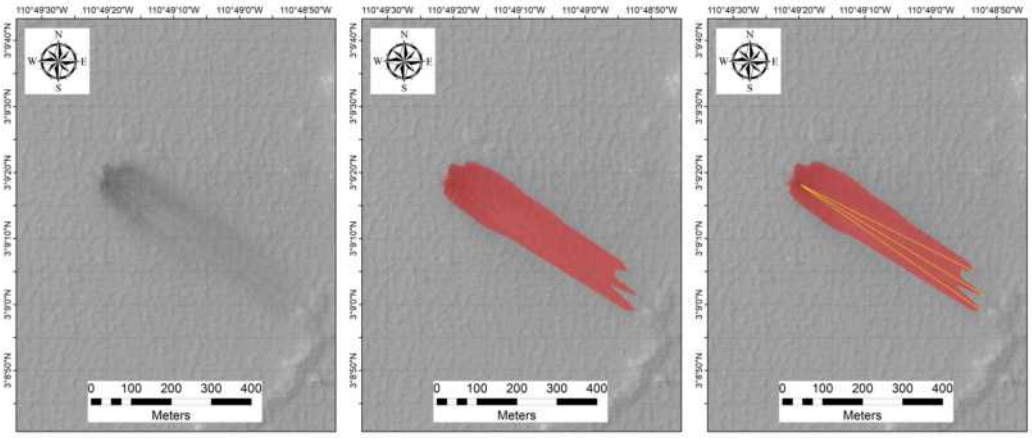

Latitude	Longitude	HiRISE ID	Area (m^2)	Diam.(m)	DCI	TI day	TI night	Epoch	Azimuth
3.155°	249.178°	PSP_010147_1830	55969.5	4.9	0.955	30	87	Amaz./Hesp.	121.0

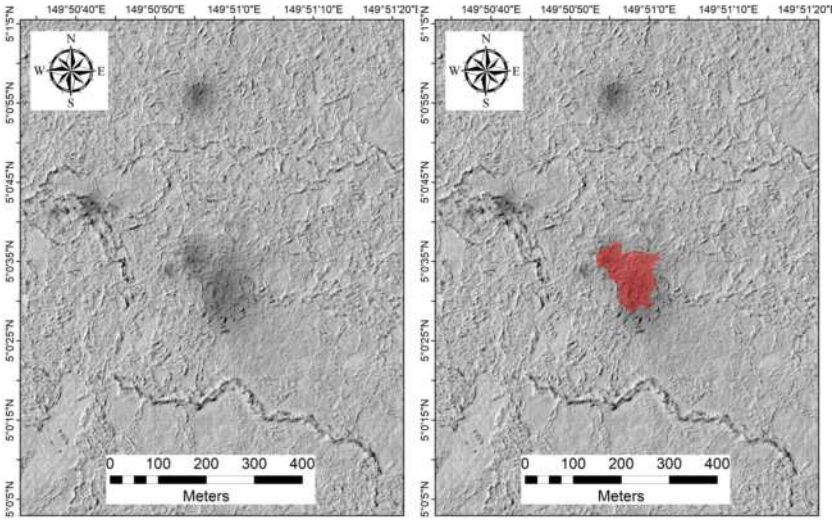

Latitude	Longitude	HiRISE ID	Area (m^2)	Diam.(m)	DCI	TI day	TI night	Epoch
5.009°	149.849°	PSP_010177_1850	11010.0	2.2	0.943	88	137	Late Amaz.

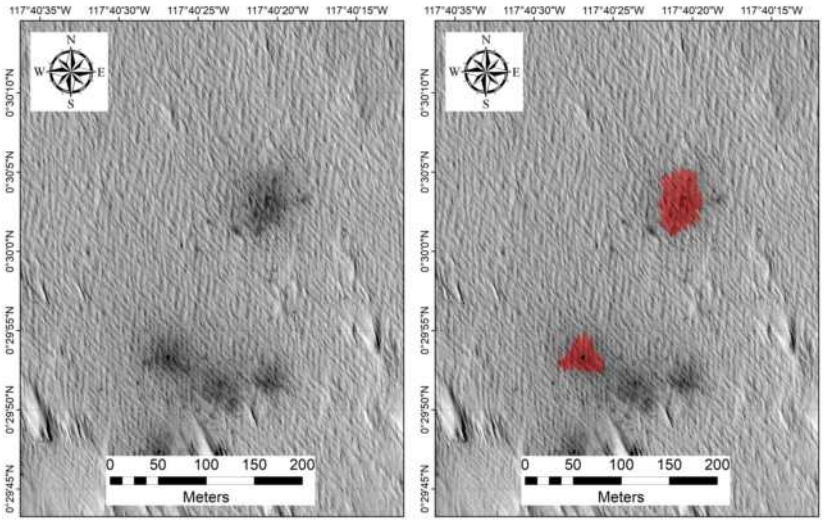

Latitude	Longitude	HiRISE ID	Area (m^2)	Diam.(m)	DCI	TI day	TI night	Epoch
0.499°	242.327°	PSP_010200_1805	1119.7	4.6	0.947	46	22	Amaz./Hesp.
0.499°	242.327°	PSP_010200_1805	2312.7	3.7	0.947	46	22	Amaz./Hesp.

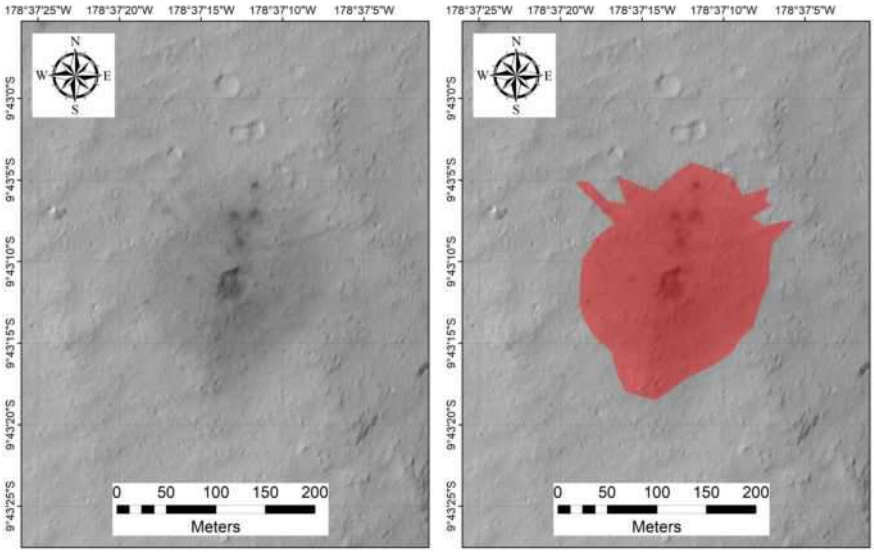

Latitude	Longitude	HiRISE ID	Area (m^2)	Diam.(m)	DCI	TI day	TI night	Epoch
−9.720°	181.380°	PSP_010255_1700	33005.0	3.1	0.925	57	20	Amaz./Hesp.

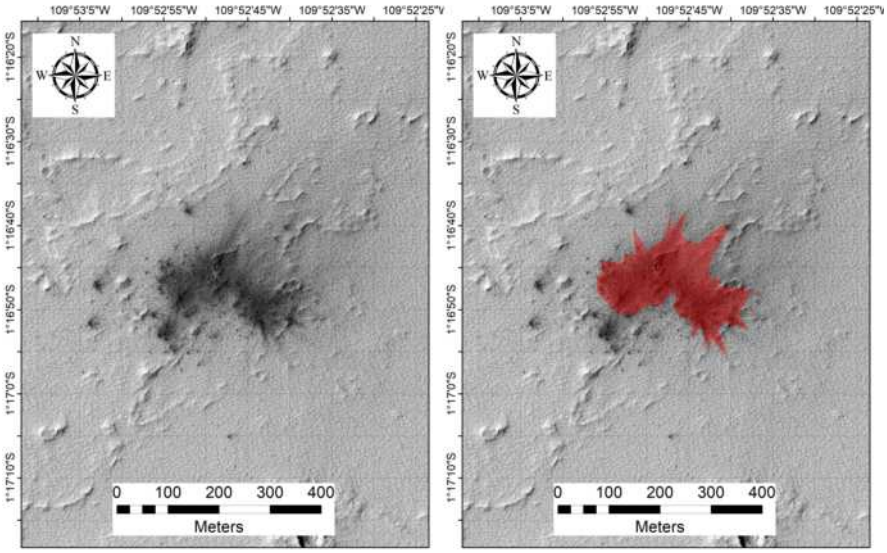

Latitude	Longitude	HiRISE ID	Area (m^2)	Diam.(m)	DCI	TI day	TI night	Epoch
−1.280°	250.120°	PSP_010292_1785	35895.6	6.2	0.929	62	84	Amaz./Hesp.

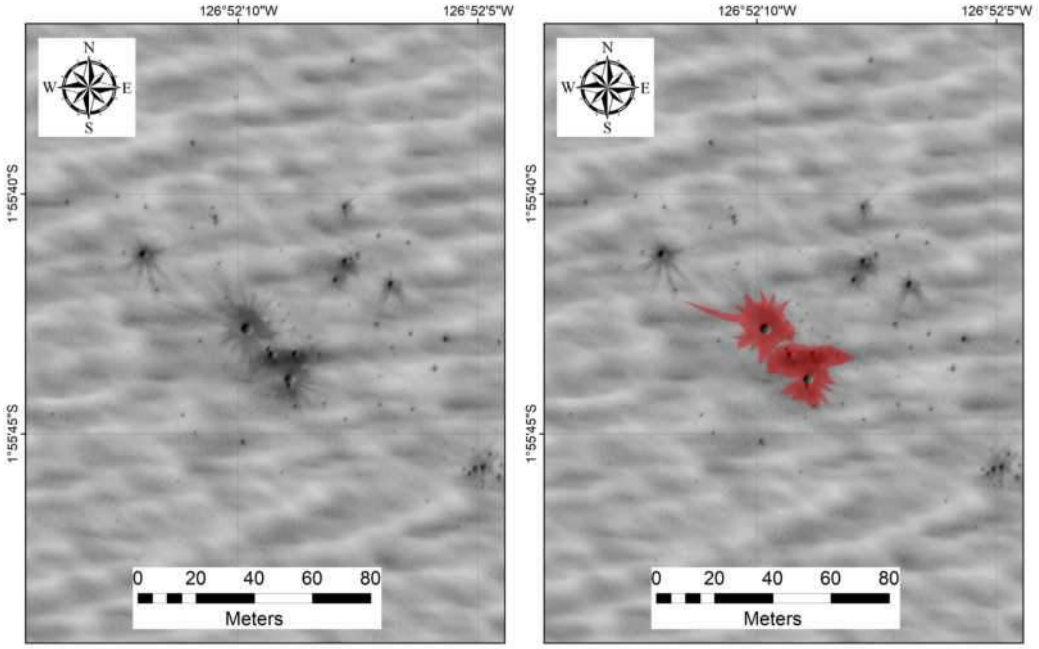

Latitude	Longitude	HiRISE ID	Area (m^2)	Diam.(m)	DCI	TI day	TI night	Epoch
−1.928°	233.131°	PSP_010319_1780	295.9	3.5	0.932	52	20	Amaz./Hesp.
−1.928°	233.131°	PSP_010319_1780	350.7	3.1	0.932	52	20	Amaz./Hesp.

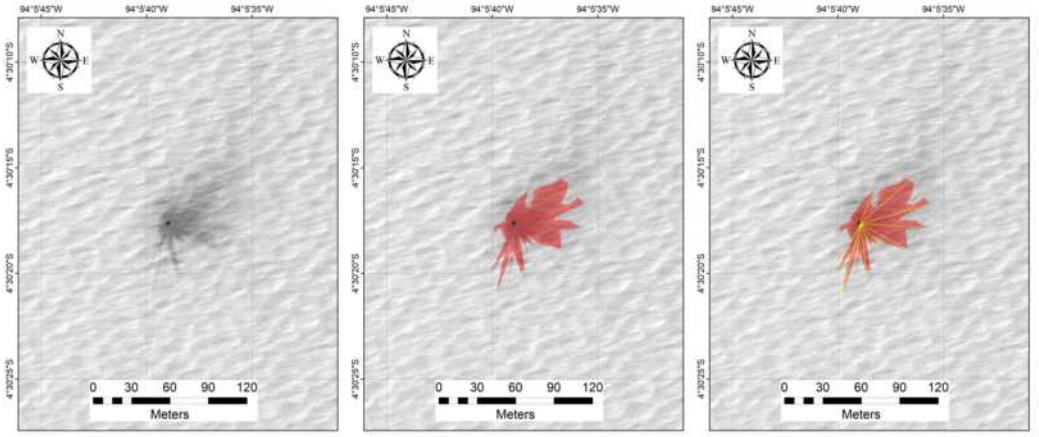

Latitude	Longitude	HiRISE ID	Area (m^2)	Diam.(m)	DCI	TI day	TI night	Epoch	Azimuth
−4.505°	265.906°	PSP_010331_1755	2222.0	3.3	0.921	127	92	Noachian	126.8

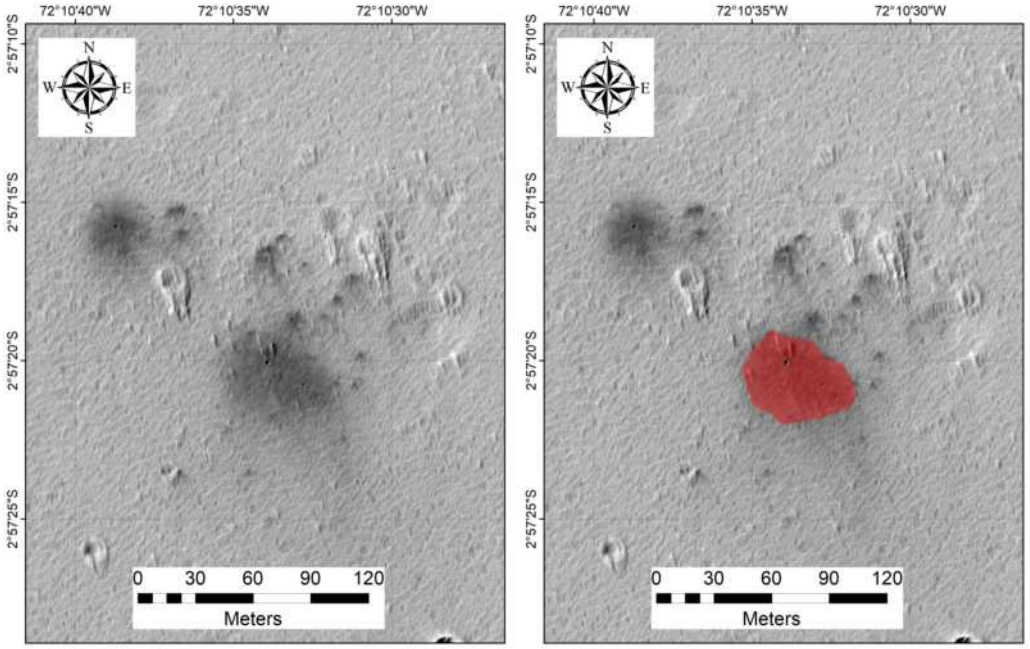

Latitude	Longitude	HiRISE ID	Area (m^2)	Diam.(m)	DCI	TI day	TI night	Epoch
−2.955°	287.823°	PSP_010528_1770	1951.0	2.7	0.950	127	72	Early Hesp.

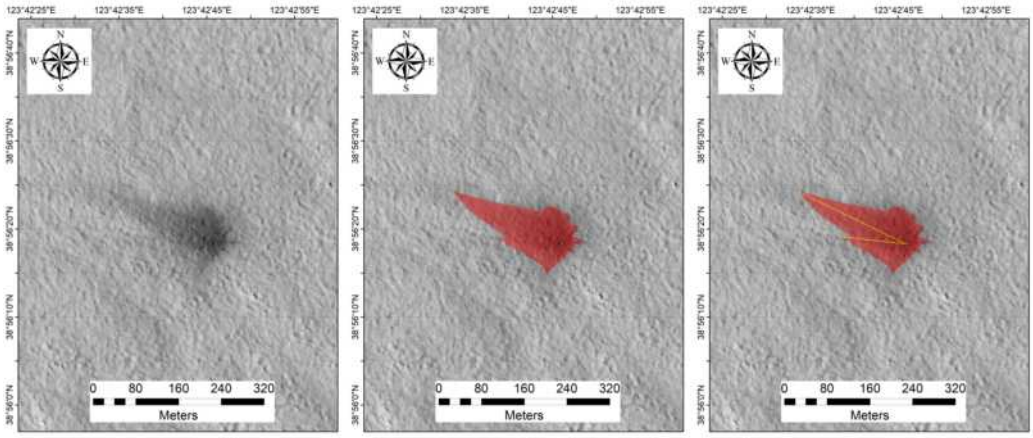

Latitude	Longitude	HiRISE ID	Area (m^2)	Diam.(m)	DCI	TI day	TI night	Epoch	Azimuth
38.938°	123.713°	PSP_010547_2195	14952.5	6.9	0.944	182	172	Amazonian	288.9

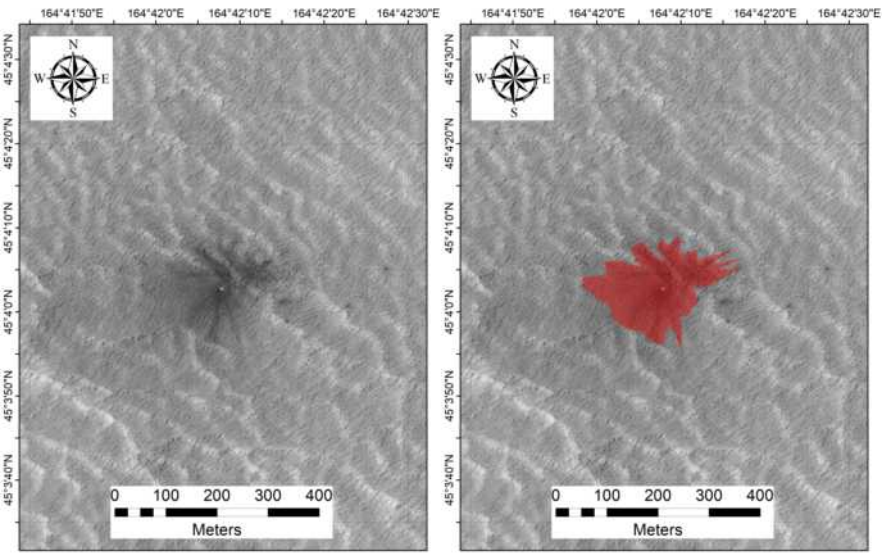

Latitude	Longitude	HiRISE ID	Area (m^2)	Diam.(m)	DCI	TI day	TI night	Epoch
45.067°	164.702°	PSP_010585_2255	30871.5	4.5	0.940	159	158	Early Hesp.

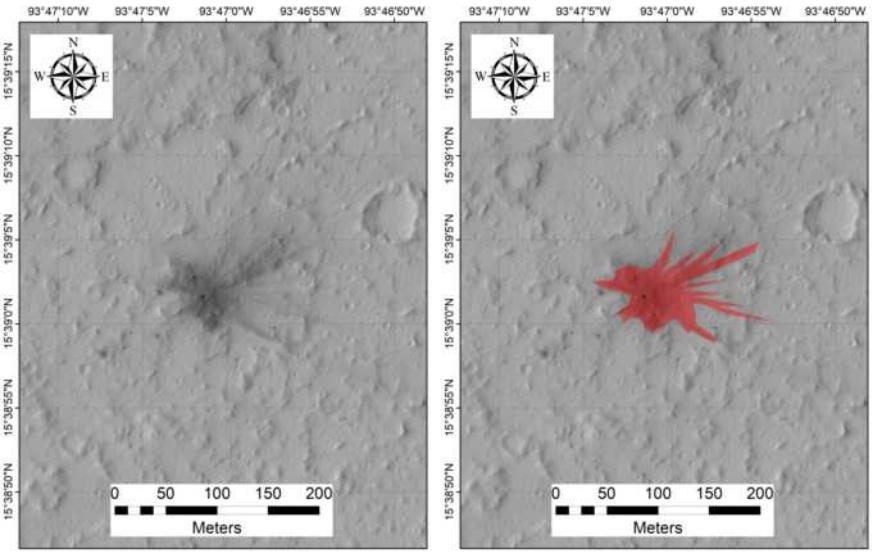

Latitude	Longitude	HiRISE ID	Area (m^2)	Diam.(m)	DCI	TI day	TI night	Epoch
15.650°	266.216°	PSP_010621_1960	5814.2	3.7	0.934	26	60	Amaz./Hesp.

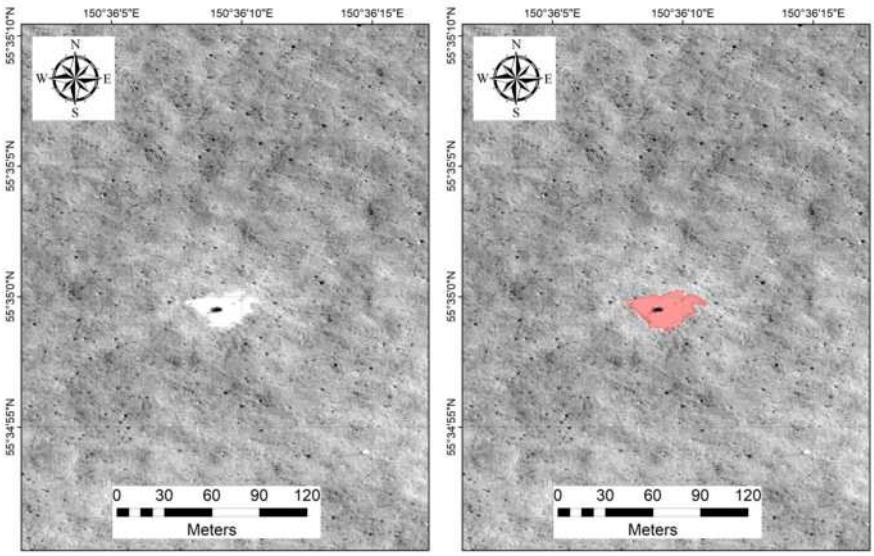

Latitude	Longitude	HiRISE ID	Area (m^2)	Diam.(m)	DCI	TI day	TI night	Epoch
55.583°	150.603°	PSP_010625_2360	730.7	4.2	0.964	265	254	Late Hesp.

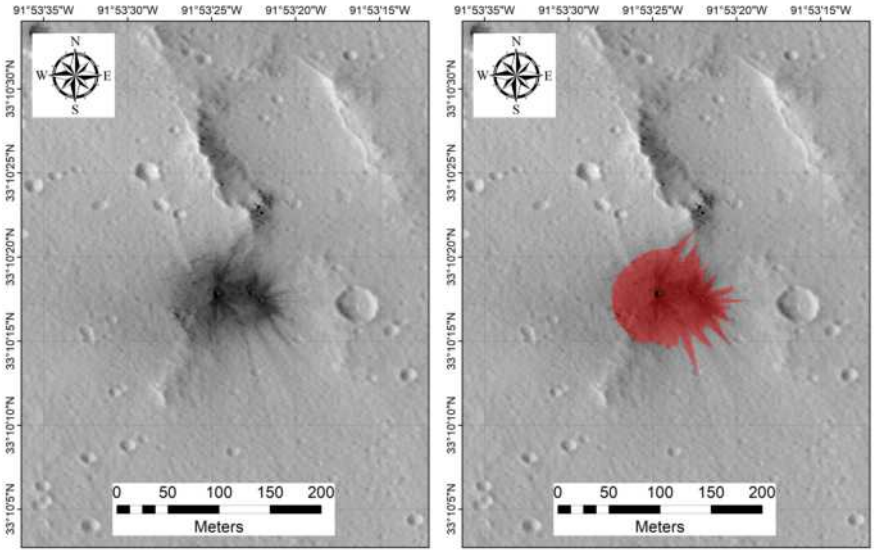

Latitude	Longitude	HiRISE ID	Area (m^2)	Diam.(m)	DCI	TI day	TI night	Epoch
33.172°	268.110°	PSP_010634_2135	8344.9	5.3	0.937	20	35	Late Hesp.

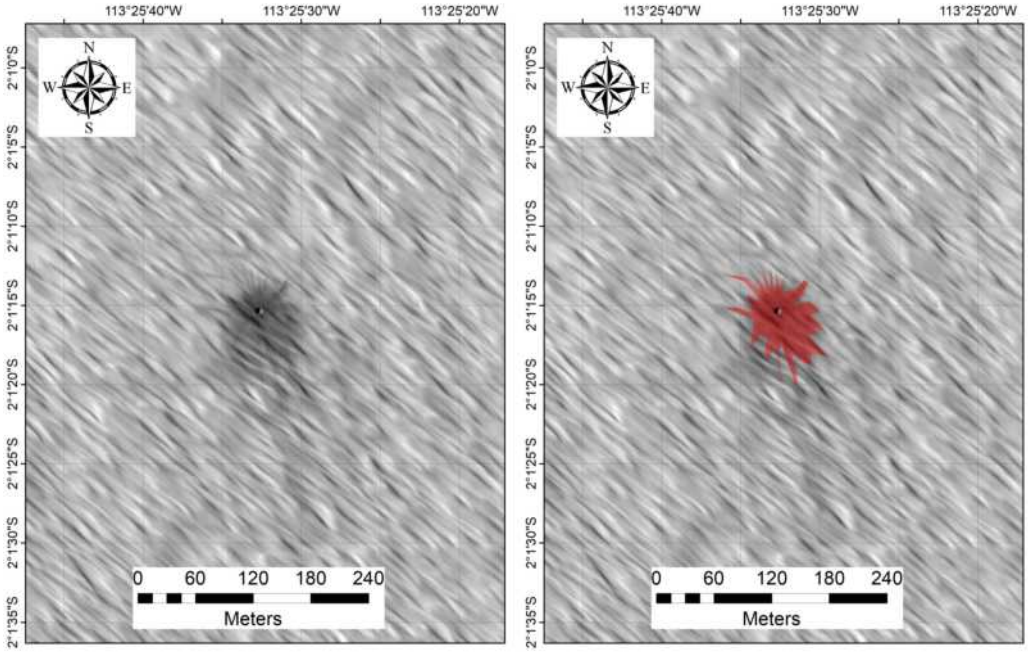

Latitude	Longitude	HiRISE ID	Area (m^2)	Diam.(m)	DCI	TI day	TI night	Epoch
−2.021°	246.574°	PSP_010635_1780	4727.6	6.5	0.939	79	25	Late Amaz.

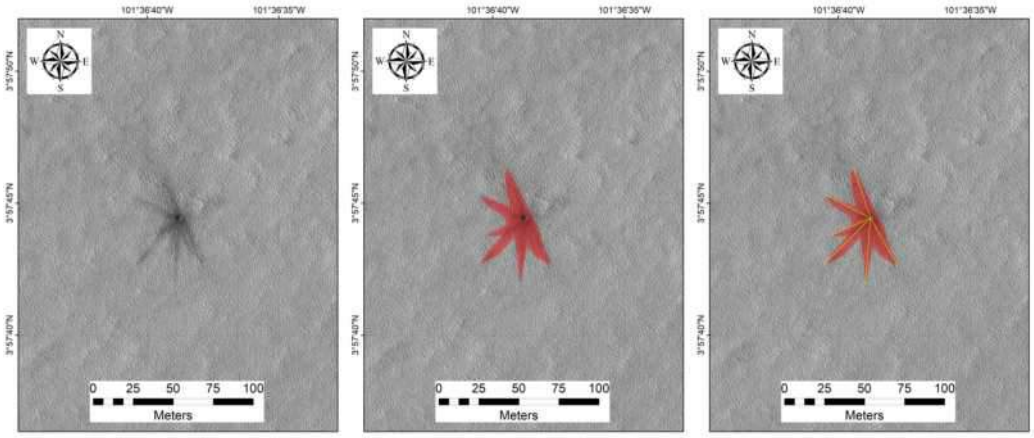

Latitude	Longitude	HiRISE ID	Area (m^2)	Diam.(m)	DCI	TI day	TI night	Epoch	Azimuth
3.962°	258.389°	PSP_010740_1840	1010.7	3.3	0.941	25	57	Amaz./Hesp.	237.4

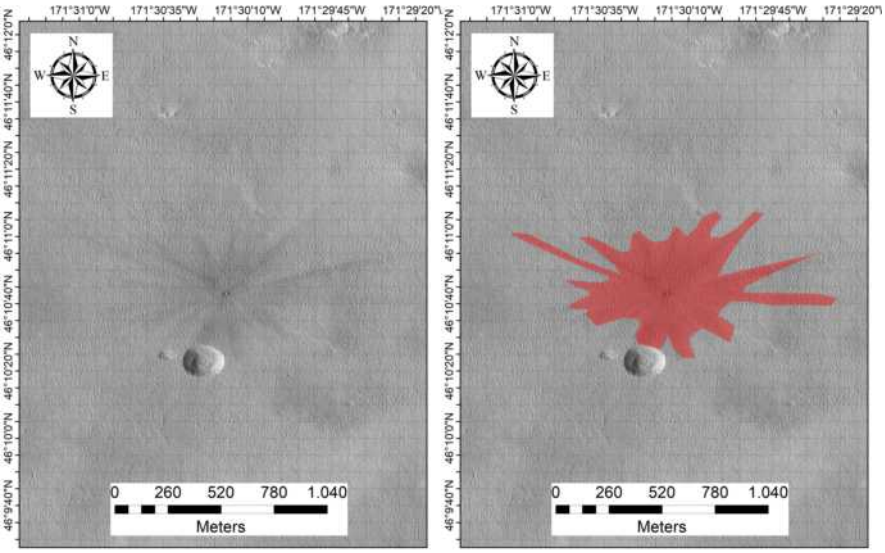

Latitude	Longitude	HiRISE ID	Area (m^2)	Diam.(m)	DCI	TI day	TI night	Epoch
46.179°	188.495°	PSP_010861_2265	391601.1	12.1	0.923	197	116	Amazonian

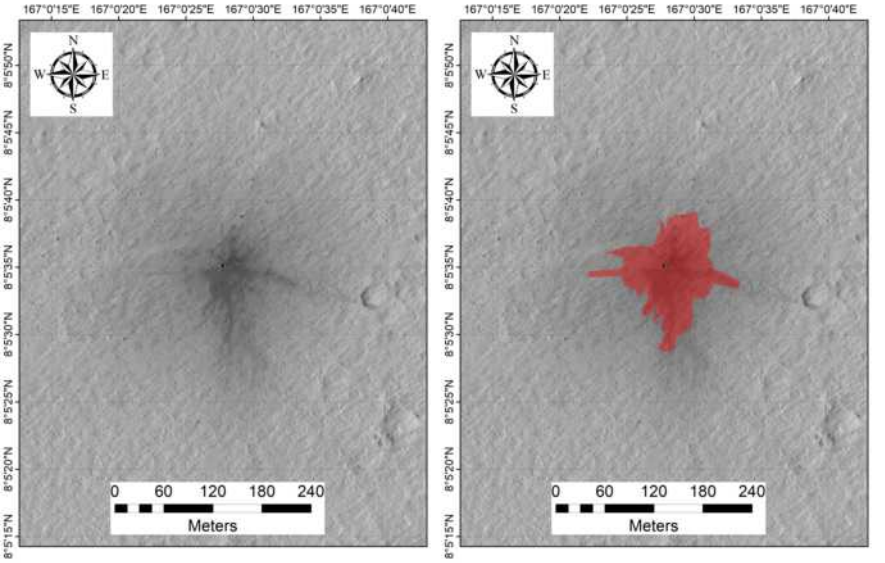

Latitude	Longitude	HiRISE ID	Area (m^2)	Diam.(m)	DCI	TI day	TI night	Epoch
8.093°	167.008°	PSP_010862_1880	11815.5	4.9	0.925	82	62	Late Amaz.

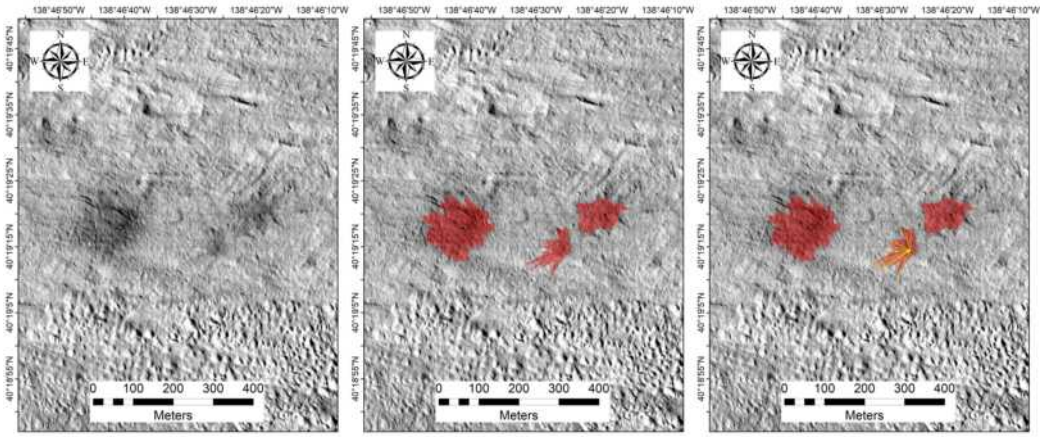

Latitude	Longitude	HiRISE ID	Area (m^2)	Diam.(m)	DCI	TI day	TI night	Epoch	Azimuth
40.322°	221.222°	ESP_011295_2205	17441.2	8.6	0.935	79	42	Amaz./Hesp.	
40.322°	221.222°	ESP_011295_2205	7210.5	6.8	0.935	79	42	Amaz./Hesp.	
40.322°	221.222°	ESP_011295_2205	4983.8	5.4	0.935	79	42	Amaz./Hesp.	267.7

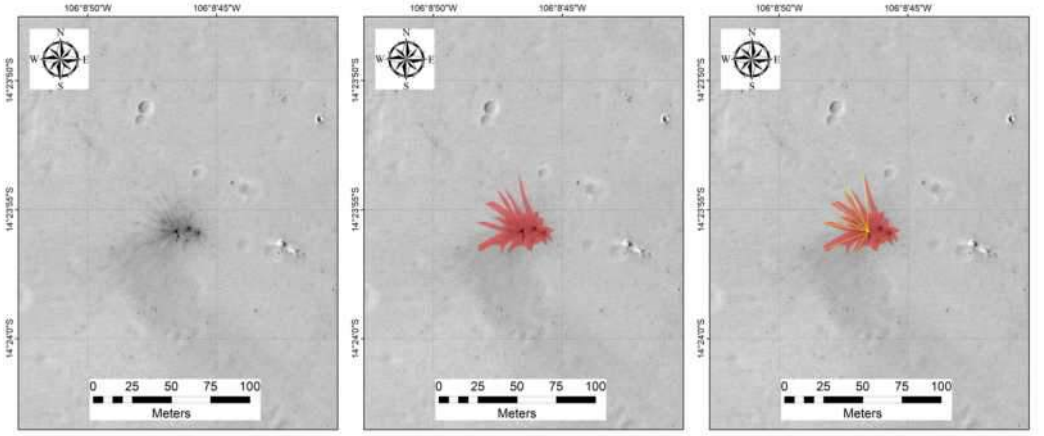

Latitude	Longitude	HiRISE ID	Area (m^2)	Diam.(m)	DCI	TI day	TI night	Epoch	Azimuth
−14.399°	253.854°	ESP_011360_1655	894.0	2.1	0.946	153	196	Late Hesp.	292.7

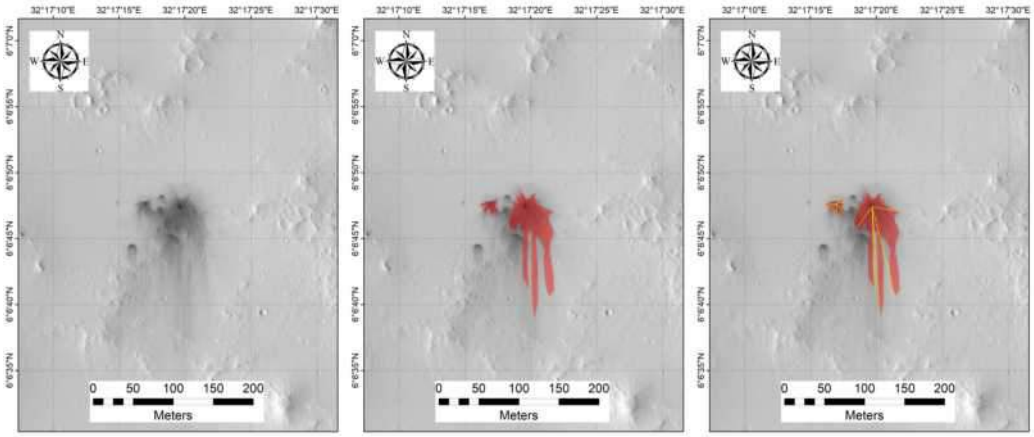

Latitude	Longitude	HiRISE ID	Area (m^2)	Diam.(m)	DCI	TI day	TI night	Epoch	Azimuth
6.113°	32.289°	ESP_011368_1860	3738.7	3.1	0.934	36	24	Middle Noach.	170.6
6.113°	32.289°	ESP_011368_1860	233.6	1.8	0.934	36	24	Middle Noach.	161.0

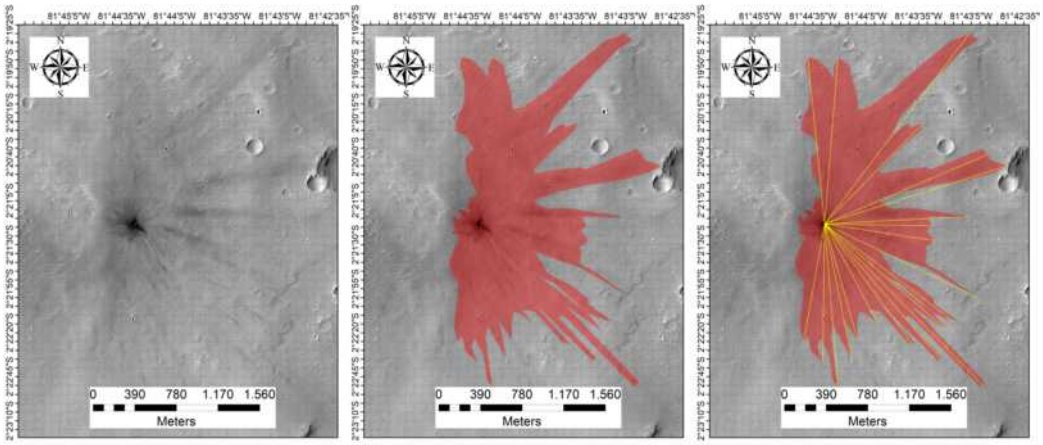

Latitude	Longitude	HiRISE ID	Area (m^2)	Diam.(m)	DCI	TI day	TI night	Epoch	Azimuth
−2.355°	278.259°	ESP_011425_1775	2670781.2	50.1	0.951	79	89	Early Hesp.	106.2

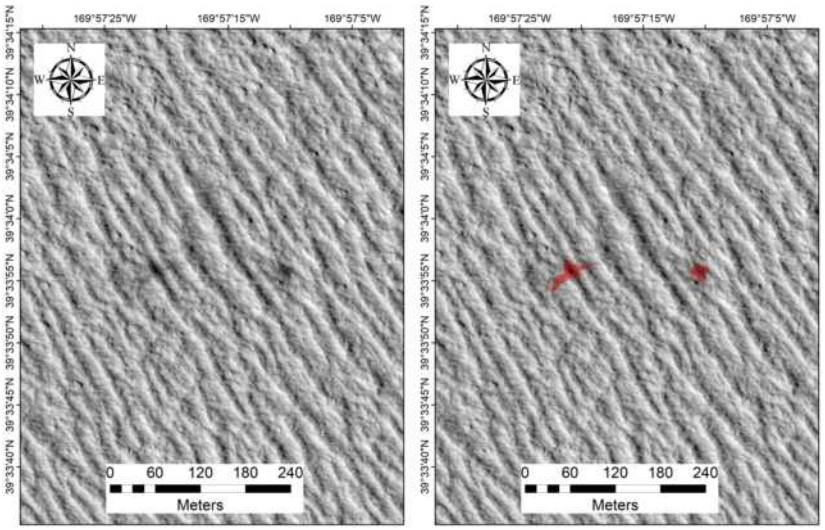

Latitude	Longitude	HiRISE ID	Area (m^2)	Diam.(m)	DCI	TI day	TI night	Epoch
39.565°	190.046°	ESP_011428_2200	738.9	3.1	0.935	65	123	Hesp./Noach.
39.565°	190.046°	ESP_011428_2200	348.8	2.2	0.935	65	123	Hesp./Noach.

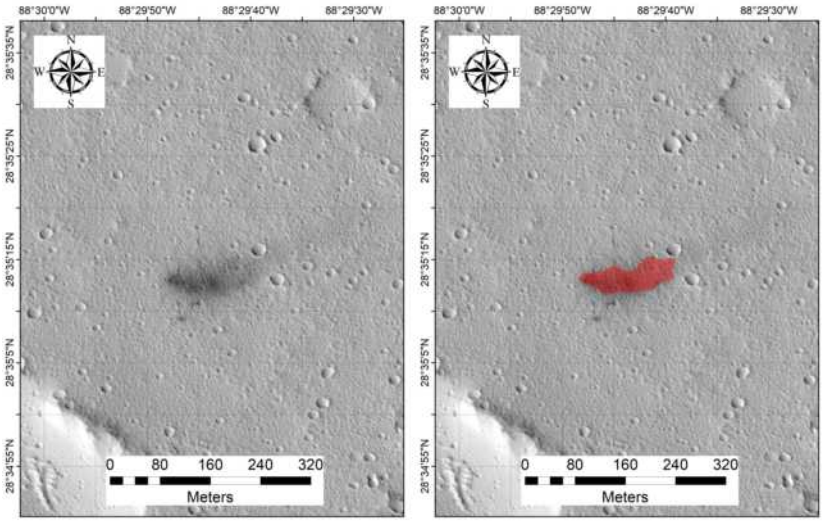

Latitude	Longitude	HiRISE ID	Area (m^2)	Diam.(m)	DCI	TI day	TI night	Epoch
28.587°	271.504°	ESP_011491_2090	5358.0	2.5	0.926	32	44	Amaz./Hesp.

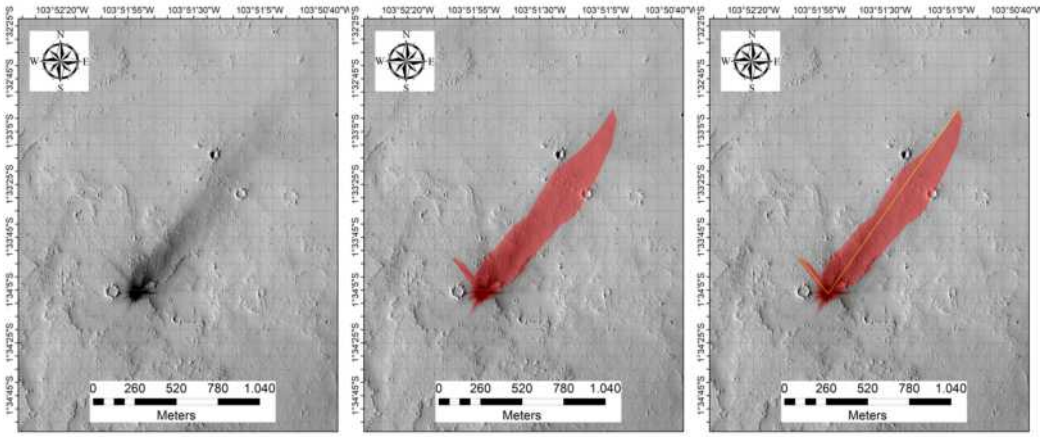

Latitude	Longitude	HiRISE ID	Area (m^2)	Diam.(m)	DCI	TI day	TI night	Epoch	Azimuth
−1.568°	256.136°	ESP_011584_1785	282024.1	6.2	0.935	54	21	Amaz./Hesp.	81.6

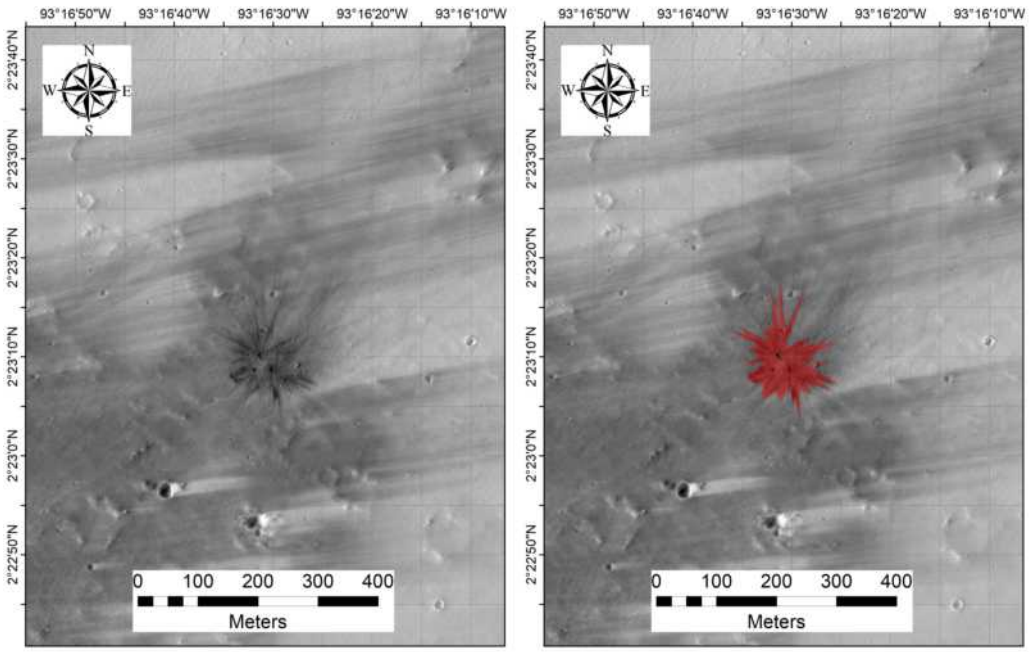

Latitude	Longitude	HiRISE ID	Area (m^2)	Diam.(m)	DCI	TI day	TI night	Epoch
2.386°	266.725°	ESP_011610_1825	11668.2	7.2	0.937	54	28	Late Hesp.

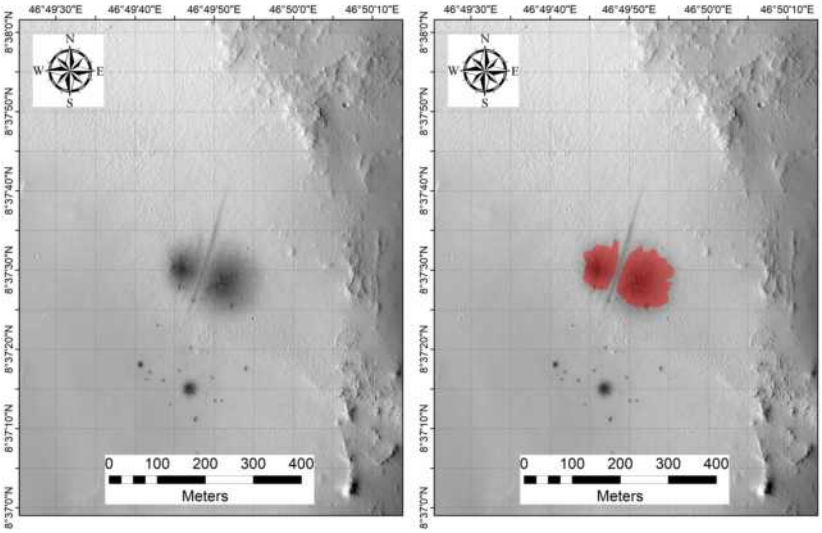

Latitude	Longitude	HiRISE ID	Area (m^2)	Diam.(m)	DCI	TI day	TI night	Epoch
8.625°	46.830°	ESP_011618_1885	10909.5	3.2	0.937	50	51	Middle Noach.
8.625°	46.830°	ESP_011618_1885	5456.5	2.6	0.937	50	51	Middle Noach.

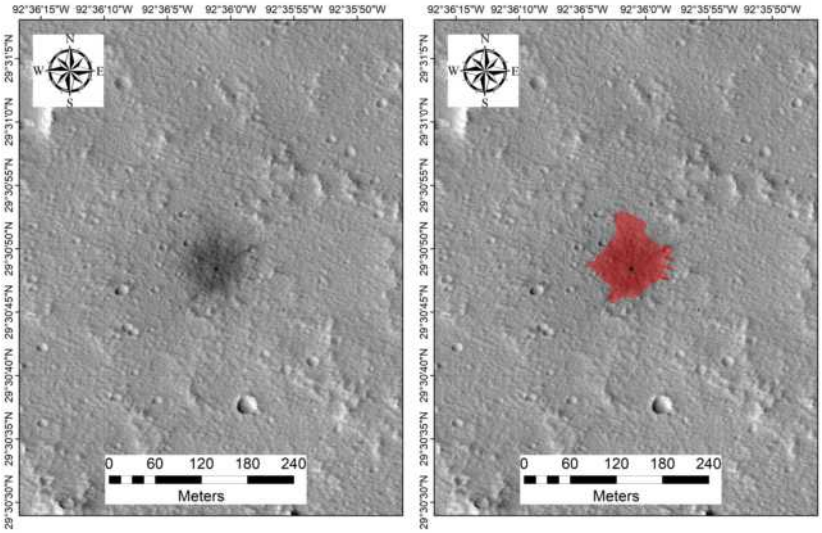

Latitude	Longitude	HiRISE ID	Area (m^2)	Diam.(m)	DCI	TI day	TI night	Epoch
29.513°	267.400°	ESP_011623_2100	6928.2	6.7	0.938	38	55	Amaz./Hesp.

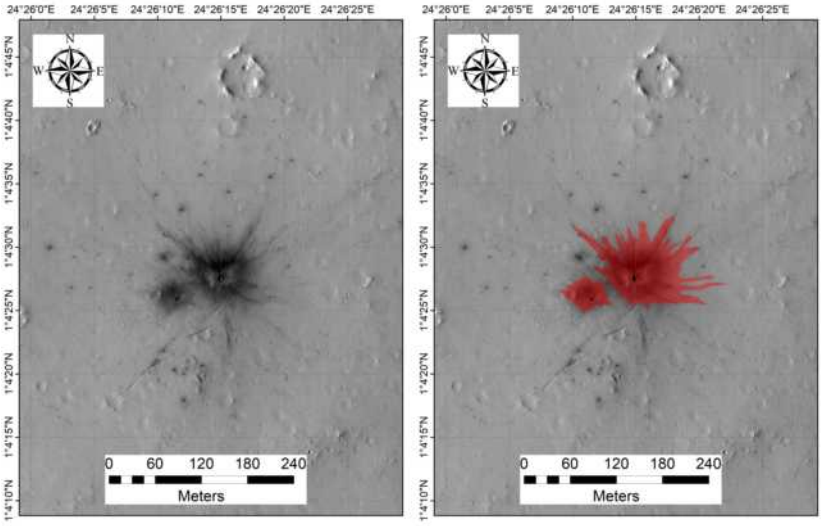

Latitude	Longitude	HiRISE ID	Area (m^2)	Diam.(m)	DCI	TI day	TI night	Epoch
1.074°	24.437°	ESP_011698_1810	9640.6	6.2	0.937	125	164	Middle Noach.
1.074°	24.437°	ESP_011698_1810	1779.4	3.3	0.937	125	164	Middle Noach.

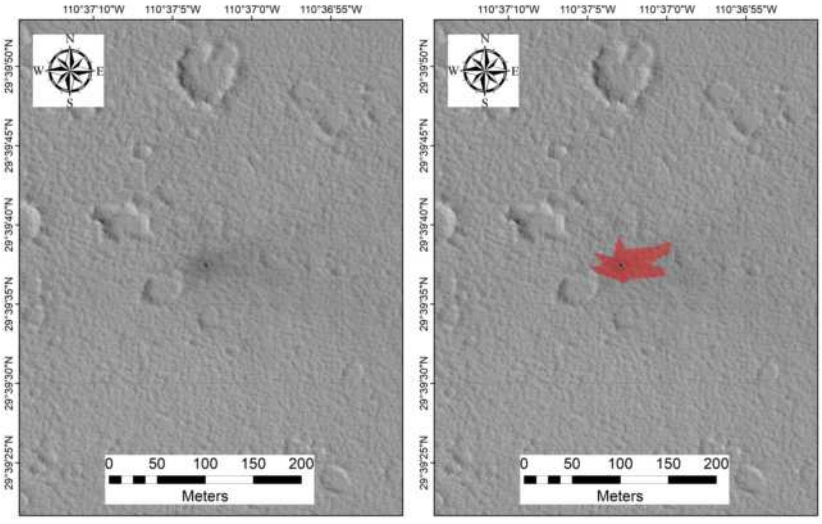

Latitude	Longitude	HiRISE ID	Area (m^2)	Diam.(m)	DCI	TI day	TI night	Epoch
29.660°	249.383°	ESP_011716_2100	2089.7	4.7	0.932	44	57	Early Hesp.

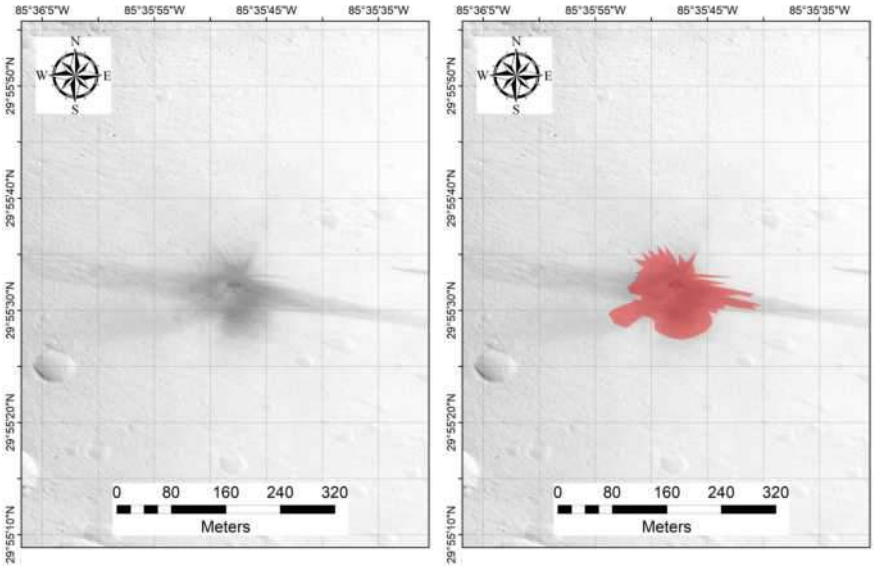

Latitude	Longitude	HiRISE ID	Area (m^2)	Diam.(m)	DCI	TI day	TI night	Epoch
29.926°	274.403°	ESP_011781_2100	13996.6	3.2	0.919	40	30	Amaz./Hesp.

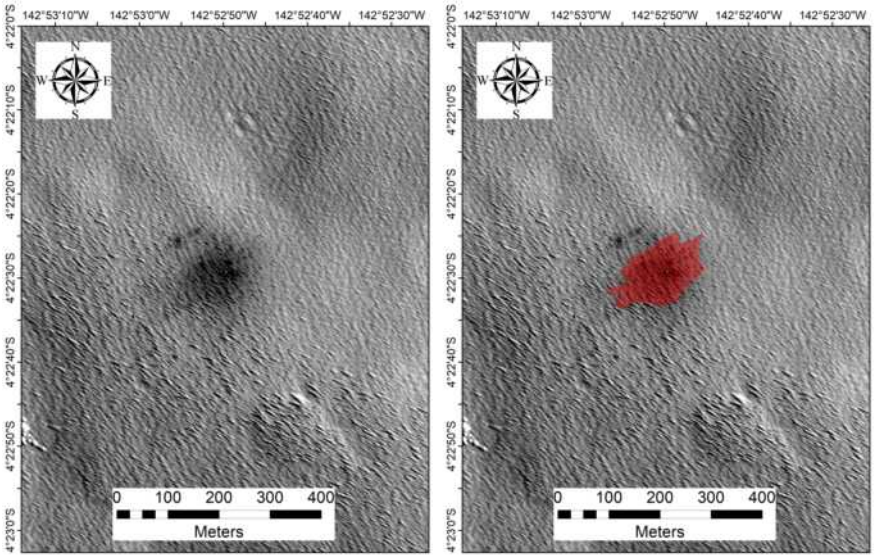

Latitude	Longitude	HiRISE ID	Area (m^2)	Diam.(m)	DCI	TI day	TI night	Epoch
−4.375°	217.119°	ESP_012047_1755	16265.2	8.4	0.933	23	65	Middle Noach.

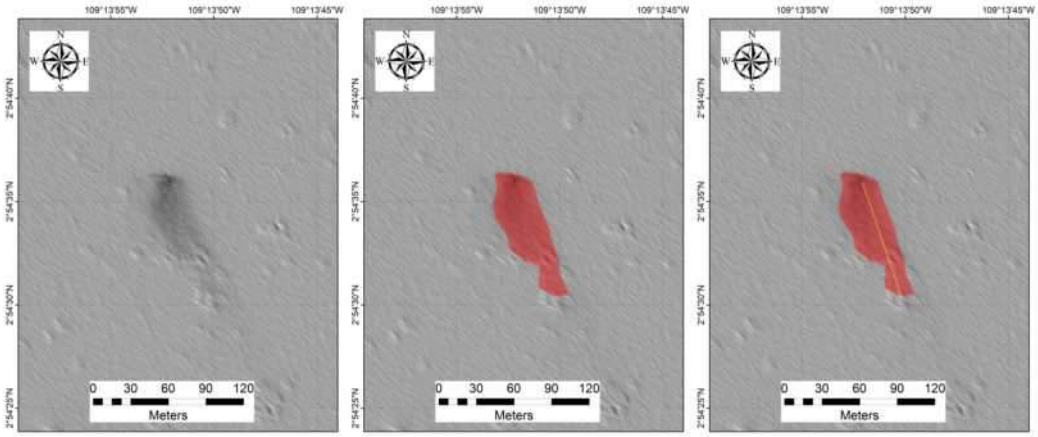

Latitude	Longitude	HiRISE ID	Area (m^2)	Diam.(m)	DCI	TI day	TI night	Epoch	Azimuth
2.910°	250.769°	ESP_012349_1830	2836.0	2.7	0.935	39	35	Amaz./Hesp.	161.1

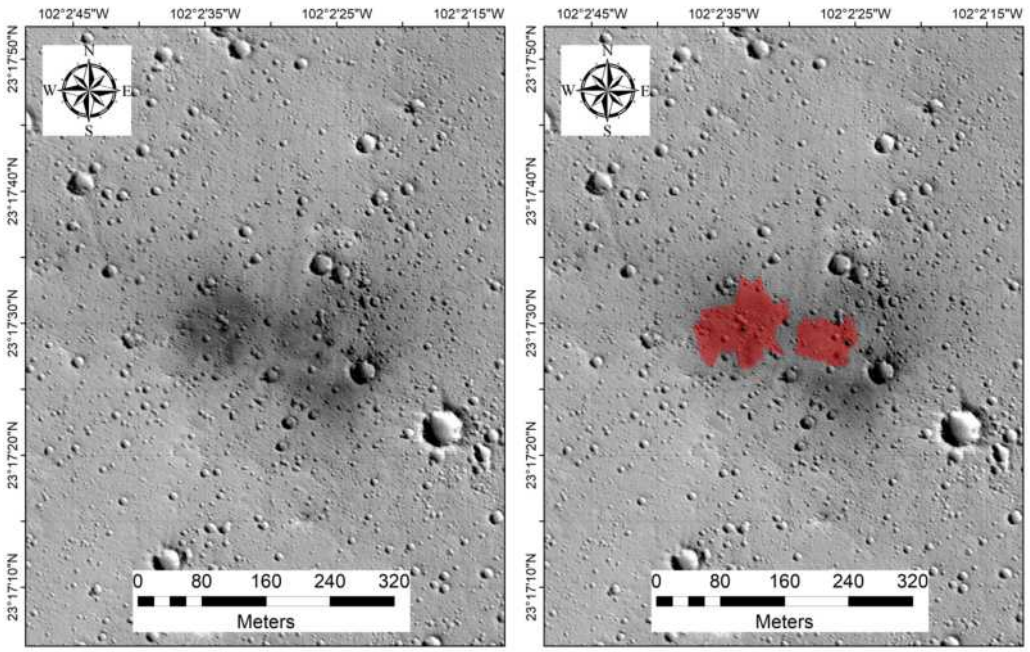

Latitude	Longitude	HiRISE ID	Area (m^2)	Diam.(m)	DCI	TI day	TI night	Epoch
23.291°	257.960°	ESP_012375_2035	3563.8	7.0	0.937	43	70	Late Hesp.
23.291°	257.960°	ESP_012375_2035	7974.2	5.5	0.937	43	70	Late Hesp.

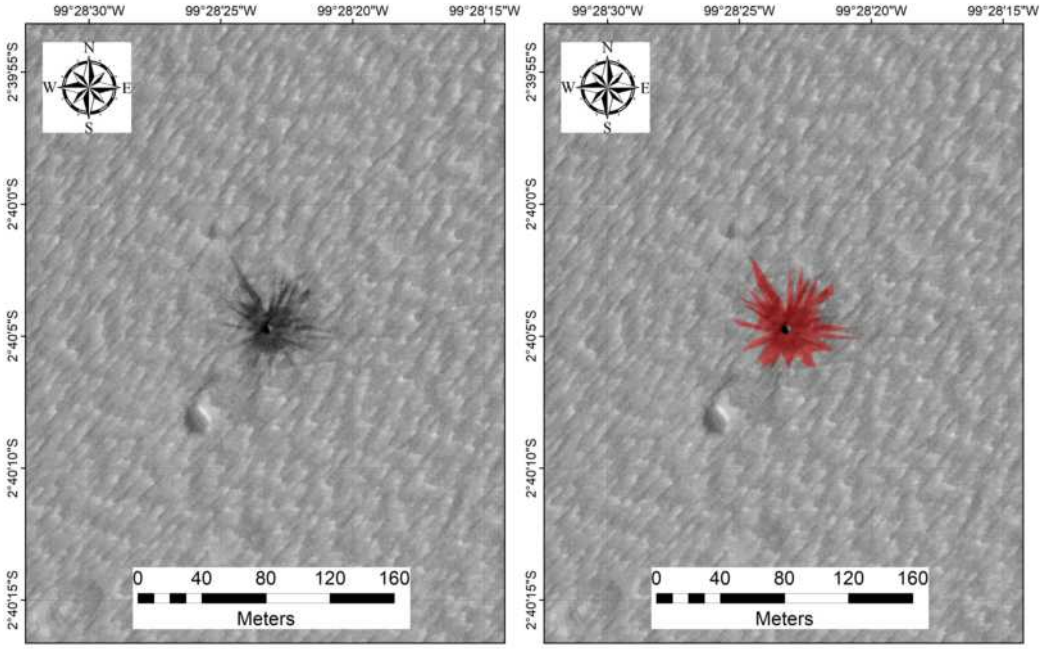

Latitude	Longitude	HiRISE ID	Area (m^2)	Diam.(m)	DCI	TI day	TI night	Epoch
−2.668°	260.527°	ESP_012441_1775	2018.6	5.9	0.943	62	115	Late Hesp.

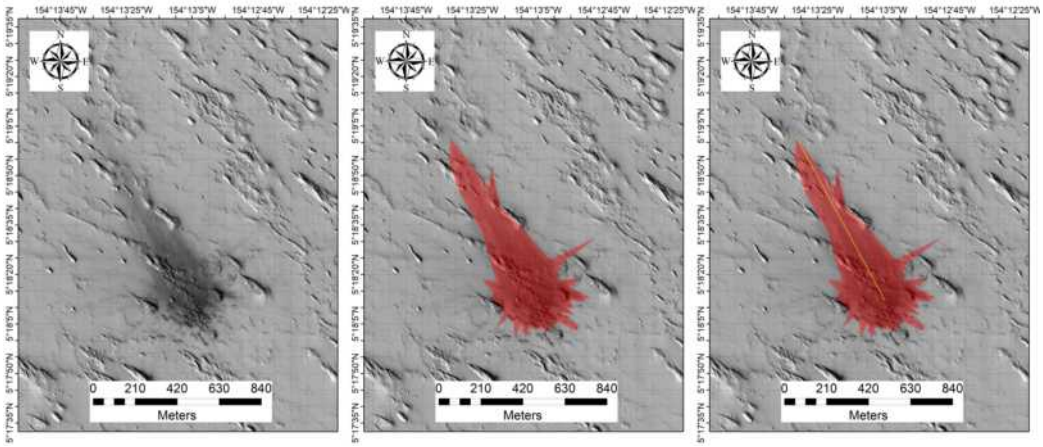

Latitude	Longitude	HiRISE ID	Area (m^2)	Diam.(m)	DCI	TI day	TI night	Epoch	Azimuth
5.303°	205.782°	ESP_012588_1855	228285.1	9.5	0.934	48	68	Late Hesp.	331.4

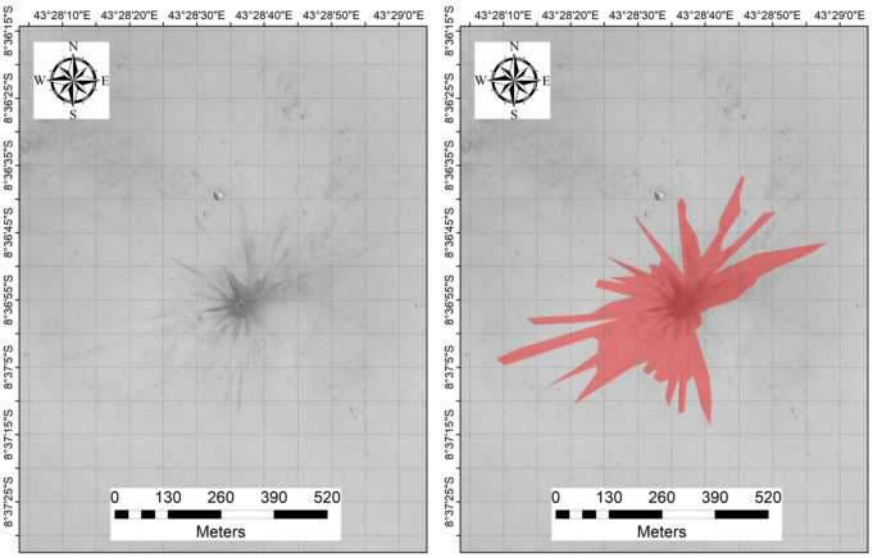

Latitude	Longitude	HiRISE ID	Area (m^2)	Diam.(m)	DCI	TI day	TI night	Epoch
−8.615°	43.477°	ESP_013161_1715	114433.0	5.2	0.950	109	164	Early Noach.

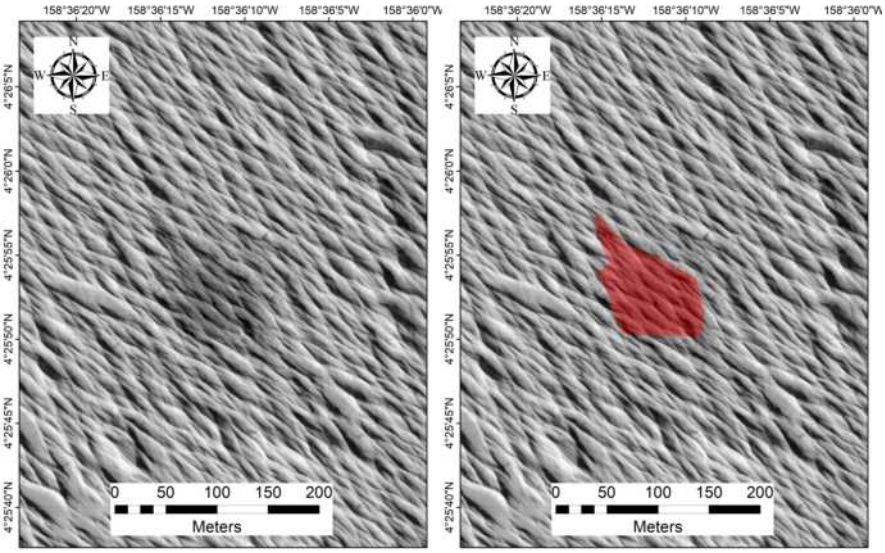

Latitude	Longitude	HiRISE ID	Area (m^2)	Diam.(m)	DCI	TI day	TI night	Epoch
4.431°	201.397°	ESP_013287_1845	7178.8	4.0	0.934	28	45	Amaz./Hesp.

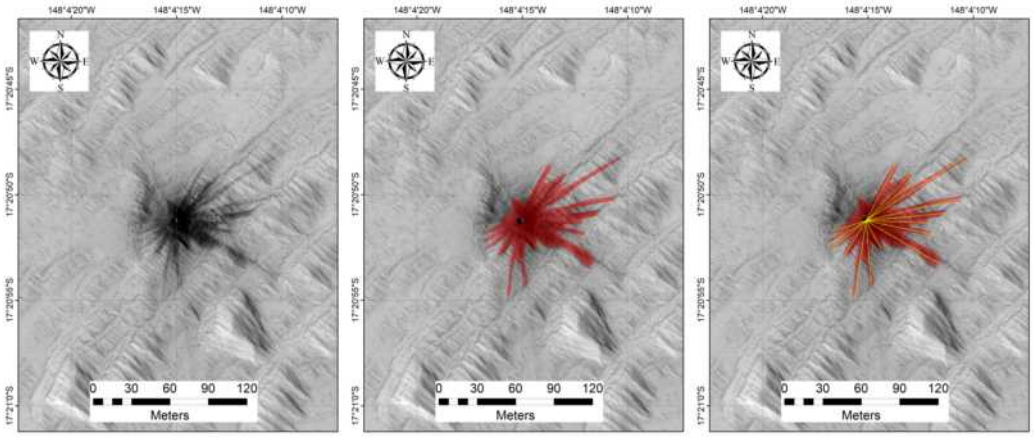

Latitude	Longitude	HiRISE ID	Area (m^2)	Diam.(m)	DCI	TI day	TI night	Epoch	Azimuth
−17.348°	211.929°	ESP_013590_1625	3147.5	5.0	0.936	263	69	Early Noach.	115.9

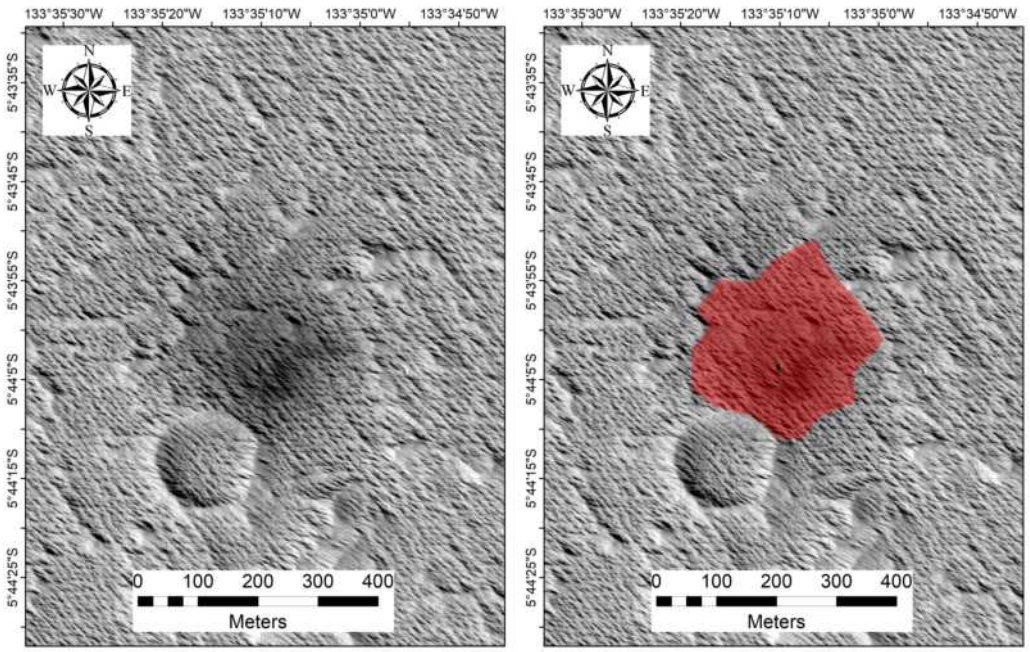

Latitude	Longitude	HiRISE ID	Area (m^2)	Diam.(m)	DCI	TI day	TI night	Epoch
−5.734°	226.414°	ESP_013629_1740	66160.2	9.6	0.937	80	44	Amaz./Hesp.

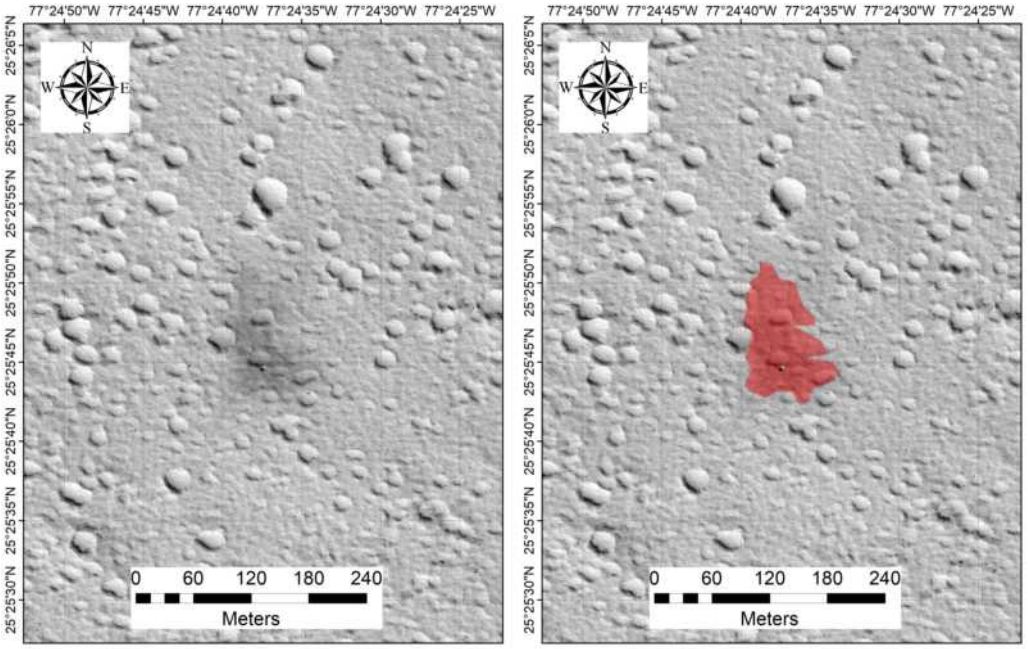

Latitude	Longitude	HiRISE ID	Area (m^2)	Diam.(m)	DCI	TI day	TI night	Epoch
25.429°	282.590°	ESP_013640_2055	8567.6	5.6	0.937	65	76	Early Hesp.

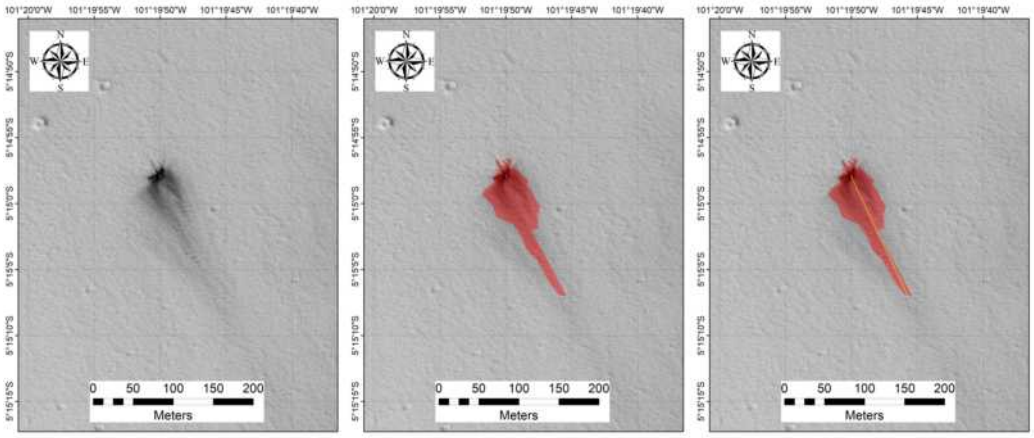

Latitude	Longitude	HiRISE ID	Area (m^2)	Diam.(m)	DCI	TI day	TI night	Epoch	Azimuth
−5.249°	258.669°	ESP_013641_1745	4887.2	3.5	0.931	28	51	Late Hesp.	154.5

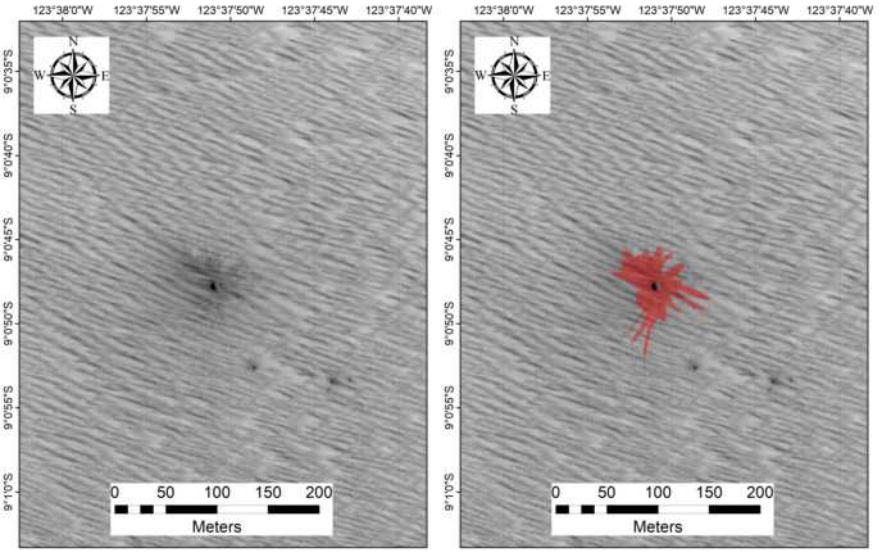

Latitude	Longitude	HiRISE ID	Area (m^2)	Diam.(m)	DCI	TI day	TI night	Epoch
−9.013°	236.369°	ESP_013655_1710	3193.1	8.3	0.943	57	51	Amazonian

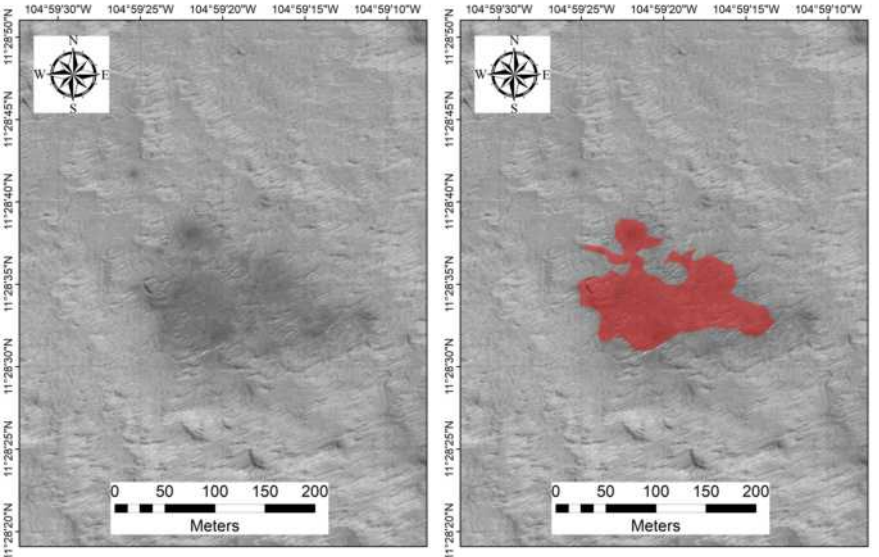

Latitude	Longitude	HiRISE ID	Area (m^2)	Diam.(m)	DCI	TI day	TI night	Epoch
11.476°	255.011°	ESP_013707_1915	12493.0	3.0	0.945	227	78	Amazonian

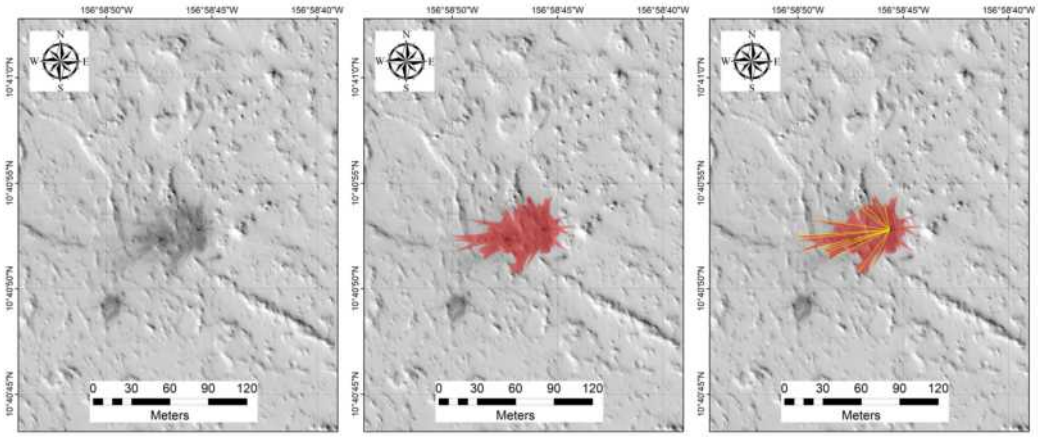

Latitude	Longitude	HiRISE ID	Area (m^2)	Diam.(m)	DCI	TI day	TI night	Epoch	Azimuth
10.681°	203.020°	ESP_013788_1910	2244.7	1.6	0.932	41	50	Late Hesp.	265.4

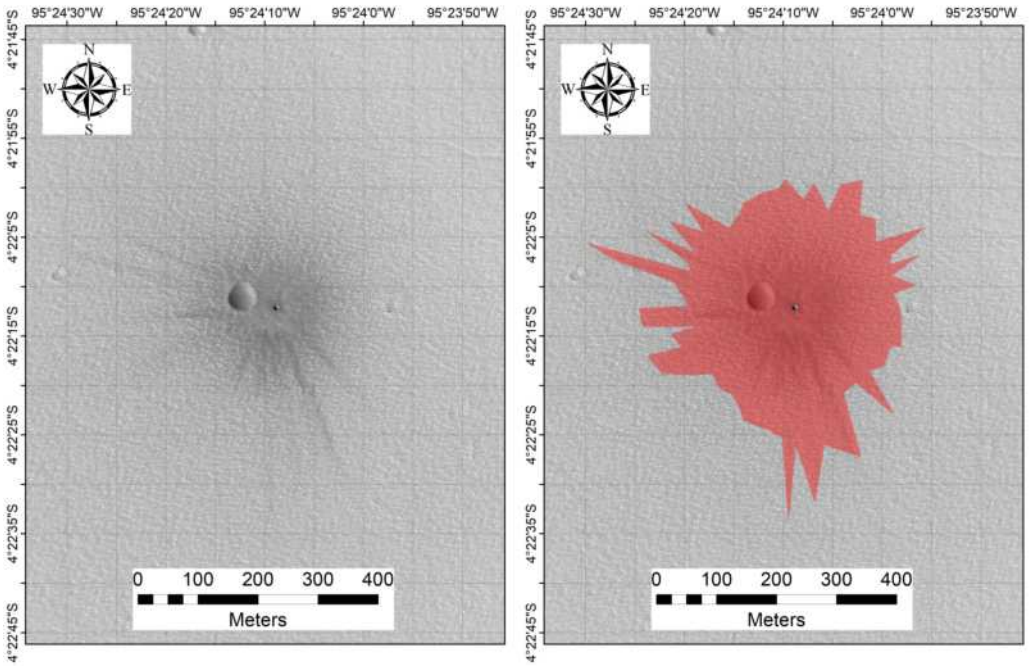

Latitude	Longitude	HiRISE ID	Area (m^2)	Diam.(m)	DCI	TI day	TI night	Epoch
−4.370°	264.598°	ESP_013799_1755	133765.4	9.9	0.939	30	32	Late Hesp.

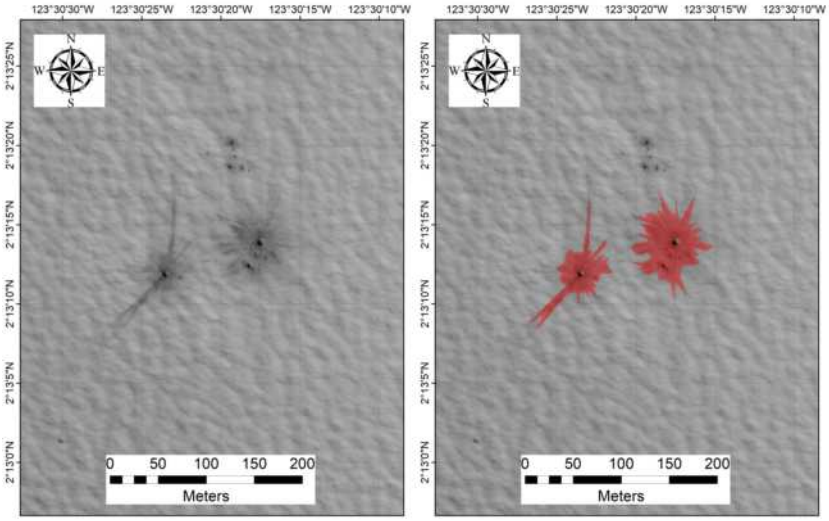

Latitude	Longitude	HiRISE ID	Area (m^2)	Diam.(m)	DCI	TI day	TI night	Epoch
2.221°	236.494°	ESP_013800_1820	3860.1	6.3	0.932	94	69	Hesperian
2.221°	236.494°	ESP_013800_1820	2286.7	5.7	0.932	94	69	Hesperian

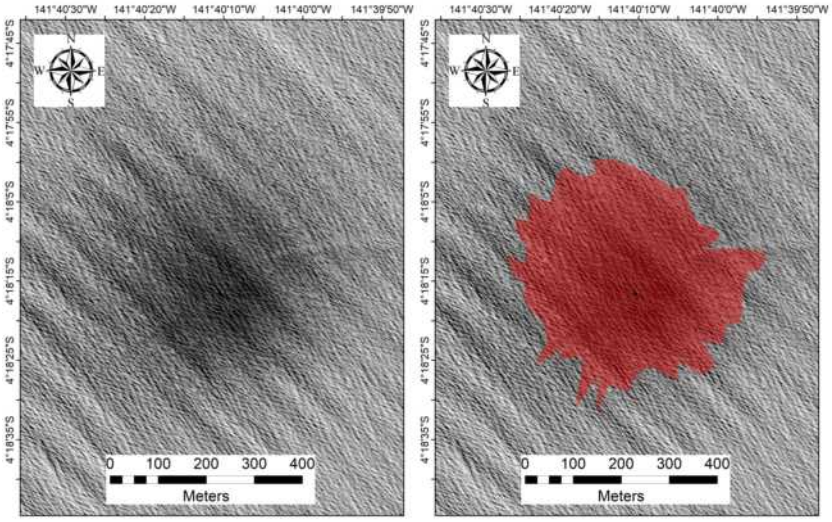

Latitude	Longitude	HiRISE ID	Area (m^2)	Diam.(m)	DCI	TI day	TI night	Epoch
−4.305°	218.330°	ESP_013893_1755	161714.7	8.0	0.937	59	47	Amaz./Hesp.

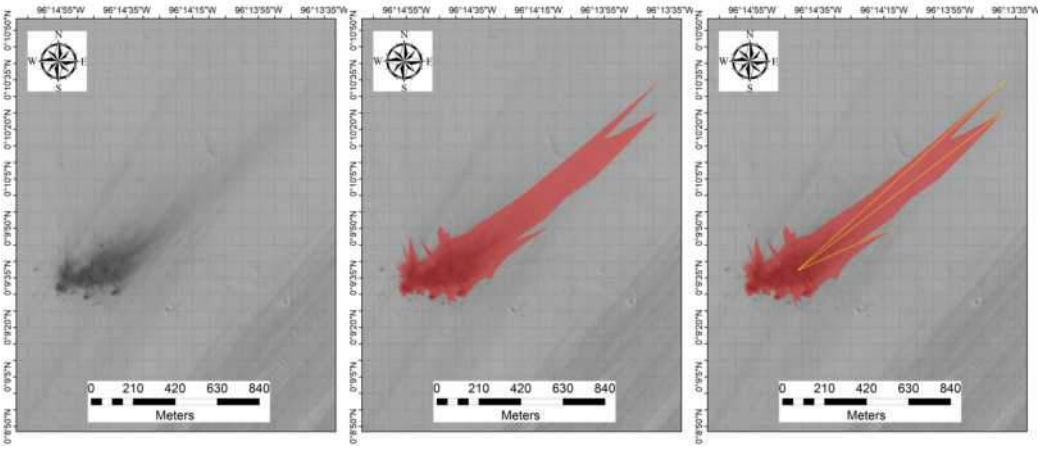

Latitude	Longitude	HiRISE ID	Area (m^2)	Diam.(m)	DCI	TI day	TI night	Epoch	Azimuth
0.160°	263.752°	ESP_014010_1800	268760.1	5.2	0.936	28	11	Amaz./Hesp.	52.6

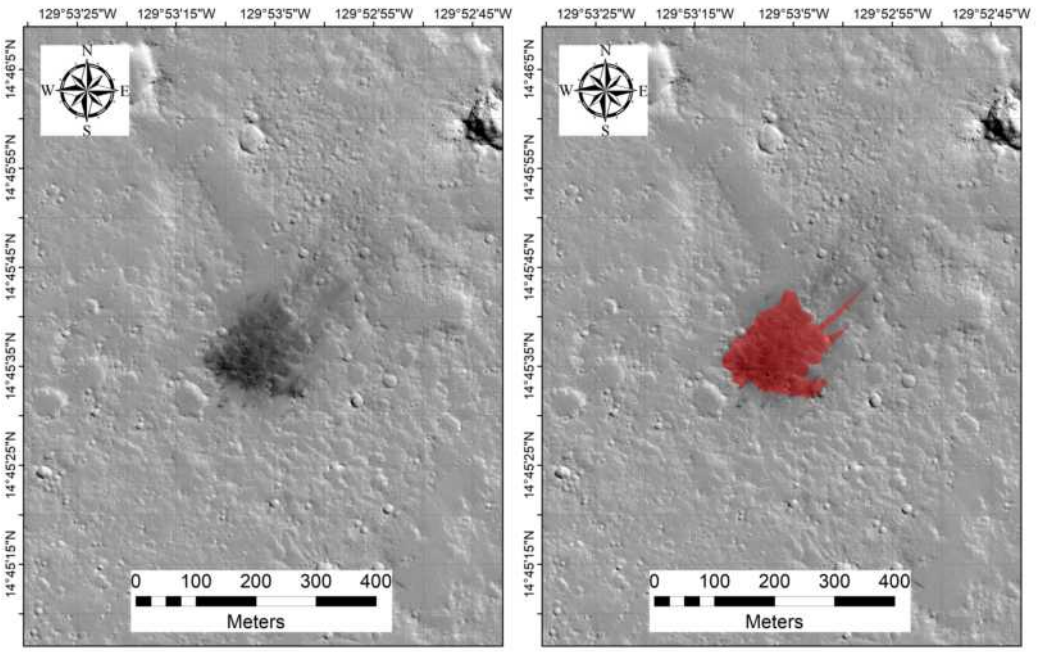

Latitude	Longitude	HiRISE ID	Area (m^2)	Diam.(m)	DCI	TI day	TI night	Epoch
14.760°	230.115°	ESP_014143_1950	20122.8	5.5	0.928	15	38	Late Amaz.

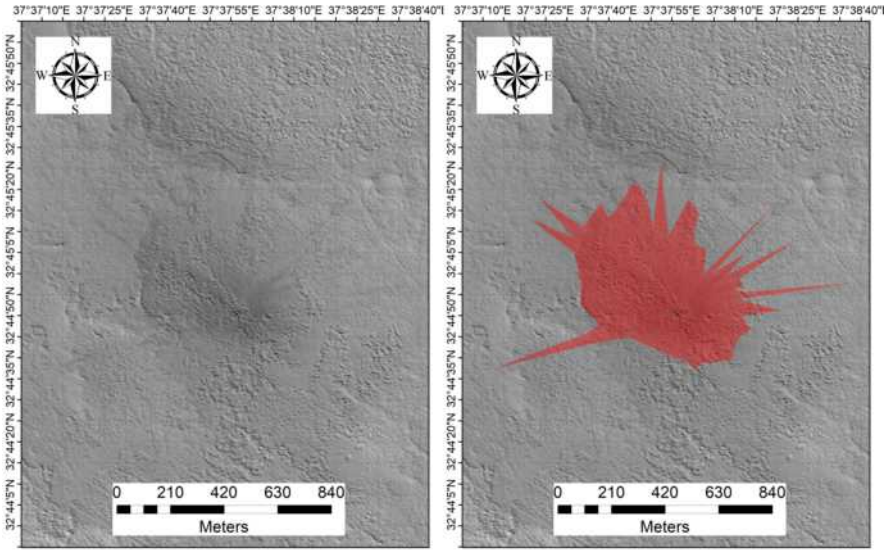

Latitude	Longitude	HiRISE ID	Area (m^2)	Diam.(m)	DCI	TI day	TI night	Epoch
32.747°	37.632°	ESP_014150_2130	346881.3	13.1	0.923	48	61	Middle Noach.

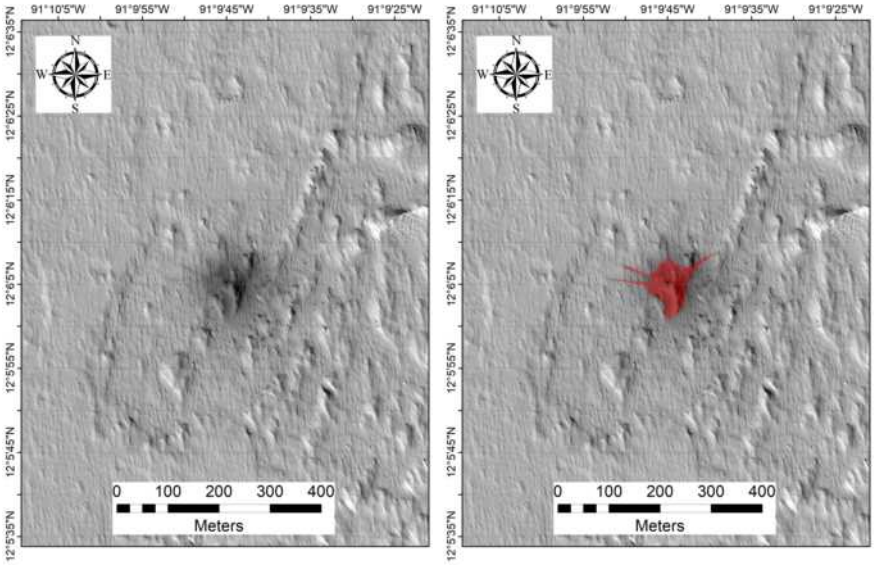

Latitude	Longitude	HiRISE ID	Area (m^2)	Diam.(m)	DCI	TI day	TI night	Epoch
12.101°	268.838°	ESP_014168_1920	7037.3	4.7	0.935	34	70	Amaz./Hesp.

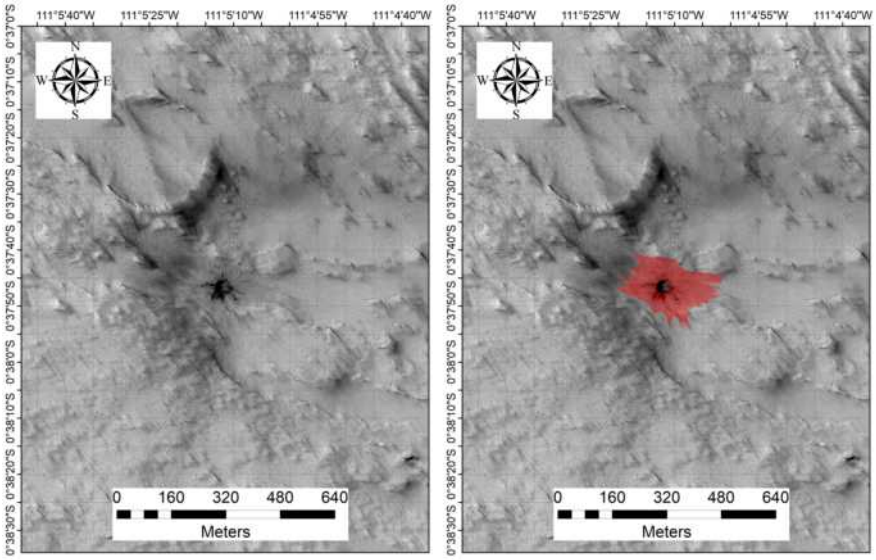

Latitude	Longitude	HiRISE ID	Area (m^2)	Diam.(m)	DCI	TI day	TI night	Epoch
−0.630°	248.913°	ESP_015949_1795	32561.8	38.0	0.939	131	13	Amazonian

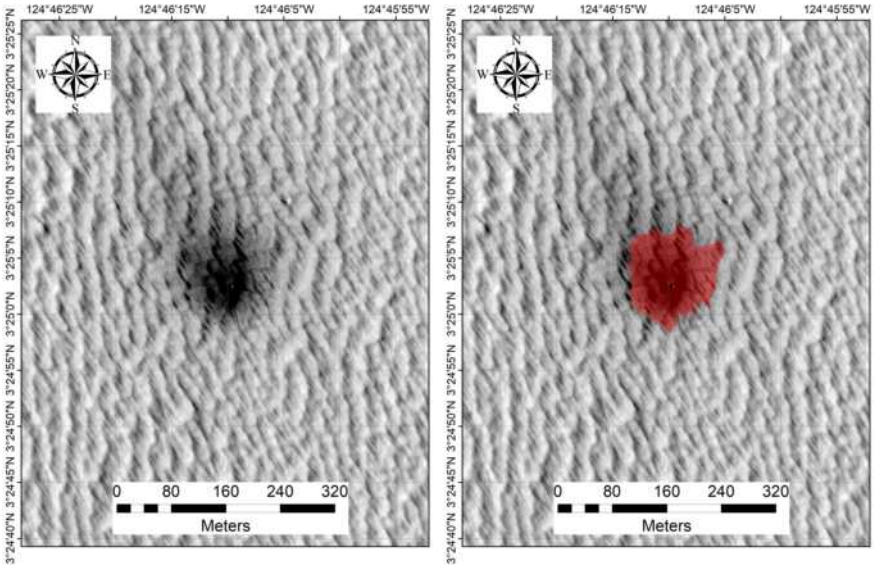

Latitude	Longitude	HiRISE ID	Area (m^2)	Diam.(m)	DCI	TI day	TI night	Epoch
3.417°	235.231°	ESP_015989_1835	14650.2	5.9	0.936	88	82	Hesperian

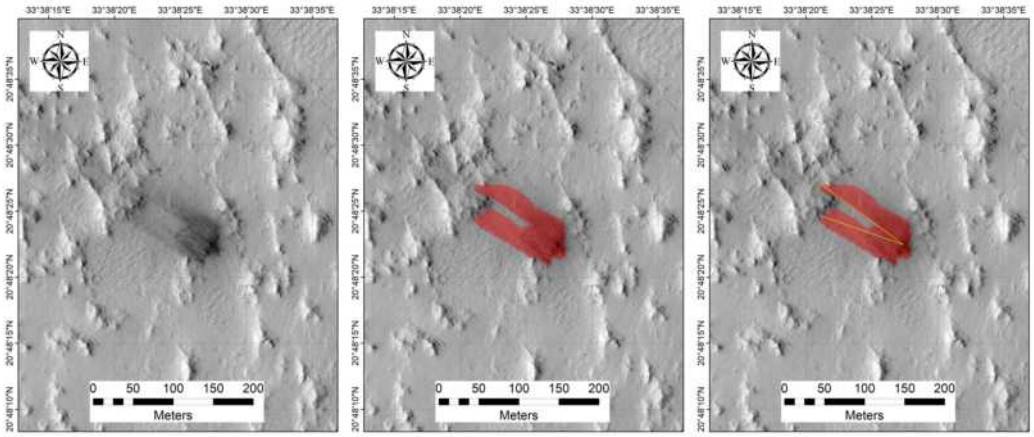

Latitude	Longitude	HiRISE ID	Area (m^2)	Diam.(m)	DCI	TI day	TI night	Epoch	Azimuth
20.806°	33.641°	ESP_016115_2010	5996.8	3.2	0.933	17	84	Early Noach.	298.5

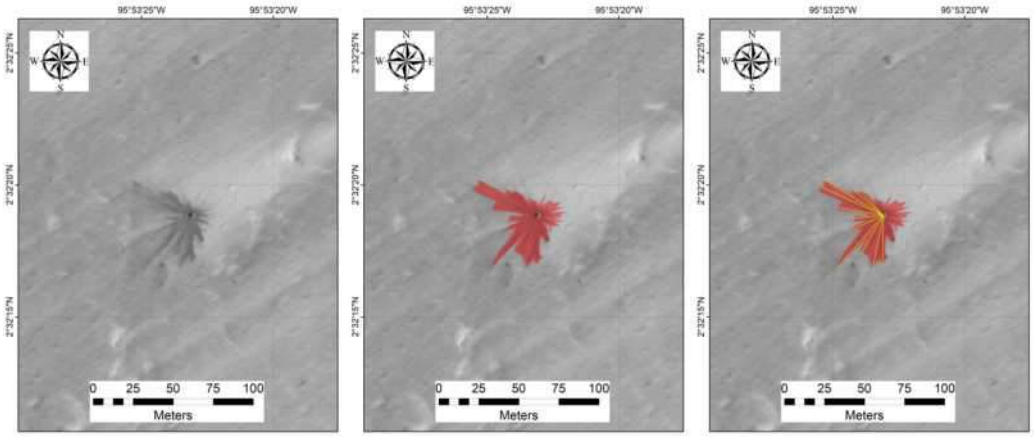

Latitude	Longitude	HiRISE ID	Area (m^2)	Diam.(m)	DCI	TI day	TI night	Epoch	Azimuth
2.539°	264.110°	ESP_016133_1825	1159.1	3.8	0.938	50	62	Amaz./Hesp.	255.0

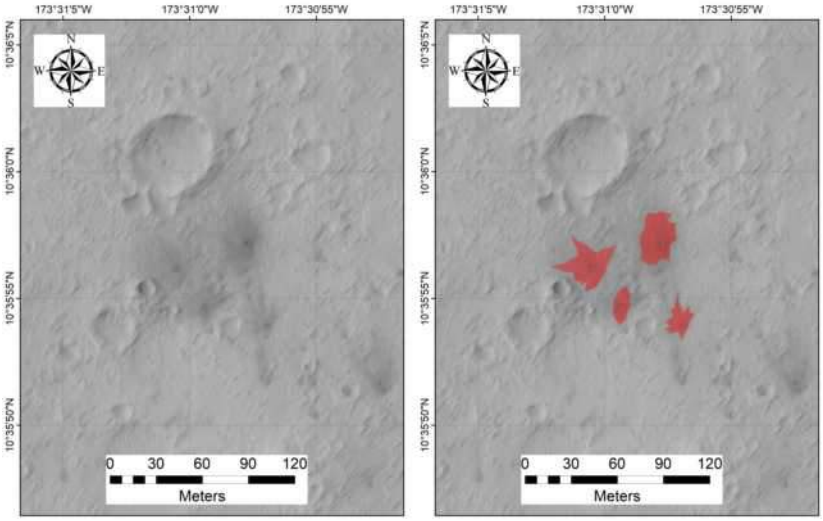

Latitude	Longitude	HiRISE ID	Area (m^2)	Diam.(m)	DCI	TI day	TI night	Epoch
10.599°	186.484°	ESP_016149_1905	603.8	2.7	0.934	77	50	Amaz./Hesp.
10.599°	186.484°	ESP_016149_1905	587.7	2.0	0.934	77	50	Amaz./Hesp.
10.599°	186.484°	ESP_016149_1905	189.4	1.9	0.934	77	50	Amaz./Hesp.
10.599°	186.484°	ESP_016149_1905	230.2	1.4	0.934	77	50	Amaz./Hesp.

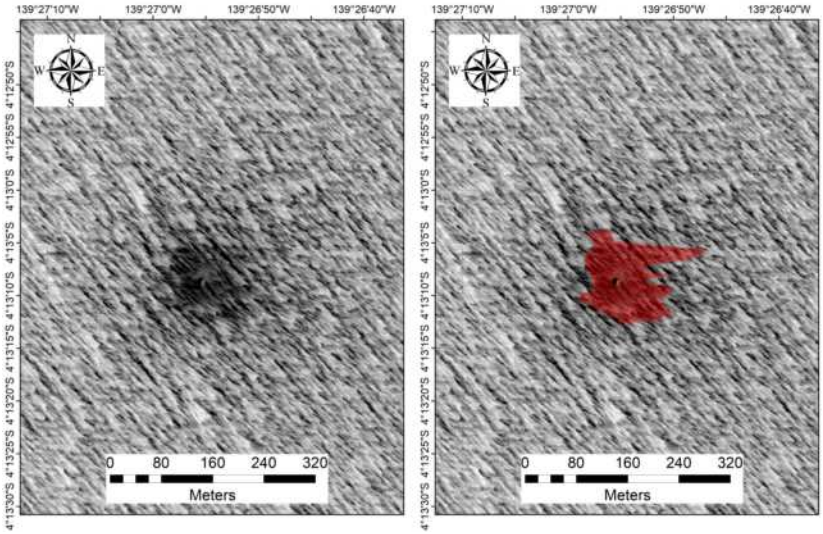

Latitude	Longitude	HiRISE ID	Area (m^2)	Diam.(m)	DCI	TI day	TI night	Epoch
−4.219°	220.551°	ESP_016161_1755	15102.5	10.6	0.941	23	73	Amaz./Hesp.

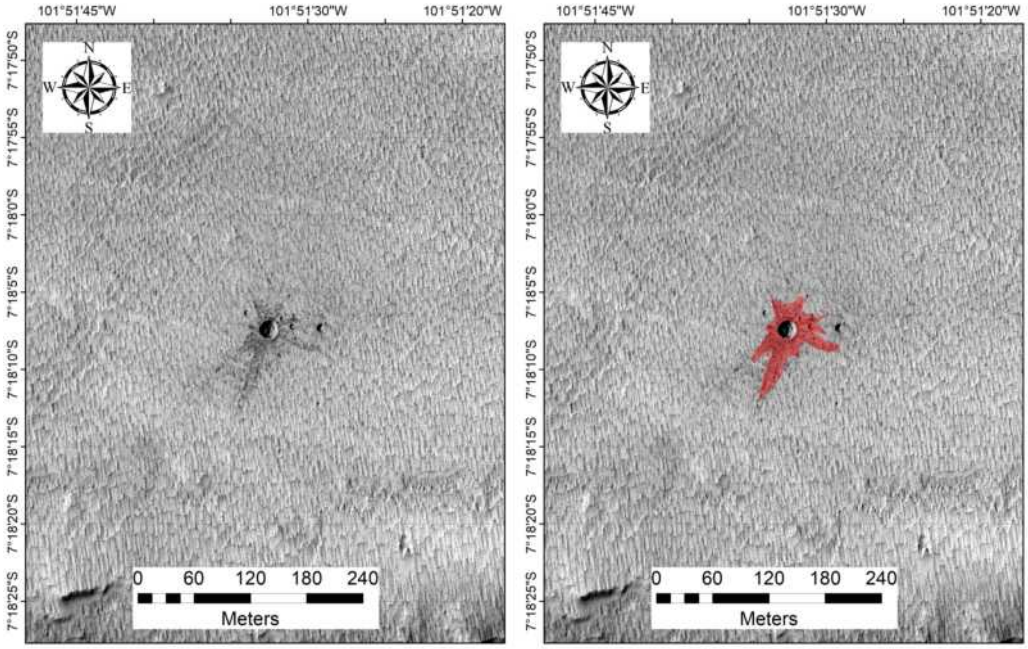

Latitude	Longitude	HiRISE ID	Area (m^2)	Diam.(m)	DCI	TI day	TI night	Epoch
−7.302°	258.141°	ESP_016186_1725	3461.4	19.9	0.950	70	47	Late Hesp.

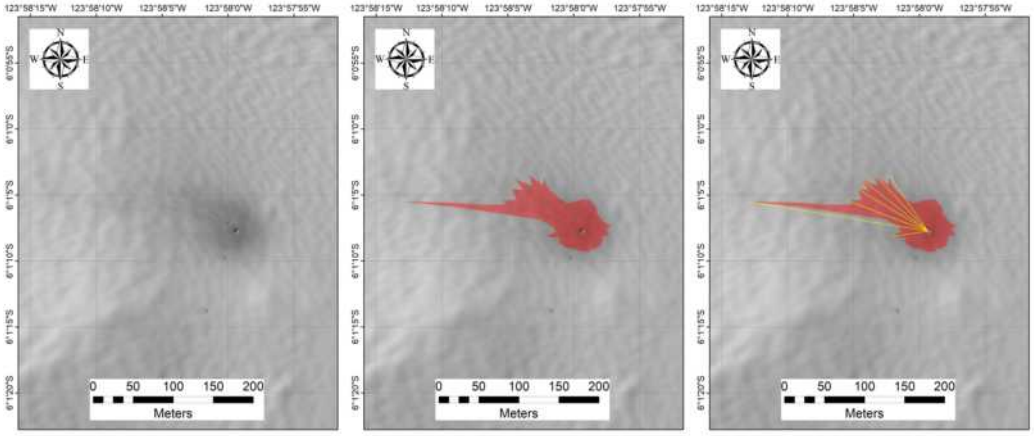

Latitude	Longitude	HiRISE ID	Area (m^2)	Diam.(m)	DCI	TI day	TI night	Epoch	Azimuth
−6.019°	236.034°	ESP_016200_1740	6470.6	4.9	0.931	57	52	Late Amaz.	296.3

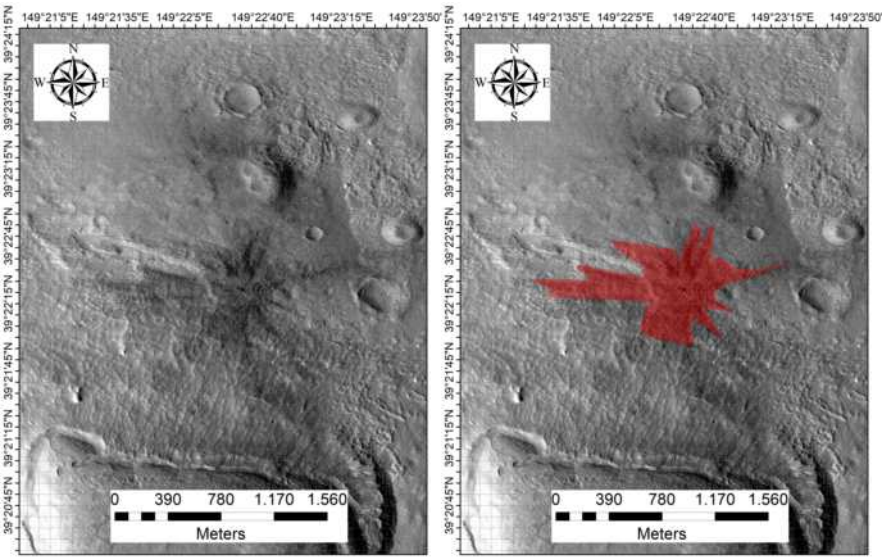

Latitude	Longitude	HiRISE ID	Area (m^2)	Diam.(m)	DCI	TI day	TI night	Epoch
39.373°	149.375°	ESP_016203_2195	552116.1	20.1	0.929	77	92	Late Hesp.

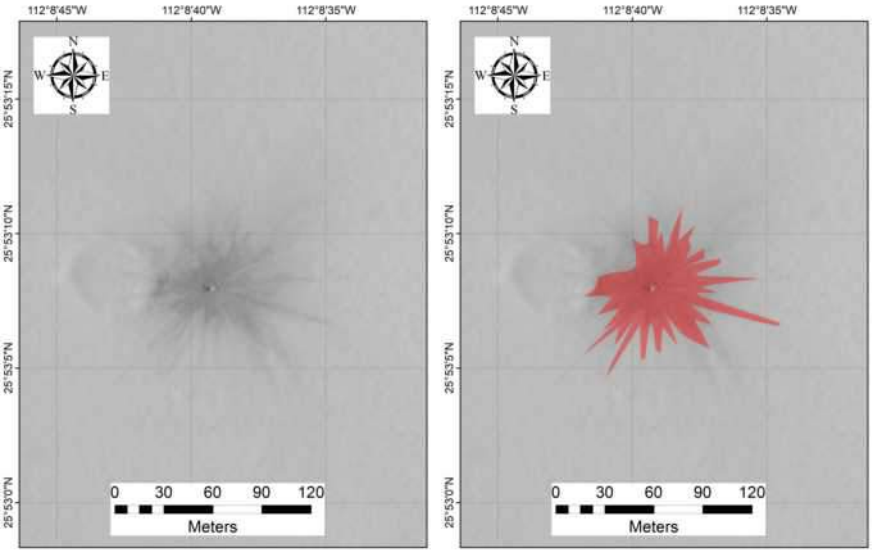

Latitude	Longitude	HiRISE ID	Area (m^2)	Diam.(m)	DCI	TI day	TI night	Epoch
25.886°	247.886°	ESP_016239_2060	3663.5	3.2	0.934	47	60	Late Amaz.

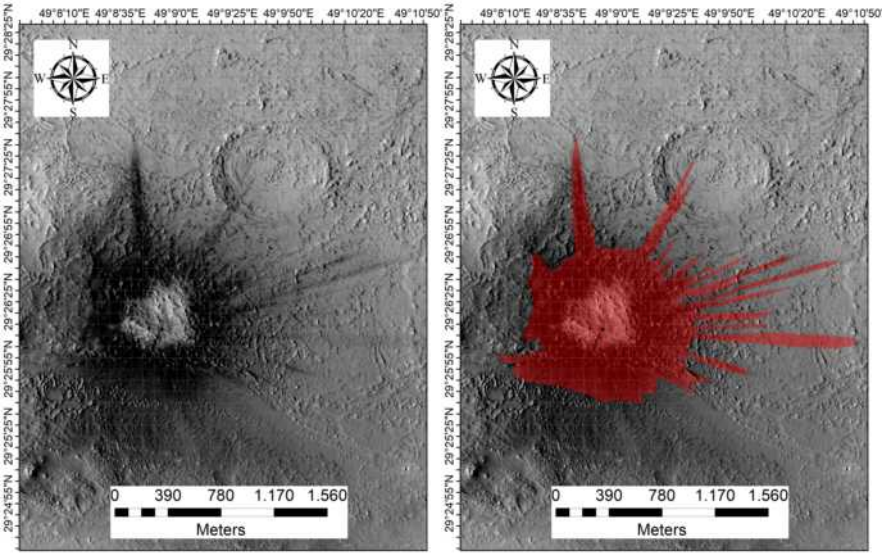

Latitude	Longitude	HiRISE ID	Area (m^2)	Diam.(m)	DCI	TI day	TI night	Epoch
29.437°	49.148°	ESP_016299_2095	1571096.5	25.7	0.941	166	167	Amaz./Hesp.

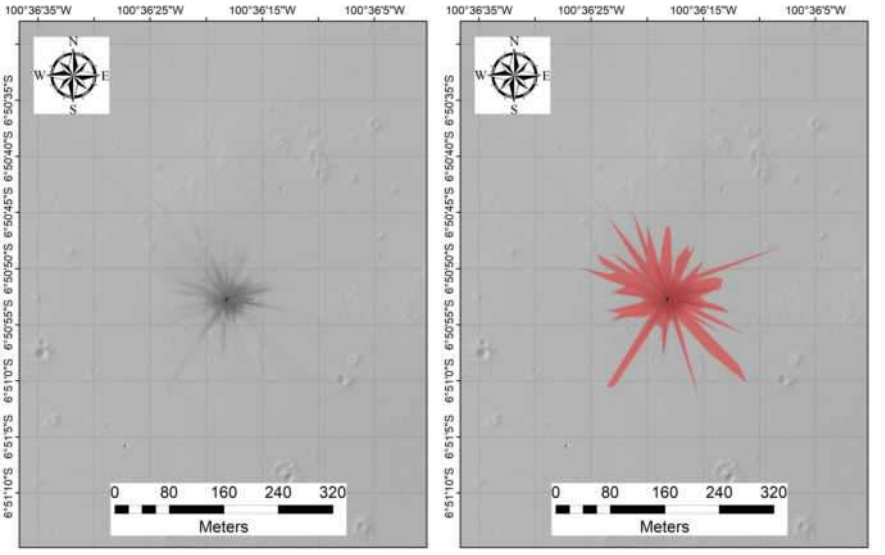

Latitude	Longitude	HiRISE ID	Area (m^2)	Diam.(m)	DCI	TI day	TI night	Epoch
−6.848°	259.395°	ESP_016331_1730	17391.3	6.0	0.942	56	81	Late Hesp.

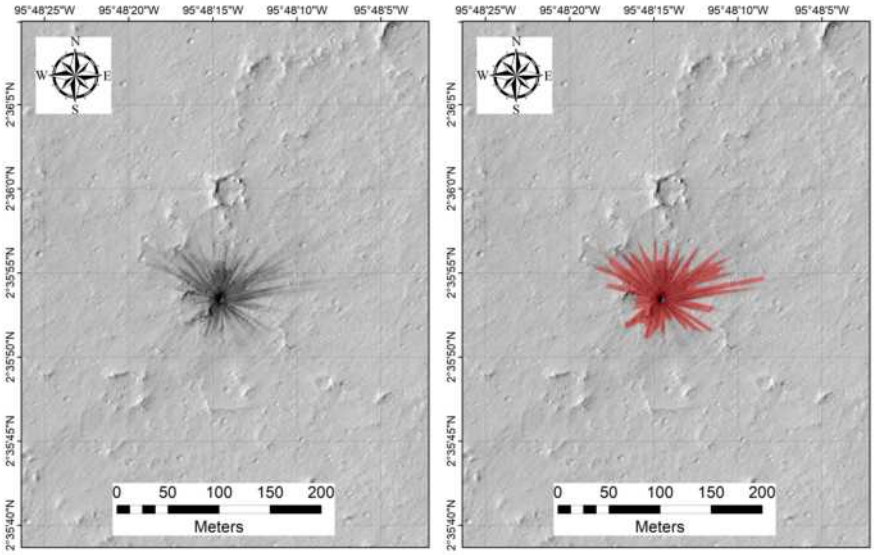

Latitude	Longitude	HiRISE ID	Area (m^2)	Diam.(m)	DCI	TI day	TI night	Epoch
2.598°	264.196°	ESP_016344_1825	5676.7	6.0	0.932	24	20	Amaz./Hesp.

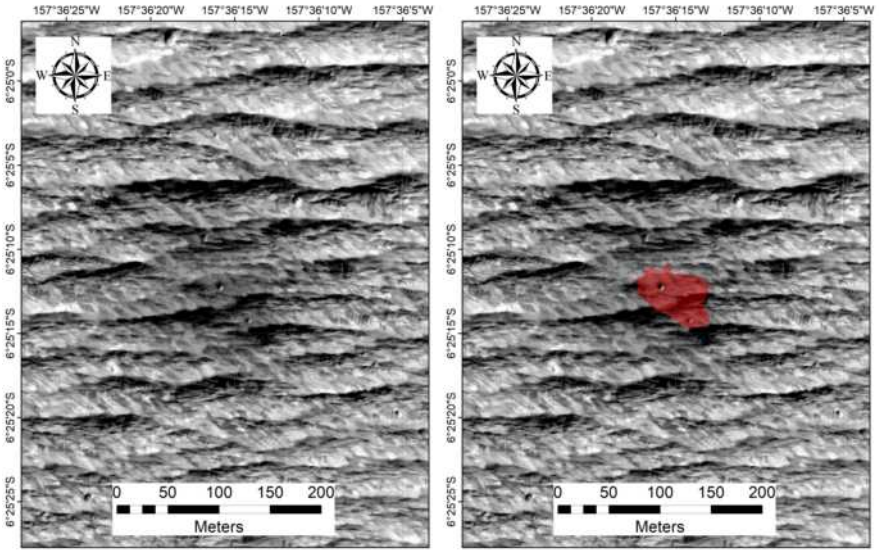

Latitude	Longitude	HiRISE ID	Area (m^2)	Diam.(m)	DCI	TI day	TI night	Epoch
−6.420°	202.396°	ESP_016465_1735	2839.0	5.6	0.937	97	41	Amaz./Hesp.

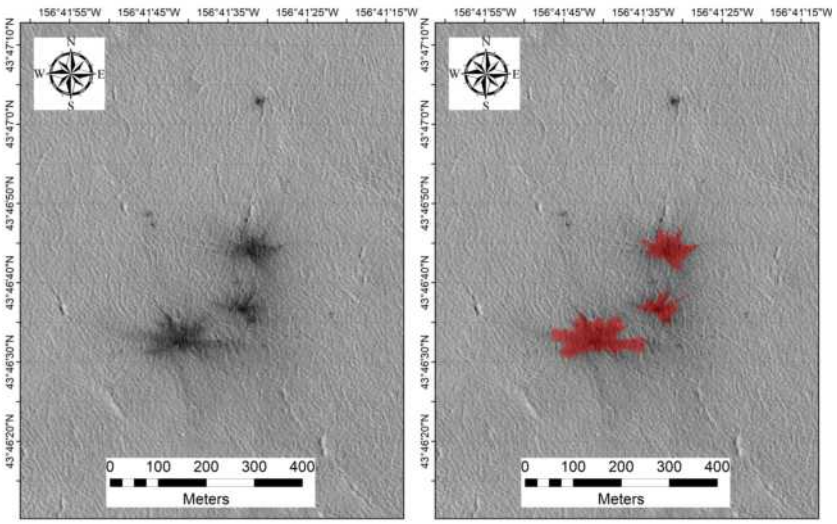

Latitude	Longitude	HiRISE ID	Area (m^2)	Diam.(m)	DCI	TI day	TI night	Epoch
43.778°	203.307°	ESP_016557_2240	9838.0	5.9	0.944	212	202	Amaz./Hesp.
43.778°	203.307°	ESP_016557_2240	4547.4	5.1	0.944	212	202	Amaz./Hesp.
43.778°	203.307°	ESP_016557_2240	2517.2	4.3	0.944	212	202	Amaz./Hesp.

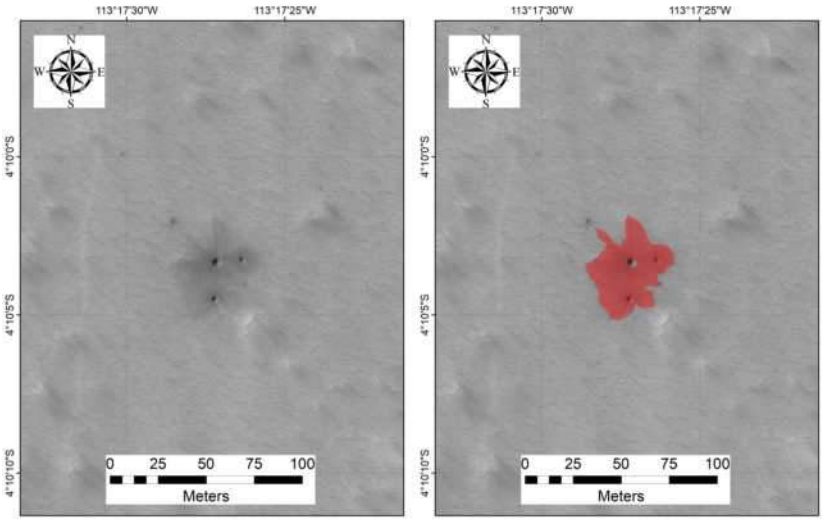

Latitude	Longitude	HiRISE ID	Area (m^2)	Diam.(m)	DCI	TI day	TI night	Epoch
−4.168°	246.709°	ESP_016582_1760	1356.9	4.3	0.937	51	29	Late Amaz.

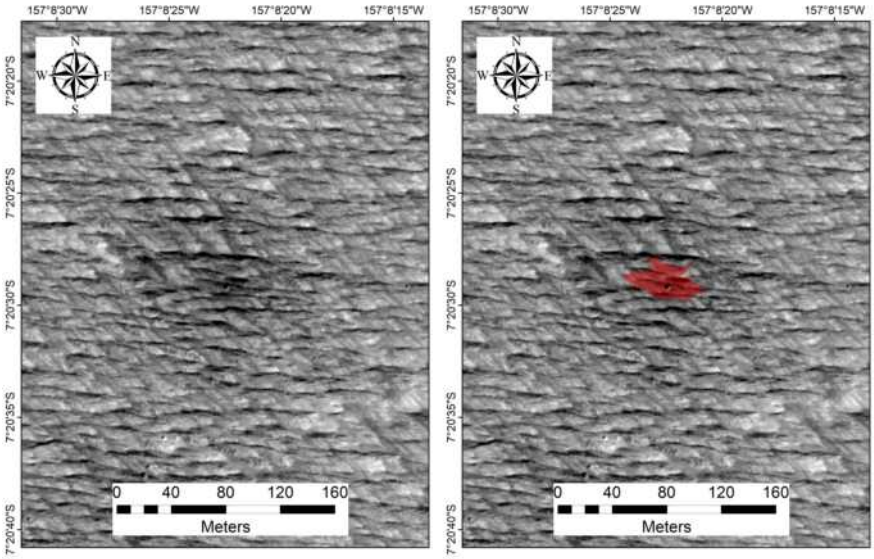

Latitude	Longitude	HiRISE ID	Area (m^2)	Diam.(m)	DCI	TI day	TI night	Epoch
−7.343°	202.860°	ESP_016610_1725	1000.0	3.7	0.945	33	57	Middle Noach.

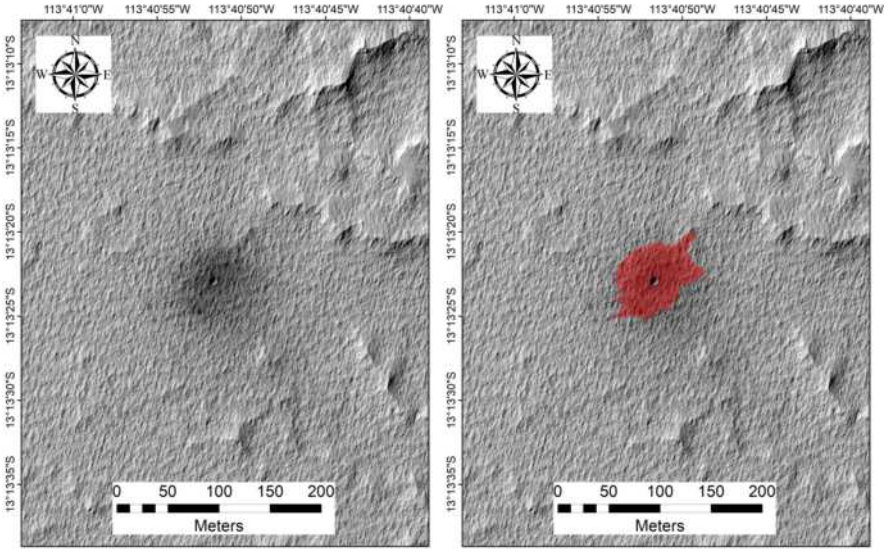

Latitude	Longitude	HiRISE ID	Area (m^2)	Diam.(m)	DCI	TI day	TI night	Epoch
−13.223°	246.319°	ESP_016648_1665	4398.9	8.2	0.951	45	66	Amaz./Hesp.

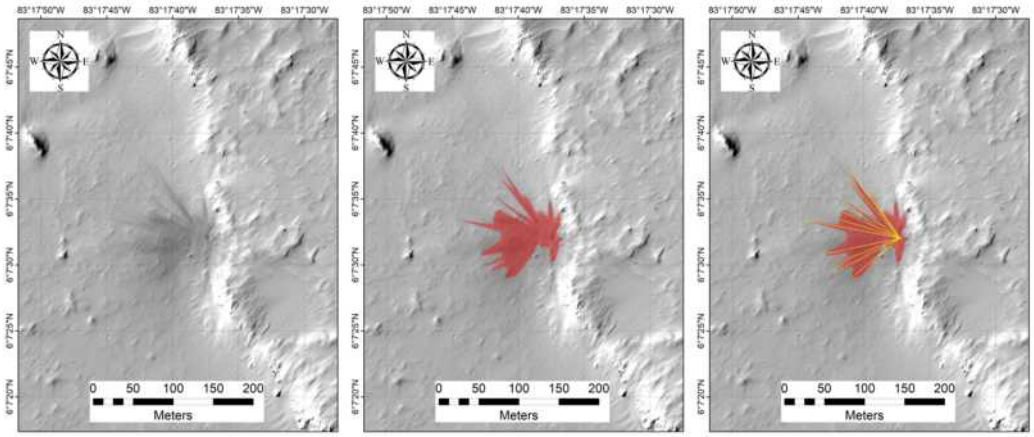

Latitude	Longitude	HiRISE ID	Area (m^2)	Diam.(m)	DCI	TI day	TI night	Epoch	Azimuth
6.126°	276.706°	ESP_016660_1860	5448.4	3.0	0.934	95	51	Amaz./Hesp.	283.1

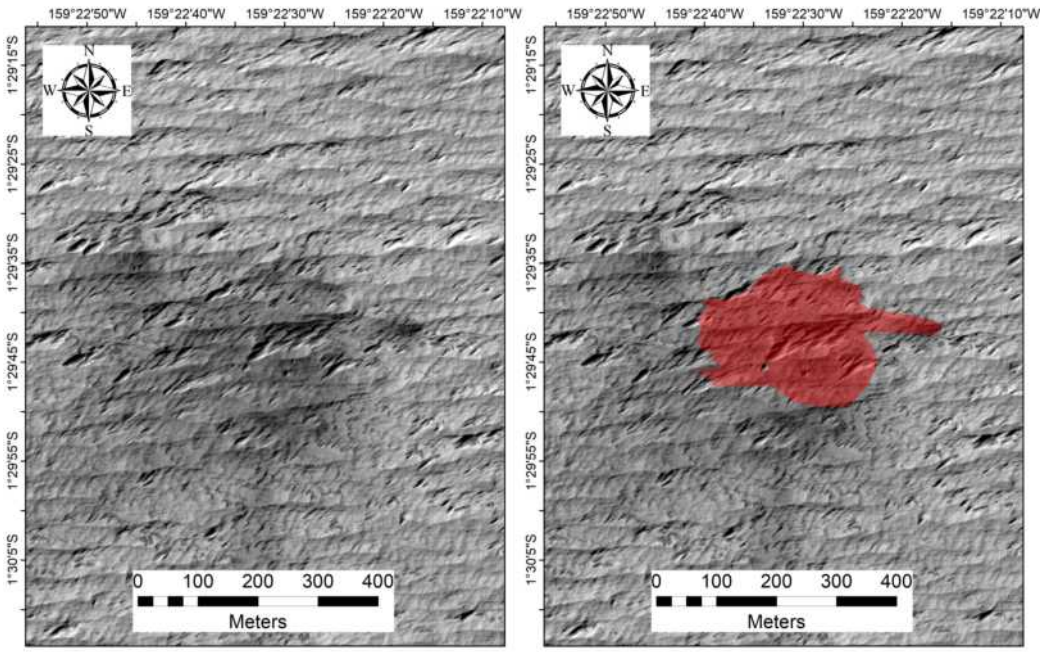

Latitude	Longitude	HiRISE ID	Area (m^2)	Diam.(m)	DCI	TI day	TI night	Epoch
−1.496°	200.624°	ESP_016676_1785	54458.5	9.8	0.943	19	77	Amaz./Hesp.

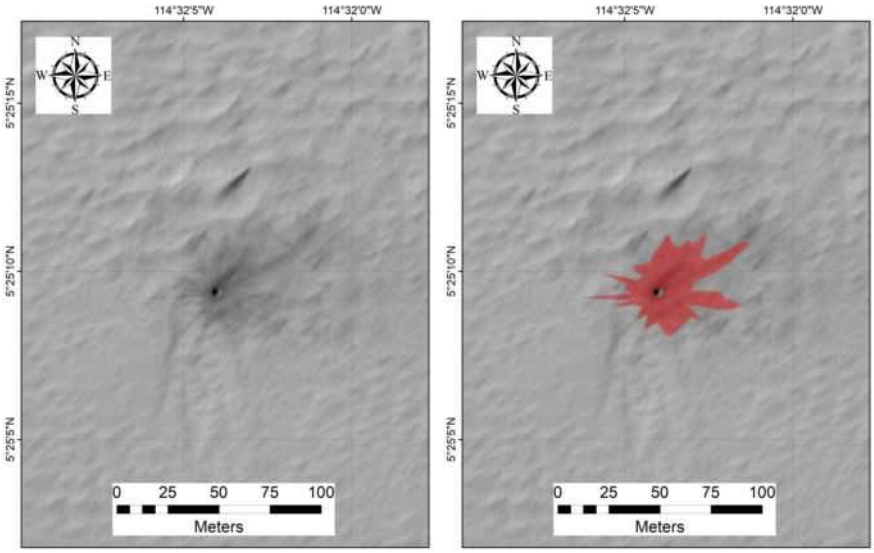

Latitude	Longitude	HiRISE ID	Area (m^2)	Diam.(m)	DCI	TI day	TI night	Epoch
5.419°	245.466°	ESP_016793_1855	1508.5	4.3	0.934	51	59	Late Amaz.

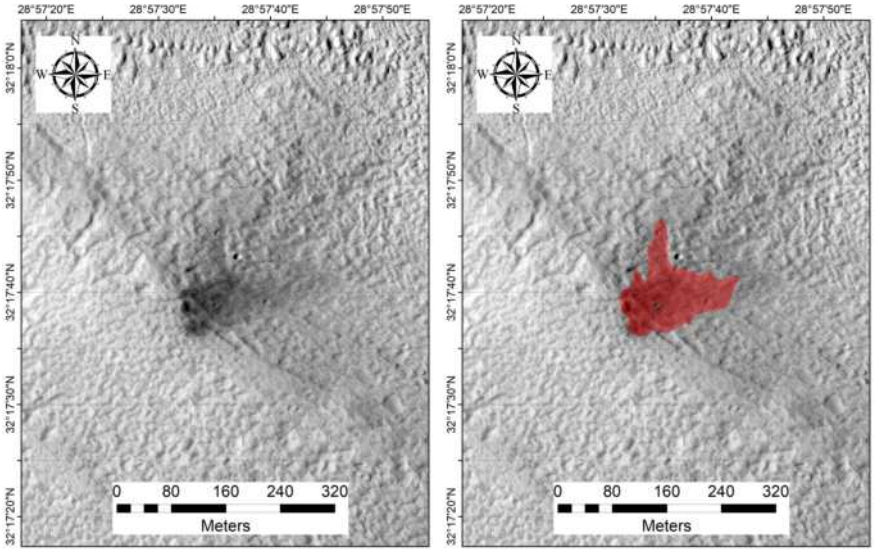

Latitude	Longitude	HiRISE ID	Area (m^2)	Diam.(m)	DCI	TI day	TI night	Epoch
32.294°	28.959°	ESP_016814_2125	13338.4	8.7	0.924	52	71	Middle Noach.

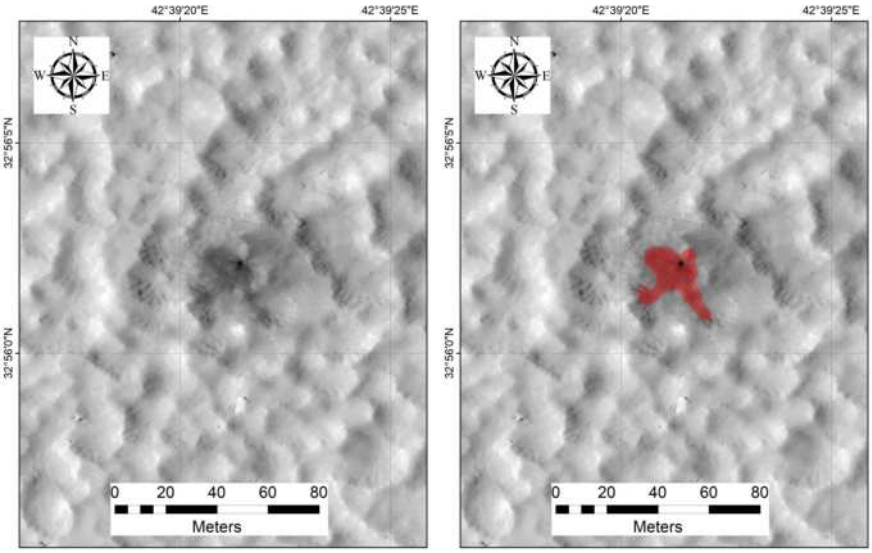

Latitude	Longitude	HiRISE ID	Area (m^2)	Diam.(m)	DCI	TI day	TI night	Epoch
32.934°	42.656°	ESP_016919_2130	407.0	2.2	0.917	72	55	Middle Noach.

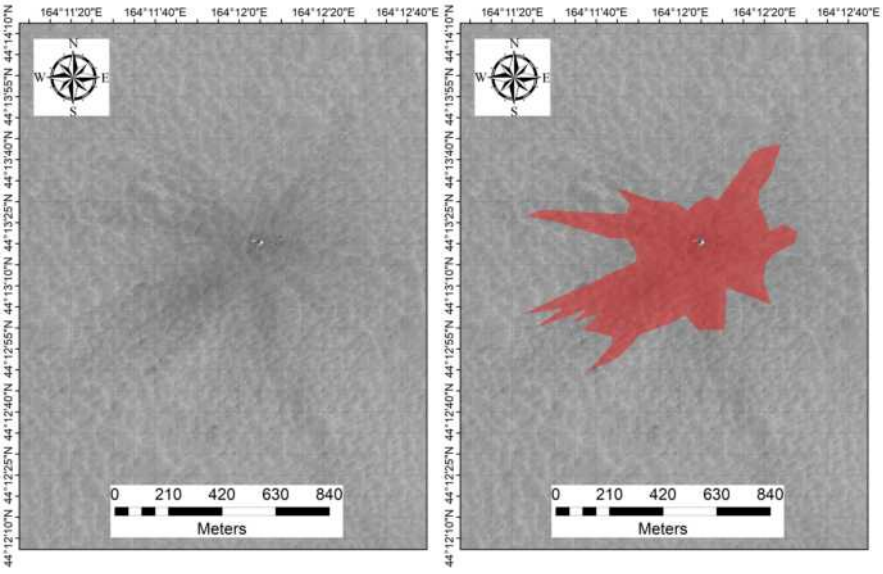

Latitude	Longitude	HiRISE ID	Area (m^2)	Diam.(m)	DCI	TI day	TI night	Epoch
44.222°	164.201°	ESP_016954_2245	362943.1	26.8	0.945	131	145	Early Hesp.

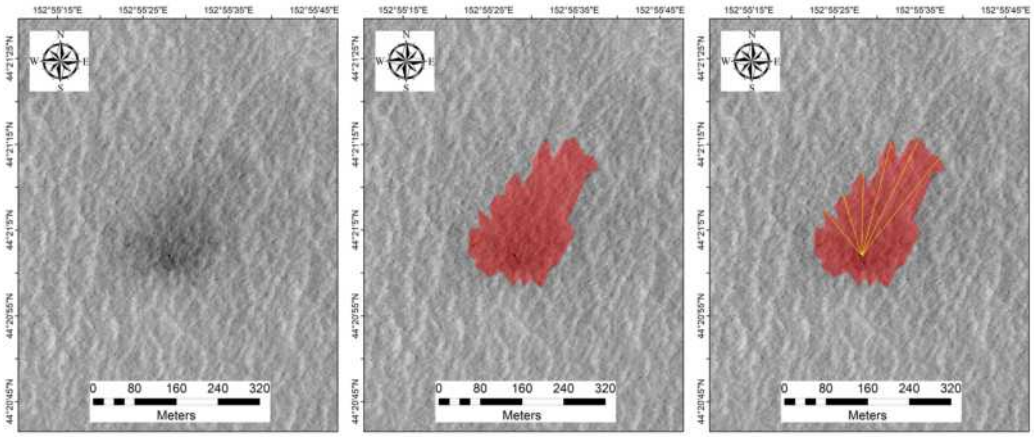

Latitude	Longitude	HiRISE ID	Area (m^2)	Diam.(m)	DCI	TI day	TI night	Epoch	Azimuth
44.350°	152.925°	ESP_016994_2245	38366.9	6.5	0.924	157	189	Late Hesp.	11.5

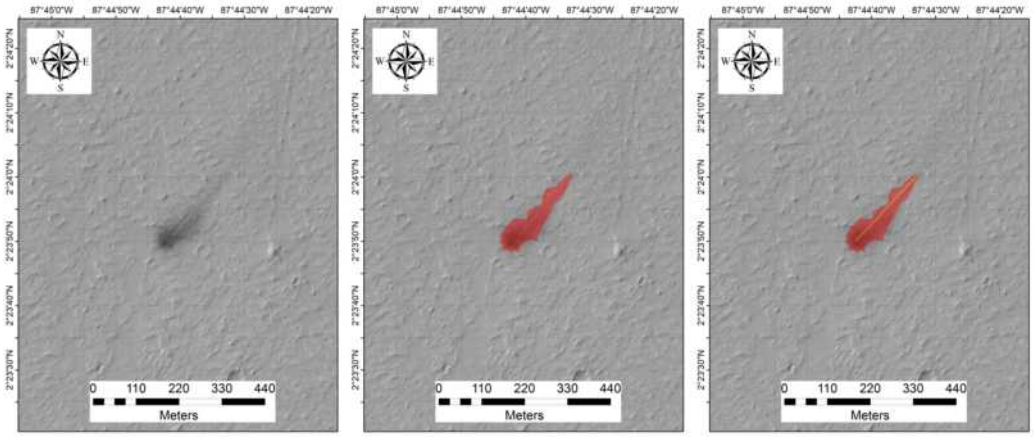

Latitude	Longitude	HiRISE ID	Area (m^2)	Diam.(m)	DCI	TI day	TI night	Epoch	Azimuth
2.397°	272.255°	ESP_017003_1825	10945.4	4.3	0.939	101	79	Amaz./Hesp.	43.2

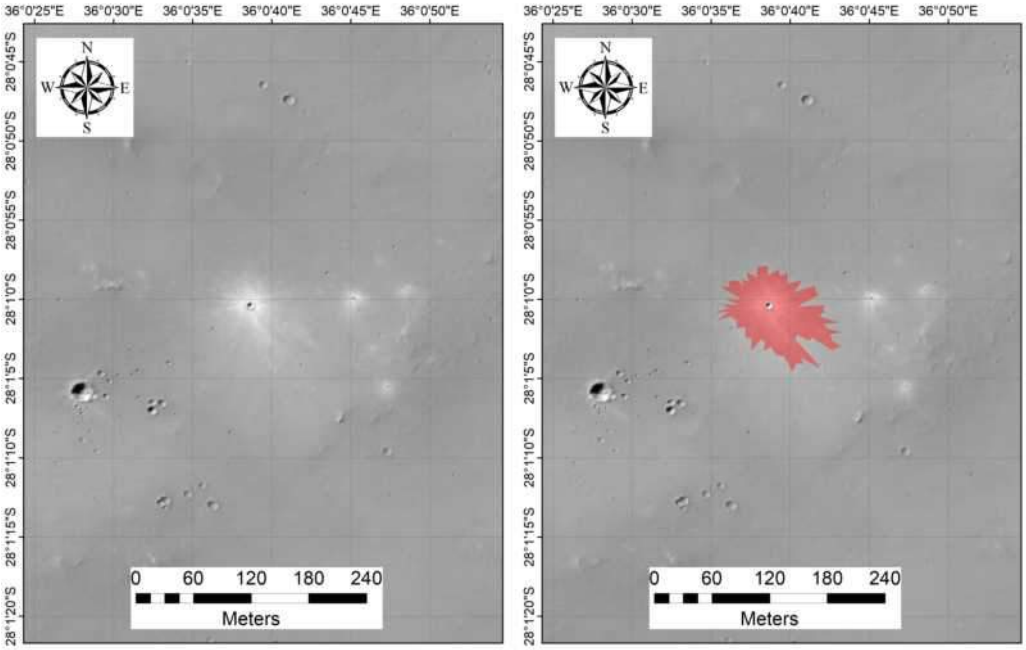

Latitude	Longitude	HiRISE ID	Area (m^2)	Diam.(m)	DCI	TI day	TI night	Epoch
−28.017°	36.011°	ESP_017025_1515	6726.1	7.4	0.976	125	213	Middle Noach.

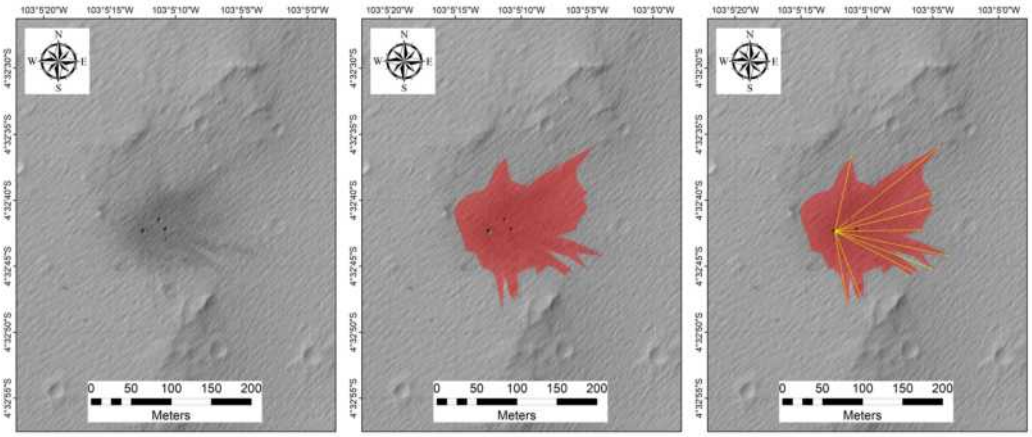

Latitude	Longitude	HiRISE ID	Area (m^2)	Diam.(m)	DCI	TI day	TI night	Epoch	Azimuth
−4.545°	256.913°	ESP_017030_1755	17336.9	6.4	0.941	88	162	Late Hesp.	92.4

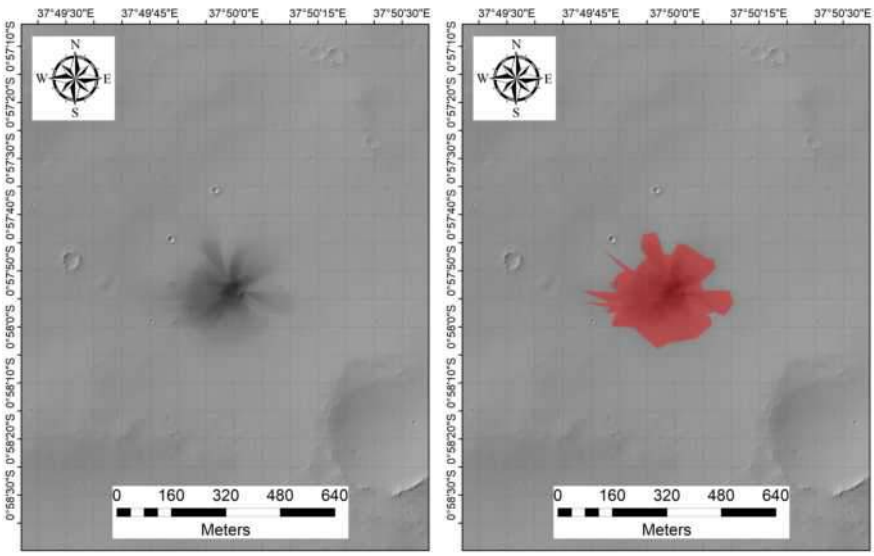

Latitude	Longitude	HiRISE ID	Area (m^2)	Diam.(m)	DCI	TI day	TI night	Epoch
−0.965°	37.833°	ESP_017038_1790	74883.0	4.7	0.937	53	62	Middle Noach.

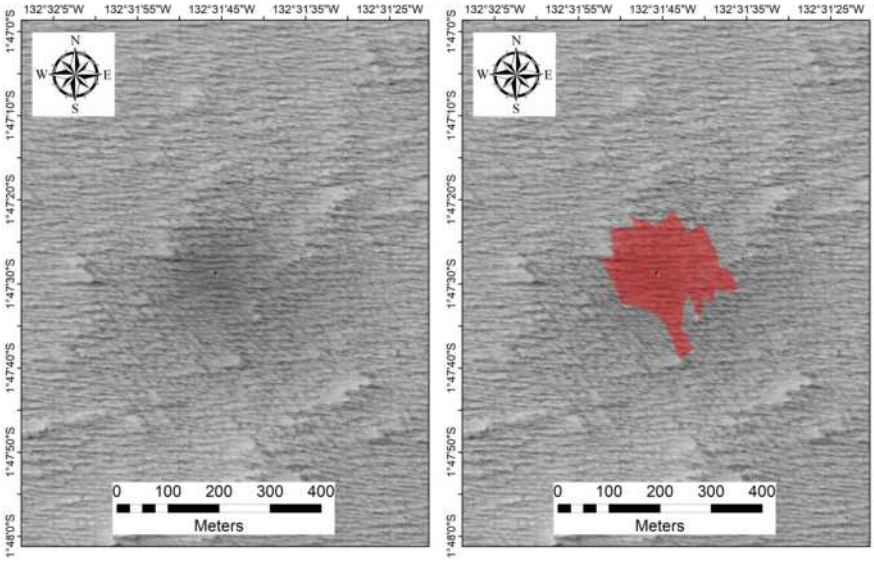

Latitude	Longitude	HiRISE ID	Area (m^2)	Diam.(m)	DCI	TI day	TI night	Epoch
−1.791°	227.471°	ESP_017097_1780	36424.9	8.1	0.930	31	26	Amaz./Hesp.

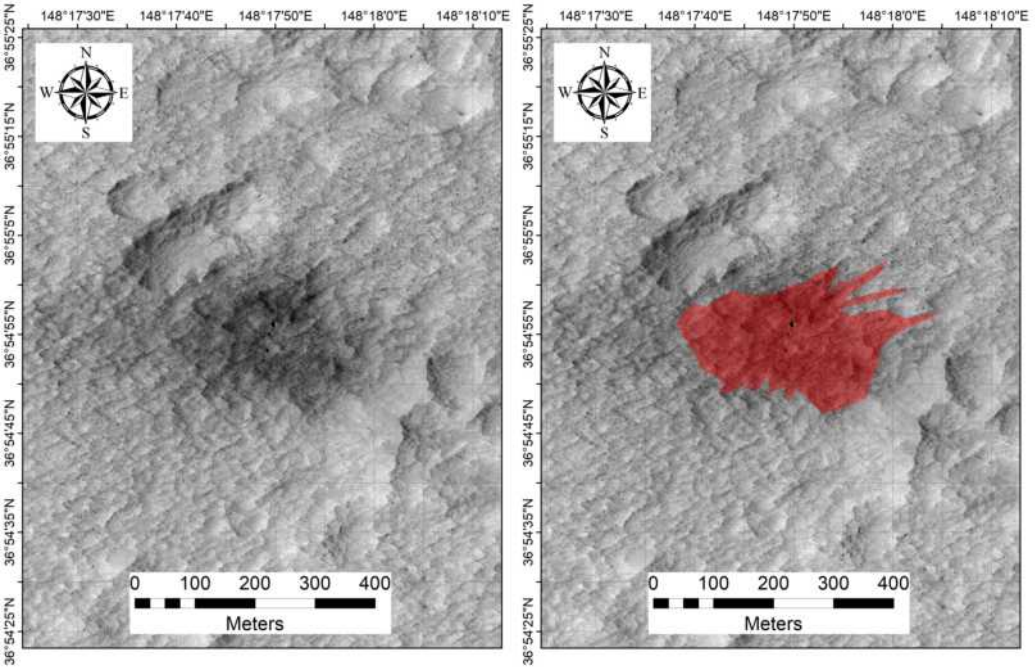

Latitude	Longitude	HiRISE ID	Area (m^2)	Diam.(m)	DCI	TI day	TI night	Epoch
36.915°	148.297°	ESP_017192_2170	55382.9	8.4	0.929	94	101	Late Hesp.

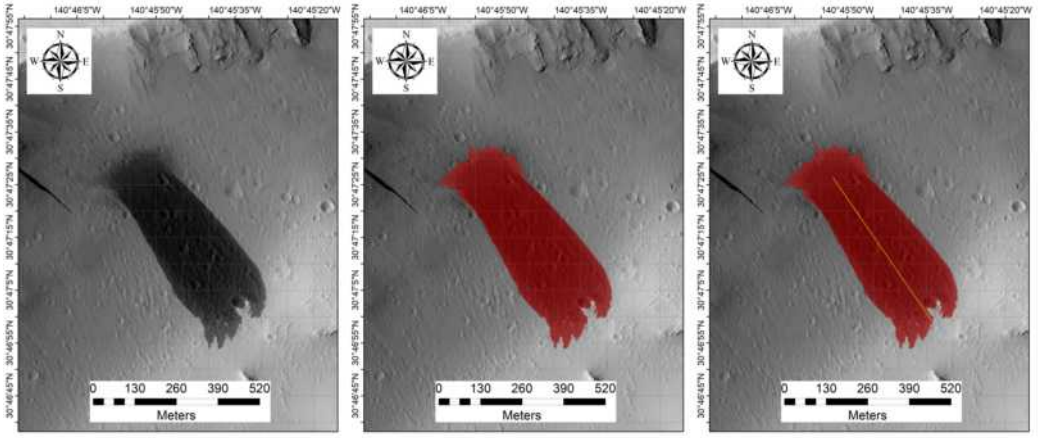

Latitude	Longitude	HiRISE ID	Area (m^2)	Diam.(m)	DCI	TI day	TI night	Epoch	Azimuth
30.791°	219.235°	ESP_017229_2110	139508.9	4.8	0.930	48	34	Amazonian	145.3

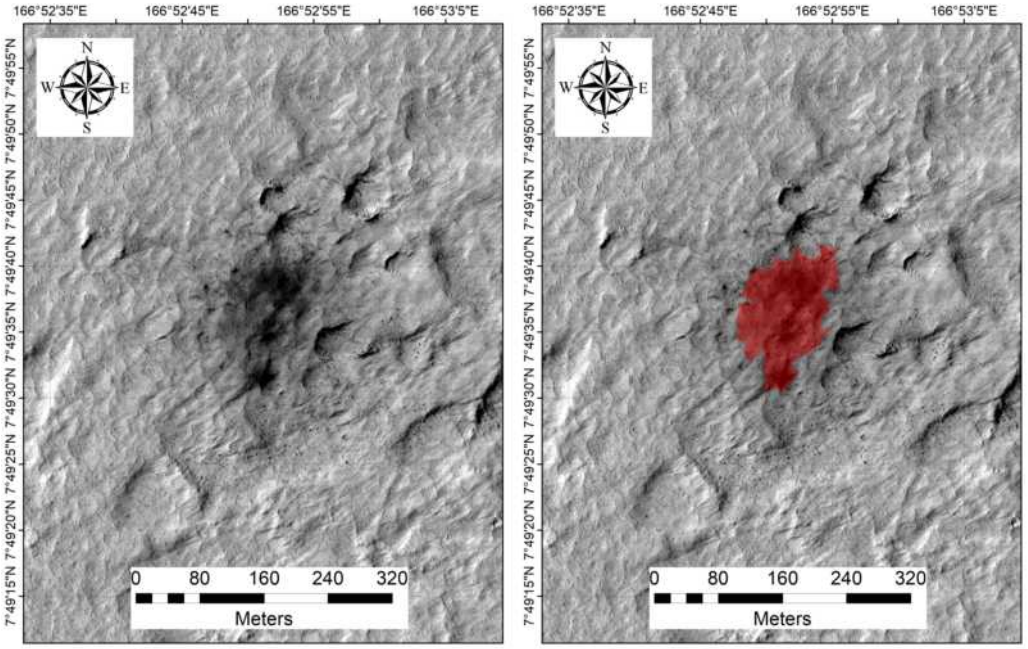

Latitude	Longitude	HiRISE ID	Area (m^2)	Diam.(m)	DCI	TI day	TI night	Epoch
7.827°	166.881°	ESP_017231_1880	14051.9	4.8	0.929	115	91	Late Amaz.

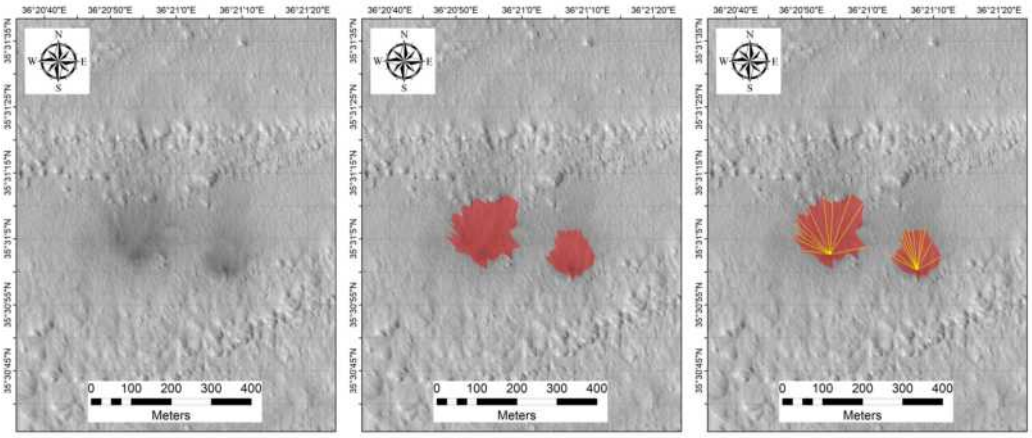

Latitude	Longitude	HiRISE ID	Area (m^2)	Diam.(m)	DCI	TI day	TI night	Epoch	Azimuth
35.517°	36.348°	ESP_017262_2160	21276.5	6.5	0.918	62	78	Middle Noach.	345.7
35.517°	36.348°	ESP_017262_2160	9677.5	3.8	0.918	62	78	Middle Noach.	350.4

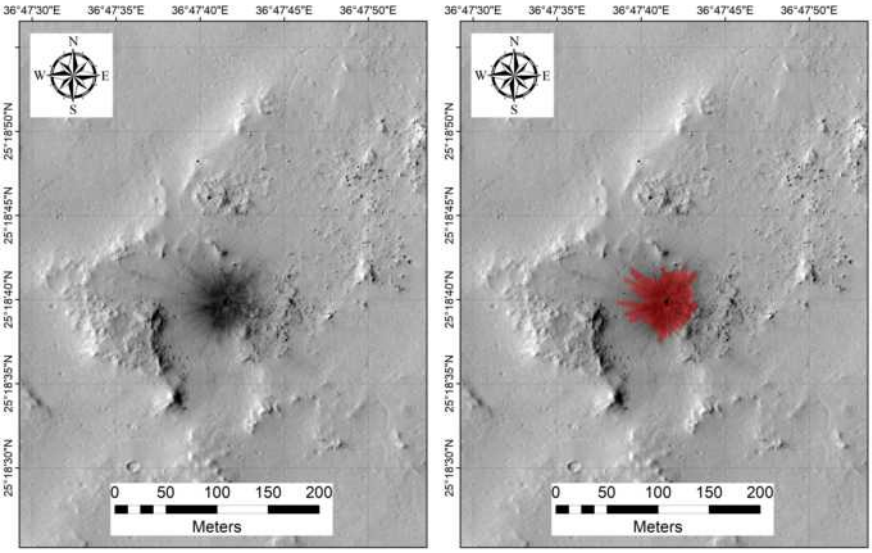

Latitude	Longitude	HiRISE ID	Area (m^2)	Diam.(m)	DCI	TI day	TI night	Epoch
25.311°	36.795°	ESP_017328_2055	3212.5	4.6	0.925	30	32	Middle Noach.

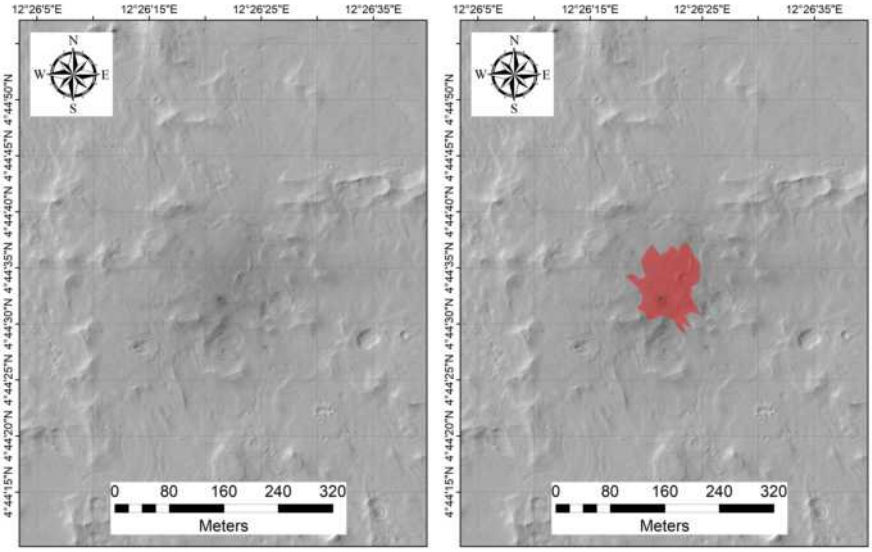

Latitude	Longitude	HiRISE ID	Area (m^2)	Diam.(m)	DCI	TI day	TI night	Epoch
4.742°	12.439°	ESP_017329_1850	8316.0	5.3	0.949	242	151	Hesp./Noach.

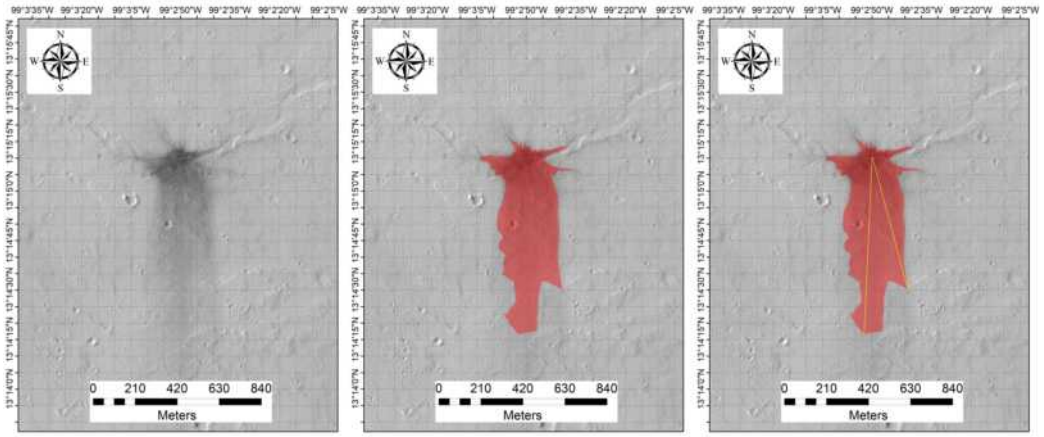

Latitude	Longitude	HiRISE ID	Area (m^2)	Diam.(m)	DCI	TI day	TI night	Epoch	Azimuth
13.243°	260.953°	ESP_017333_1935	220567.8	7.4	0.935	57	73	Amaz./Hesp.	174.8

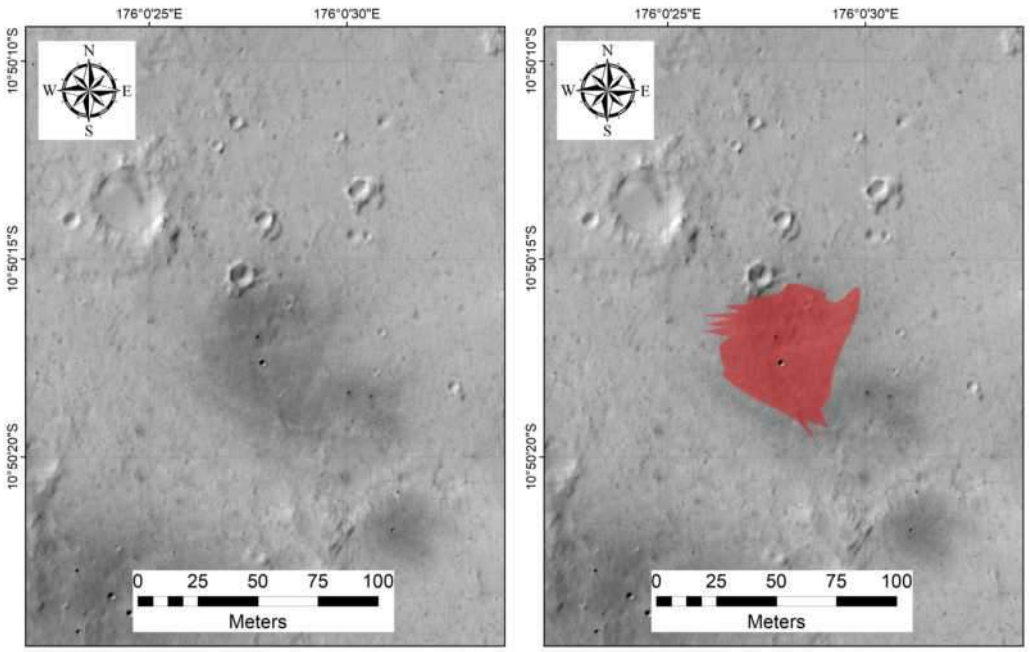

Latitude	Longitude	HiRISE ID	Area (m^2)	Diam.(m)	DCI	TI day	TI night	Epoch
−10.839°	176.007°	ESP_017389_1690	2294.0	2.6	0.928	96	42	Hesperian

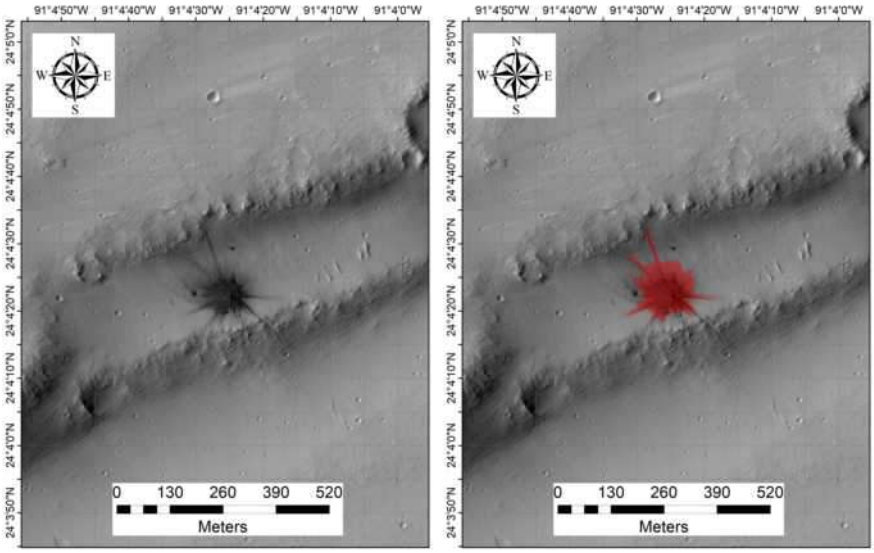

Latitude	Longitude	HiRISE ID	Area (m^2)	Diam.(m)	DCI	TI day	TI night	Epoch
24.073°	268.927°	ESP_017425_2045	17390.1	6.1	0.933	27	84	Early Hesp.

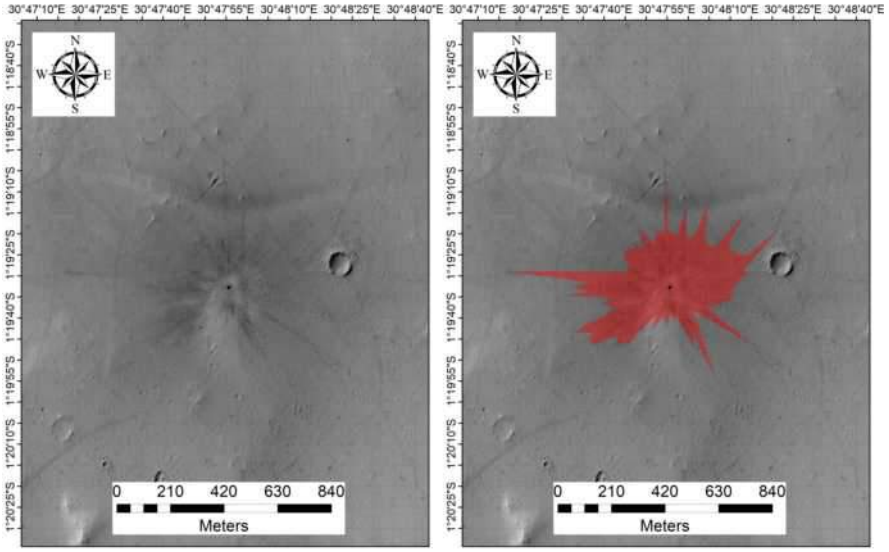

Latitude	Longitude	HiRISE ID	Area (m^2)	Diam.(m)	DCI	TI day	TI night	Epoch
−1.326°	30.799°	ESP_017447_1785	195860.9	16.5	0.951	27	55	Middle Noach.

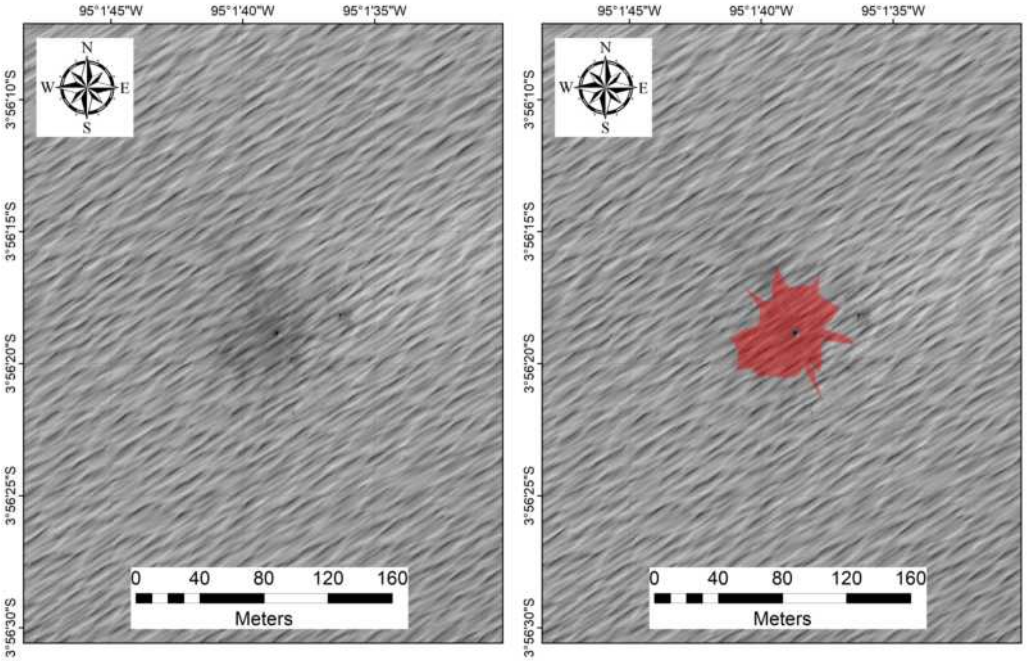

Latitude	Longitude	HiRISE ID	Area (m^2)	Diam.(m)	DCI	TI day	TI night	Epoch
−3.938°	264.973°	ESP_017478_1760	2752.2	4.7	0.939	100	18	Late Hesp.

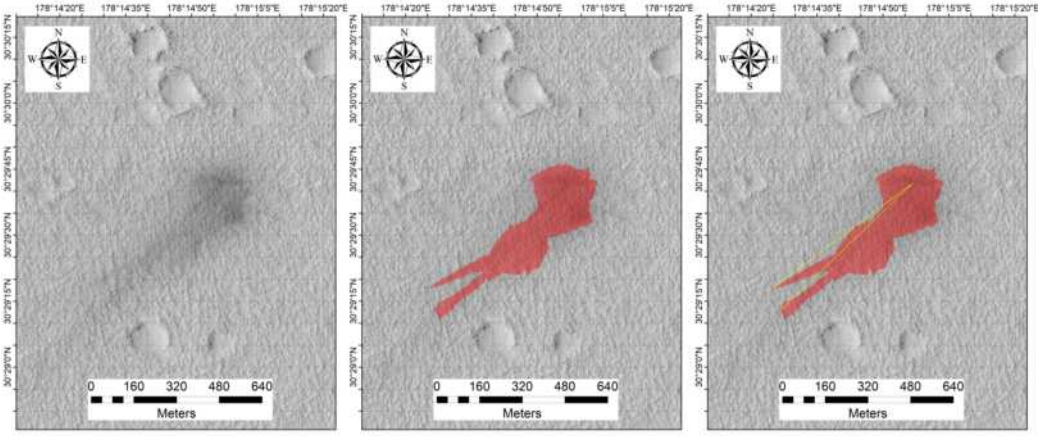

Latitude	Longitude	HiRISE ID	Area (m^2)	Diam.(m)	DCI	TI day	TI night	Epoch	Azimuth
30.494°	178.249°	ESP_017481_2110	100804.9	9.4	0.949	47	22	Early Hesp.	229.6

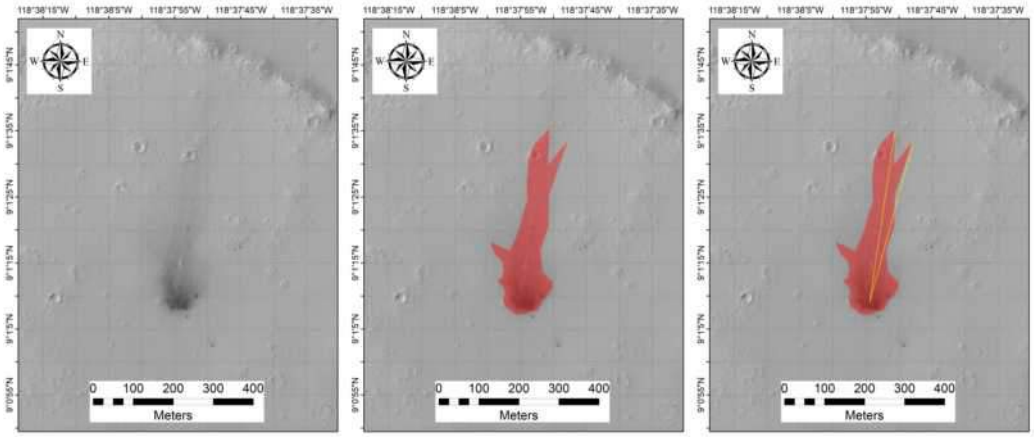

Latitude	Longitude	HiRISE ID	Area (m^2)	Diam.(m)	DCI	TI day	TI night	Epoch	Azimuth
9.019°	241.368°	ESP_017492_1890	34504.8	4.1	0.941	20	89	Early Hesp.	11.7

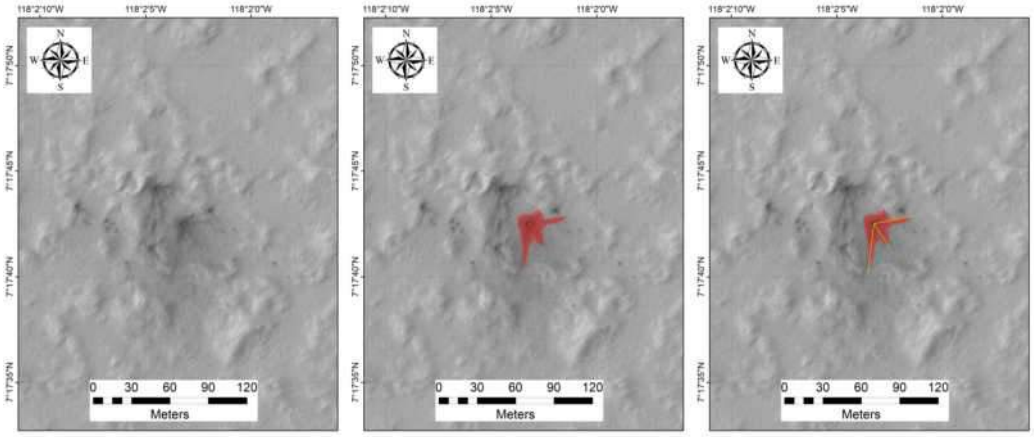

Latitude	Longitude	HiRISE ID	Area (m^2)	Diam.(m)	DCI	TI day	TI night	Epoch	Azimuth
7.295°	241.965°	ESP_017637_1875	543.5	3.2	0.941	35	79	Amaz./Hesp.	139.9

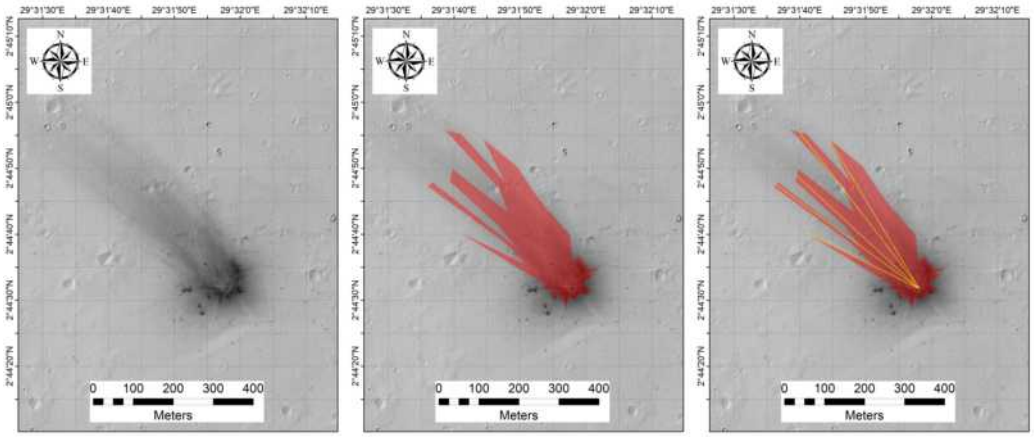

Latitude	Longitude	HiRISE ID	Area (m^2)	Diam.(m)	DCI	TI day	TI night	Epoch	Azimuth
2.742°	29.533°	ESP_017658_1830	53537.9	5.0	0.939	51	88	Amaz./Hesp.	314.4

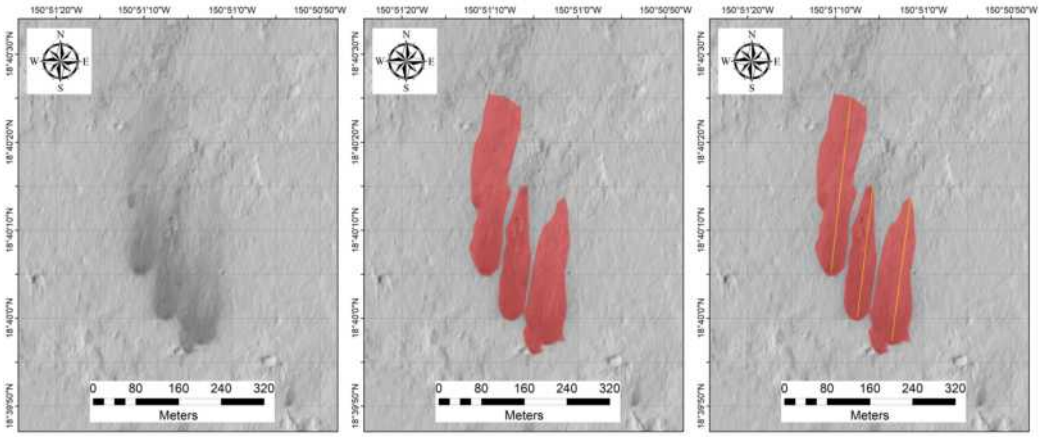

Latitude	Longitude	HiRISE ID	Area (m^2)	Diam.(m)	DCI	TI day	TI night	Epoch	Azimuth
18.667°	209.148°	ESP_017770_1990	20887.7	3.0	0.908	50	82	Late Amaz.	6.5
18.667°	209.148°	ESP_017770_1990	16092.8	2.5	0.908	50	82	Late Amaz.	7.5
18.667°	209.148°	ESP_017770_1990	10339.5	2.5	0.908	50	82	Late Amaz.	6.8

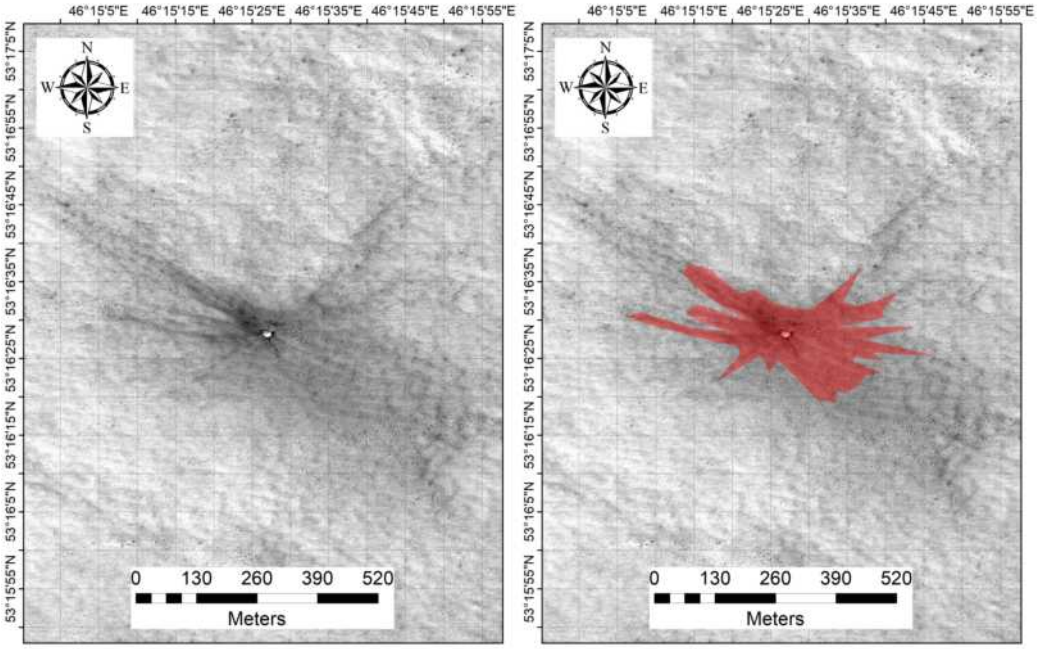

Latitude	Longitude	HiRISE ID	Area (m^2)	Diam.(m)	DCI	TI day	TI night	Epoch
53.274°	46.258°	ESP_017789_2335	66262.5	3.3	0.948	205	191	Middle Amaz.

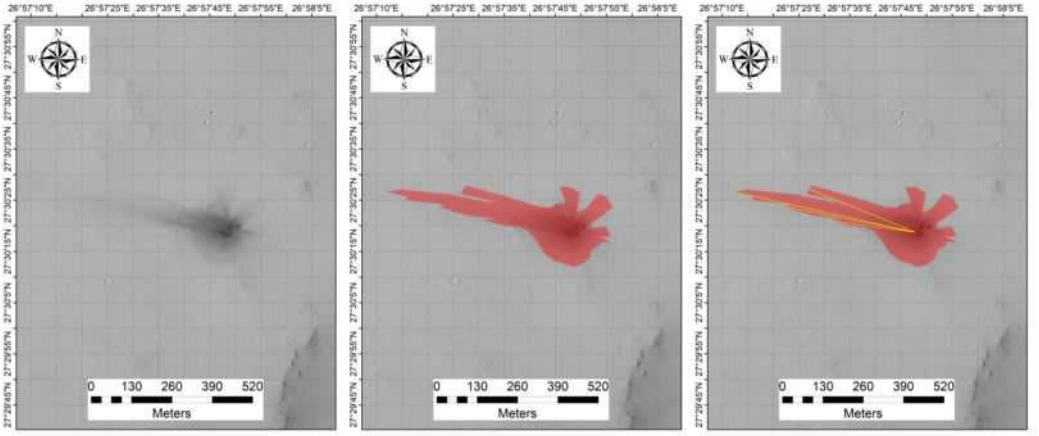

Latitude	Longitude	HiRISE ID	Area (m^2)	Diam.(m)	DCI	TI day	TI night	Epoch	Azimuth
27.505°	26.964°	ESP_017803_2080	68232.0	3.8	0.935	72	64	Middle Noach.	283.5

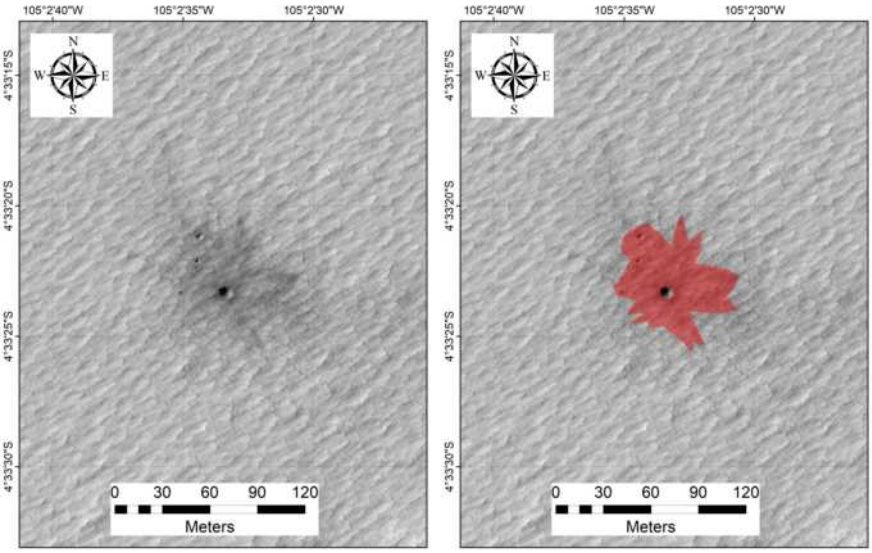

Latitude	Longitude	HiRISE ID	Area (m^2)	Diam.(m)	DCI	TI day	TI night	Epoch
−4.556°	254.957°	ESP_017808_1755	3481.6	7.1	0.945	95	132	Late Hesp.

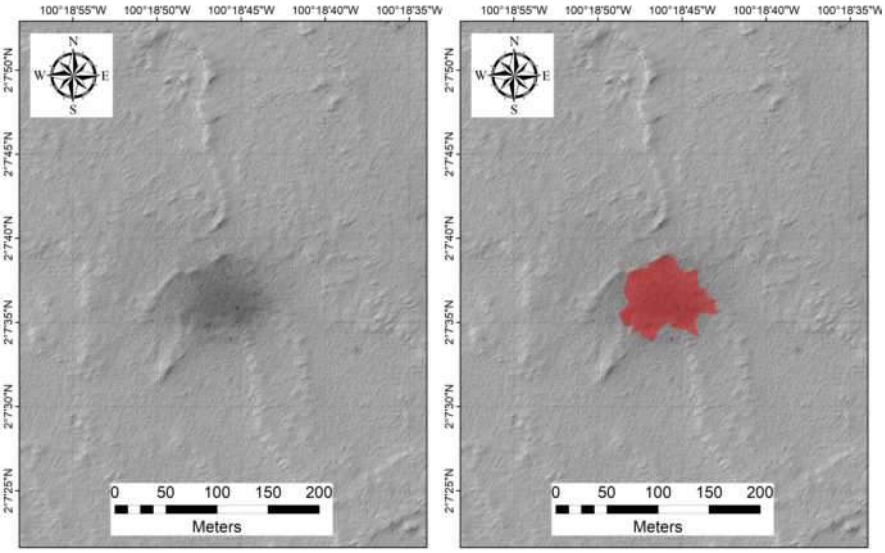

Latitude	Longitude	HiRISE ID	Area (m^2)	Diam.(m)	DCI	TI day	TI night	Epoch
2.127°	259.687°	ESP_017821_1820	4856.9	3.4	0.946	32	153	Amaz./Hesp.

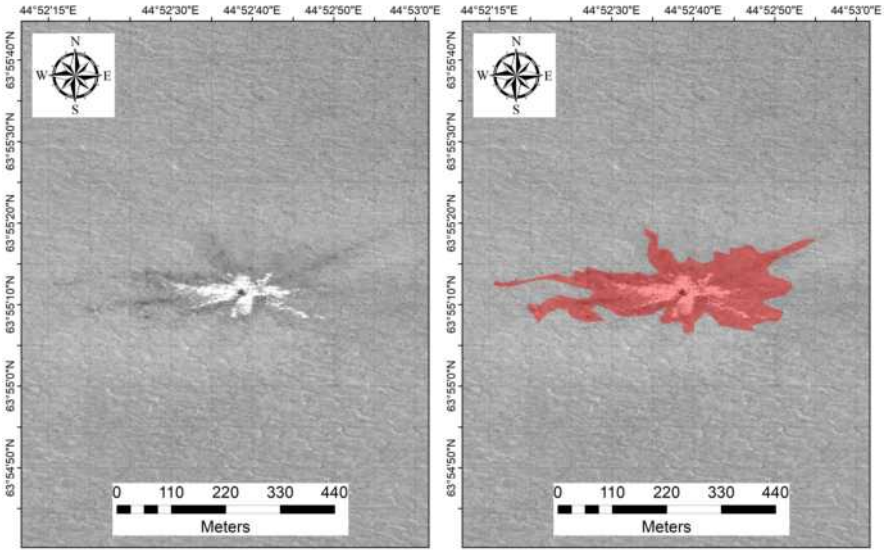

Latitude	Longitude	HiRISE ID	Area (m^2)	Diam.(m)	DCI	TI day	TI night	Epoch
63.919°	44.878°	ESP_017868_2440	54093.5	5.3		364	246	Late Hesp.

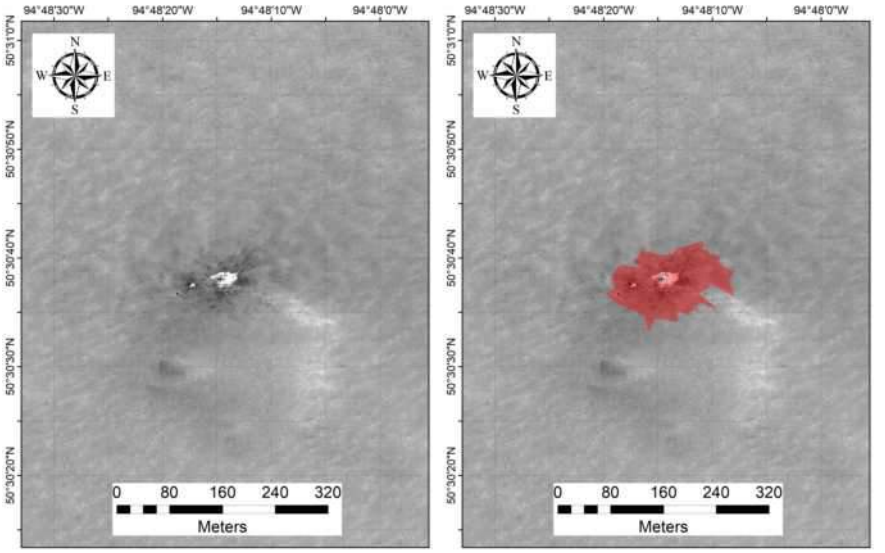

Latitude	Longitude	HiRISE ID	Area (m^2)	Diam.(m)	DCI	TI day	TI night	Epoch
50.51°	265.196°	ESP_017926_2310	14141.4	9.8	0.949	139	135	Amaz./Hesp.

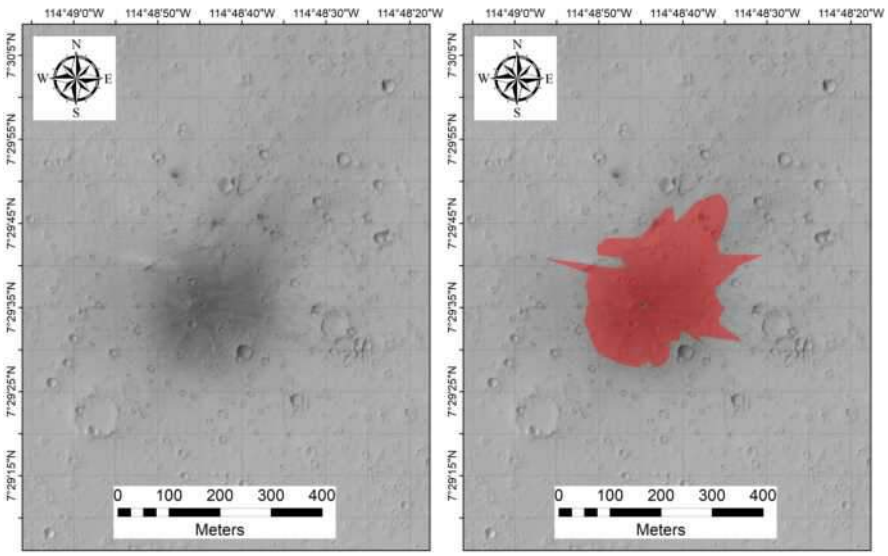

Latitude	Longitude	HiRISE ID	Area (m^2)	Diam.(m)	DCI	TI day	TI night	Epoch
7.493°	245.188°	ESP_017927_1875	66845.5	8.9	0.929	64	19	Amaz./Hesp.

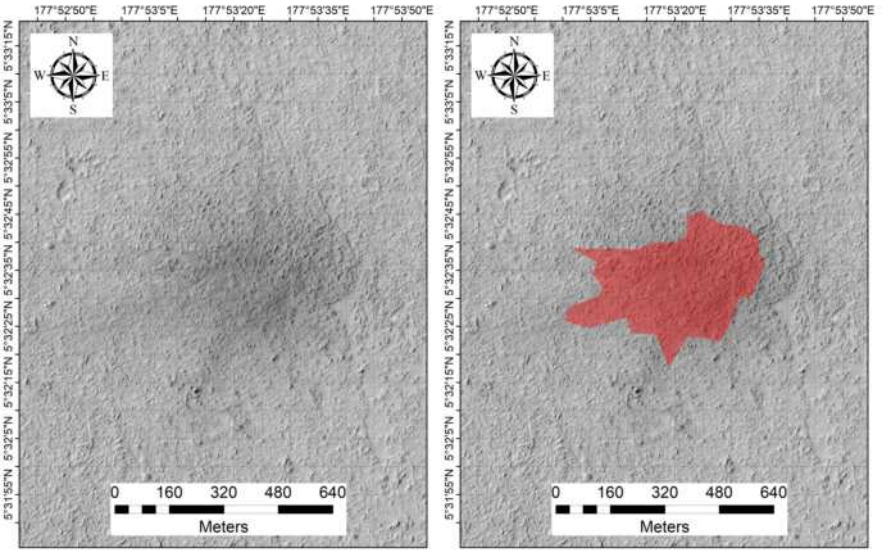

Latitude	Longitude	HiRISE ID	Area (m^2)	Diam.(m)	DCI	TI day	TI night	Epoch
5.543°	177.891°	ESP_017969_1855	138051.3	7.9	0.927	92	54	Late Amaz.

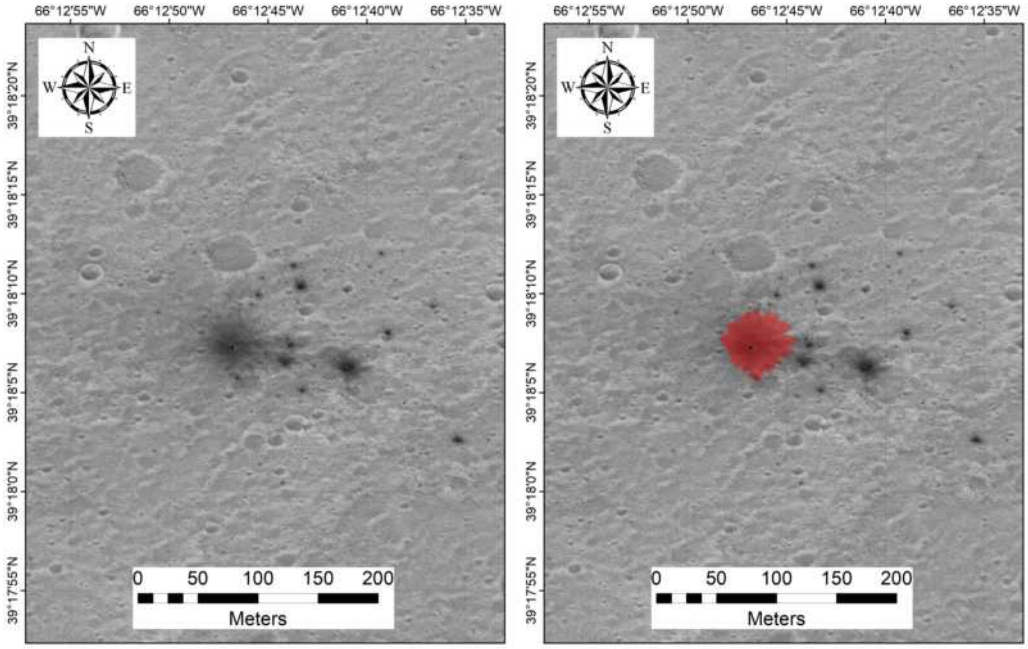

Latitude	Longitude	HiRISE ID	Area (m^2)	Diam.(m)	DCI	TI day	TI night	Epoch
39.302°	293.787°	ESP_017991_2195	2281.7	3.0	0.940	141	177	Amaz./Hesp.

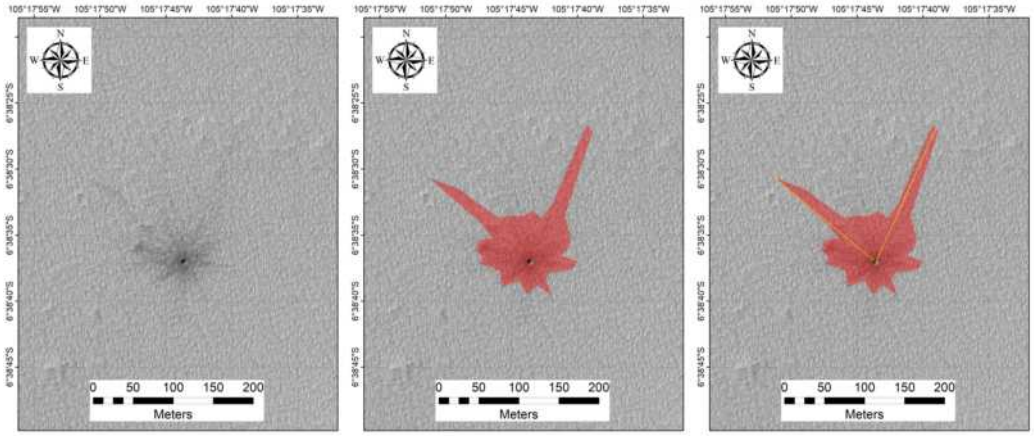

Latitude	Longitude	HiRISE ID	Area (m^2)	Diam.(m)	DCI	TI day	TI night	Epoch	Azimuth
−6.644°	254.705°	ESP_018019_1735	11201.5	7.1	0.969	22	20	Late Hesp.	159.7

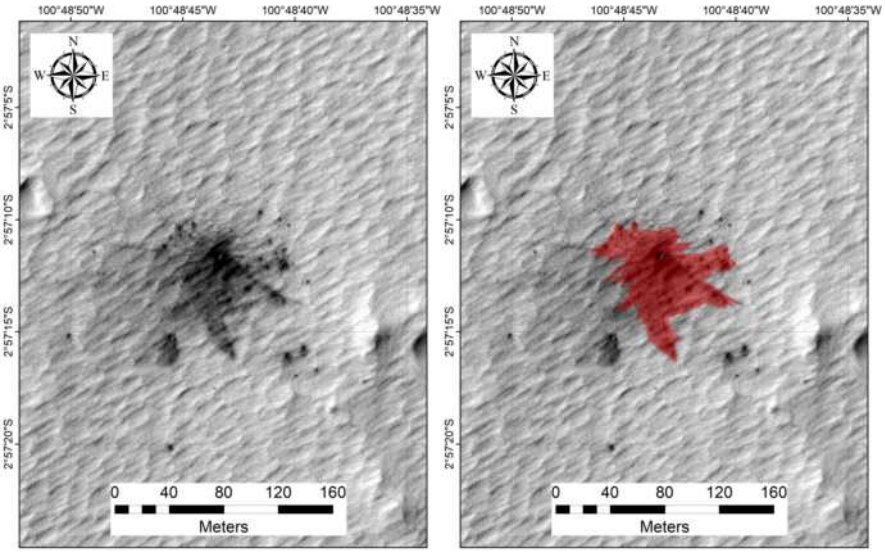

Latitude	Longitude	HiRISE ID	Area (m^2)	Diam.(m)	DCI	TI day	TI night	Epoch
−2.953°	259.188°	ESP_018032_1770	4851.9	4.3	0.933	31	53	Late Hesp.

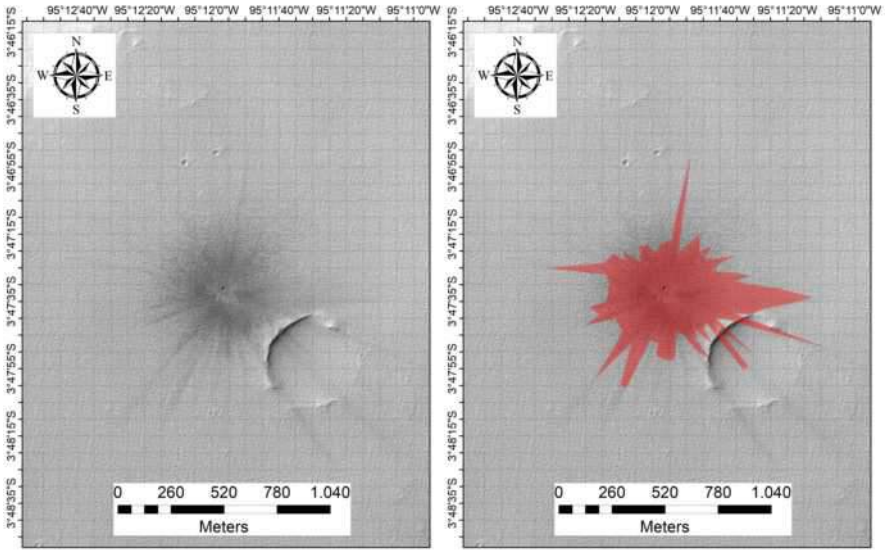

Latitude	Longitude	HiRISE ID	Area (m^2)	Diam.(m)	DCI	TI day	TI night	Epoch
−3.792°	264.801°	ESP_018045_1760	352881.5	16.1	0.933	39	64	Late Hesp.

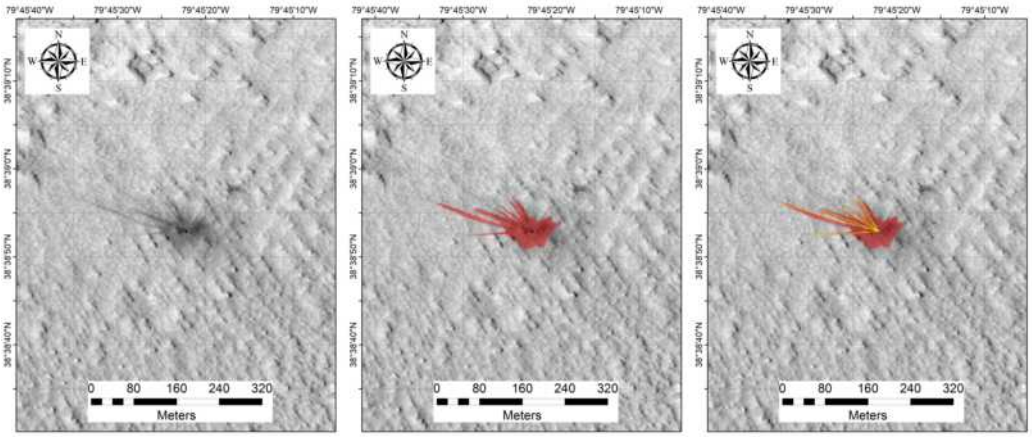

Latitude	Longitude	HiRISE ID	Area (m^2)	Diam.(m)	DCI	TI day	TI night	Epoch	Azimuth
38.648°	280.244°	ESP_018097_2190	6631.9	6.7	0.934	32	55	Early Hesp.	295.8

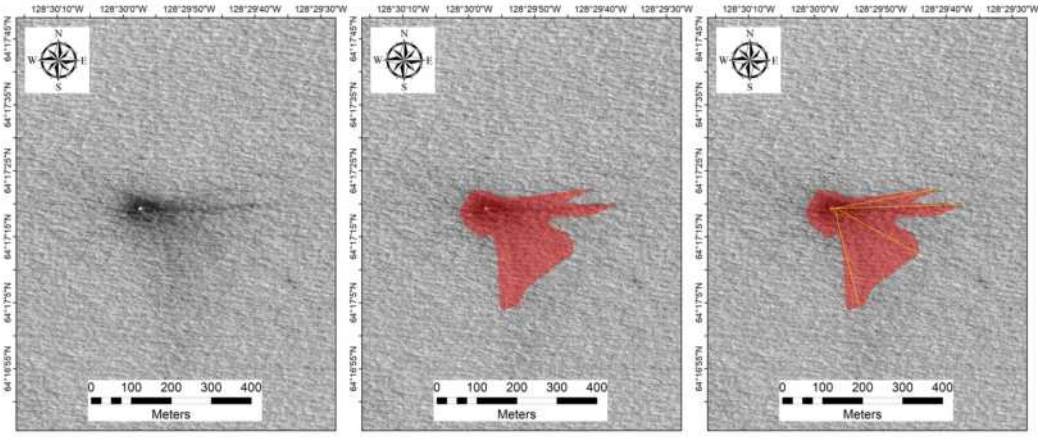

Latitude	Longitude	HiRISE ID	Area (m^2)	Diam.(m)	DCI	TI day	TI night	Epoch	Azimuth
64.288°	231.501°	ESP_018125_2445	50713.5	4.4		321	167	Late Hesp.	110.8

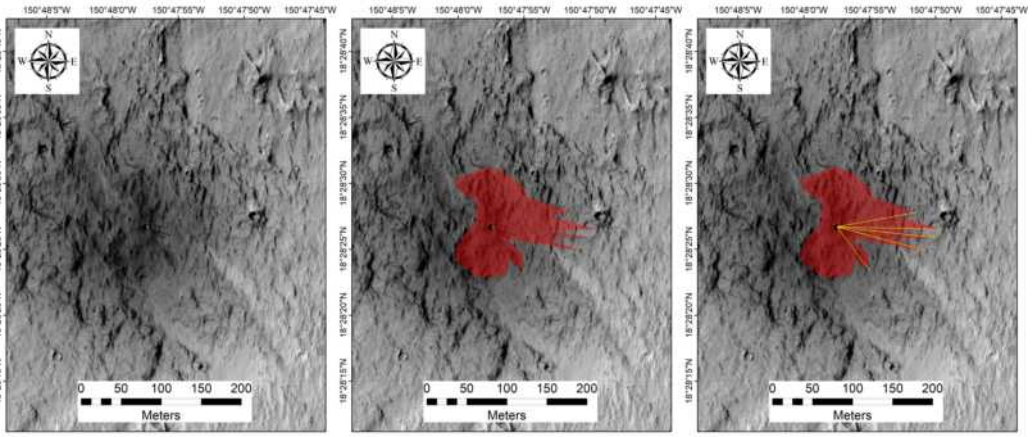

Latitude	Longitude	HiRISE ID	Area (m^2)	Diam.(m)	DCI	TI day	TI night	Epoch	Azimuth
18.474°	209.201°	ESP_018192_1985	11615.2	6.6	0.917	51	43	Late Amaz.	99.6

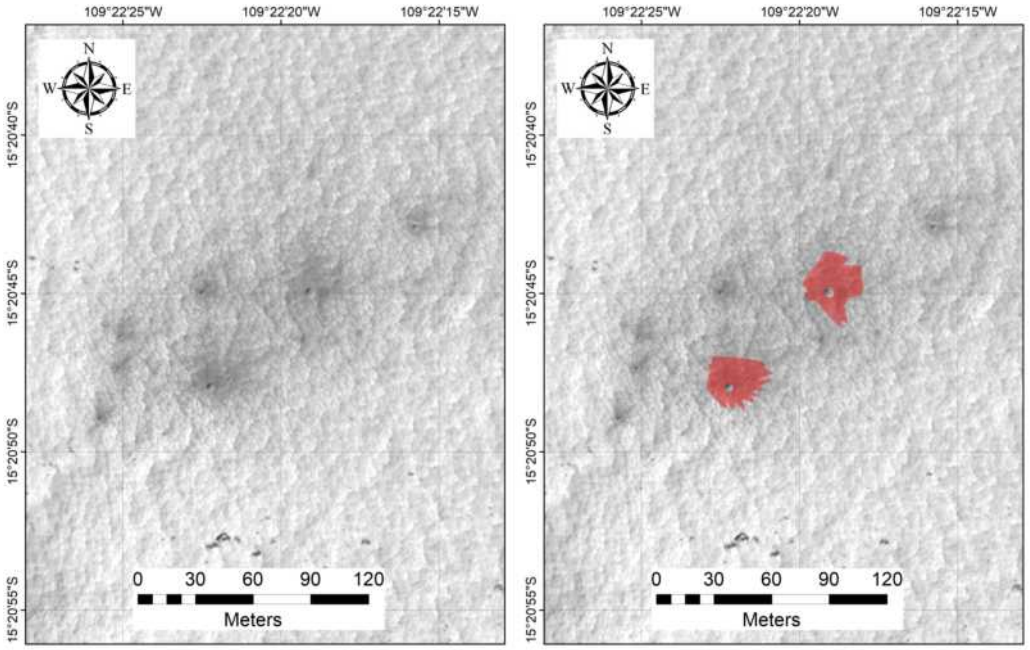

Latitude	Longitude	HiRISE ID	Area (m^2)	Diam.(m)	DCI	TI day	TI night	Epoch
−15.346°	250.627°	ESP_018217_1645	694.2	5.1	0.960	84	120	Late Noachian
−15.346°	250.627°	ESP_018217_1645	628.7	4.2	0.960	84	120	Late Noachian

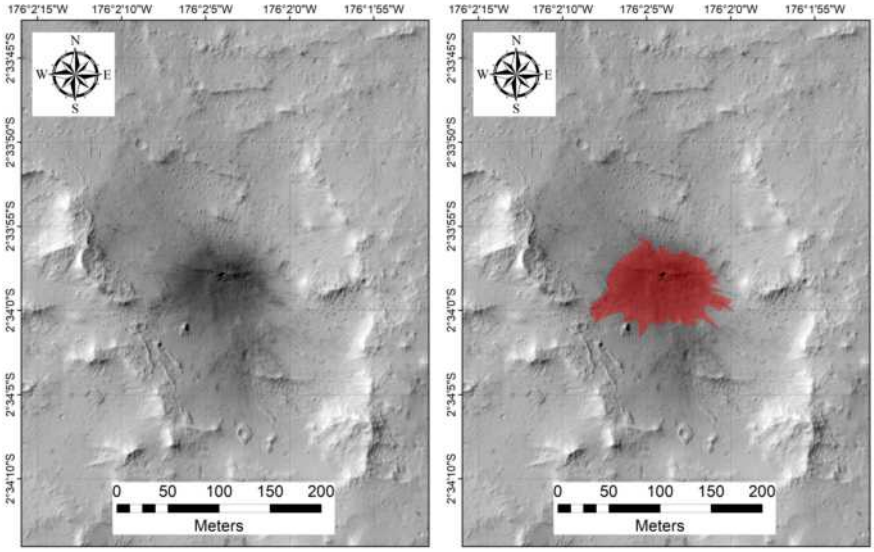

Latitude	Longitude	HiRISE ID	Area (m^2)	Diam.(m)	DCI	TI day	TI night	Epoch
−2.566°	183.966°	ESP_018404_1775	7264.5	4.9	0.932	27	26	Hesperian

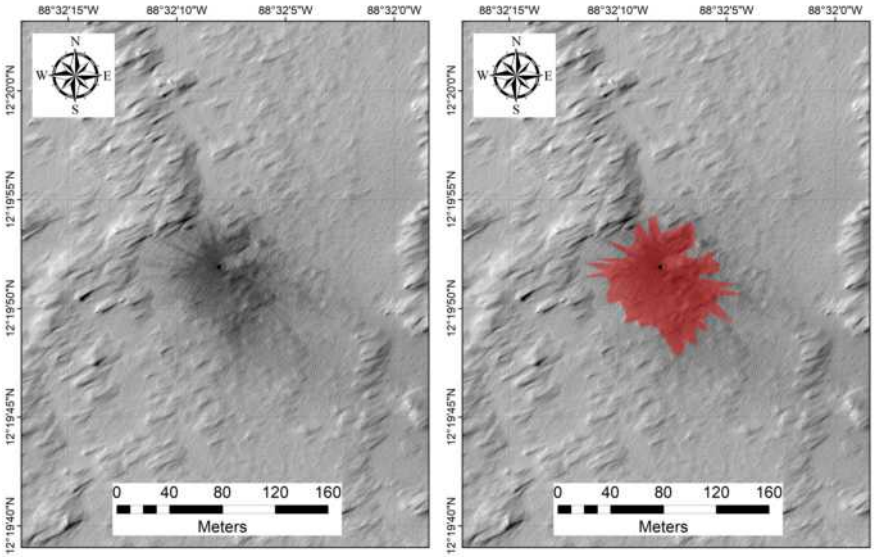

Latitude	Longitude	HiRISE ID	Area (m^2)	Diam.(m)	DCI	TI day	TI night	Epoch
12.331°	271.464°	ESP_018493_1925	5641.2	3.6	0.919	43	70	Amaz./Hesp.

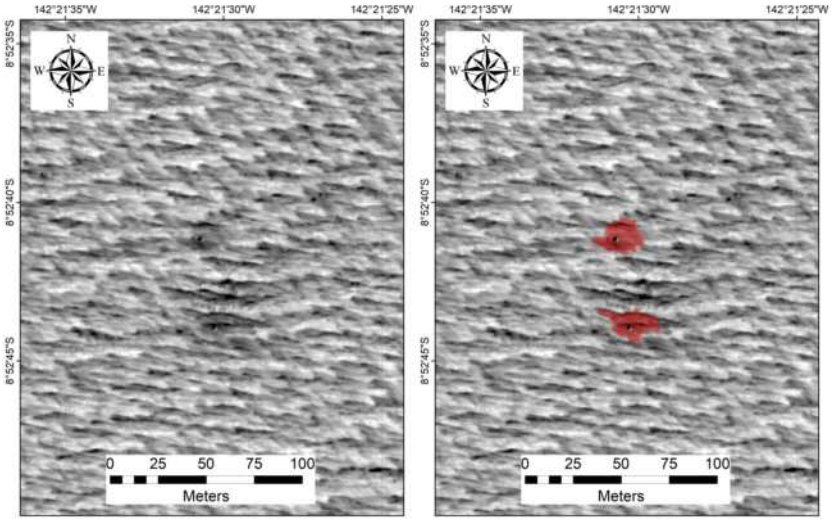

Latitude	Longitude	HiRISE ID	Area (m^2)	Diam.(m)	DCI	TI day	TI night	Epoch
−8.878°	217.642°	ESP_018561_1710	309.2	3.0	0.930	34	86	Amaz./Hesp.
−8.878°	217.642°	ESP_018561_1710	297.4	2.7	0.930	34	86	Amaz./Hesp.

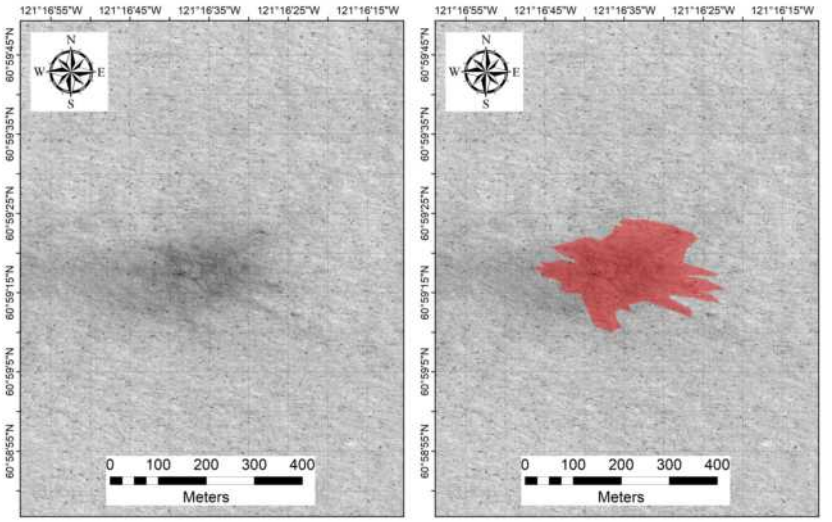

Latitude	Longitude	HiRISE ID	Area (m^2)	Diam.(m)	DCI	TI day	TI night	Epoch
60.987°	238.723°	ESP_018573_2415	47504.2	7.3	0.967	237	184	Late Hesp.

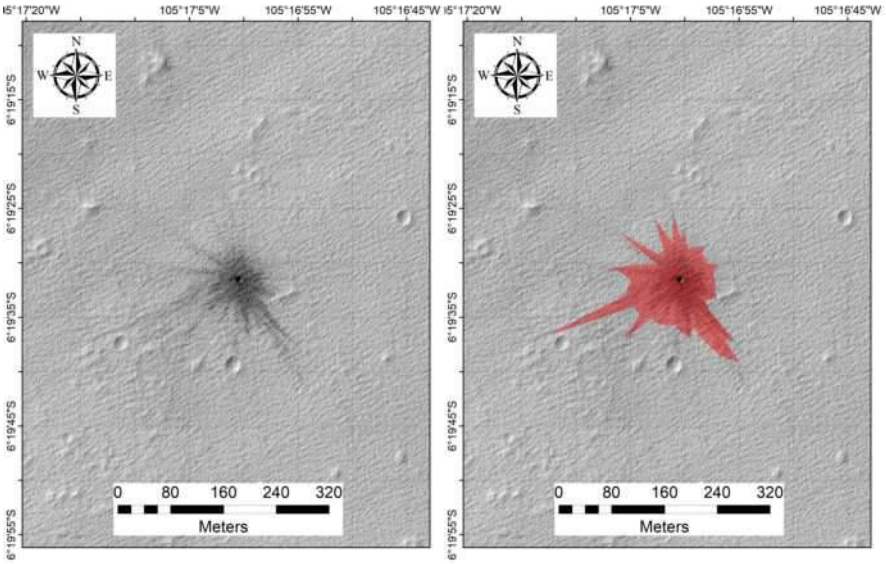

Latitude	Longitude	HiRISE ID	Area (m^2)	Diam.(m)	DCI	TI day	TI night	Epoch
−6.325°	254.717°	ESP_018586_1735	18126.5	9.9	0.944	91	41	Late Hesp.

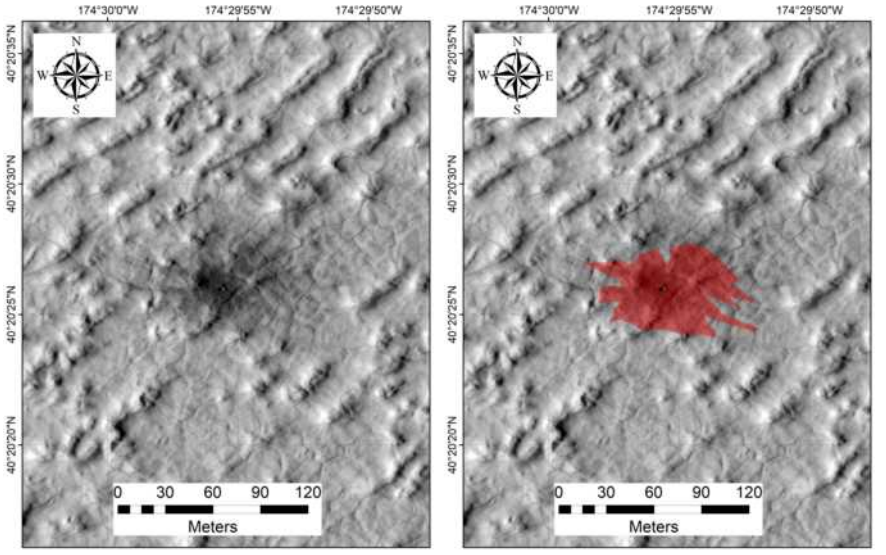

Latitude	Longitude	HiRISE ID	Area (m^2)	Diam.(m)	DCI	TI day	TI night	Epoch
40.341°	185.501°	ESP_018707_2205	3647.5	3.2	0.956	249	188	Late Amaz.

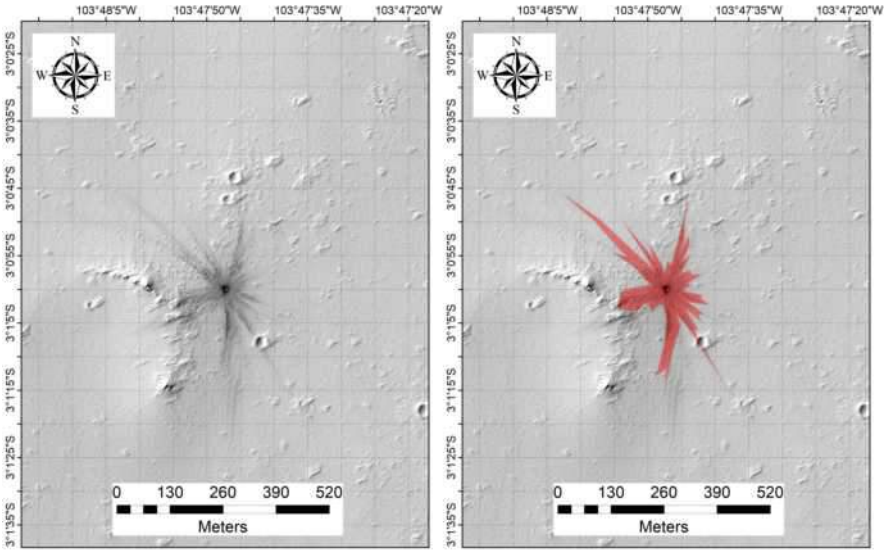

Latitude	Longitude	HiRISE ID	Area (m^2)	Diam.(m)	DCI	TI day	TI night	Epoch
−3.017°	256.204°	ESP_018731_1770	29744.1	11.4	0.944	21	59	Late Hesp.

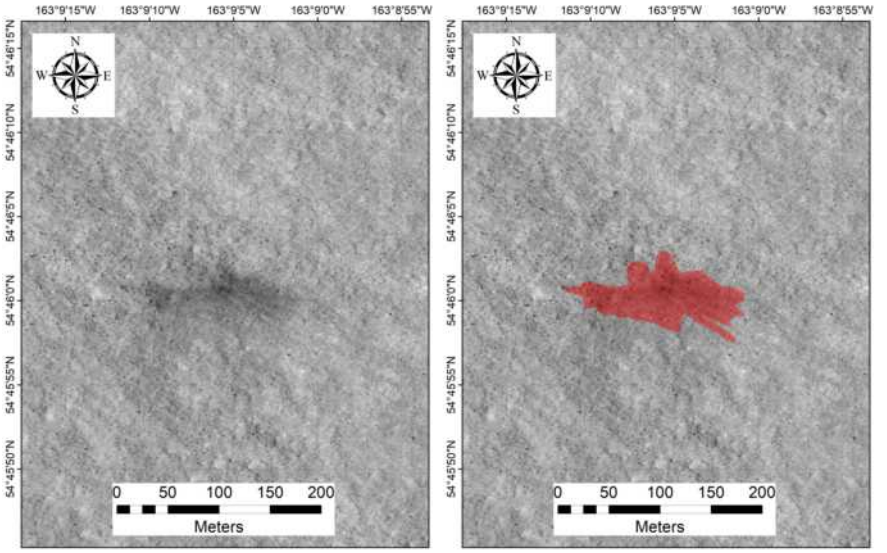

Latitude	Longitude	HiRISE ID	Area (m^2)	Diam.(m)	DCI	TI day	TI night	Epoch
54.767°	196.848°	ESP_018746_2350	7151.8	3.3	0.949	223	207	Late Hesp.

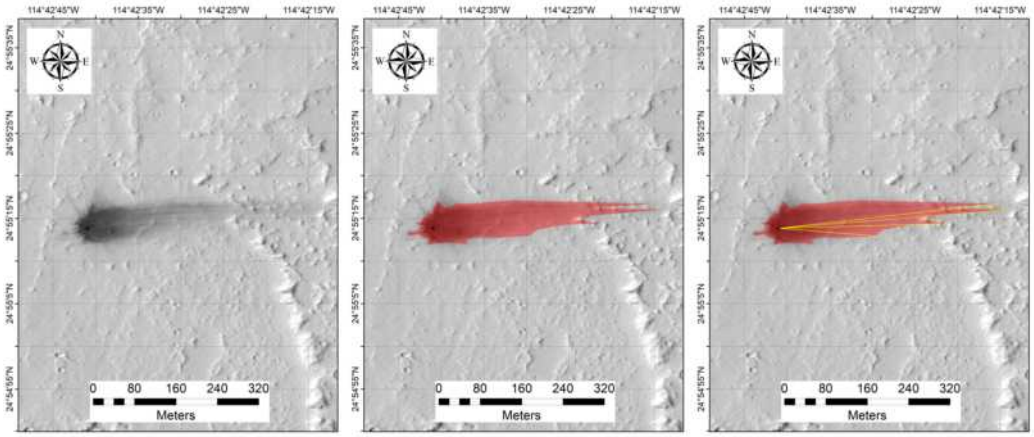

Latitude	Longitude	HiRISE ID	Area (m^2)	Diam.(m)	DCI	TI day	TI night	Epoch	Azimuth
24.921°	245.289°	ESP_018784_2050	21491.0	5.2	0.935	20	48	Amaz./Hesp.	86.8

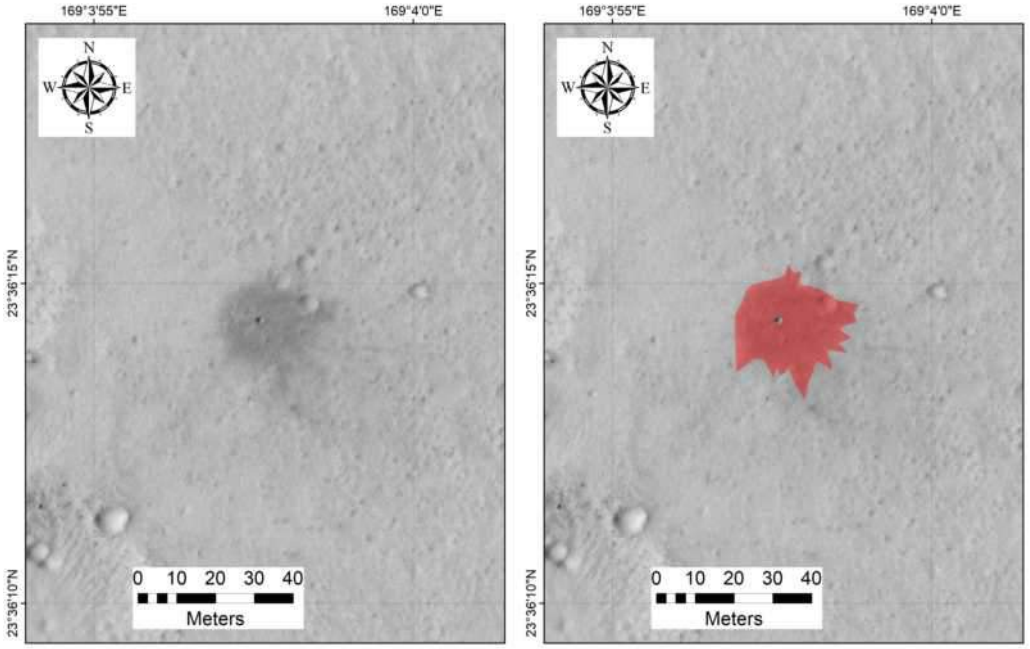

Latitude	Longitude	HiRISE ID	Area (m^2)	Diam.(m)	DCI	TI day	TI night	Epoch
23.604°	169.066°	ESP_018800_2040	595.8	2.1	0.931	118	164	Late Amaz.

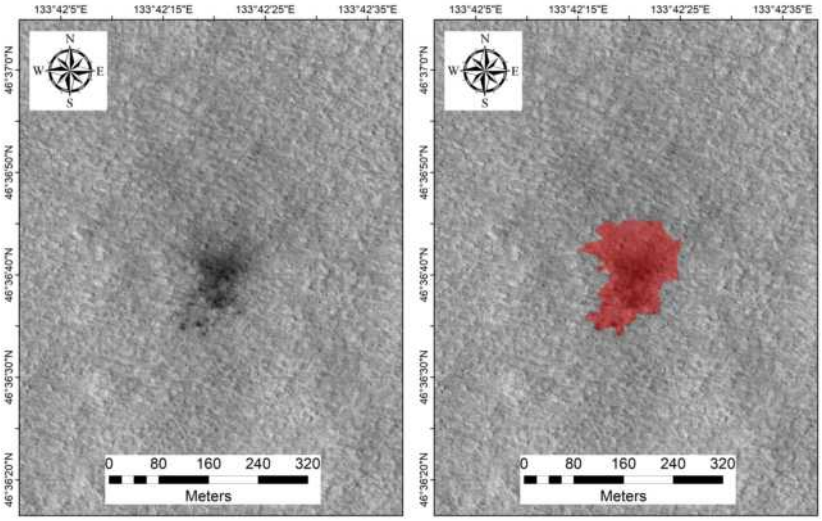

Latitude	Longitude	HiRISE ID	Area (m^2)	Diam.(m)	DCI	TI day	TI night	Epoch
46.611°	133.706°	ESP_018854_2270	18265.0	3.1	0.941	274	240	Late Hesp.

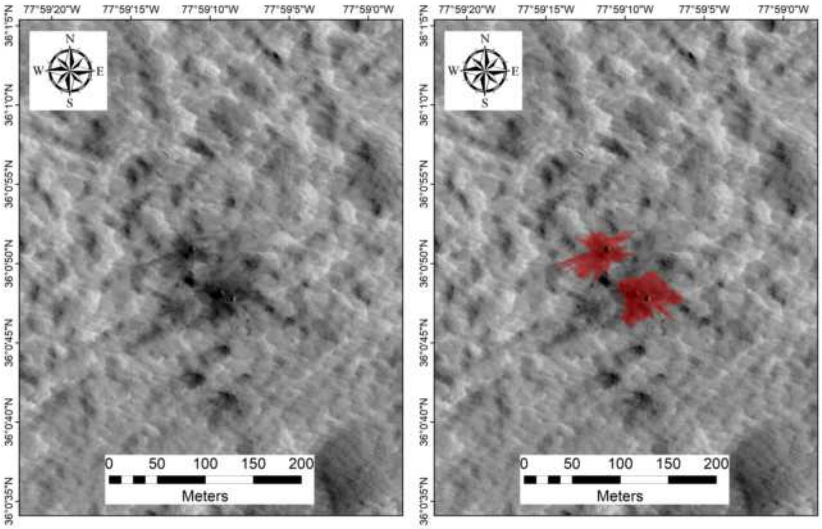

Latitude	Longitude	HiRISE ID	Area (m^2)	Diam.(m)	DCI	TI day	TI night	Epoch
36.014°	282.014°	ESP_019165_2165	2209.3	5.2	0.921	47	41	Early Hesp.
36.014°	282.014°	ESP_019165_2165	1830.2	5.1	0.921	47	41	Early Hesp.

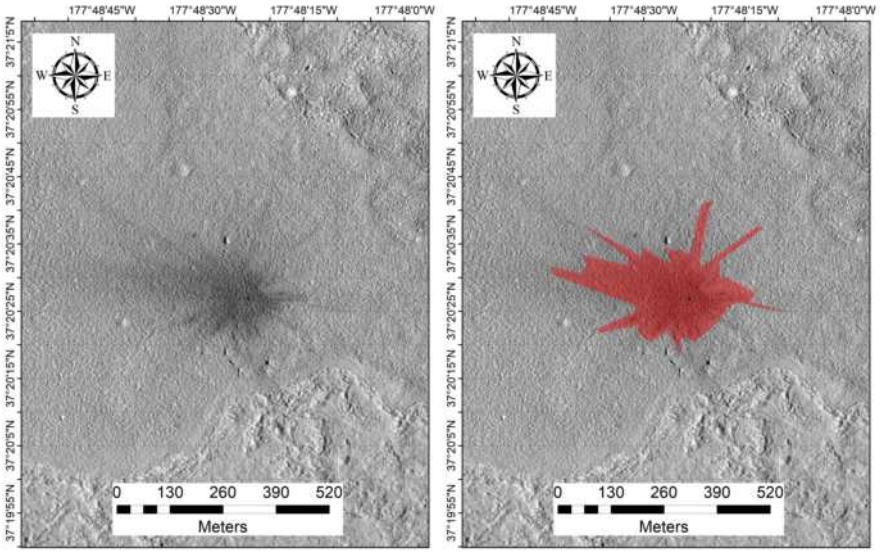

Latitude	Longitude	HiRISE ID	Area (m^2)	Diam.(m)	DCI	TI day	TI night	Epoch
37.341°	182.194°	ESP_019195_2175	65927.7	8.2	0.966	155	211	Late Amaz.

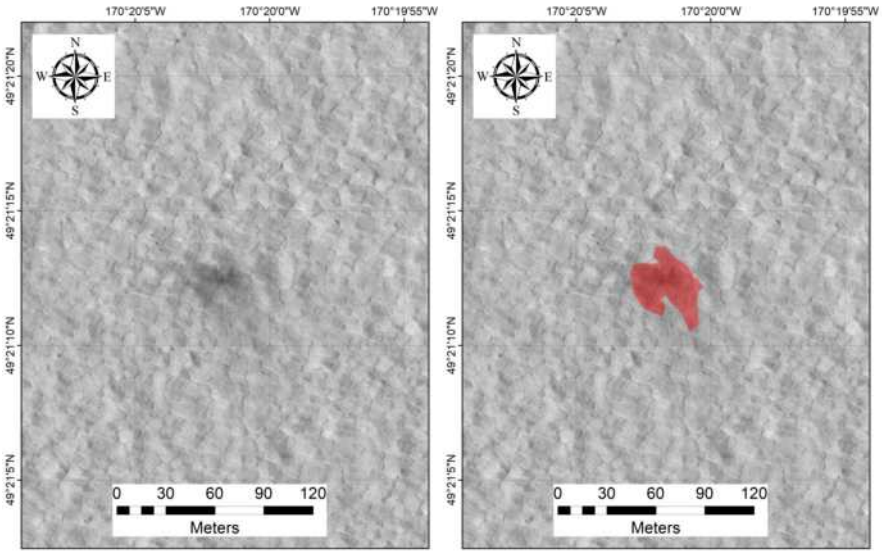

Latitude	Longitude	HiRISE ID	Area (m^2)	Diam.(m)	DCI	TI day	TI night	Epoch
49.353°	189.666°	ESP_019287_2295	1246.9	1.8	0.948	209	254	Amazonian

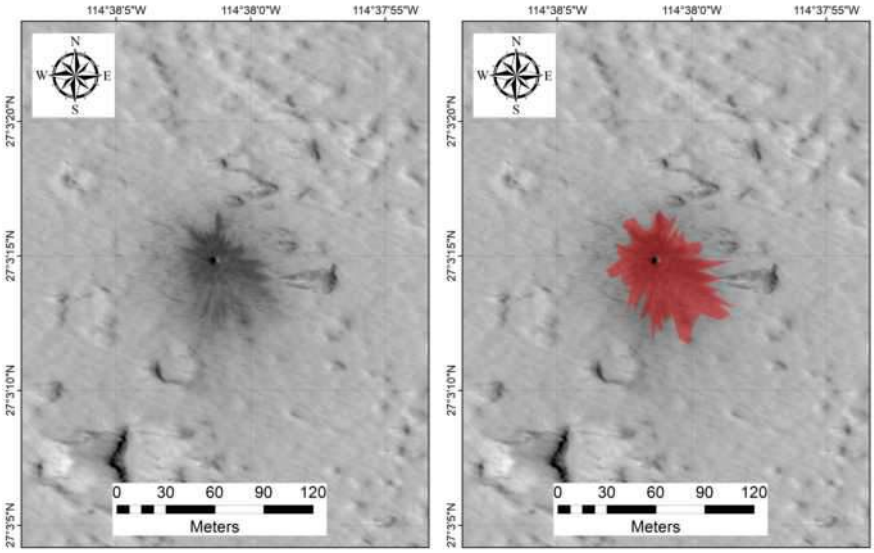

Latitude	Longitude	HiRISE ID	Area (m^2)	Diam.(m)	DCI	TI day	TI night	Epoch
27.054°	245.366°	ESP_019707_2075	3030.4	4.9	0.922	24	66	Amaz./Hesp.

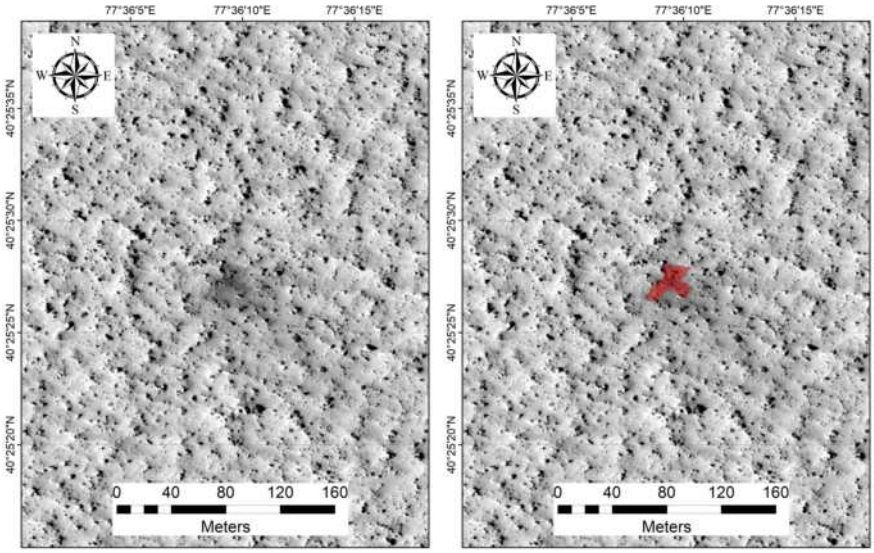

Latitude	Longitude	HiRISE ID	Area (m^2)	Diam.(m)	DCI	TI day	TI night	Epoch
40.424°	77.603°	ESP_019779_2205	470.2	2.0	0.928	316	253	Late Hesp.

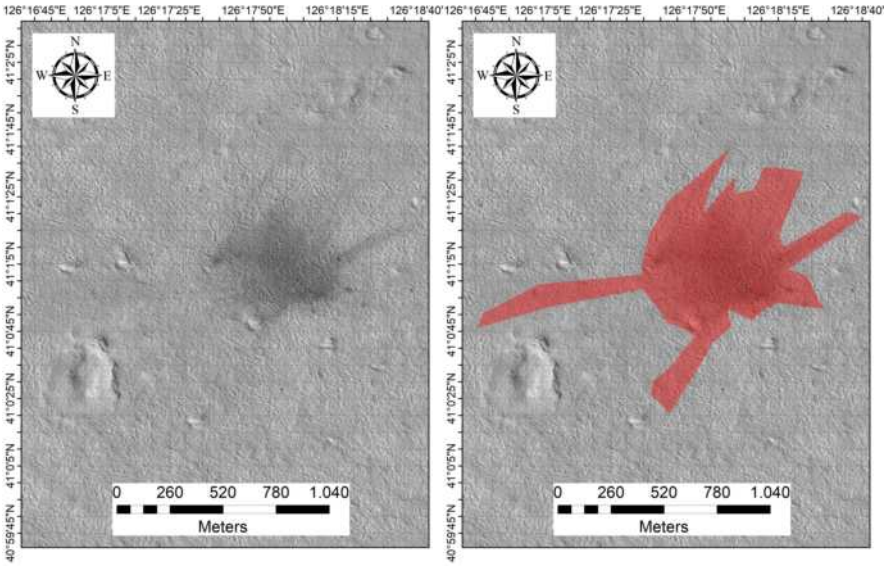

Latitude	Longitude	HiRISE ID	Area (m^2)	Diam.(m)	DCI	TI day	TI night	Epoch
41.017°	126.301°	ESP_019830_2215	623726.8	14.5	0.935	249	227	Amazonian

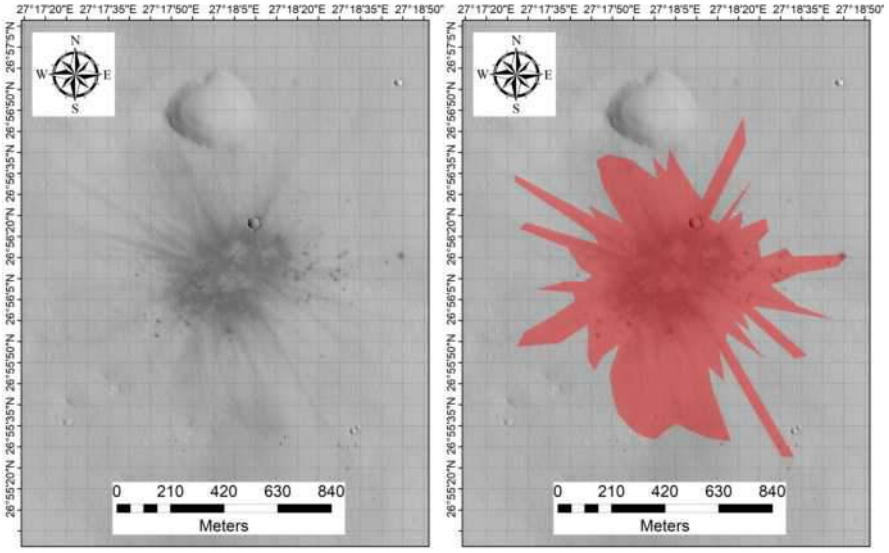

Latitude	Longitude	HiRISE ID	Area (m^2)	Diam.(m)	DCI	TI day	TI night	Epoch
26.936°	27.301°	ESP_019926_2070	690229.9	4.8	0.927	37	40	Middle Noach.

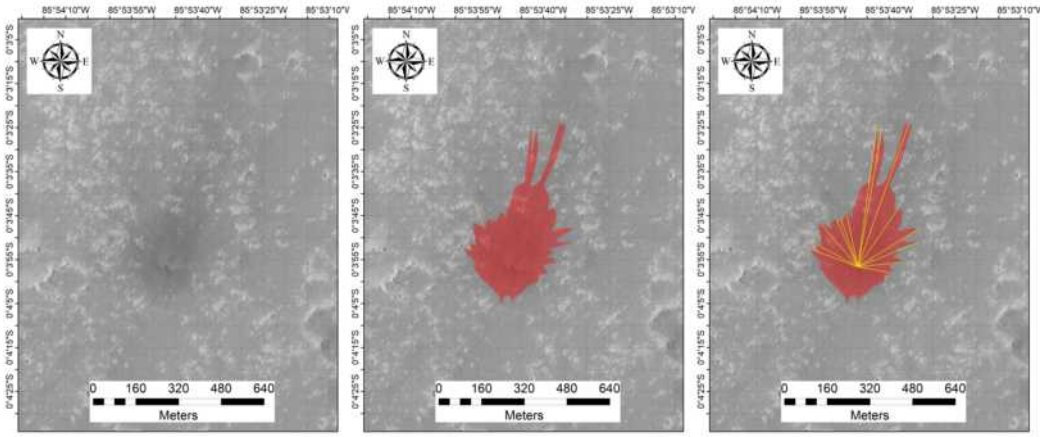

Latitude	Longitude	HiRISE ID	Area (m^2)	Diam.(m)	DCI	TI day	TI night	Epoch	Azimuth
−0.066°	274.104°	ESP_019983_1800	105420.7	4.9	0.943	80	95	Amaz./Hesp.	11.3

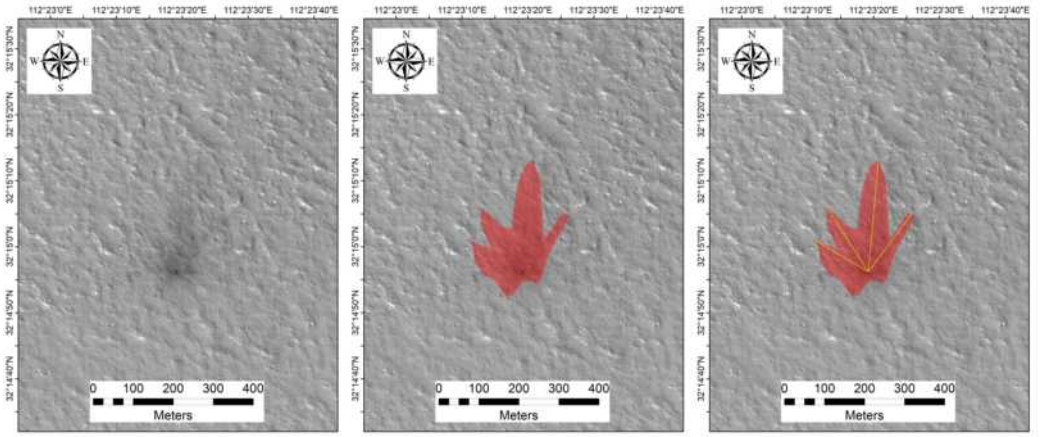

Latitude	Longitude	HiRISE ID	Area (m^2)	Diam.(m)	DCI	TI day	TI night	Epoch	Azimuth
32.249°	112.389°	ESP_020714_2125	35597.7	4.5	0.958	383	326	Amaz./Hesp.	351.2

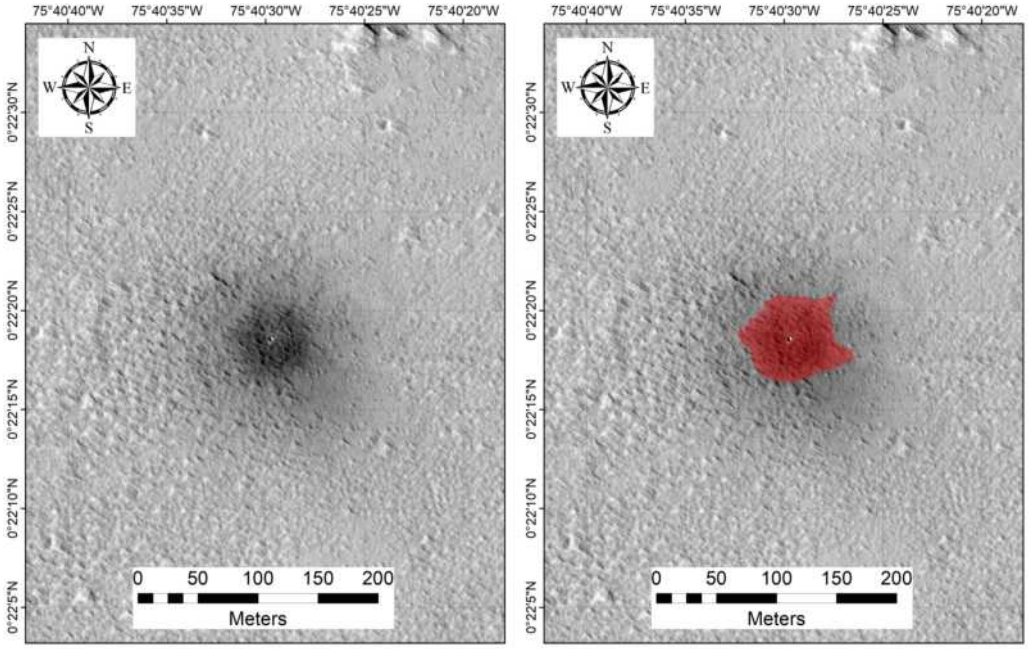

Latitude	Longitude	HiRISE ID	Area (m^2)	Diam.(m)	DCI	TI day	TI night	Epoch
0.372°	284.325°	ESP_020787_1805	4622.0	4.0	0.940	67	44	Early Hesp.

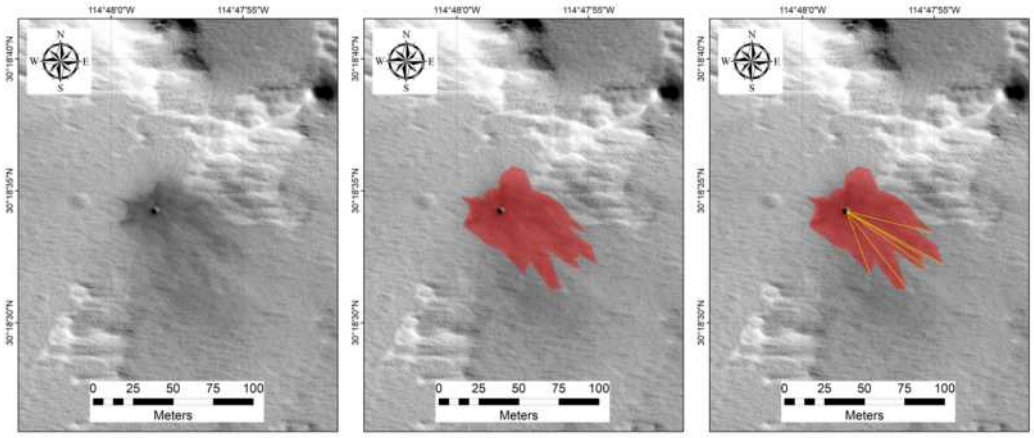

Latitude	Longitude	HiRISE ID	Area (m^2)	Diam.(m)	DCI	TI day	TI night	Epoch	Azimuth
30.310°	245.200°	ESP_020841_2105	3006.1	4.2	0.938	18	61	Amaz./Hesp.	126.6

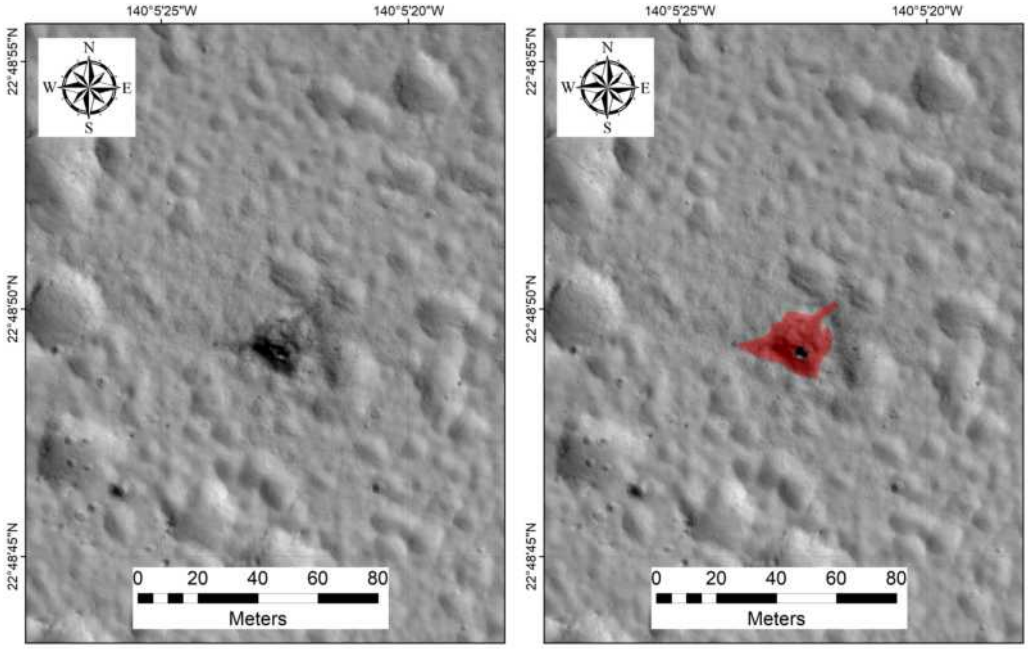

Latitude	Longitude	HiRISE ID	Area (m^2)	Diam.(m)	DCI	TI day	TI night	Epoch
22.814°	219.910°	ESP_020842_2030	387.9	4.4	0.933	141	60	Late Amaz.

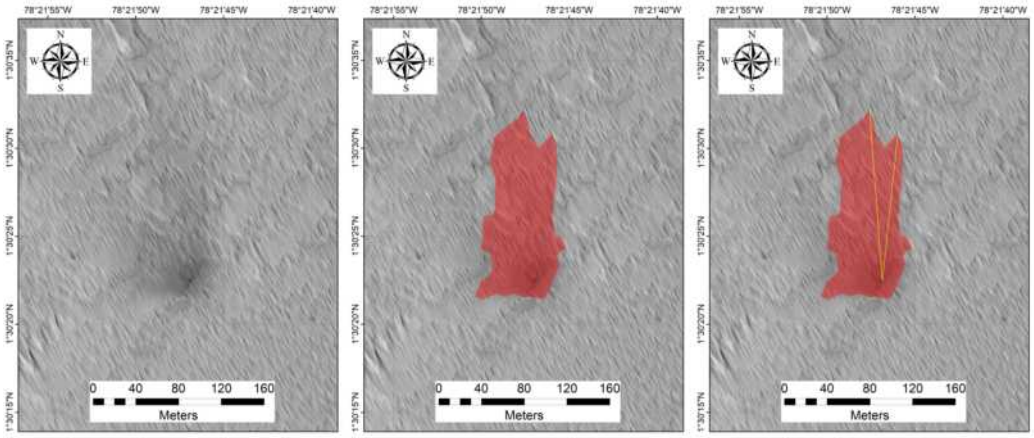

Latitude	Longitude	HiRISE ID	Area (m^2)	Diam.(m)	DCI	TI day	TI night	Epoch	Azimuth
1.506°	281.637°	ESP_020853_1815	9545.1	3.4	0.935	73	72	Noachian	0.5

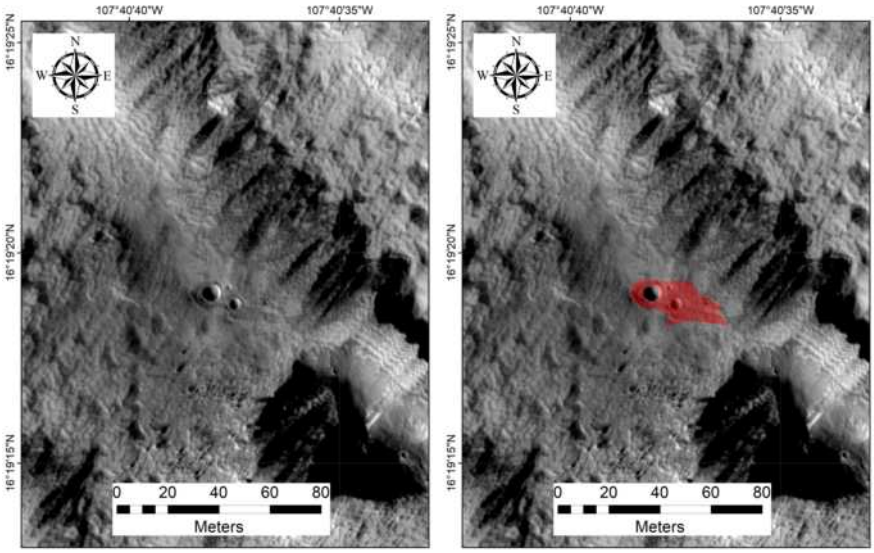

Latitude	Longitude	HiRISE ID	Area (m^2)	Diam.(m)	DCI	TI day	TI night	Epoch
16.322°	252.323°	ESP_020854_1965	393.7	6.2	0.936	33	85	Amaz./Hesp.

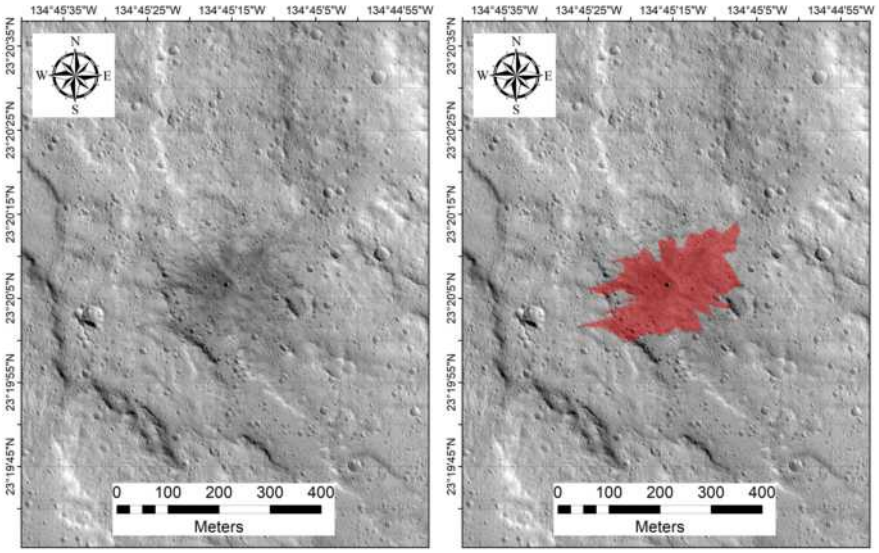

Latitude	Longitude	HiRISE ID	Area (m^2)	Diam.(m)	DCI	TI day	TI night	Epoch
23.335°	225.246°	ESP_020855_2035	37889.1	7.5	0.939	30	155	Amazonian

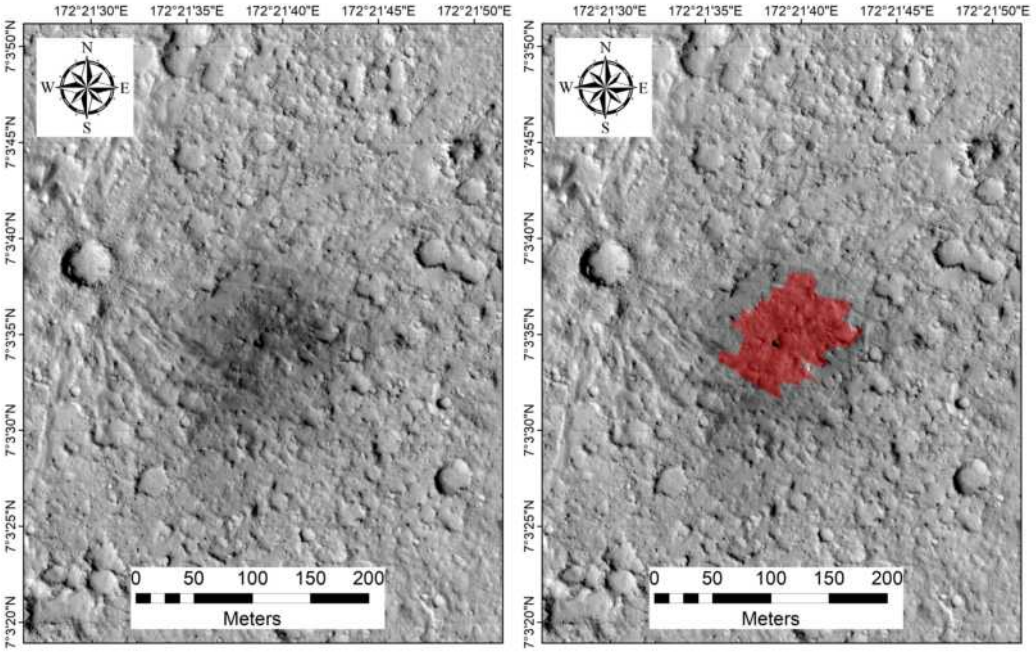

Latitude	Longitude	HiRISE ID	Area (m^2)	Diam.(m)	DCI	TI day	TI night	Epoch
7.060°	172.361°	ESP_020857_1870	6772.2	5.9	0.922	28	44	Late Amaz.

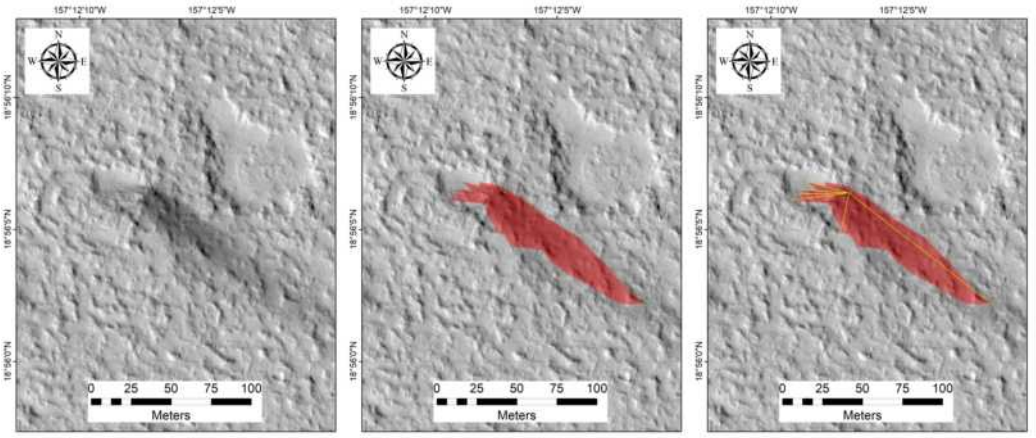

Latitude	Longitude	HiRISE ID	Area (m^2)	Diam.(m)	DCI	TI day	TI night	Epoch	Azimuth
18.935°	202.796°	ESP_020869_1990	2384.6	2.9	0.933	78	49	Amaz./Hesp.	202.5

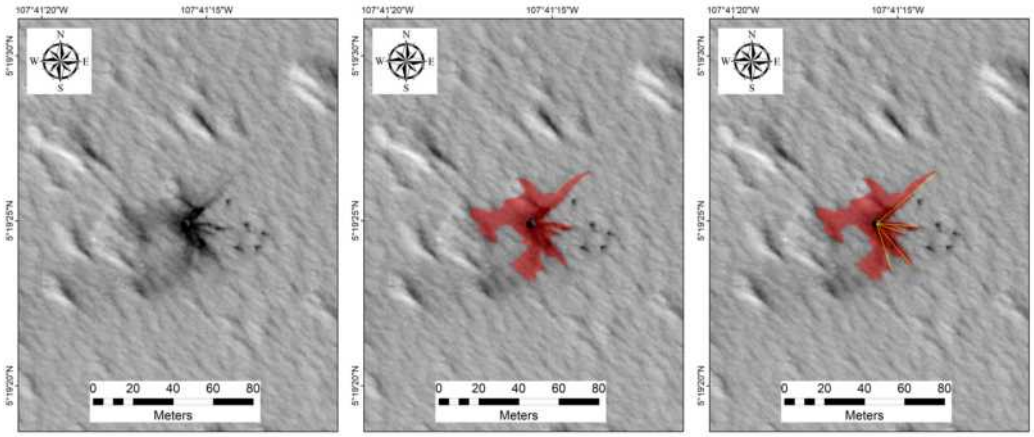

Latitude	Longitude	HiRISE ID	Area (m^2)	Diam.(m)	DCI	TI day	TI night	Epoch	Azimuth
5.324°	252.312°	ESP_020920_1855	1066.3	4.5	0.932	36	53	Amaz./Hesp.	105.7

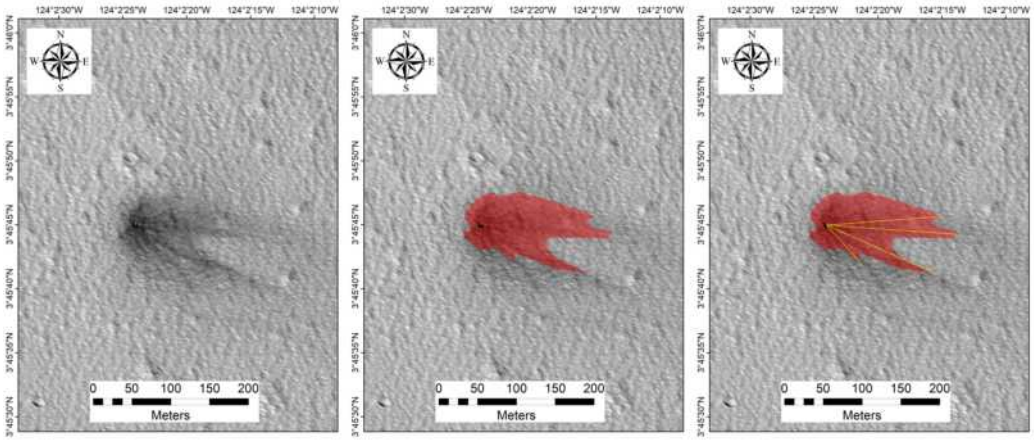

Latitude	Longitude	HiRISE ID	Area (m^2)	Diam.(m)	DCI	TI day	TI night	Epoch	Azimuth
3.763°	235.960°	ESP_020947_1840	10622.2	6.1	0.934	57	29	Amaz./Hesp.	102.9

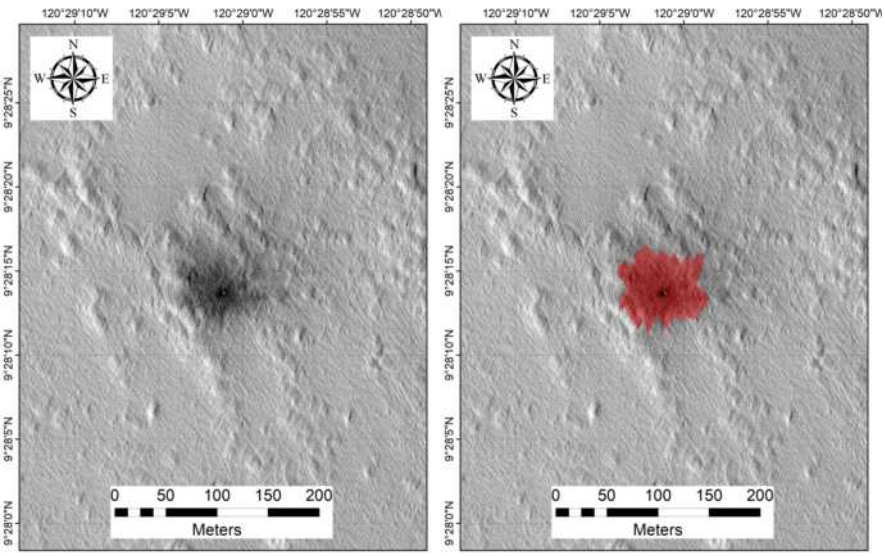

Latitude	Longitude	HiRISE ID	Area (m^2)	Diam.(m)	DCI	TI day	TI night	Epoch
9.470°	239.516°	ESP_020960_1895	4997.6	5.5	0.940	43	101	Early Hesp.

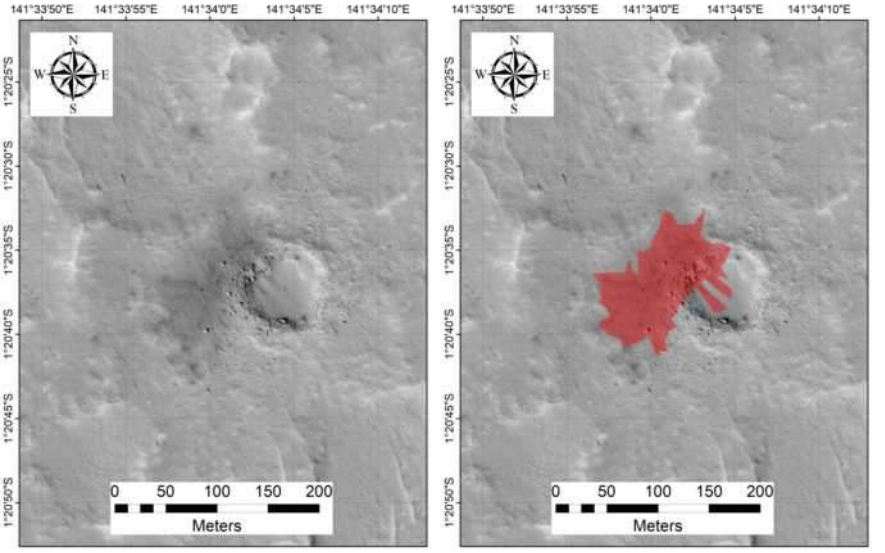

Latitude	Longitude	HiRISE ID	Area (m^2)	Diam.(m)	DCI	TI day	TI night	Epoch
−1.344°	141.567°	ESP_021768_1785	9460.8	2.9	0.933	167	122	Early Hesp.

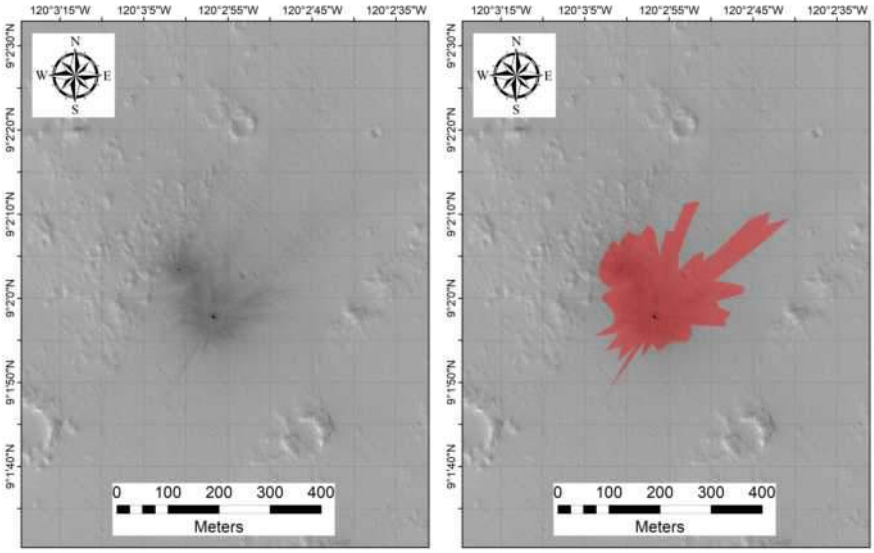

Latitude	Longitude	HiRISE ID	Area (m^2)	Diam.(m)	DCI	TI day	TI night	Epoch
9.034°	239.950°	ESP_021883_1890	51738.6	7.6	0.938	67	148	Early Hesp.

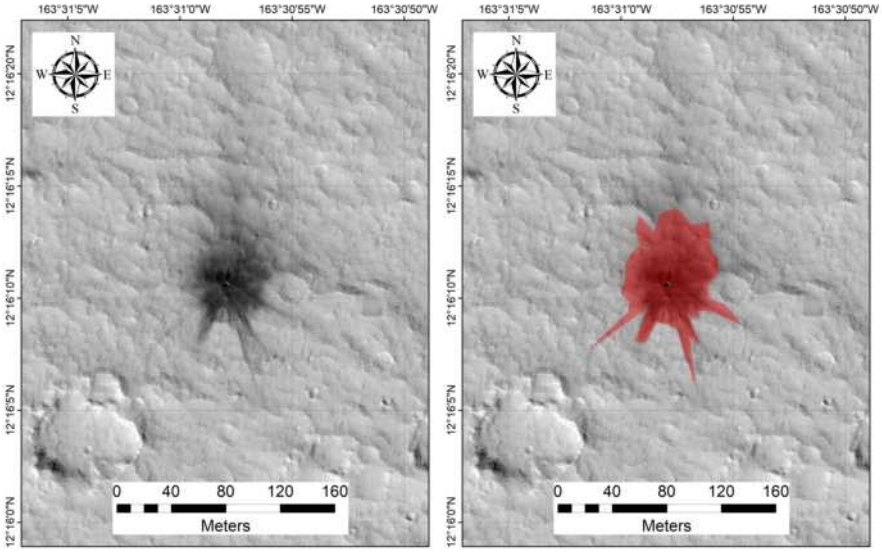

Latitude	Longitude	HiRISE ID	Area (m^2)	Diam.(m)	DCI	TI day	TI night	Epoch
12.270°	196.484°	ESP_022056_1925	5089.9	3.4	0.932	77	55	Late Hesp.

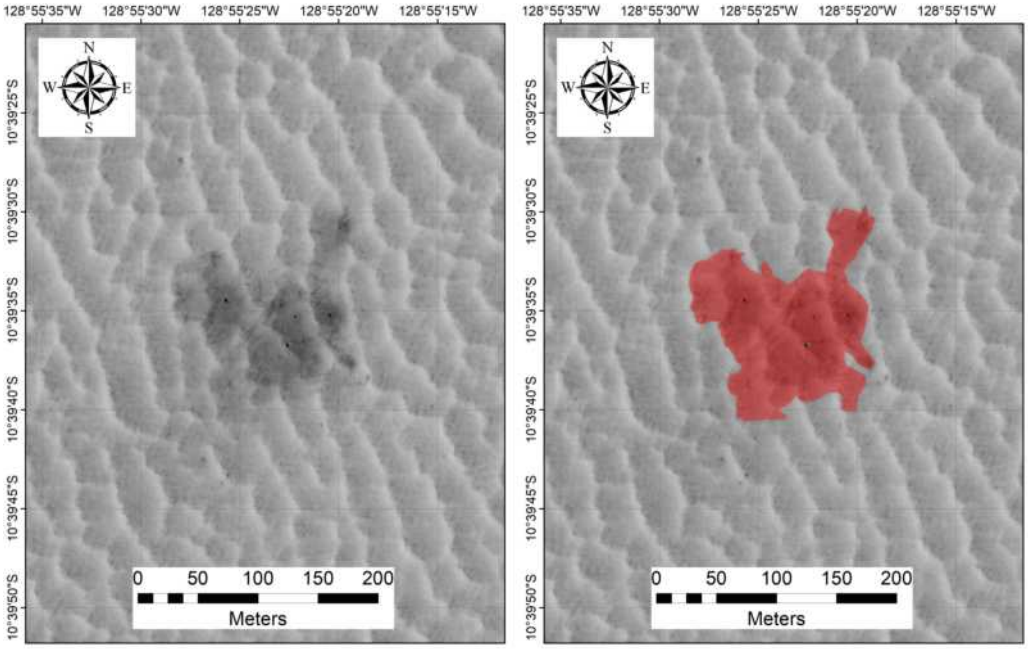

Latitude	Longitude	HiRISE ID	Area (m^2)	Diam.(m)	DCI	TI day	TI night	Epoch
−10.660°	231.077°	ESP_022279_1690	15456.8	4.0	0.932	56	58	Amaz./Hesp.

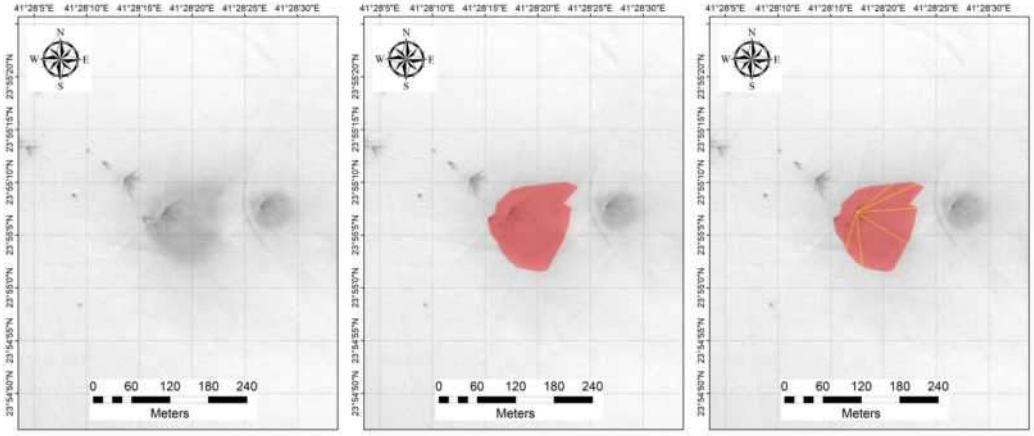

Latitude	Longitude	HiRISE ID	Area (m^2)	Diam.(m)	DCI	TI day	TI night	Epoch	Azimuth
23.919°	41.471°	ESP_022299_2040	13265.1	2.2	0.934	33	53	Middle Noach.	110.5

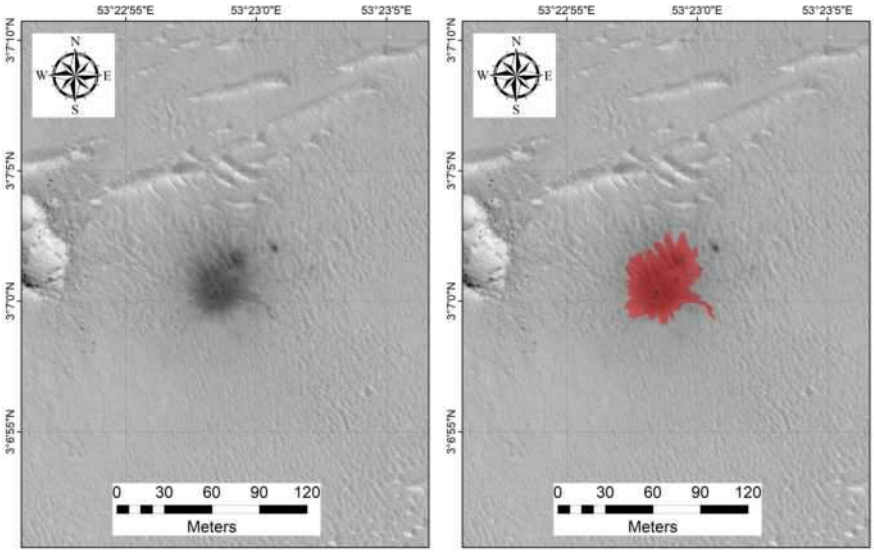

Latitude	Longitude	HiRISE ID	Area (m^2)	Diam.(m)	DCI	TI day	TI night	Epoch
3.117°	53.383°	ESP_022536_1830	1864.0	2.6	0.954	131	134	Amaz./Hesp.

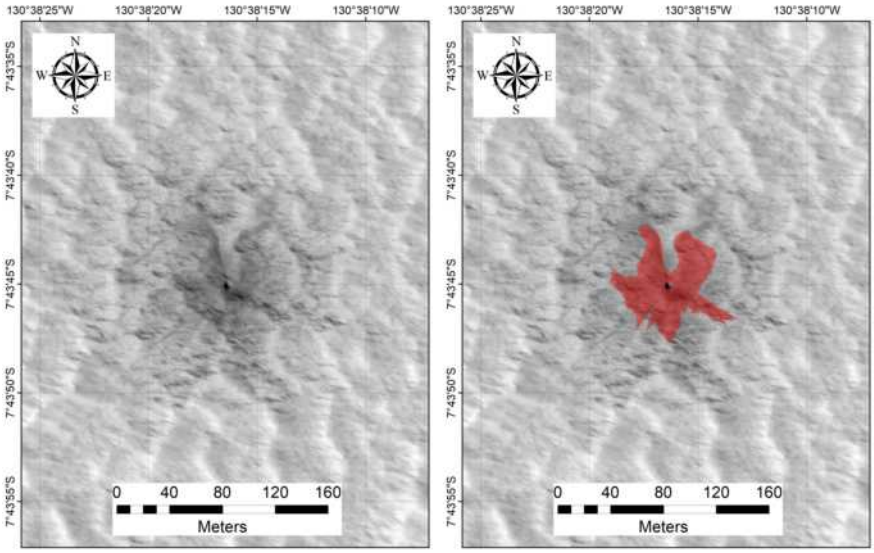

Latitude	Longitude	HiRISE ID	Area (m^2)	Diam.(m)	DCI	TI day	TI night	Epoch
−7.729°	229.362°	ESP_022912_1720	3713.4	4.7	0.937	10	8	Amaz./Hesp.

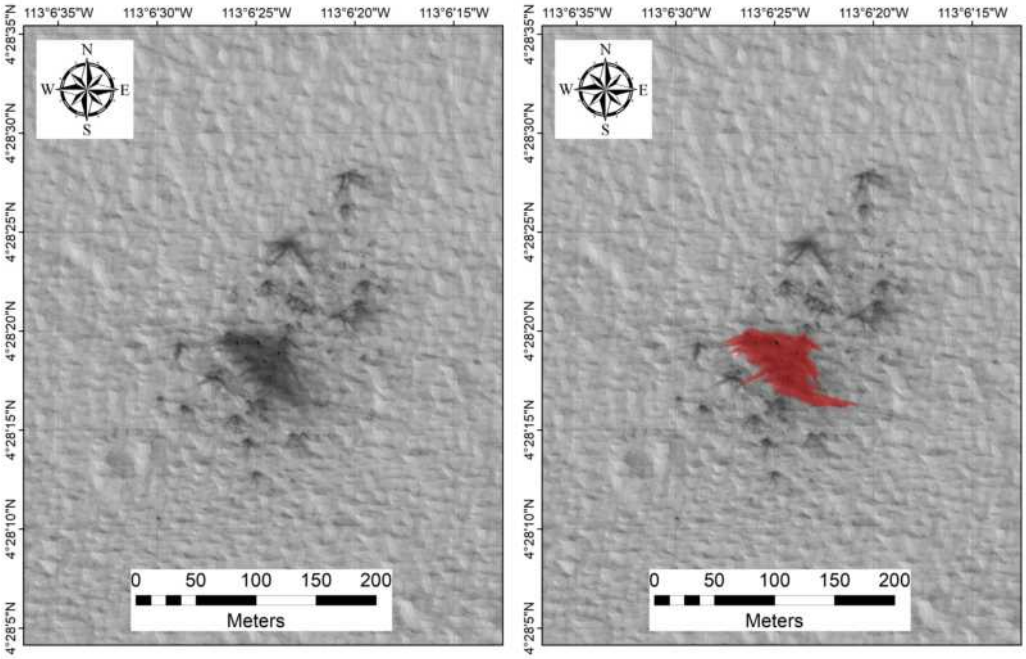

Latitude	Longitude	HiRISE ID	Area (m^2)	Diam.(m)	DCI	TI day	TI night	Epoch
4.472°	246.893°	ESP_022964_1845	3014.4	3.0	0.935	24	68	Late Amaz.

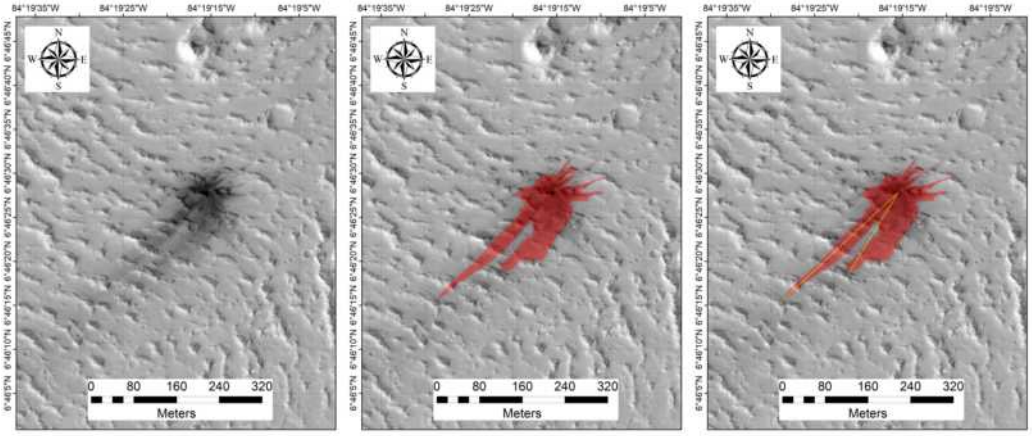

Latitude	Longitude	HiRISE ID	Area (m^2)	Diam.(m)	DCI	TI day	TI night	Epoch	Azimuth
6.774°	275.679°	ESP_023108_1870	17648.1	5.7	0.937	64	48	Amaz./Hesp.	221.3

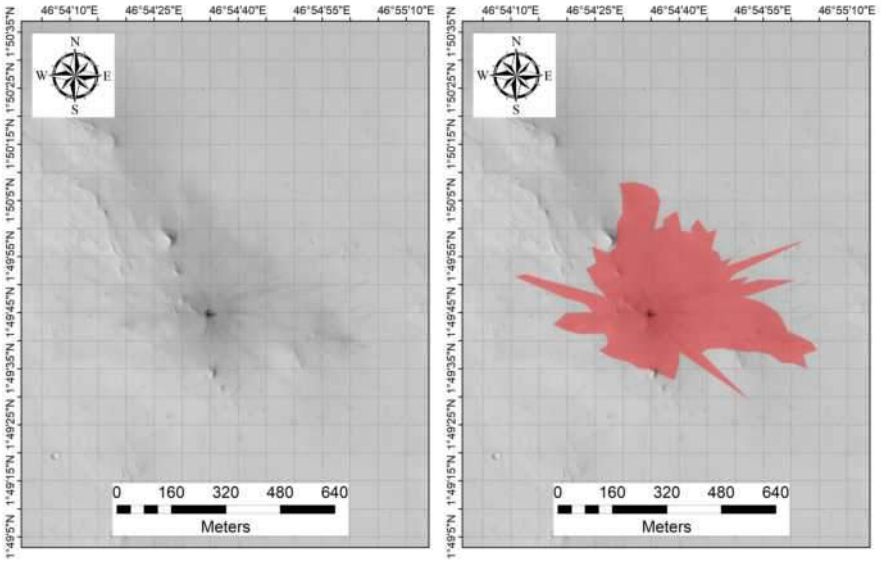

Latitude	Longitude	HiRISE ID	Area (m^2)	Diam.(m)	DCI	TI day	TI night	Epoch
1.829°	46.910°	ESP_023156_1820	213718.2	9.6	0.934	68	43	Middle Noach.

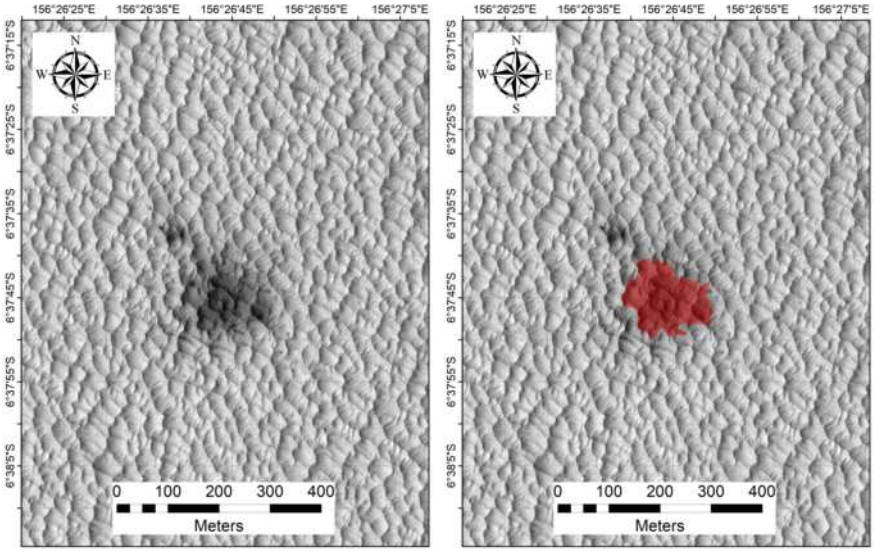

Latitude	Longitude	HiRISE ID	Area (m^2)	Diam.(m)	DCI	TI day	TI night	Epoch
−6.630°	156.445°	ESP_023363_1735	17368.1	5.4	0.931	80	145	Hesperian

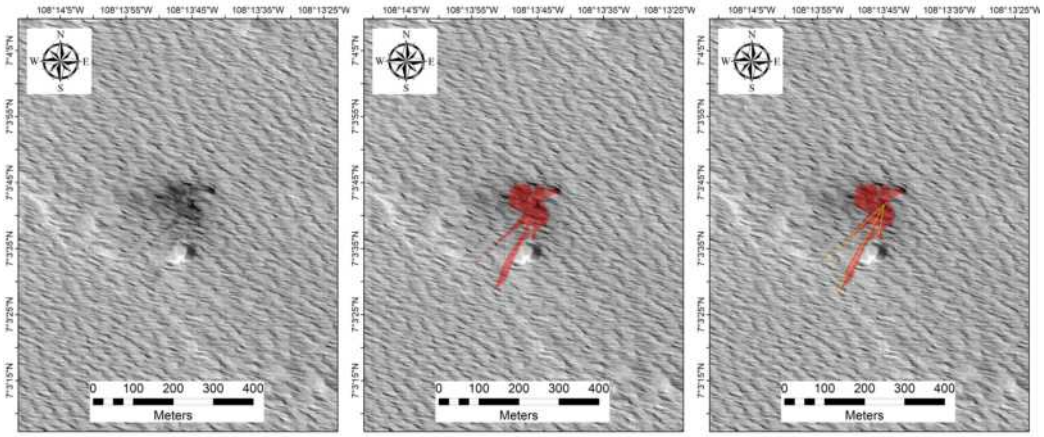

Latitude	Longitude	HiRISE ID	Area (m^2)	Diam.(m)	DCI	TI day	TI night	Epoch	Azimuth
7.062°	251.771°	ESP_023399_1870	11791.0	9.2	0.934	34	70	Amaz./Hesp.	212.3

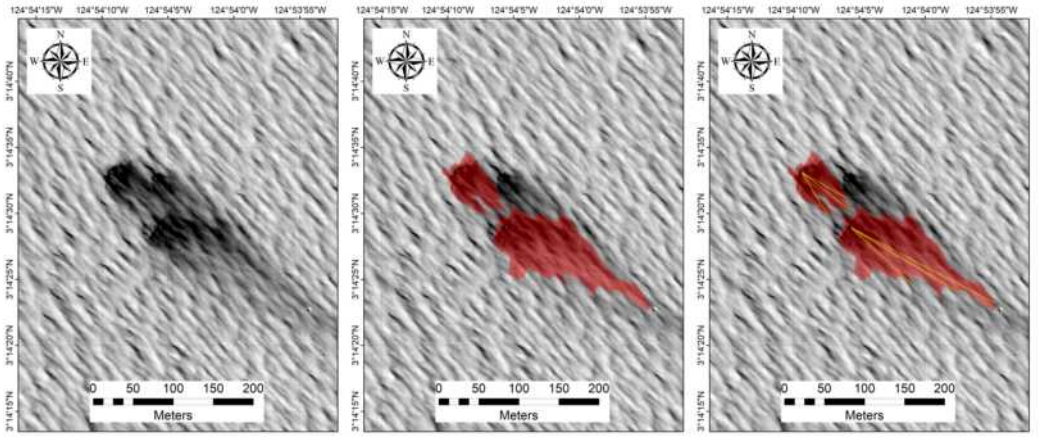

Latitude	Longitude	HiRISE ID	Area (m^2)	Diam.(m)	DCI	TI day	TI night	Epoch	Azimuth
3.241°	235.100°	ESP_023426_1835	9795.7	4.7	0.935	150	138	Hesperian	122.2
3.241°	235.100°	ESP_023426_1835	2937.5	4.5	0.935	150	138	Hesperian	131.5

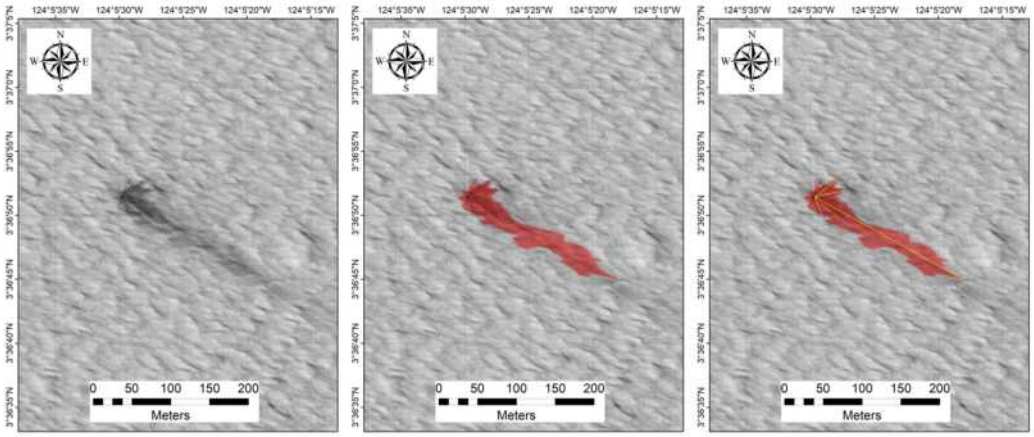

Latitude	Longitude	HiRISE ID	Area (m^2)	Diam.(m)	DCI	TI day	TI night	Epoch	Azimuth
3.614°	235.908°	ESP_023571_1835	5576.5	4.5	0.935	28	40	Amaz./Hesp.	109.7

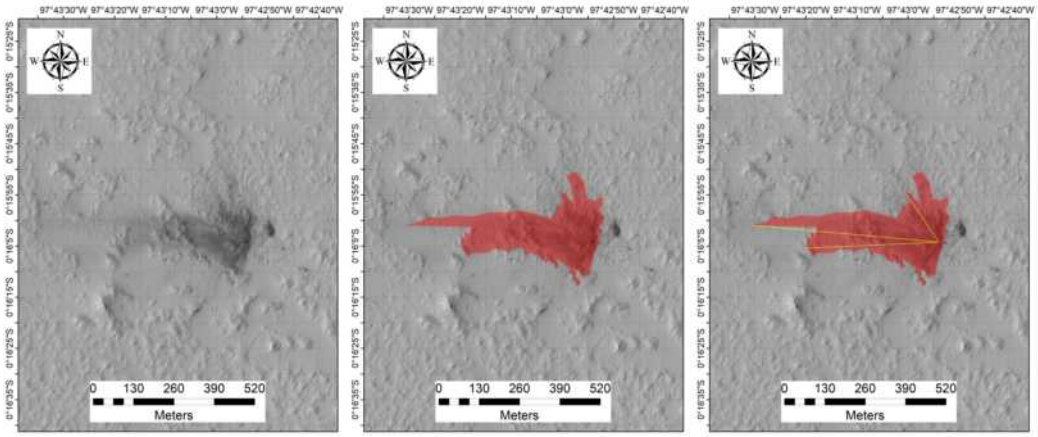

Latitude	Longitude	HiRISE ID	Area (m^2)	Diam.(m)	DCI	TI day	TI night	Epoch	Azimuth
−0.268°	262.285°	ESP_024203_1795	76529.8	9.7	0.937	8	47	Amaz./Hesp.	280.5

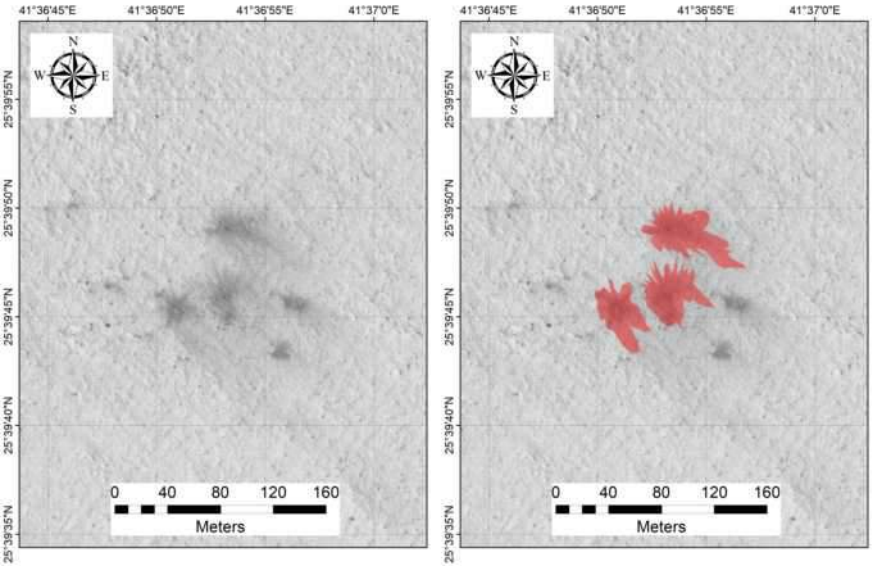

Latitude	Longitude	HiRISE ID	Area (m^2)	Diam.(m)	DCI	TI day	TI night	Epoch
25.663°	41.615°	ESP_024211_2060	1157.1	2.0	0.917	22	56	Middle Noach.
25.663°	41.615°	ESP_024211_2060	1689.3	1.6	0.917	22	56	Middle Noach.
25.663°	41.615°	ESP_024211_2060	1335.7	1.6	0.917	22	56	Middle Noach.

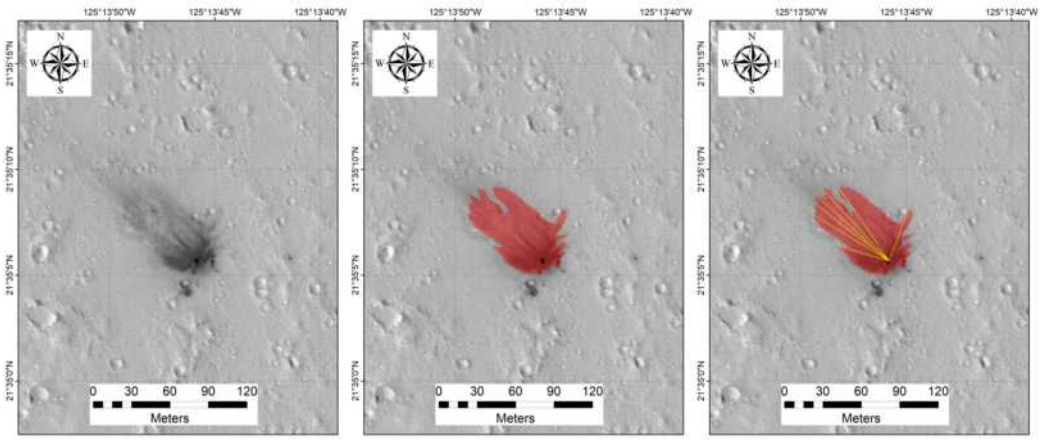

Latitude	Longitude	HiRISE ID	Area (m^2)	Diam.(m)	DCI	TI day	TI night	Epoch	Azimuth
21.585°	234.771°	ESP_024349_2020	3011.8	3.8	0.936	44	45	Late Amaz.	316.8

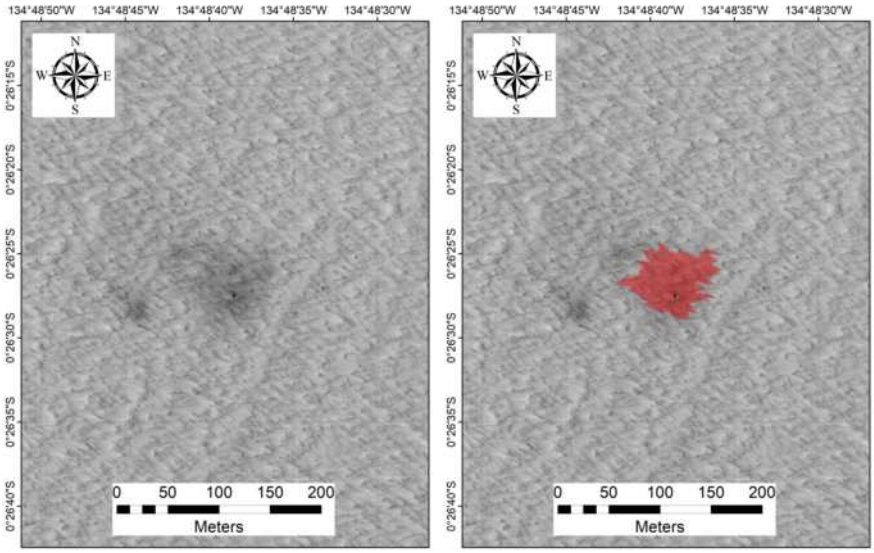

Latitude	Longitude	HiRISE ID	Area (m^2)	Diam.(m)	DCI	TI day	TI night	Epoch
−0.441°	225.189°	ESP_024389_1795	4052.1	4.6	0.937	40	20	Amaz./Hesp.

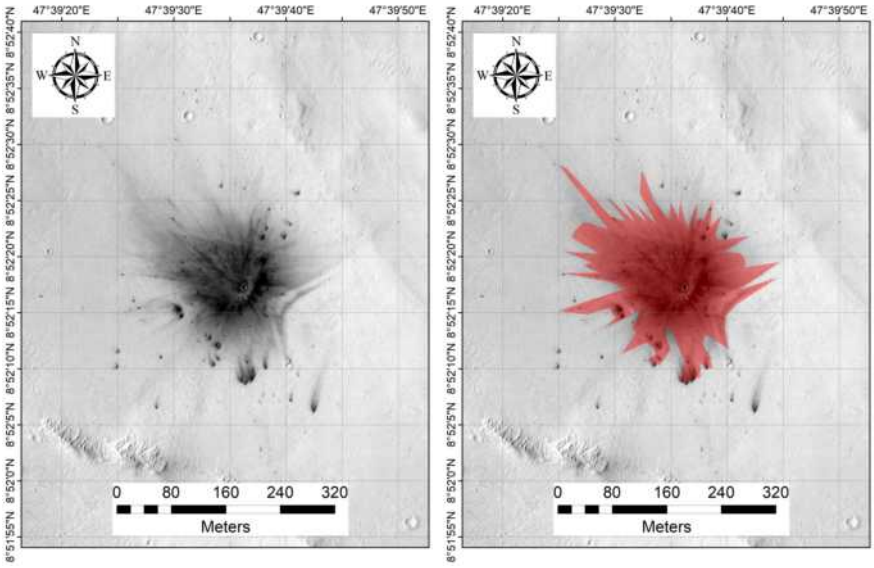

Latitude	Longitude	HiRISE ID	Area (m^2)	Diam.(m)	DCI	TI day	TI night	Epoch
8.871°	47.660°	ESP_024646_1890	41594.8	6.1	0.932	38	107	Middle Noach.

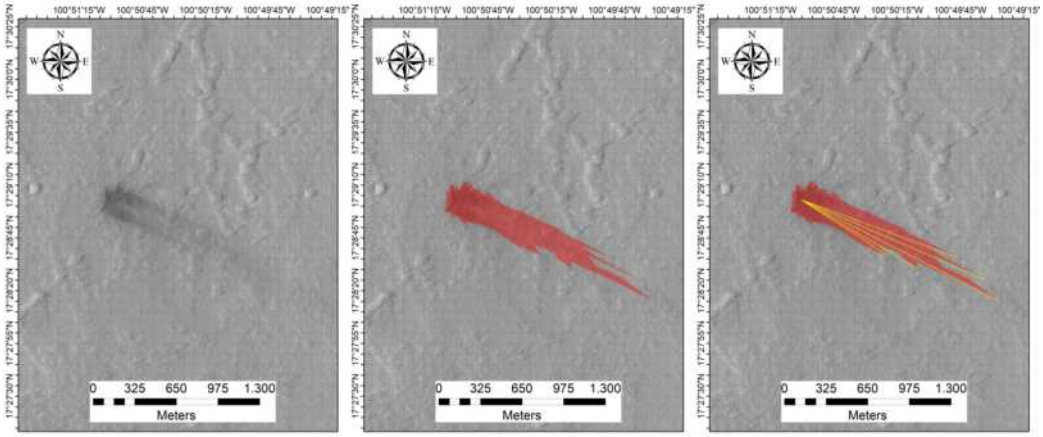

Latitude	Longitude	HiRISE ID	Area (m^2)	Diam.(m)	DCI	TI day	TI night	Epoch	Azimuth
17.484°	259.150°	ESP_024836_1975	295176.7	9.4	0.935	275	58	Amaz./Hesp.	116.1

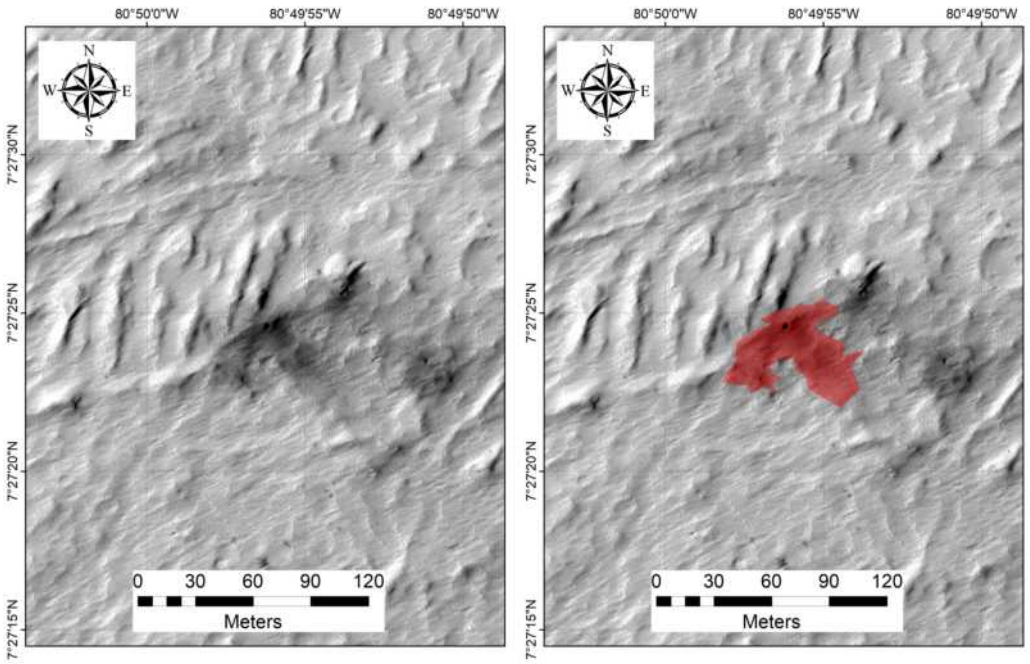

Latitude	Longitude	HiRISE ID	Area (m^2)	Diam.(m)	DCI	TI day	TI night	Epoch
7.457°	279.168°	ESP_025732_1875	2083.6	2.8	0.939	209	41	Amaz./Hesp.

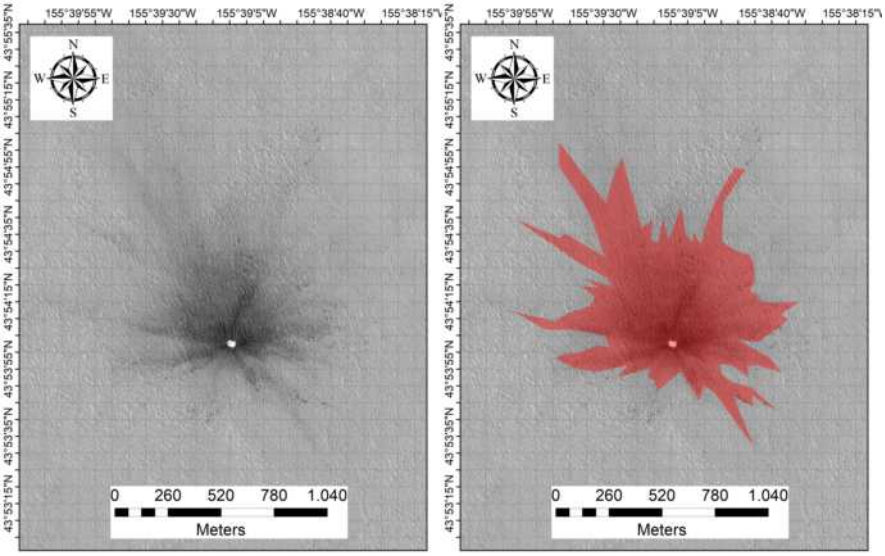

Latitude	Longitude	HiRISE ID	Area (m^2)	Diam.(m)	DCI	TI day	TI night	Epoch
43.901°	204.347°	ESP_025840_2240	730339.8	7.2	0.933	181	201	Late Hesp.

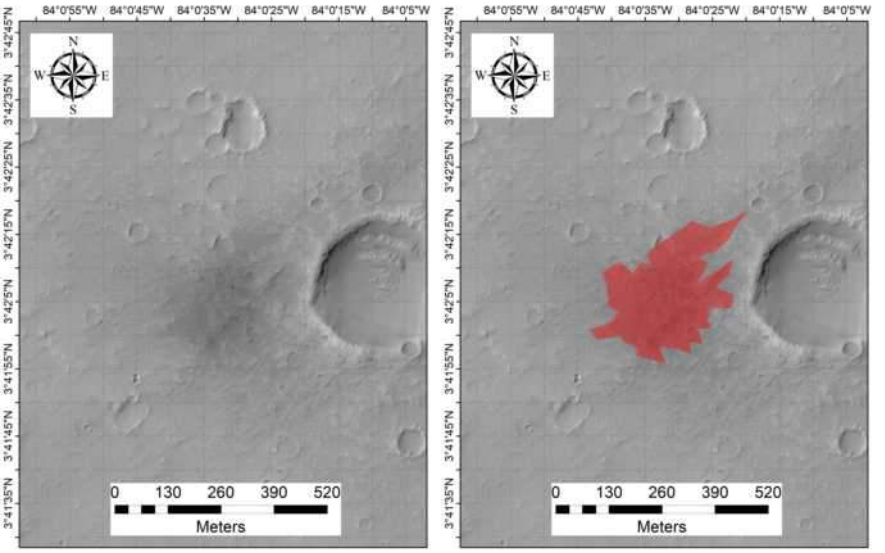

Latitude	Longitude	HiRISE ID	Area (m^2)	Diam.(m)	DCI	TI day	TI night	Epoch
3.702°	275.991°	ESP_025864_1835	68286.7	7.0	0.950	65	25	Amaz./Hesp.

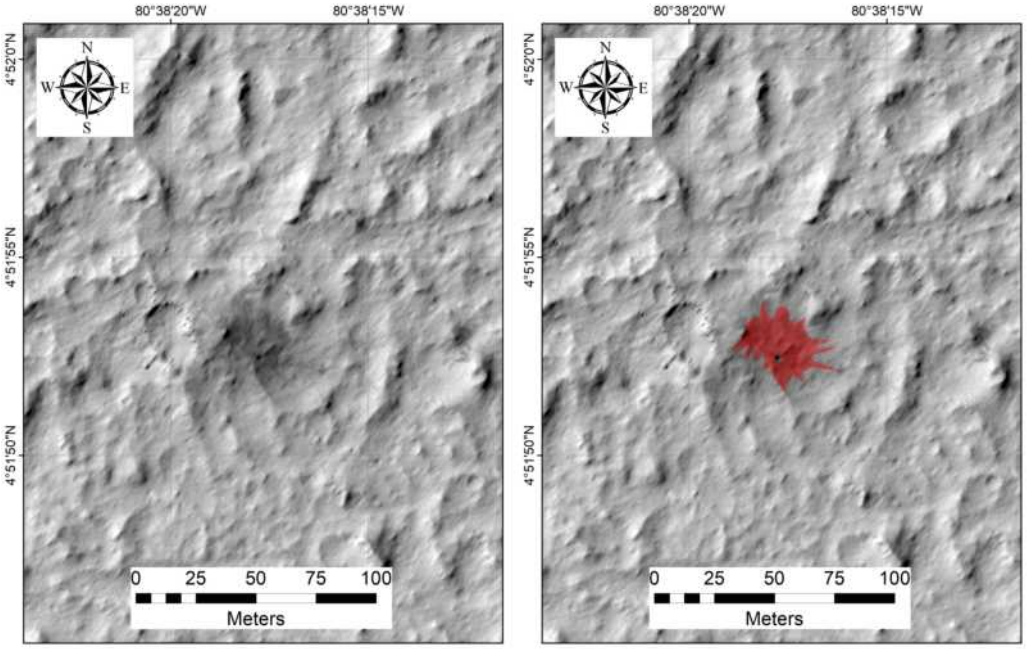

Latitude	Longitude	HiRISE ID	Area (m^2)	Diam.(m)	DCI	TI day	TI night	Epoch
4.865°	279.362°	ESP_025943_1850	669.4	3.0	0.938	67	110	Amaz./Hesp.

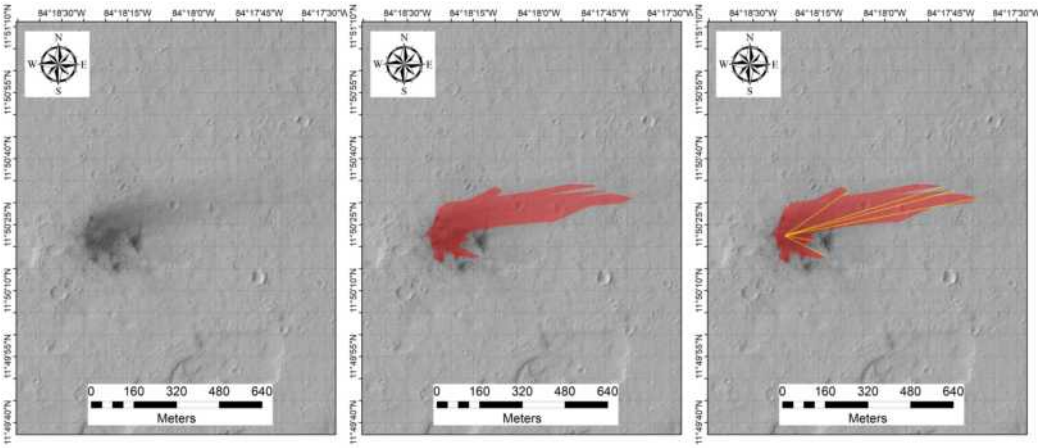

Latitude	Longitude	HiRISE ID	Area (m^2)	Diam.(m)	DCI	TI day	TI night	Epoch	Azimuth
11.840°	275.694°	ESP_026009_1920	84900.6	4.3	0.938	46	54	Amaz./Hesp.	77.1

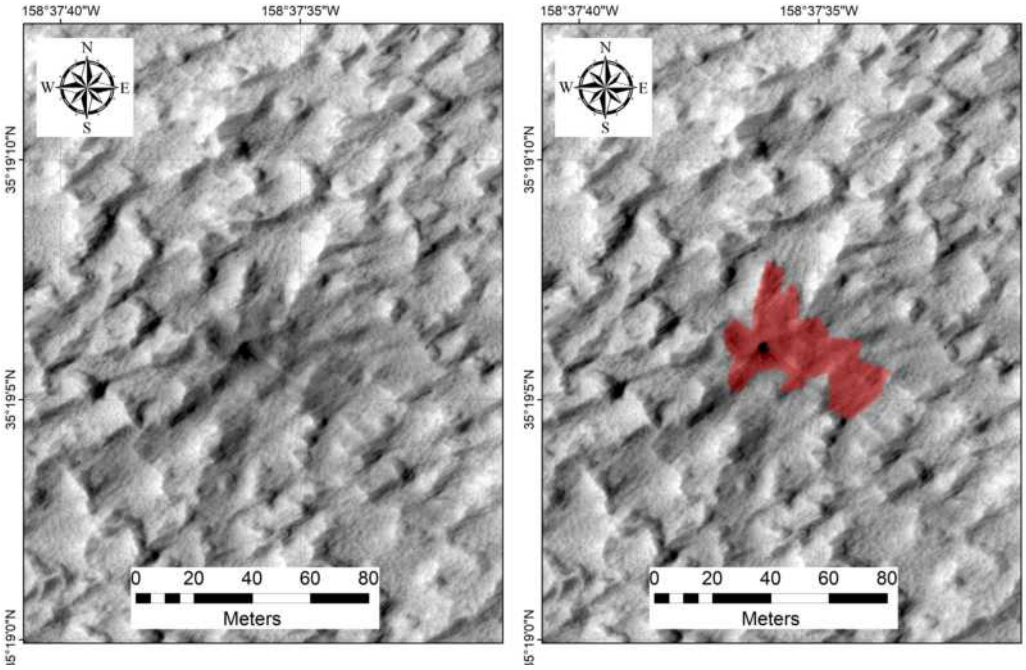

Latitude	Longitude	HiRISE ID	Area (m^2)	Diam.(m)	DCI	TI day	TI night	Epoch
35.318°	201.373°	ESP_026038_2155	1280.6	3.8	0.951	46	78	Amazonian

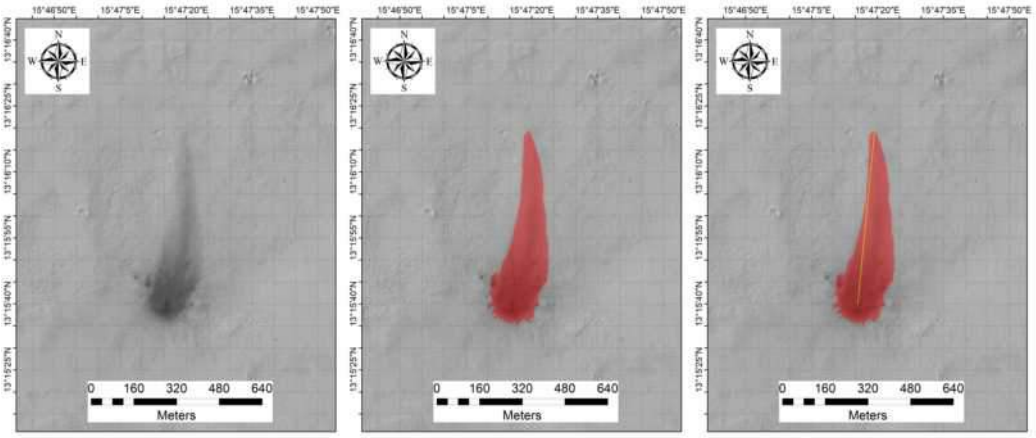

Latitude	Longitude	HiRISE ID	Area (m^2)	Diam.(m)	DCI	TI day	TI night	Epoch	Azimuth
13.261°	15.788°	ESP_026124_1935	83610.5	6.3	0.933	36	44	Middle Noach.	5.6

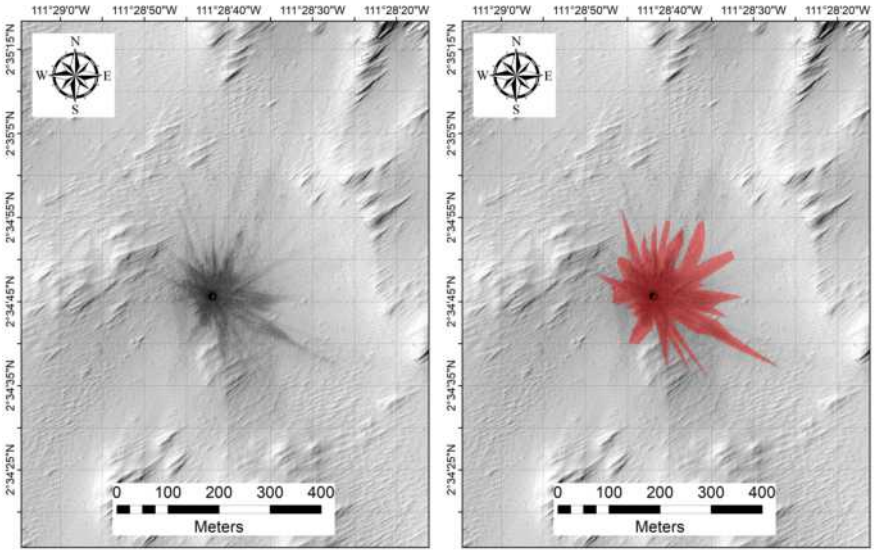

Latitude	Longitude	HiRISE ID	Area (m^2)	Diam.(m)	DCI	TI day	TI night	Epoch
2.579°	248.522°	ESP_026221_1825	36609.3	11.6	0.939	86	89	Amazonian

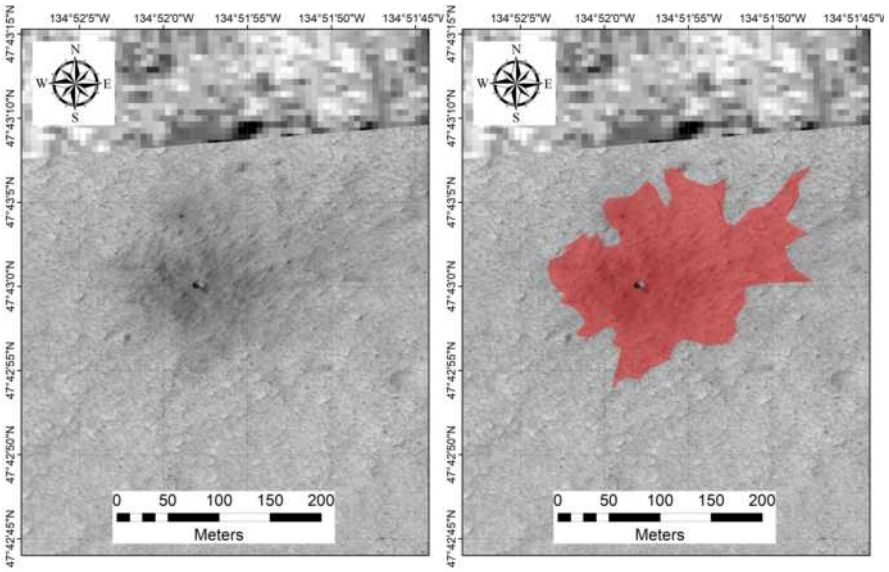

Latitude	Longitude	HiRISE ID	Area (m^2)	Diam.(m)	DCI	TI day	TI night	Epoch
47.717°	225.134°	ESP_026248_2280	28670.2	8.1	0.933	111	96	Amaz./Hesp.

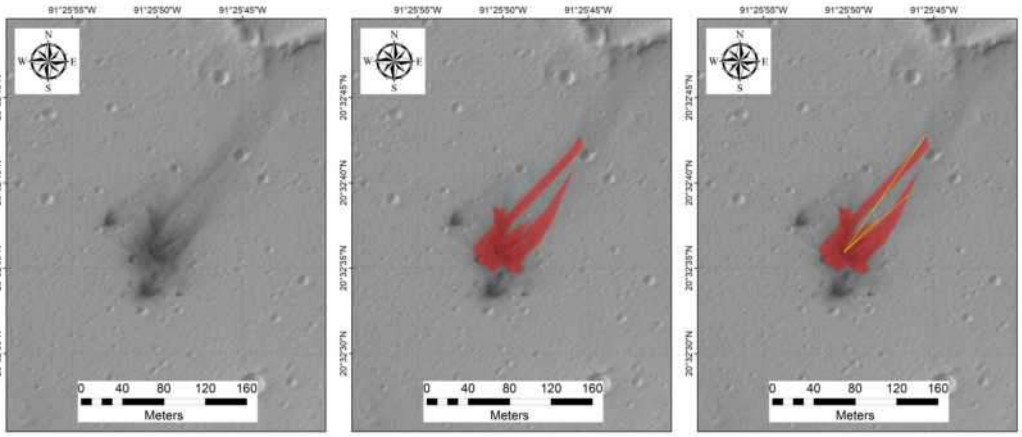

Latitude	Longitude	HiRISE ID	Area (m^2)	Diam.(m)	DCI	TI day	TI night	Epoch	Azimuth
20.543°	268.569°	ESP_026418_2010	3714.1	3.4	0.937	39	61	Amaz./Hesp.	40.9

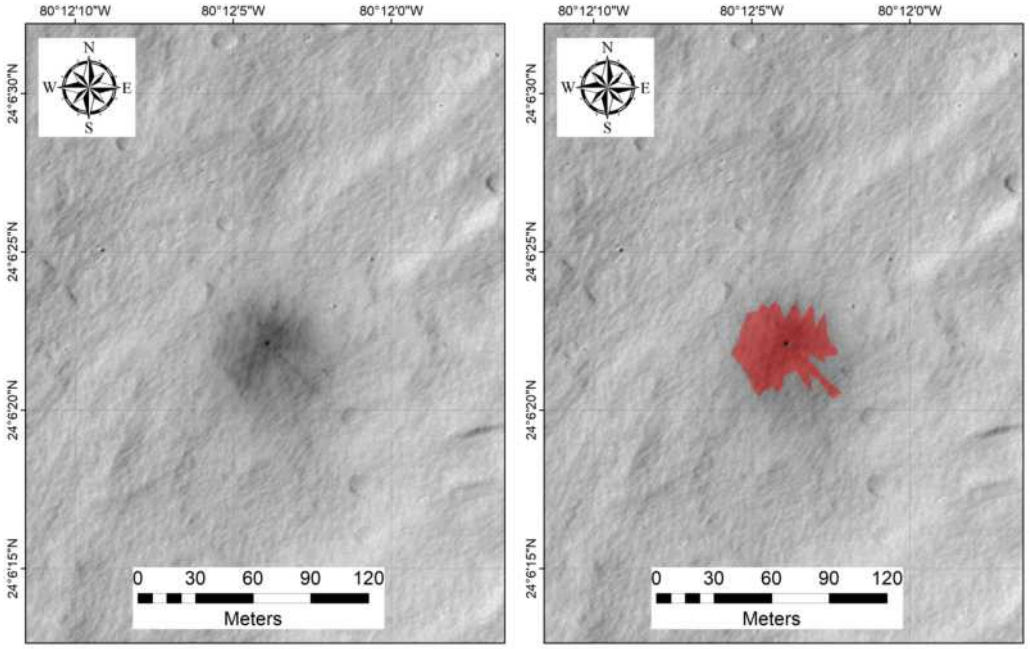

Latitude	Longitude	HiRISE ID	Area (m^2)	Diam.(m)	DCI	TI day	TI night	Epoch
24.106°	279.799°	ESP_026589_2045	1675.2	3.1	0.940	97	75	Early Hesp.

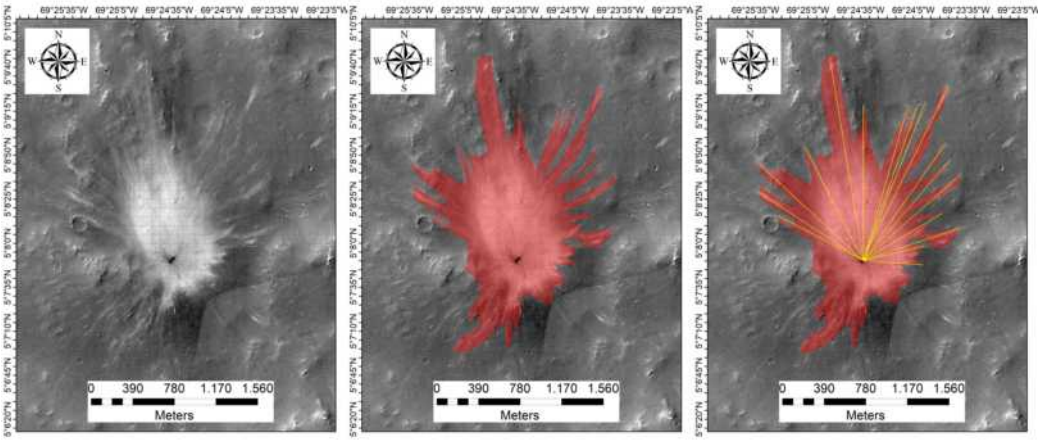

Latitude	Longitude	HiRISE ID	Area (m^2)	Diam.(m)	DCI	TI day	TI night	Epoch	Azimuth
5.131°	290.591°	ESP_026892_1850	1986326.2	35.5	0.953	202	126	Early Hesp.	12.7

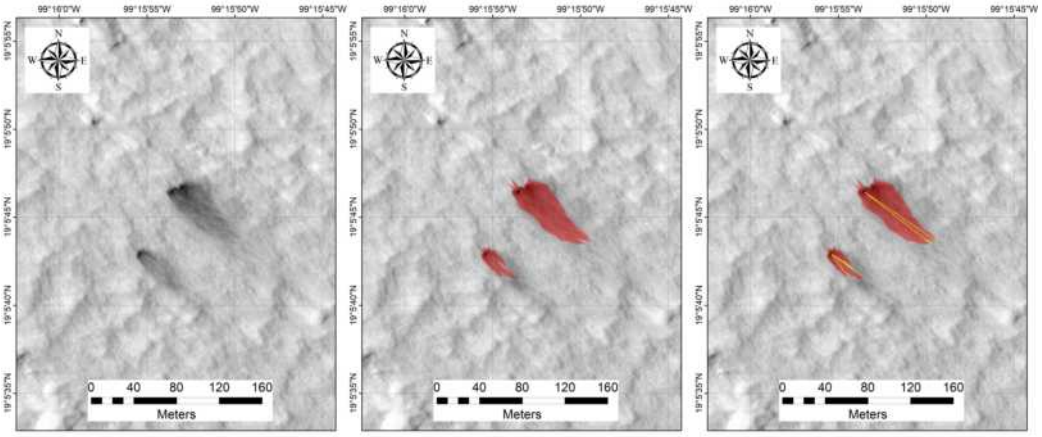

Latitude	Longitude	HiRISE ID	Area (m^2)	Diam.(m)	DCI	TI day	TI night	Epoch	Azimuth
19.096°	260.735°	ESP_026893_1995	1898.4	2.4	0.935	40	63	Amaz./Hesp.	125.9
19.096°	260.735°	ESP_026893_1995	373.9	2.0	0.935	40	63	Amaz./Hesp.	130.0

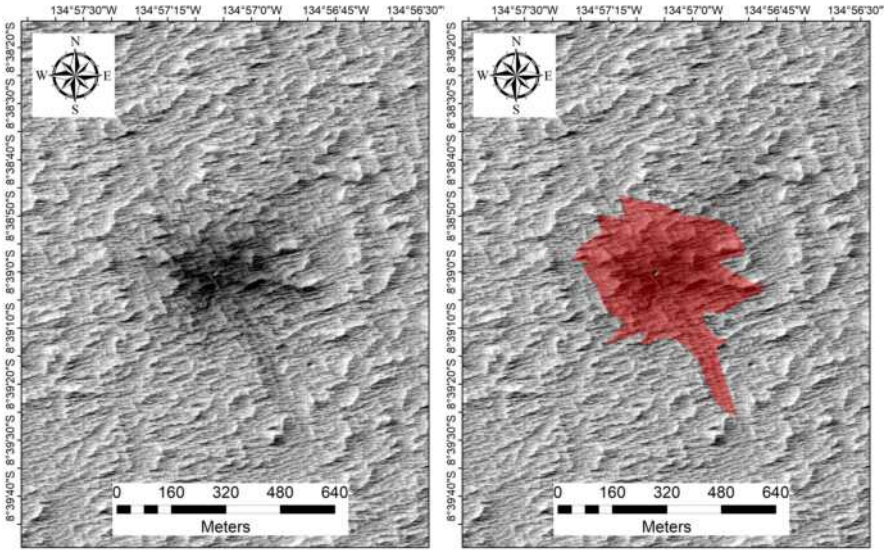

Latitude	Longitude	HiRISE ID	Area (m^2)	Diam.(m)	DCI	TI day	TI night	Epoch
−8.650°	225.048°	ESP_026934_1715	160140.7	15.8	0.943	42	101	Amaz./Hesp.

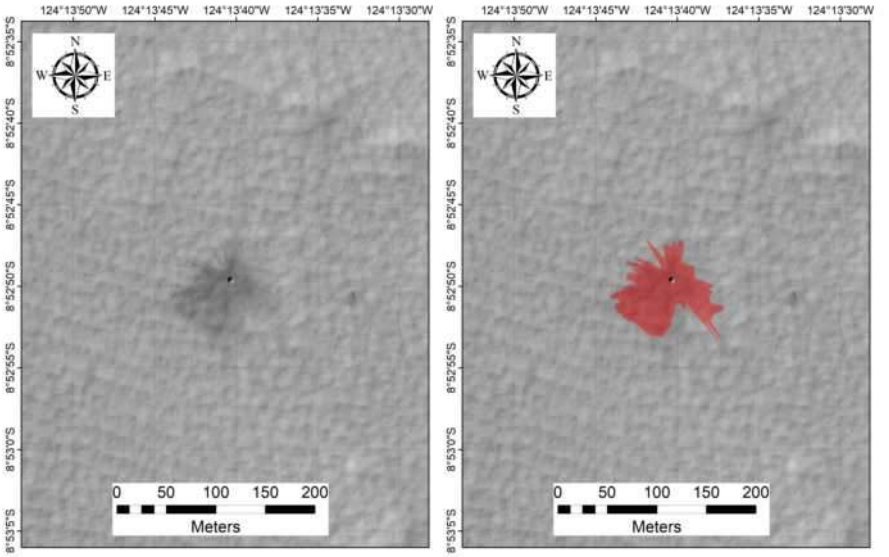

Latitude	Longitude	HiRISE ID	Area (m^2)	Diam.(m)	DCI	TI day	TI night	Epoch
−8.880°	235.772°	ESP_026960_1710	5504.6	5.7	0.937	69	26	Amaz./Hesp.

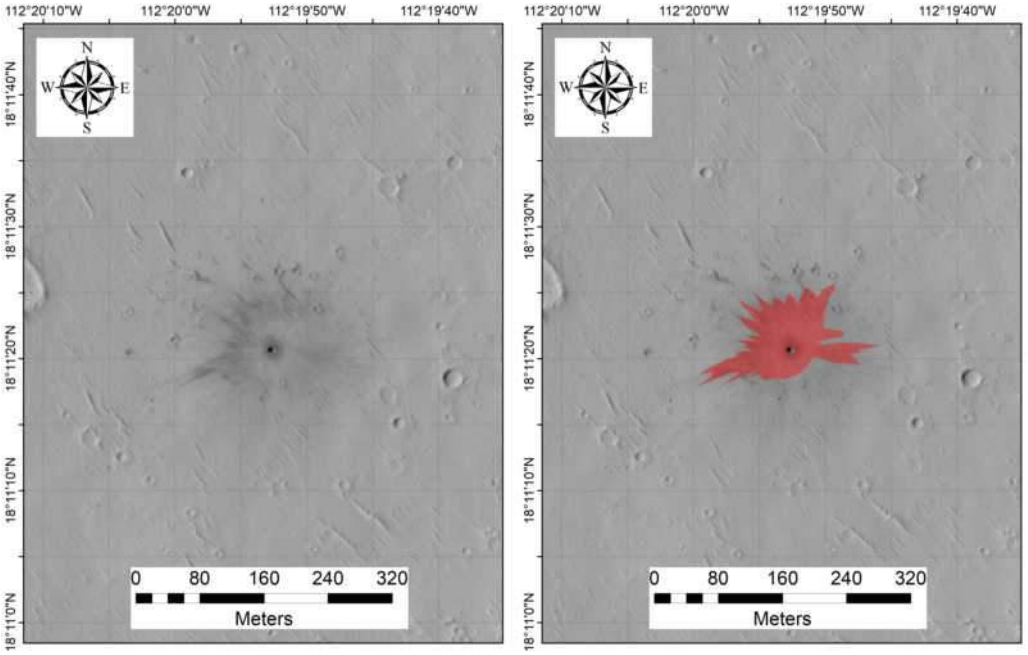

Latitude	Longitude	HiRISE ID	Area (m^2)	Diam.(m)	DCI	TI day	TI night	Epoch
18.189°	247.669°	ESP_026999_1985	11224.5	9.1	0.940	16	58	Amaz./Hesp.

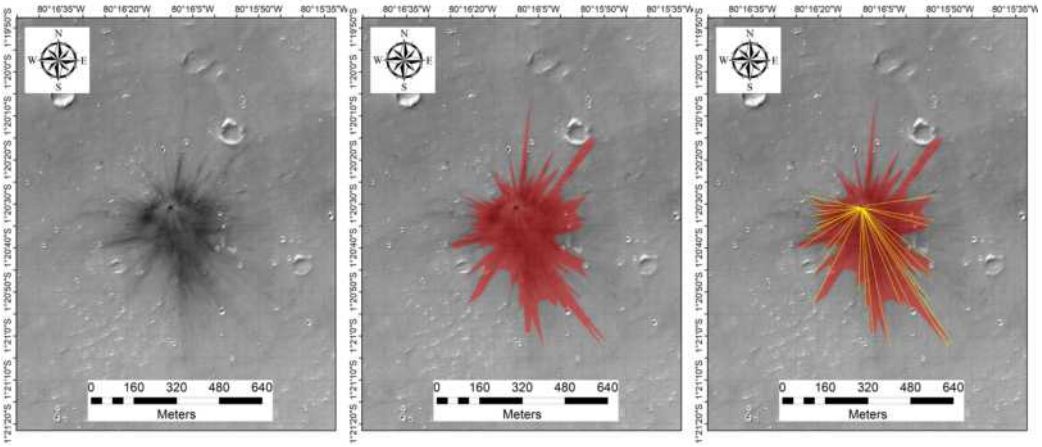

Latitude	Longitude	HiRISE ID	Area (m^2)	Diam.(m)	DCI	TI day	TI night	Epoch	Azimuth
−1.342°	279.731°	ESP_027077_1785	161092.4	10.4	0.957	160	105	Early Hesp.	174.6

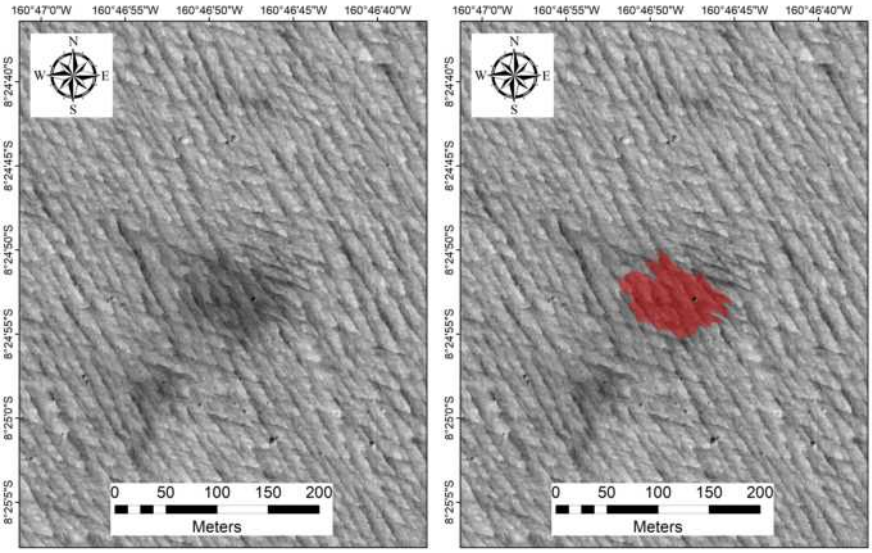

Latitude	Longitude	HiRISE ID	Area (m^2)	Diam.(m)	DCI	TI day	TI night	Epoch
−8.415°	199.220°	ESP_027080_1715	5045.1	4.6	0.946	58	50	Middle Noach.

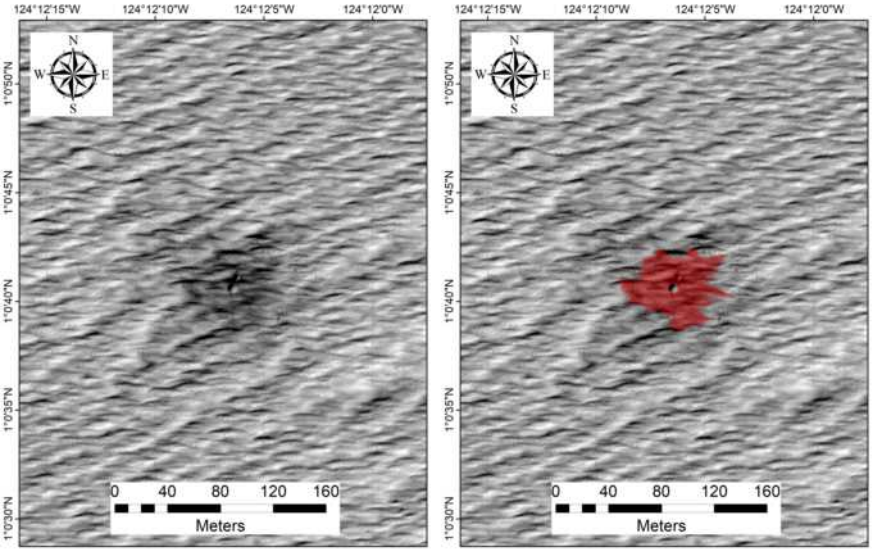

Latitude	Longitude	HiRISE ID	Area (m^2)	Diam.(m)	DCI	TI day	TI night	Epoch
1.011°	235.798°	ESP_027316_1810	2864.7	6.3	0.933	34	65	Amaz./Hesp.

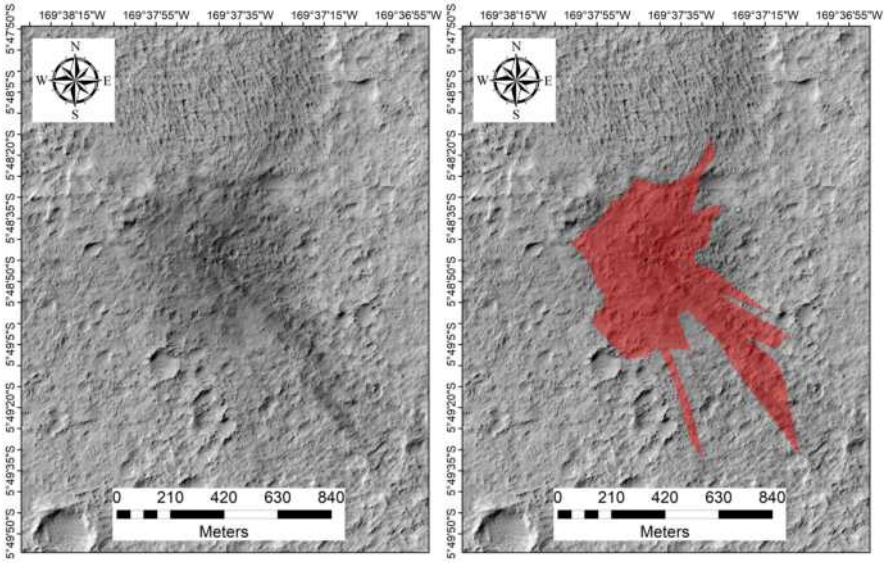

Latitude	Longitude	HiRISE ID	Area (m^2)	Diam.(m)	DCI	TI day	TI night	Epoch
−5.812°	190.371°	ESP_027410_1740	378973.6	13.8	0.942	75	23	Early Hesp.

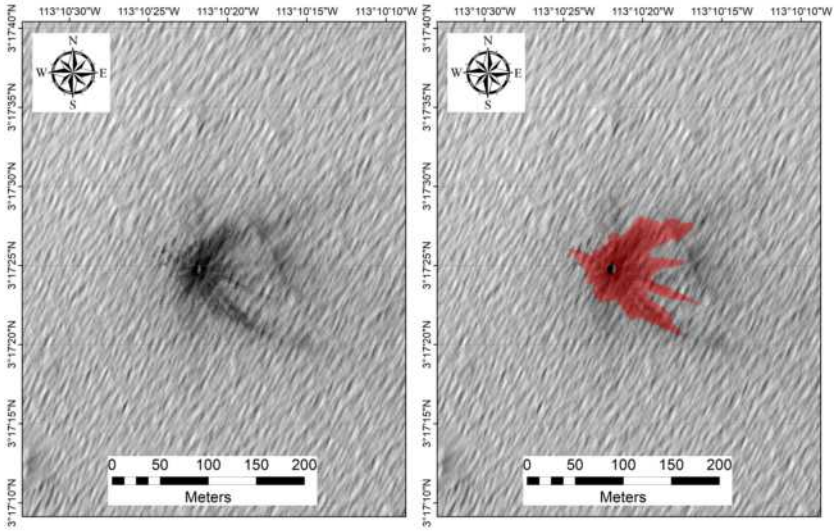

Latitude	Longitude	HiRISE ID	Area (m^2)	Diam.(m)	DCI	TI day	TI night	Epoch
3.290°	246.827°	ESP_027975_1835	7212.6	9.6	0.933	50	121	Amazonian

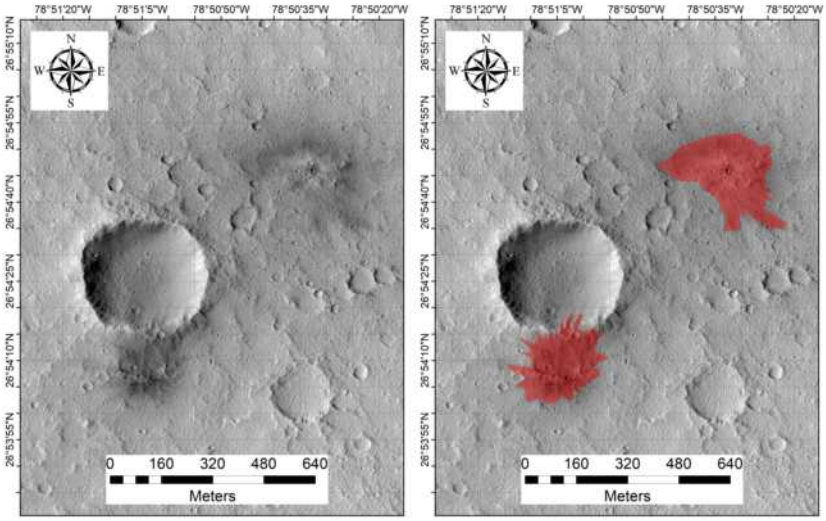

Latitude	Longitude	HiRISE ID	Area (m^2)	Diam.(m)	DCI	TI day	TI night	Epoch
26.902°	281.149°	ESP_028000_2070	62925.1	9.6	0.938	15	79	Early Hesp.
26.902°	281.149°	ESP_028000_2070	46571.6	7.9	0.938	15	79	Early Hesp.

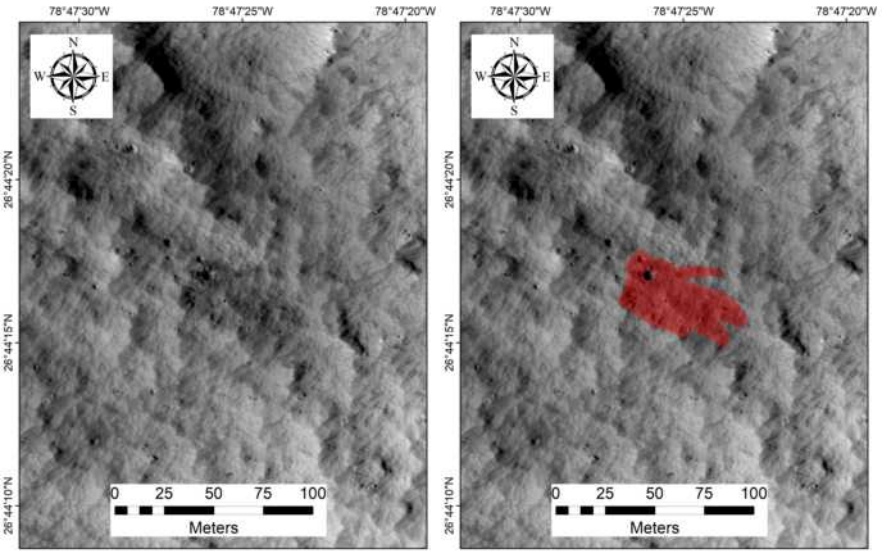

Latitude	Longitude	HiRISE ID	Area (m^2)	Diam.(m)	DCI	TI day	TI night	Epoch
26.738°	281.209°	ESP_028633_2070	1718.9	5.1	0.939	67	59	Early Hesp.

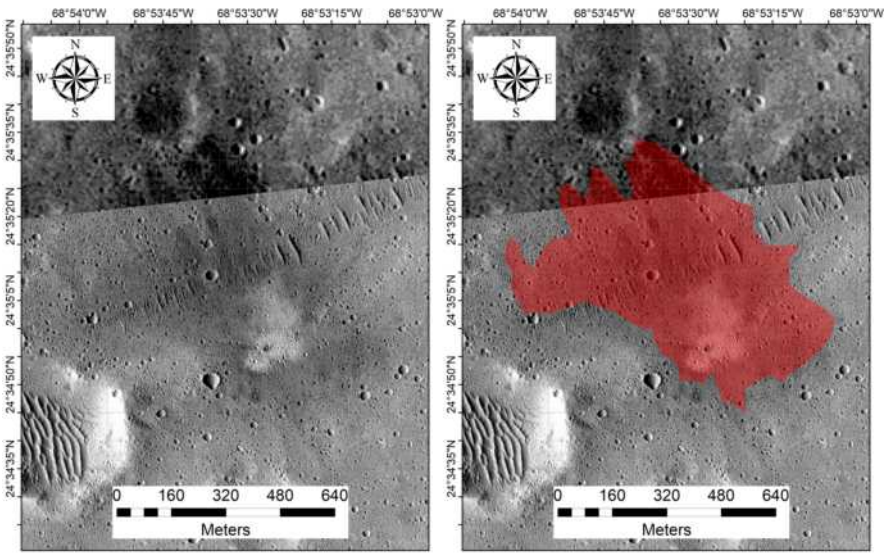

Latitude	Longitude	HiRISE ID	Area (m^2)	Diam.(m)	DCI	TI day	TI night	Epoch
24.582°	291.109°	ESP_028659_2050	370142.8	10.7	0.944	40	71	Early Hesp.

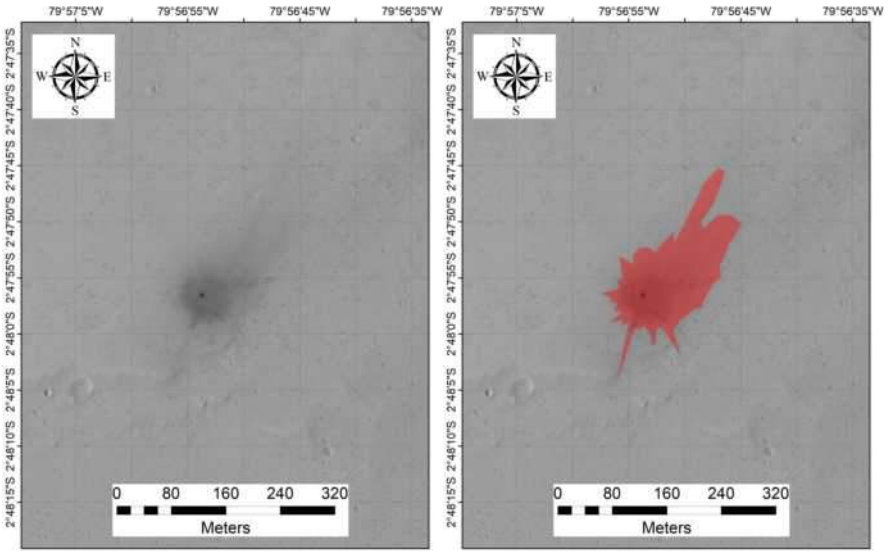

Latitude	Longitude	HiRISE ID	Area (m^2)	Diam.(m)	DCI	TI day	TI night	Epoch
−2.799°	280.052°	ESP_028976_1770	21250.8	4.2	0.949	180	62	Early Hesp.

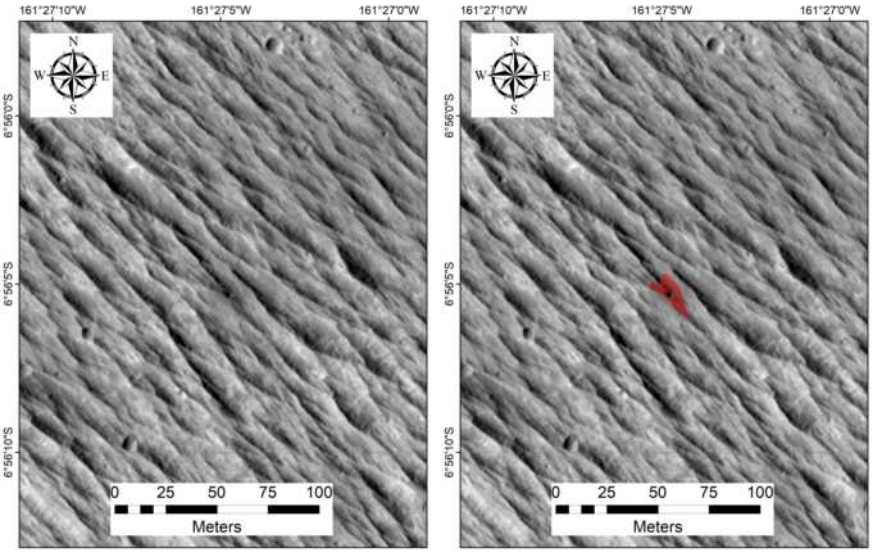

Latitude	Longitude	HiRISE ID	Area (m^2)	Diam.(m)	DCI	TI day	TI night	Epoch
−6.935°	198.549°	ESP_028979_1730	164.6	3.5	0.941	64	46	Middle Noach.

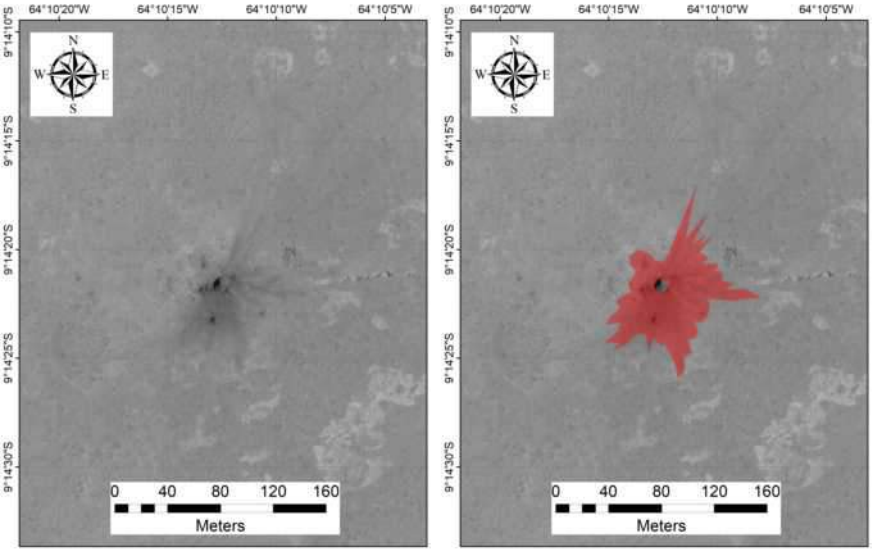

Latitude	Longitude	HiRISE ID	Area (m^2)	Diam.(m)	DCI	TI day	TI night	Epoch
−9.239°	295.830°	ESP_029015_1705	5244.8	9.7	0.952	212	173	Early Hesp.

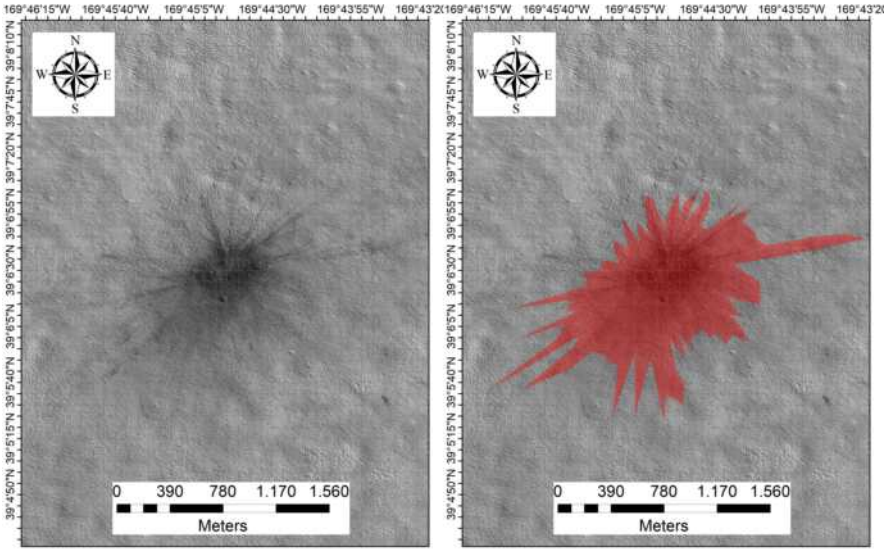

Latitude	Longitude	HiRISE ID	Area (m^2)	Diam.(m)	DCI	TI day	TI night	Epoch
39.092°	190.276°	ESP_029256_2195	1370958.9	12.5	0.941	124	141	Amazonian

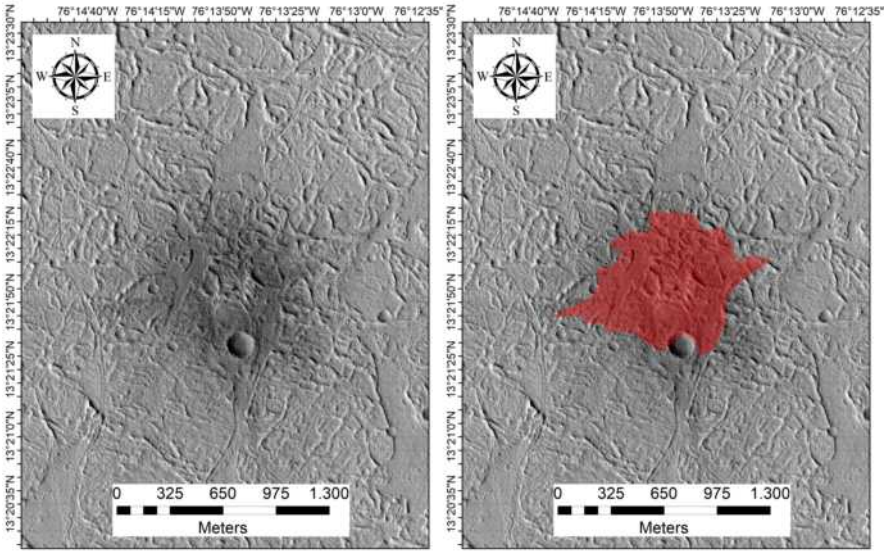

Latitude	Longitude	HiRISE ID	Area (m^2)	Diam.(m)	DCI	TI day	TI night	Epoch
13.336°	283.772°	ESP_029701_1935	582627.5	15.6	0.937	99	89	Amaz./Hesp.

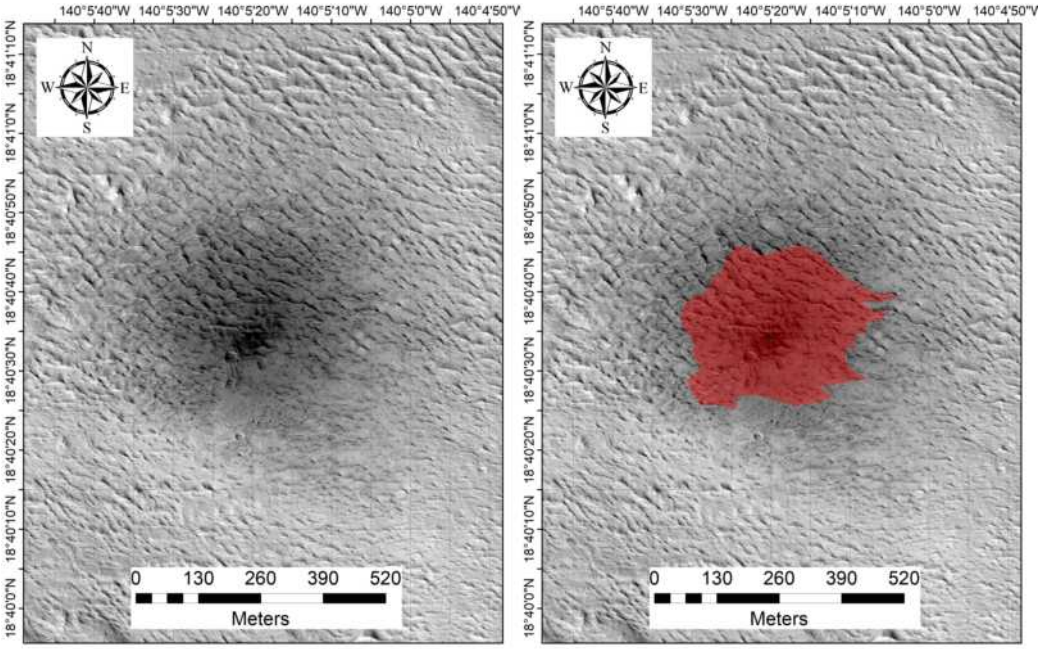

Latitude	Longitude	HiRISE ID	Area (m^2)	Diam.(m)	DCI	TI day	TI night	Epoch
18.676°	219.911°	ESP_030178_1990	99825.5	8.9	0.929	116	65	Amazonian

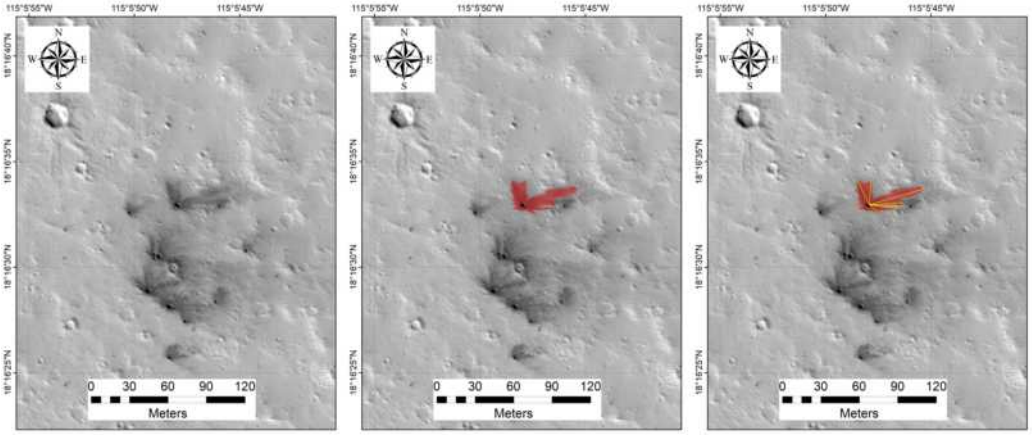

Latitude	Longitude	HiRISE ID	Area (m^2)	Diam.(m)	DCI	TI day	TI night	Epoch	Azimuth
18.222°	244.905°	ESP_030243_1985	604.4	3.5	0.932	70	80	Late Hesp.	65.4

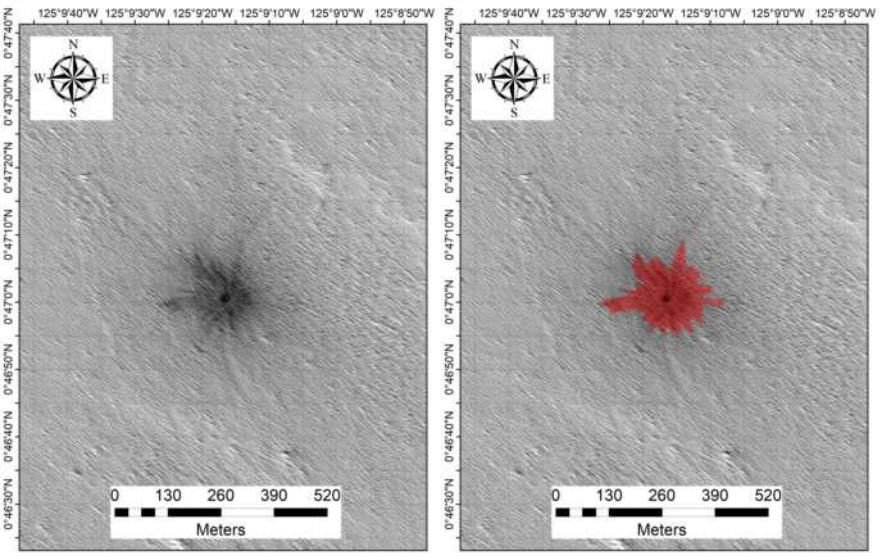

Latitude	Longitude	HiRISE ID	Area (m^2)	Diam.(m)	DCI	TI day	TI night	Epoch
0.783°	234.845°	ESP_030705_1810	29223.5	9.7	0.939	57	20	Amaz./Hesp.

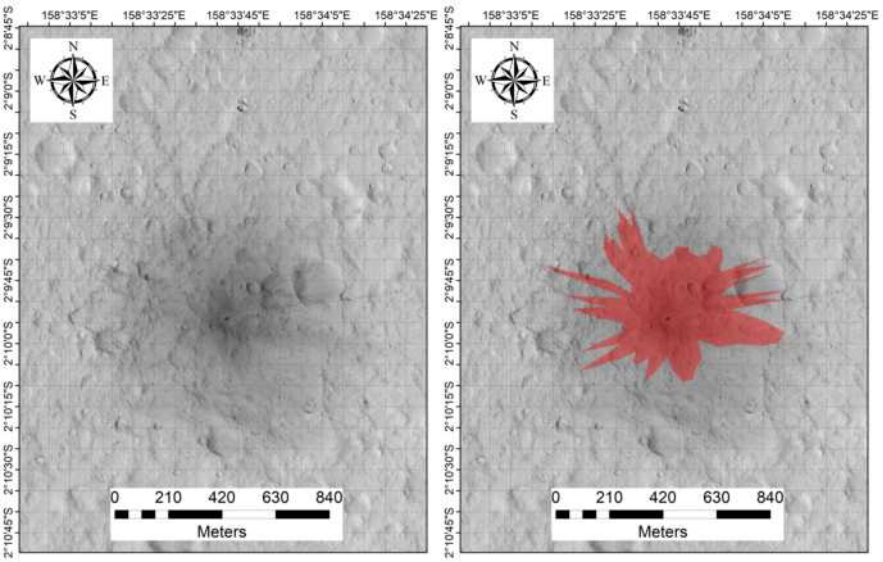

Latitude	Longitude	HiRISE ID	Area (m^2)	Diam.(m)	DCI	TI day	TI night	Epoch
−2.165°	158.562°	ESP_032211_1780	254051.3	7.9	0.936	104	105	Early Hesp.

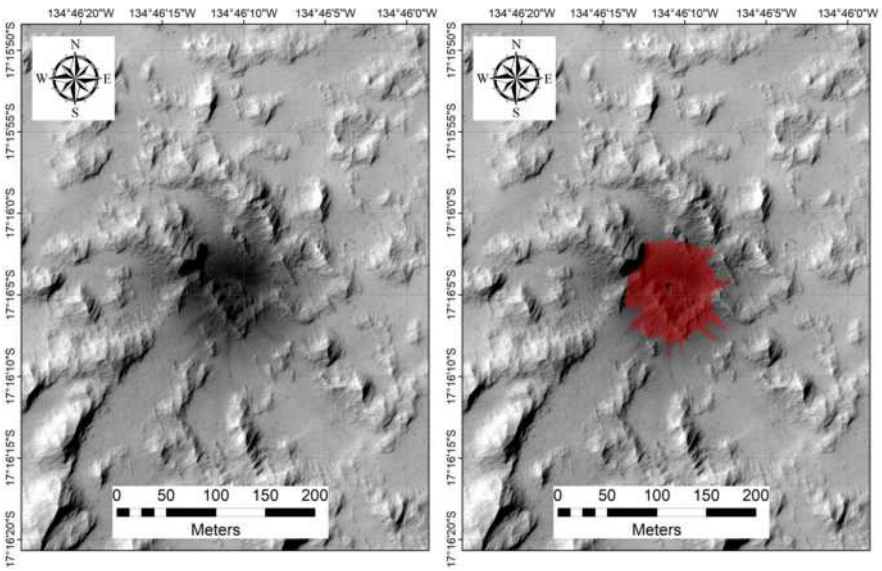

Latitude	Longitude	HiRISE ID	Area (m^2)	Diam.(m)	DCI	TI day	TI night	Epoch
−17.268°	225.230°	ESP_033870_1625	7406.3	5.6	0.937	15	31	Amaz./Hesp.

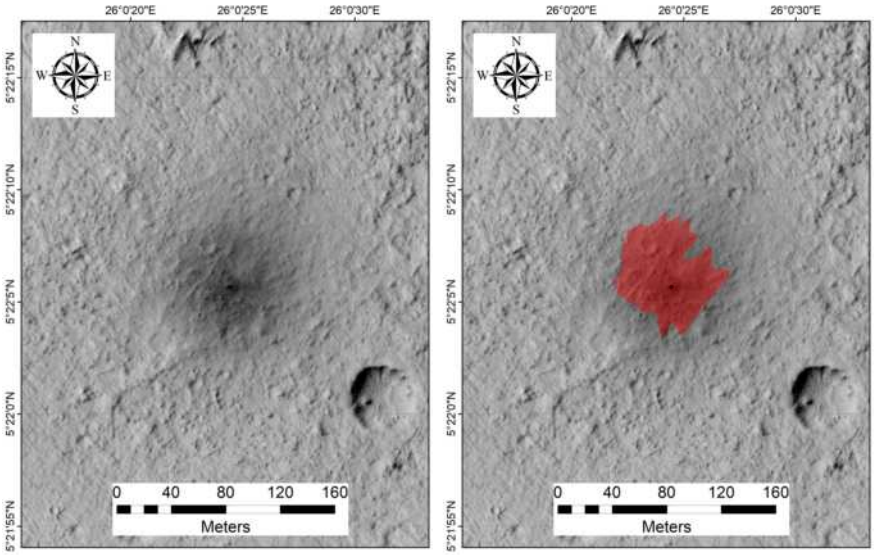

Latitude	Longitude	HiRISE ID	Area (m^2)	Diam.(m)	DCI	TI day	TI night	Epoch
5.368°	26.007°	ESP_035354_1855	4340.5	2.9	0.943	19	42	Middle Noach.

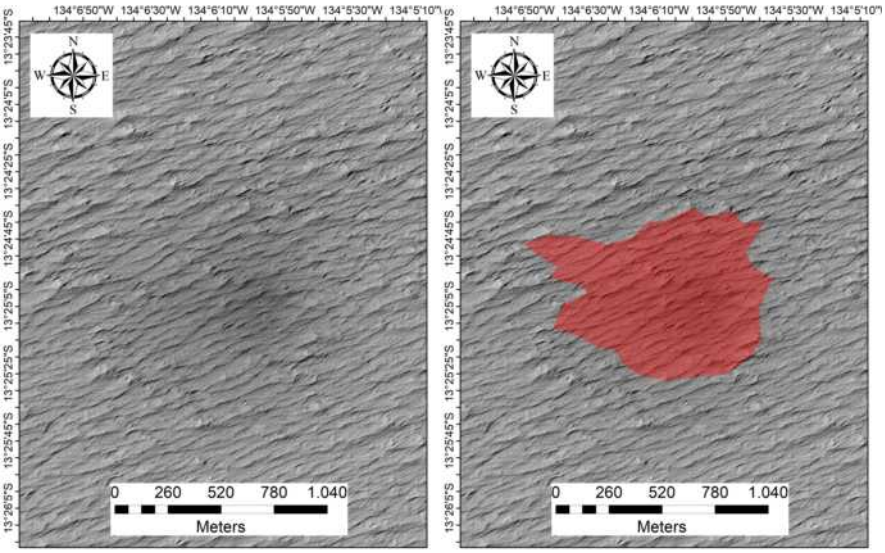

Latitude	Longitude	HiRISE ID	Area (m^2)	Diam.(m)	DCI	TI day	TI night	Epoch
−13.418°	225.897°	ESP_036916_1665	655657.4	15.3	0.936	22	21	Amaz./Hesp.

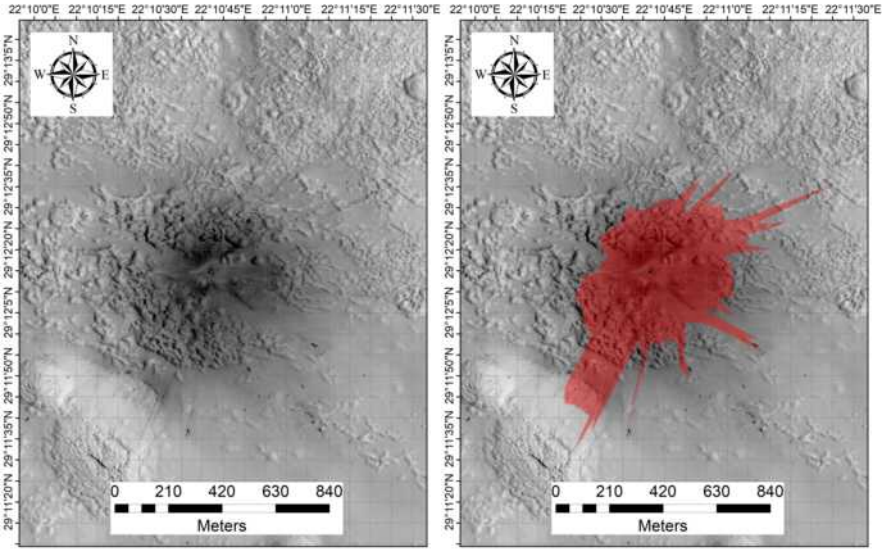

Latitude	Longitude	HiRISE ID	Area (m^2)	Diam.(m)	DCI	TI day	TI night	Epoch
29.203°	22.179°	ESP_036976_2095	348456.2	13.6	0.921	56	37	Middle Noach.

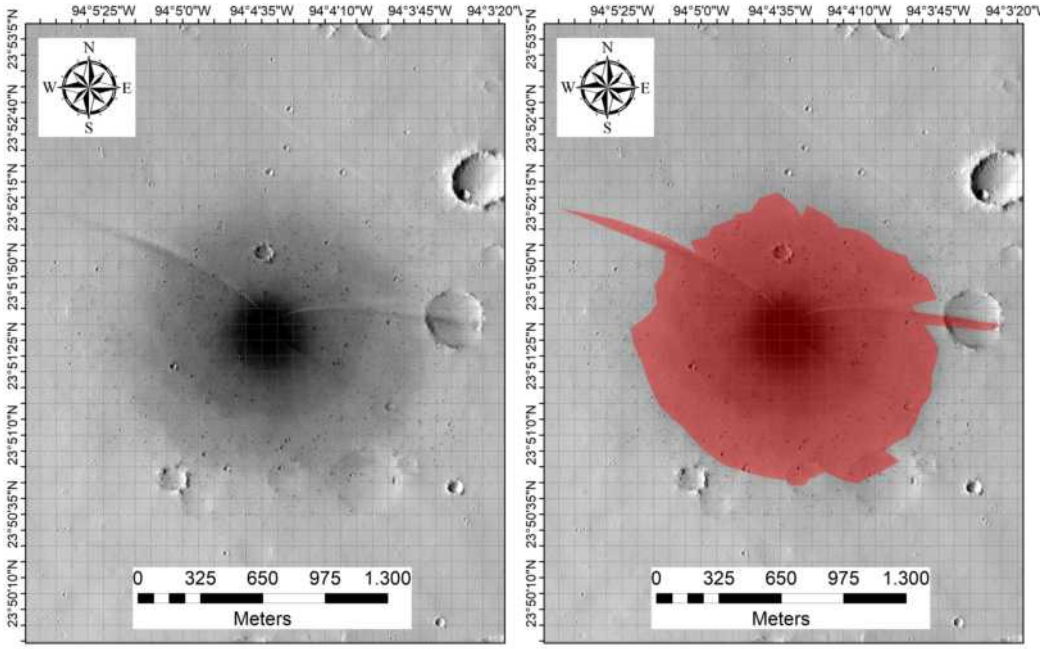

Latitude	Longitude	HiRISE ID	Area (m^2)	Diam.(m)	DCI	TI day	TI night	Epoch
23.858°	265.925°	ESP_037033_2040	1751859.2	4.7	0.936	19	45	Amaz./Hesp.

Bibliography

Andrews-Hanna, J.C., Zuber, M.T. and Banerdt., W.B., 2008. *The Borealis basin and the origin of the martian crustal dichotomy*, Nature 453, 1212-1215. doi:10.1038/nature07011.

Balme M. and Greeley R., 2006. *Dust devils on Earth and Mars*, Rev. Geophys. 44, RG3003. doi:10.1029/2005RG000188.

Barlow, N.G. and Boyce, J.M. 2016. *The role of target characteristics in the formation of impact crater ejecta morphologies at high latitude on Mars.* In: The Sixth International Conference on Mars Polar Science and Exploration, held 5-9 September, 2016 in Reykjavik, Iceland. LPI Contribution No. 1926, id.6019.

Bart, G.D. et al., 2019. *Dark halos produced by current impact cratering on Mars*, Icarus 328, 45–57. doi:10.1016/j.icarus.2019.03.004.

Bell III, J.F. et al., 2013. *Calibration and performance of the Mars Reconnaissance Orbiter Context Camera (CTX)*, MARS 8, 1-14. doi:10.1555/mars.2013.0001.

Berman, D.C. and Hartmann, W.K., 2002. *Recent Fluvial, Volcanic, and Tectonic Activity on the Cerberus Plains of Mars*, Icarus 159, 1–17. doi:10.1006/icar.2002.6920.

Carr, M.H. and Head, J.W., 2010. *Geologic history of Mars*, Earth Planet. Sci. Lett. 294, 185–203. doi:10.1016/j.epsl.2009.06.042.

Christensen, P.R. et al., 2004. *The Thermal Emission Imaging System (THEMIS) for the Mars 2001 Odyssey mission*, Space Sci. Rev. 110(1), 85-130. doi:10.1023/B:SPAC.0000021008.16305.94.

Clifford, S.M., 1993. *A Model for the Hydrologic and Climatic Behavior of Water on Mars*, J. Geophys. Res. 98 (E6), 10,973–11,016. doi:10.1029/93JE00225.

Daubar, I.J. et al., 2013. *The current martian cratering rate*, Icarus 225, 506-516. doi:10.1016/j.icarus.2013.04.009.

Daubar, I.J. et al., 2014. *The morphology of small fresh craters on Mars and the Moon*, J. Geophys. Res. Planets, 119, 2620–2639, doi:10.1002/2014JE004671.

Daubar, I.J. et al., 2015. *Changes in blast zone albedo patterns around new martian impact craters*, Icarus 267, 86-105. doi: 10.1016/j.icarus.2015.11.032.

Davila, A.F. et al., 2013. *Perchlorate on Mars: a chemical hazard and a resource for humans*, Int. J. Astrobiol. 12 (4), 321-325. doi:10.1017/S1473550413000189.

Delamere, A., 2003. *MRO High Resolution Imaging Science Experiment (HiRISE): Instrument Development*, Sixth International Conference on Mars, held 20-25 July, 2003 in Pasadena, United States.

Dohm, J.M. et al., 2009. *GRS evidence and the possibility of paleooceans on Mars*, Planet. Space Sci. 57, 664-684. doi:10.1016/j.pss.2008.10.008.

Dundas, C.M. et al., 2014. *HiRISE observations of new impact crater exposing Martian ground ice*, J. Geophys. Res. Planets 119, 109–127. doi: 10.1002/2013JE004482.

Franz, H.B. et al., 2017. *Initial SAM calibration gas experiments on Mars: Quadrupole mass spectrometer results and implications*, Planet. Space Sci. 138, 44-54. doi:10.1016/j.pss.2017.01.014.

Jakosky, B.M. et al., 2015. *Initial results from the MAVEN mission to Mars*, Geophys. Res. Lett. 42, 8791–8802. doi:10.1002/2015GL065271.

Kostama, V.-P., Kreslavsky, M.A. and Head, J.W., 2006. *Recent high-latitude icy mantle in the northern plains of Mars: Characteristics and ages of emplacement*, Geophys. Res. Lett. 33, L11201. doi:10.1029/2006GL025946.

Kreslavsky, M.A. and Head, J.W., 2002. *Fate of outflow channel effluents in the northern lowlands of Mars: The Vastitas Borealis Formation as a sublimation residue from frozen ponded bodies of water*, J. Geophys. Res. 107, 5121. doi:10.1029/2001JE001831.

Malin, M.C. and Edgett K.S., 2003. *Evidence for Persistent Flow and Aqueous Sedimentation on Early Mars*, Science 302, 1931. doi:10.1126/science.1090544.

McGill, G.E., 1989. *Buried topography of Utopia, Mars: Persistence of a giant impact depression*, J. Geophys. Res. 94, 2753-2759. doi:10.1029/JB094iB03p02753.

McSween, H.Y. et al., 2009 *Elemental Composition of the Martian Crust*, Science 324, 736. doi:10.1126/science.1165871.

Moore, J.M. and Wilhelms, D.E., 2001. *Hellas as a Possible Site of Ancient Ice-Covered Lakes on Mars*, Icarus 154, 258-276. doi:10.1006/icar.2001.6736.

Neumann, G.A. et al., 2004. *Crustal structure of Mars from gravity and topography*, J. Geophys. Res. 109, E08002. doi:10.1029/2004JE002262.

Osinski, G.R., 2004. *Hypervelocity impact into sedimentary targets: Pro-*

cesses and products (PhD Thesis). University of New Brunswick.

Pajola, M. et al., 2019. *Planetary Mapping for Landing Sites Selection: The Mars Case Study*, In: Hargitai, H. (ed.), *Planetary Cartography and GIS.* Lecture Notes in Geoinformation and Cartography. Springer. `https://link.springer.com/chapter/10.1007/978-3-319-62849-3_7`. doi: 10.1007/978-3-319-62849-3_7.

Putzig, N.E. and Mellon M.T., 2007. *Apparent thermal inertia and the surface heterogeneity of Mars*, Icarus 191, 68–94. doi:10.1016/j.icarus.2007.05.013.

Putzig, N.E. et al., 2005. *Global thermal inertia and surface properties of Mars from the MGS mapping mission*, Icarus 173, 325–341. doi:10.1016/j.icarus.2004.08.017.

Rossi, A.P. and van Gasselt, S. (Eds.), 2018. *Planetary Geology*, pp. 123-144. Springer. doi:10.1007/978-3-319-65179-8.

Ruff, S.W. and Christensen, P.R., 2002. *Bright and dark regions on Mars: Particle size and mineralogical characteristics based on Thermal Emission Spectrometer data*, J. Geophys. Res. 107 (E12), 5127. doi:10.1029/2001JE001580.

Schneider, N.M. et al., 2015. *Discovery of diffuse aurora on Mars*, Science 350, 6261. doi:10.1126/science.aad0313.

Smith, B.A. et al., 1979. *The Jupiter system through the eyes of Voyager 1*, Science 204, 4396, 951–972. doi:10.1126/science.204.4396.951.

Smith, D.E. et al., 2001. *Mars Orbiter Laser Altimeter: Experiment summary after the first year of global mapping of Mars*, J. Geophys. Res. 106 E10, 23,689-23,722. doi:10.1029/2000JE001364.

Tanaka, K.L. et al., 2014. *Geologic Map of Mars*, U.S. Geological Survey Scientific Investigations Map 3292, pamphlet 43 p. doi:10.3133/sim3292.

Werner, S.C., 2009. *The global martian volcanic evolutionary history*, Icarus 201, 44-68. doi:10.1016/j.icarus.2008.12.019.